Experimental and Computational Study of Hypervelocity Impact on Brittle Materials and Composites

A Thesis Submitted for the Degree of Doctor of Philosophy

by

Emma Ariane Taylor

April 1998

The Unit for Space Sciences and Astrophysics
School of Physical Sciences
University of Kent at Canterbury

Abstract

Retrieval and analysis of space-exposed surfaces from Low Earth Orbit (LEO) can lead to an improved understanding of the space debris and micrometeoroid particulate environment. A large volume of data has been accumulated from analysis of space-exposed ductile materials, including the LDEF satellite. The Hubble Space Telescope (HST) and EURECA solar arrays provide a large, new source of information on the LEO particulate flux. Below a certain crater diameter, these solar arrays are equivalent to semi-infinite brittle material targets and thus the impact crater fluxes are analogous to impact fluxes on returned lunar rocks and Apollo/Gemini windows.

An extensive shot programme has been executed onto glass, aluminium and spacecraft honeycomb (used as exterior spacecraft wall and solar array support structure). The data supplement the large database of brittle material hypervelocity impact tests used in this thesis. These data have been used to (i) develop new, target-dependent, empirically-determined brittle material damage equations, (ii) derive a conversion factor between the brittle material conchoidal diameter (D_{co}) and the ballistic limit in aluminium for a particular exposure and shielding history (F_{max}), and (iii) investigate the ballistic limit of spacecraft honeycomb. In addition, the response of brittle materials to hypervelocity impact has been explored via hydrocode modelling, including the implementation and validation of the Johnson-Holmquist brittle material model at velocities beyond the experimental calibration regime.

The converted semi-infinite brittle material fluxes from the HST and EURECA solar arrays have been directly compared with both an experimentally-measured LDEF mean flux and a modelled flux prediction for meteoroids (excluding space debris). The solar array fluxes are in good agreement with the LDEF data and modelling results for F_{max} greater than 20-30 μm. Below this value of F_{max}, the data do not reproduce the space debris flux enhancement shown by LDEF.

Acknowledgements

My supervisors (Laurie Kay and Tony McDonnell) have had the unenviable task of steering me through to the end of my PhD. Their patience, intelligent suggestions and creative approach to finding funds for experimental programmes and conference attendance have allowed me to present my work to as wide an audience as possible. Thanks are also due to Simon Green, Mark Burchell, Neil McBride, John Zarnecki, Bob Newport and Paul Ratcliff for suggestions, guidance and snippets of good advice during my research. This PhD was sponsored by John Hobbs (Matra Marconi Space) and the University of Kent at Canterbury. Thanks are due to both John Hobbs and Lucy Berthoud (also MMS) for providing the engineering balance to the research activities carried out at Kent. My conference presentations have been funded by grants from the Hypervelocity Impact Society, Institute of Physics, Institute of Materials, UKC Alumni Fund, Royal Academy of Engineering and Commercial Space Technologies Limited, as well as the contribution made by the Unit for Space Sciences and Astrophysics.

Century Dynamics Limited have made available to me a special version of their AUTODYN hydrocode, taking it to new brittle material modelling heights. Thanks to Nigel Francis, Colin Hayhurst and Norman Robertson for the CDL time and technical support over the past year. Kostas Tsembelis, as the resident shock physics theoretician, was the other team member working to develop a brittle material model. Thanks also go to Cathy Cowdery and Major MacKenzie (DERA Chertsey) who tested our brittle material model against their data. Neil Bourne (Shock Physics Group, Cambridge University), Ian Cullis and Phil Church (DERA Fort Halstead) kindly allowed me to sit in on a research meeting or two, to further my understanding of brittle material models. Back on the experimental side, Mike Cole has been invaluable in helping me to run my extensive shot programmes. Don and his team in the Physics Workshop made me laugh, managed to make sense of my drawings, and always managed to get my 'rush jobs' done in time.

When I first thought about doing hypervelocity impact tests on spacecraft honeycomb in my first year of my PhD, I had to search long and hard to meet people in the field. Thanks go to Marcel Kay (National Physical Laboratory), Gerald Manuelpillai and Chantal Lamontagne (University of Toronto Institute of Aerospace Studies) for ideas and discussions. Obtaining targets was a difficult task, finally achieved by Mark Herbert (formerly MMS, now GKN Westland Ltd). Mark Herbert has also collaborated with me throughout the honeycomb research programme. The Metop team at MMS also deserve thanks for sourcing honeycomb samples and answering questions in the early days of the research. The shot programmes were supported by Mike Cole and Rob Thomson and the photography by Spencer Scott (UKC Photographic Unit). Dave Clarke (GKN Westland Ltd) carried out the X-ray of the first honeycomb target, identifying the surprisingly large internal impact damage. That image is my favourite for convincing space engineers that they have to worry about debris

impact. John Hodgkinson (Centre for Composite Materials, Imperial College) let me use their X-ray facilities to uncover the hidden damage lurking behind those impact holes for all fifty or so targets.

The analysis of hypervelocity impact onto solar cells would not have been possible without Nick Shrine's help. His parallel studies of the influence of impact angle on solar cell morphology and the survey he carried out on space-exposed HST cells provided a valuable check against the conclusions obtained from my studies on soda-lime glass. We combined our data to search for the best possible solar-cell-to-aluminium crater conversion and I would like to acknowledge his help in finding the way through the large volume of data. Fortunately, we've both come up with the same answers for the conversion factors ! Thanks are also due to Neil McBride and Simon Green for providing the LDEF data against which to test the converted solar cell fluxes.

The now-notorious writing club (known as the biscuits and pants group) has been responsible for maintaining my sanity over the writing-up period: Nick Shrine, Jon Marchant, Andrew Ball and Kostas Tsembelis - thanks for the food, beer, chocolate, strange music and the company through those long days. Thanks, too, to Neil McBride for curries, beer, hi-fi consultancy and the occasional GLE tutorials. The 111A crowd, including David Gardner, Andrew Griffiths, Ian Collier and David Wallis, have had the task of sharing office space with me; thanks for answering those phone calls and keeping me on track. When I first arrived, Mark English, Neil Mackay, Hajime Yano and Wayne Brook-Thomas (as the more senior PhD third and fourth years) were friendly and helpful in pointing out the pitfalls of PhD life.

Sarah Dunkin (University College London), my partner-in-crime for the Educational Space Science and Technology Lectures (ESSTeL, funded by PPARC's Public Understanding of Science Scheme), has been an invaluable source of support throughout the PhD, both personally and professionally. I would also like to thank my friends Rosie and Jules for being musicians and not space scientists and Urs, Corinne and Anna (when we managed to meet up!) for parties and fun. The Space Education Trust are thanked for finding the money to send me to the International Space University in 1995; the ISU family themselves are too numerous to mention here.

And finally, thanks to my family for supporting me through the past few years and making this PhD possible.

Nomenclature

(I) Acronyms and Abbreviations

Al-HC	Aluminium Honeycomb
A/S	Aluminosilicate
B/S	Borosilicate
CDG	Capacitor Discharge Gun
CFRP	Carbon Fibre Reinforced Plastic
ECS	EURECA Solar Array-Front Side
ECS-R	EURECA Solar Array-Rear Side
EDA	Electrostatic Dust Accelerator
EOS	Equation Of State
E-PP	Elastic-Perfectly Plastic
EURECA	European Retrievable Carrier
FQ	Fused Quartz
FS	Fused Silica
GAM	Glass Analogue Model
GBS	Glass Buckshot (also gbs)
HC	Honeycomb
HEL	Hugoniot Elastic Limit
HGF	Hole Growth Factor
HST	Hubble Space Telescope
HVI	Hypervelocity Impact
J-H	Johnson-Holmquist
LDEF	Long Duration Exposure Facility
LEO	Low Earth Orbit
LGG	Light Gas Gun
LINAC	Linear Accelerator
LPG	Lithium Plasma Gun
M-C	Mohr-Coulomb
NRS	Non-Rear Spalling
PDA	Plasma Drag Accelerator
PFA	Post-Flight Analysis
RS	Rear Spalling
SEM	Scanning Electron Microscope
SLG	Soda-Lime Glass
SPH	Smoothed Particle Hydrodynamics
STS	Space Transportation System (Shuttle)
TCB	Tungsten Carbide
TiCCE	Timeband Capture Cell Experiment

VdG	Van der Graaff
VMA	Vertical Mass Accelerator

Boro.	Borosilicate
Cell.	Cellulose
Eul.	Eulerian
Lag.	Lagrangian
Lin.	Linear
Obl.	Oblique
Opt.	Optical
n/a	Not applicable
Poly.	Polystyrene
S/Steel	Stainless Steel

(ii) Symbols

a, A	Constant
A1, A2, A3	Constant
A	Area; along line of flight
b, B	Constant
B	Perpendicular to line of flight
C	Constant
c_0	Speed of sound
D	Damage; Diameter; Constant
d	Projectile diameter
e, E	Internal energy
E	Impact energy
F_{max}	Ballistic limit in aluminium
f	Foil thickness
G	Shear modulus
k, K	Constant
L	Length
m, M	Constant
M	Mass
n, N	Constant
p, P	Pressure
r	Radius; Linear correlation coefficient
r^2	Regression coefficient
R	Constant
S	Weighted sum of squares; Slope of U_s-u_p data
T	Tensile hydrostatic pressure; Target thickness; Temperature

T_c	Depth of penetration
T1, T2, T3	Constant
u, U	Velocity
v	Velocity of impact
v, V	Specific volume
Y	Yield strength

α	Constant
β	Constant; Fraction of elastic material energy converted to hydrostatic pressure
γ	Constant; Ratio of specific heats
Γ	Gruneisen Gamma
δ	Constant
ε	Strain
$\delta(\varepsilon)/\delta\tau$	Strain rate
θ	Impact angle (experimental data)
Θ	Impact angle (damage equations)
μ	Compression
ν	Degrees of freedom
ρ	Density
σ	Stress; Yield strength; Standard deviation
χ^2	Chi-squared

(iii) Subscripts

0	Initial condition
1	Shocked

a	Along line of flight
b	Perpendicular to line of flight
Al	Aluminium
c	Crater
cloudrear	Rear of debris cloud
co	Conchoidal
e	Internal energy
esc	Escape
f	Front; Fractured
crack	Crack
eq	Equivalent
h	Hole
H	Hugoniot reference curve; Homologous temperature
i	ith value; Intact

impact	Impact
m	Maximum damage
max	Maximum
meas	Measured
melt	Melting
p	Effective plastic Strain; Projectile; Pressure; Central pit
pr	Projectile
proj	Projectile
r	Rear; Reference
room	Room
s	Sublimation
sh	Shatter
t	Target; Total
v	Vaporisation

Chapter 1

1. Introduction

The Low Earth Orbit (LEO) particulate environment has been studied by impact detectors flown in orbit since the beginning of the space age. These detectors have also been placed on the majority of deep space missions, exploring both the interplanetary and interstellar dust environment. An additional source of data on the LEO particulate environment, consisting of both man-made (space debris) and natural (meteoroid) particles, has been collected via the analysis of retrieved spacecraft surfaces. The large area-time product of satellite surfaces and solar arrays makes them well-suited to recording the hypervelocity impact craters from a wide range of impacting particles, and complements the smaller area-time product of dedicated impact instruments. To utilise these data, an improved understanding of impact processes on spacecraft surfaces is required.

This thesis presents the results of experimental and computational hypervelocity impact studies on brittle materials and composites. These studies are primarily used to understand better the impactor parameters of space debris and meteoroids as recorded on the retrieved HST and EURECA solar arrays. The results can also be used to characterise the response of the target materials to hypervelocity impact (for engineering purposes).

The results of hypervelocity impact tests on brittle materials and composites can be used to decode impactor parameters from space exposed surfaces. They are also used for (i) development of damage equations (predictive, empirically determined power-law equations, used for characterising target damage), (ii) evaluating damage to systems in LEO, (iii) calibrating brittle material hydrocode runs; the results of which then can be used for (ii) and (iv), and (iv) comparison with planetary cratering. In this thesis the results of hypervelocity impact tests onto brittle materials and composites are presented and (i), (ii) and (iii) are examined in detail.

As the full range of impact velocities often cannot be reproduced in the laboratory for the macroscopic particle diameters of interest, the continued development of the rapidly evolving PC-based computer modelling of hypervelocity impacts is necessary. This modelling capability has allowed for the simulation of impacts onto brittle materials at a wide range of impact velocities, to assist in the development of damage equations.

The fluxes decoded from ductile material spacecraft surfaces continue to be used to update and develop new LEO environment models. The impact data from the recently retrieved brittle material spacecraft surfaces (HST and EURECA solar arrays) also provide

independent information on the LEO environment. However, they have not yet been incorporated into the LEO environment models as they have not yet been directly compared with fluxes derived from impacts on ductile materials. For the HST and EURECA solar array data to be comparable with previously decoded impact data, they must be scaled to compare with ductile material fluxes. In addition, to compare the different fluxes, the spacecraft pointing history and detector shielding (by the Earth and spacecraft) must also be taken into account. Comparison of brittle and ductile material space-exposed surfaces requires a brittle material damage equation evaluation and development programme, and then development of a scaling factor to compare the conchoidal diameter on glass to the ballistic limit in aluminium (F_{max}) for a particular exposure history (pointing, velocity distribution, orbital parameters). This work is presented in this thesis. The fluxes from a range of high resolution scans (representing impacts on the solar array coverglass alone) are converted to F_{max} and compared with results from the LDEF spacecraft and TiCCE experiment. In addition, brittle impact data from LDEF are used to create a space-based aluminium-to-quartz scaling relationship.

In chapter 1, an overview of the Low Earth Orbit environment, recently retrieved brittle material surfaces and previous fluxes decoded from space-exposed surfaces, is given as an introduction to the work presented in this thesis.

1.1 The Near Earth Particulate Environment

The particulate environment encountered by a spacecraft in LEO is composed of natural and man-made (space debris) particles. Natural particles are generally referred to as interplanetary dust. Interplanetary dust covers a wide size range; 100 μm particles and smaller are called micrometeoroids (Leinert and Grün, 1990), those in the range 100 μm to metre sizes are called meteoroids. A fraction of these survive entry into the Earth's atmosphere and their residues are, of course, meteorites. The size regime mainly considered in this thesis is micrometeoroids.

In this section the following topics will be reviewed briefly:

- sources of LEO particulates,
- measurements made at different locations in the solar system,
- the meteoroid models derived from the data sources identified,
- the viewing geometry of the data sources used in this thesis, and
- the influence of space debris within the size regime of interest.

1.1.1 Sources of LEO particulates

Natural particulates in space have three main compositional components: cometary decay products, asteroidal decay products and interstellar dust entering the solar system on hyperbolic orbits. In addition, ejecta from impacts on planetary surfaces also form part of the population. The cometary dust is probably `fluffy' (under-dense, i.e. density ~ 1 g cm

^{3}), being fragments (depleted of volatiles) of the dust and ice matrix thrown off a cometary surface. The asteroidal particles are collisional fragmentation products and are more dense (density ~ 2.5 g cm^{-3}). The encounter velocities (of gravitationally bound meteoroids) to the LEO region can range (Taylor, 1995a) from 11 km s^{-1} (defined by the escape velocity of the Earth) up to ~72 km s^{-1} (so producing impact velocities on LEO spacecraft of up to 80 km s^{-1}). A mean meteoroid encounter velocity is of order 20 km s^{-1}.

Meteoroids entering the LEO environment can generally be divided into two sources - meteoroid streams and sporadic meteoroids. Streams are associated with comets. The cometary decay mechanisms populate the region of space around the parent comet's orbit with similarly orbiting meteoroids. Meteoroid streams are observed when the Earth's orbit passes through the stream orbit and the meteoroids are sometimes observed entering the Earth's atmosphere as 'meteors' (the meteors can be detected visibly as 'shooting stars', or else by the reflection of radar pulses from the ionised meteor trail). Because the detection of the meteors is highly velocity dependent, the apparent numbers seen do not necessarily reflect the true 'picture' when it comes to impact damage on a spacecraft. McBride (1996) showed that the annual meteoroid streams contribute at most 10% of the annual mean at F_{max} = 1 mm. However, streams could be important if the exposure is such that the exposed time is short (the instantaneous flux from particular streams can be higher than the annual mean) and if the geometry of the spacecraft is such that the exposed surface is perpendicular to the stream impact direction. Sporadic meteoroids are those which are not associated with streams. These can be from cometary origin, or from asteroidal origin. The cometary particles may have dynamically evolved such that their orbits are no longer associated with their parent comets (so becoming 'sporadic').

Asteroidal collisional fragments contribute to the sporadic dust environment. The Poynting-Robertson effect causes the particles to reduce their eccentricity and semi-major axes. The particles are observed spiralling inward towards the Sun (due to the deceleration applied by radiation), so intersecting the Earth's orbit with relatively low encounter speeds. Collisional processes can also occur between fragments. This is particularly important near the Sun where the spatial density is relatively high. Sub-micron grains are accelerated along the radial vector away from the Sun by the solar radiation pressure. These accelerated fragments are detected at the Earth and are designated β meteoroids.

In addition, interstellar dust passes through the solar system. Identification of small (sub micron) particles beyond 2 AU was made by the plasma dust detector aboard the Galileo and Ulysses spacecraft (Baghul *et al.*, 1995; Grün *et al.*, 1993). Larger hyperbolic particles have also been detected at Earth by meteor radar methods (Taylor *et al.*, 1996a).

The composition of space debris is, of course, directly related to the material placed in orbit. Materials such as steel alloys, titanium, aluminium alloys, rocket motor fuel particles, and coolant from nuclear reactors have all been identified in LEO. Each piece of space debris in orbit is a possible source of more space debris as the result of a hypervelocity impact and fragmentation and/or production of ejecta. The peak in the 22 year solar cycle acts to increase the mean altitude (and thus density at a particular altitude) of the atmosphere. Space debris is then brought under an increasing influence of atmospheric air drag, which depletes the population. Explosions of upper stages and satellite bodies are, perhaps, the most 'destructive' in terms of creating large volumes of space debris. A recent review of the space debris problem is provided by Griffiths (1997).

1.1.2 Impact flux data

Models of the interplanetary dust are derived from fits to impact flux data. They are derived from a range of sources, classified by their distance from the Sun and their position with respect to the Earth's (and Lunar) gravitational well. Time-resolved impact detectors on spacecraft enable impact measurements which cover more than one of these regions (not including lunar micro-craters) to be separated into the following groups:

i. Lunar microcrater counts. The fluxes were determined by calculating the impactor properties from the pits on lunar material. (The impact formula was a function of crater diameter and projectile mass, from Hörz *et al.*, 1975). However, the difficulty in determining the exposure age of the sample meant that the data were cross checked against fluxes obtained at 1 AU from spacecraft measurements. The influence of secondary craters was also identified, when compared with these other fluxes, and was accounted for.

ii. LEO orbit detectors. LEO detectors are exposed to the impacts of meteoroids that have fallen into the Earth's gravitational well. The flux is enhanced by the presence of space debris. The relative proportion of space debris to meteoroids is a function of altitude, size and other exposure factors. Residue analysis and orbit modelling of the spacecraft, with respect to the orbital debris and the interplanetary dust populations, may be the only way to deconvolve impact measurements into the two categories.

iii. Detectors at 1 AU (no gravitational enhancement). Detectors which are away from the Earth's gravitational well will not have Earth shielding, or gravitational focusing factors acting upon the impacting dust. Missions such as Pioneer 8, 9, Helios, HEOS sampled the 1 AU environment. Deep space missions may also sample the 1 AU region at some point on their trajectories.

iv. Radar and visual observations of meteors in the atmosphere. The detection threshold of meteors in the atmosphere is strongly dependent on velocity (a dependence of approximately

v^4; N. McBride, personal communication). Many major showers are caused by streams which have high relative impact velocities (making them easier to observe). Meteor measurements generally sample particles about 1 mm and above.

v. Detectors not at 1 AU (eccentric orbits and deep space missions). For some deep space missions, interplanetary dust data have been collected (Pioneer 10, 11, HEOS), although for the purposes of this study, the measurements made at 1 AU are more important.

Brittle materials (the primary topic of this thesis) have been used for studies of the 1 AU population. Small craters are easier to detect on brittle materials compared with ductile materials as the impact features are larger for defined impactor parameters. Lunar rocks and the Mercury, Gemini, Apollo and Skylab windows all have provided data on the impact flux in several of the regions described above. However, the detectors are not time-resolved. A review of the data from the Pioneer missions, lunar microfluxes, Mercury, Gemini, Apollo and Skylab windows and the Helios and HEOS missions is provided by Leinert and Grün (1990).

1.1.3 Flux models

The Grün flux model (Grün *et al.*, 1985) is a model of meteoroid flux versus meteoroid mass, and is derived from (i) lunar flux measurements, (ii) spacecraft measurements and, (iii) radar meteors. The final flux values are presented for a spinning flat plate detector at 1 AU. The model fluxes cannot be applied to LEO without consideration of the gravitational flux enhancement. As the flux is an annual mean value, and derived with respect to a spinning plate, the fluxes are assumed to be 'isotropic', i.e. randomised in direction. Application of these isotropic fluxes is applicable if viewing directions of detectors are reasonably randomised (see below).

Another recent interplanetary meteoroid model is from Divine (1993). This model incorporates data from deep space missions in an attempt to derive a global model applicable throughout the inner solar system. The results incorporate (and thus agree with) the Grün flux model and so, for the purposes of this study, the Grün flux is used.

The Kessler space debris model, published in 1989, defines the impact flux as a function of flux versus diameter for space debris, convolved with a collision velocity distribution as a function of orbital inclination (Kessler *et al.*, 1989). The model has recently been updated, using impacts from the LDEF spacecraft and other sources (Kessler *et al.*, 1996). A detailed review and analysis of the Kessler 1996 model is provided in Griffiths (1997).

1.1.4 Viewing geometries and histories

The satellite data used in this thesis comprise surface impact data from LDEF and solar array data from HST and EURECA. It is important to understand the different viewing geometries

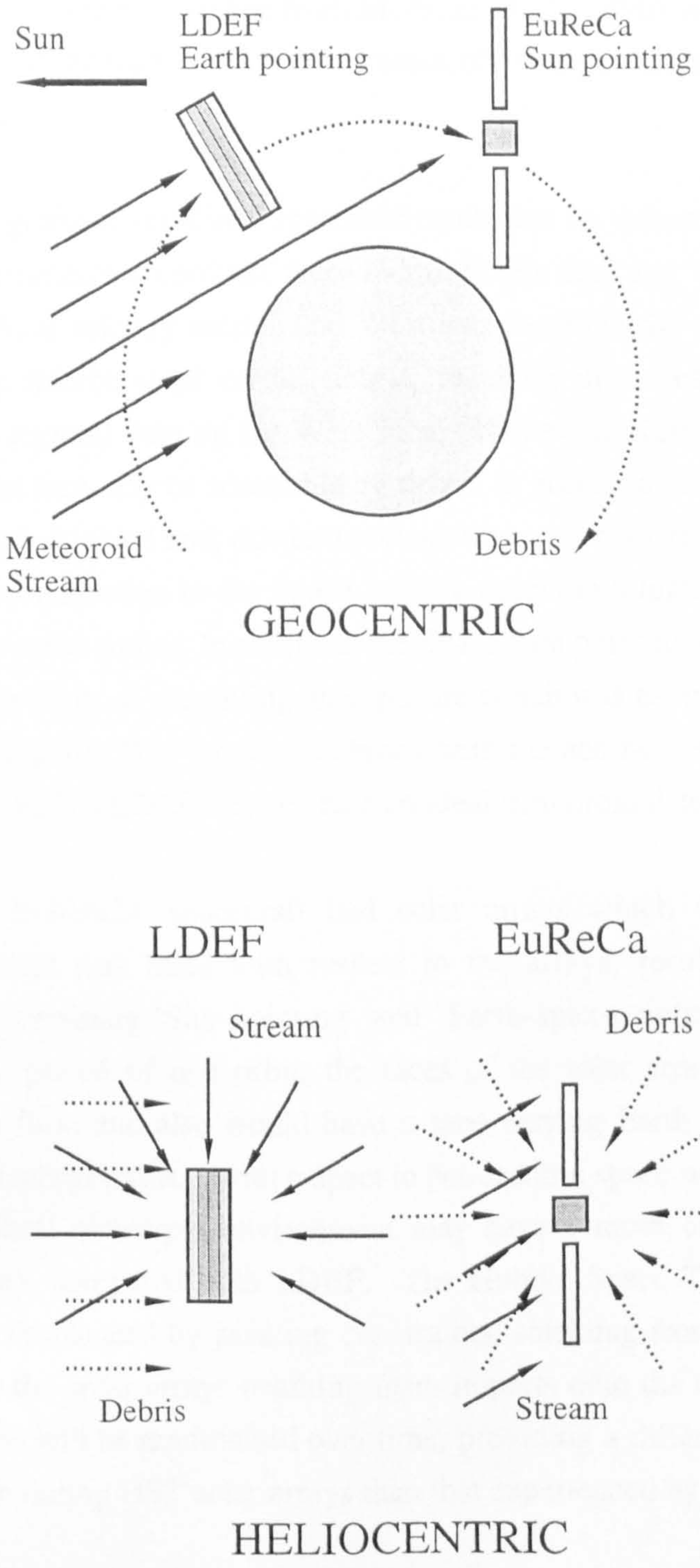

Figure 1-1. A comparison of the impact geometries of stream meteoroids and space debris, to LDEF and EURECA. Due to LDEF being Earth-pointing, and EURECA being Sun pointing, the time integrated exposure to the faces of the spacecraft appear very different when considered in the heliocentric frame.

of these missions with respect to meteoroids and space debris. The different viewing geometries of the EURECA (and also the similar HST arrays) and the LDEF spacecraft are shown schematically in Figure 1-1 (taken from McBride *et al.*, 1996) where exposures with respect to geocentric rather than heliocentric frames of reference make the impact history significantly different.

LDEF was a gravity gradient stabilised spacecraft such that its orientation with respect to Earth was fixed. It maintained `cardinal' faces North, South, East and West where East was the ram direction (orbital velocity vector) and West was therefore the wake. The East face could 'sweep up' up micron-sized orbital debris, resulting in fluxes being considerably higher (in the debris regime) than on the West face. However, Kessler *et al.* (1996) has proposed that the West face may be accessible by debris in eccentric orbits. The Space face of LDEF was not Earth shielded and, due to its orientation, was not exposed to orbital debris in circular orbits. A contribution to the Space face by debris in a highly eccentric orbit has been proposed by the same author. In addition, the Space face pointing vector would revolve over the period of one orbit, so presenting an exposure which was essentially a spinning flat plate (when time averaged). This factor, combined with the absence of Earth shielding and space debris impacts, makes LDEF's Space face an ideal meteoroid detector.

In comparison, the EURECA spacecraft had solar arrays which were generally Sun-pointing. The spacecraft was fixed with respect to the arrays, resulting in the sides of EURECA broadly maintaining `Sun-pointing' and `Earth-apex-pointing' orientations. This means that, over the period of one orbit, the faces of the solar arrays would get a time varying space debris flux, and also would have a time-varying Earth shielding. However, the orientation of meteoroid impacts with respect to heliocentric space was fixed, and so any anisotropies in the local meteoroid environment may have a more obvious effect on the EURECA faces, when compared with LDEF. The Hubble Space Telescope exposure is broadly similar but complicated by pointing constraints, shielding from the telescope body and secondaries onto the solar arrays resulting from impacts onto the main spacecraft. The telescope body motion will be randomised over time, providing a different averaged level of shielding to the sun-pointing HST solar arrays than that experienced by the EURECA arrays.

1.1.5 Space debris

As stated above, the Space face of LDEF represents a very good meteoroid detector. The other faces (particularly the East face) did receive a significant additional exposure to space debris particles. Figure 1-2 (McBride and Taylor, 1997) shows the flux data from the Space face and the `5-point mean' of the Space, East, West, South and North faces. Also shown is the result predicted by the application of a meteoroid model using the Grün flux values, incorporating LDEF's orientation history and a full meteoroid velocity distribution (McBride *et al.*, 1996). It is clear that the impact flux to the space face is well accounted for by

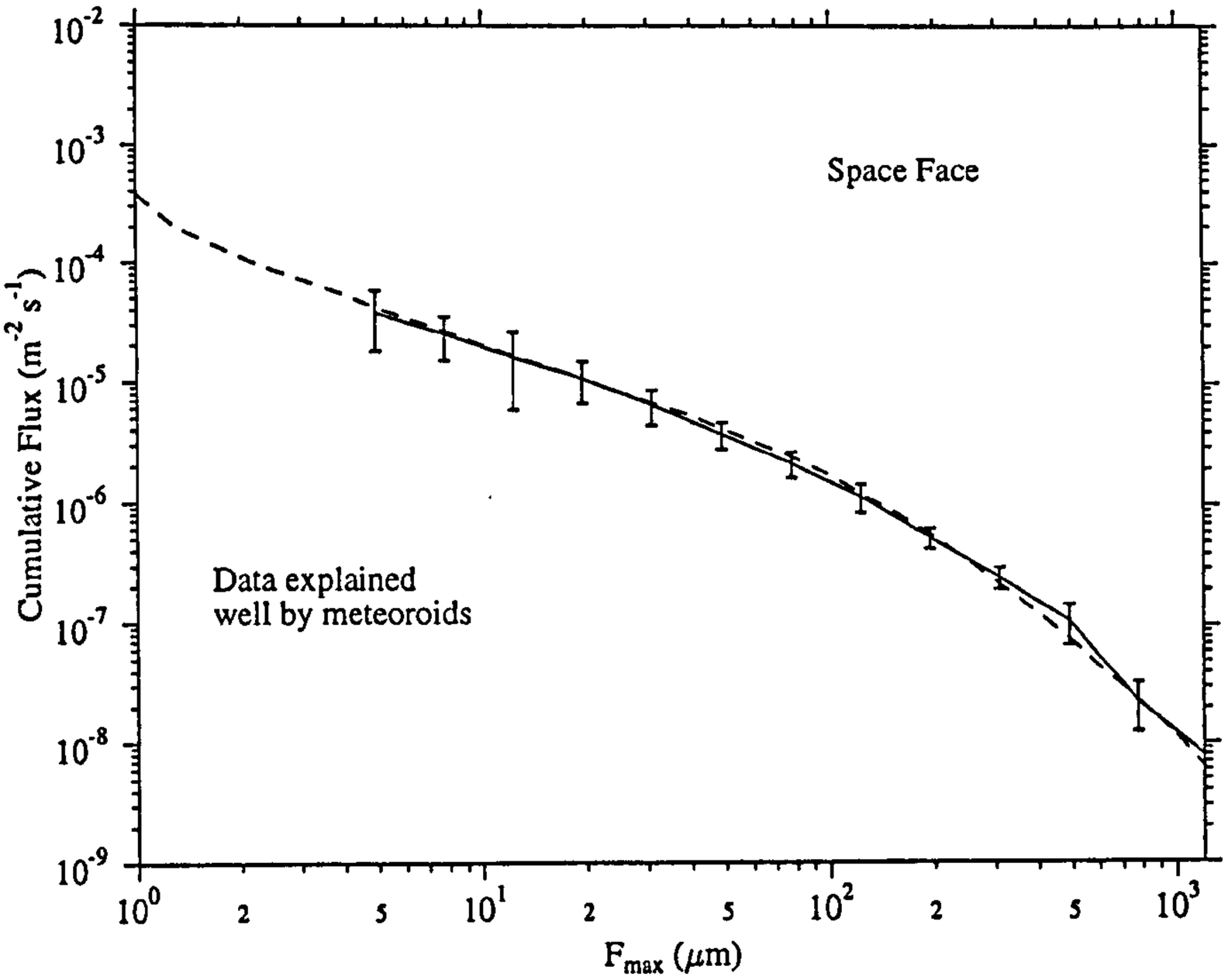

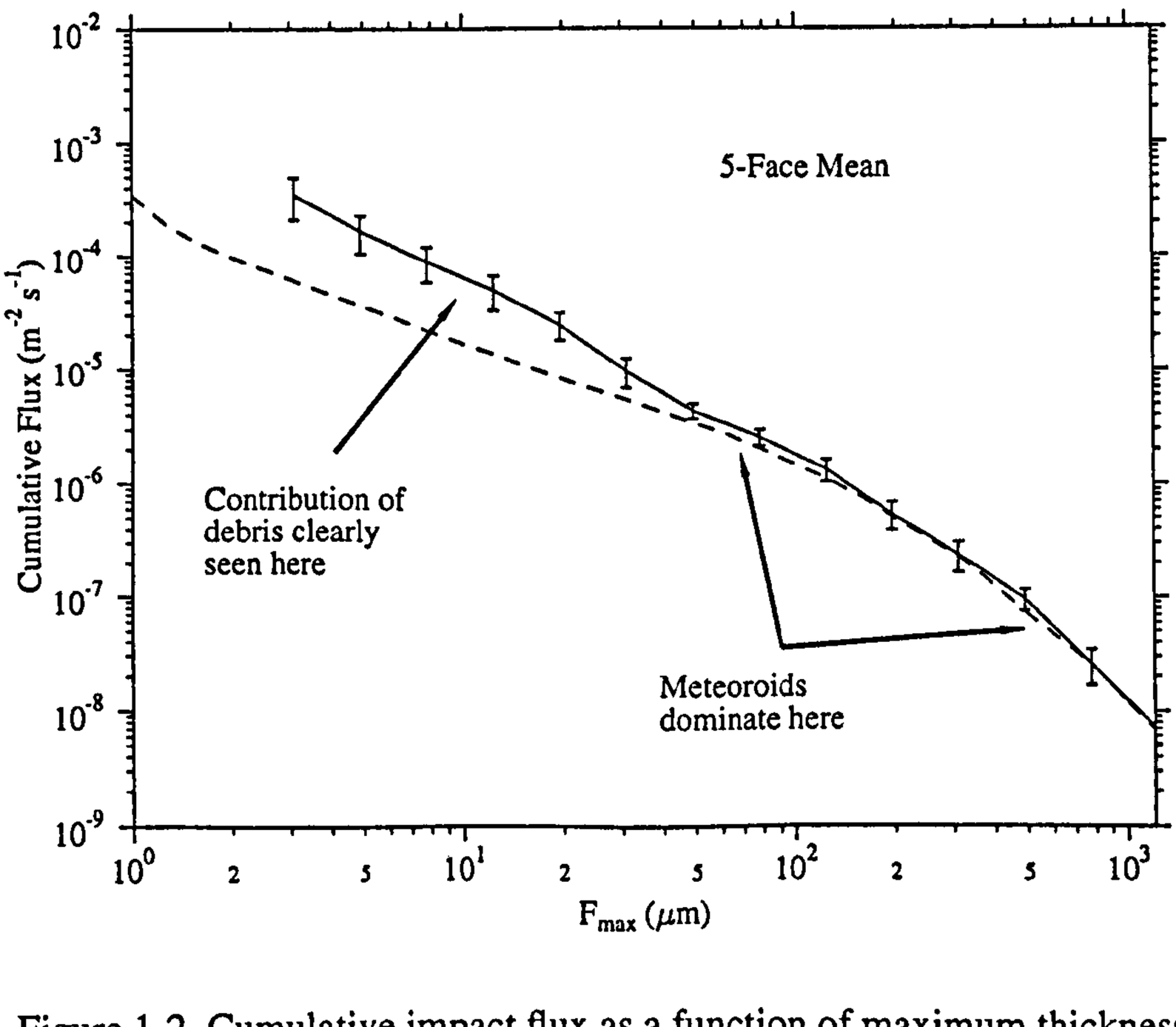

Figure 1-2. Cumulative impact flux as a function of maximum thickness of material (aluminium) perforated on the LDEF spacecraft (reproduced from McBride and Taylor 1997). LDEF data are derived from a variety of sources and are shown as a curve with error bars representing the typical spread in the data. The meteoroid model fits (run assuming a meteoroid density of 2500 kg m^{-3}) are shown for comparison (dashed curves).

meteoroids only, whereas, when including the other faces, the effect of debris becomes apparent at $F_{max} < 30$ μm. This result is also investigated in detail by McDonnell *et al.* (1997) who showed that at small sizes ($F_{max} \sim 5$ μm) meteoroids contributed only 18^{+9}_{-6} % of the flux, but that at $F_{max} > 30$ μm the meteoroids dominate (at least up to $F_{max} \sim$ centimetre scale).

1.1.6 Summary

For the Low Earth Orbit environment, it has been shown that meteoroids are important in the > 10 μm diameter particle regime, with space debris being significant below this size (and indeed at greater than centimetre sizes). The exposure history of LDEF faces (particularly the Space face) results in a good meteoroid detector. The large area-time product offered by solar arrays potentially offers an excellent meteoroid and debris detector up to centimetre sizes. However, for direct comparison with the aluminium F_{max} fluxes, a conversion factor, or an equation for the glass damage impact regime, is needed. Once the solar array fluxes have been decoded, via use of brittle material damage equations, it is desirable to compare the results with the ductile material impact data set taken from dedicated instruments (e.g. EURECA TiCCE) and spacecraft structures (LDEF). A summary of the space-exposed data sources used in this thesis is given in Table 1-1.

Table 1-1. Relevant parameters of comparable space data sources used in this thesis

Data source	Detector	Epoch	Alt. (km)	Incl. (°)	Pointing
EURECA TiCCE	Thin foils	8/92 - 6/93	502	28.5	45° between Sun and Earth apex directions
LDEF	Thin foils and semi-infinite metal	4/84 - 1/90	470	28.5	Gravity gradient stabilised
EURECA solar arrays	Solar cells	8/92 - 6/93	502	28.5	Sunwards
HST solar array wing	Solar cells	4/90 - 12/93	614	28.5	Sunwards

1.2 Post-Flight Analysis of the Solar Arrays

The initial post flight analyses (PFAs) of EURECA's exposed surfaces and the retrieved solar array wing from HST were performed with support from PPARC, and later, under ESA contract (Unispace Kent *et al.*, 1994 and Space Applications Services *et al.*, 1995). The primary output of the analyses was a photographic catalogue of impact sites from which measurements could be made. A second stage contract, 'Meteoroid and Debris: Flux and Ejecta Models', led by Unispace Kent, of which the author is a team member, is re-analysing the results of the PFA to provide a higher level of understanding and definition for engineering purposes. The contract is due for completion mid-1998.

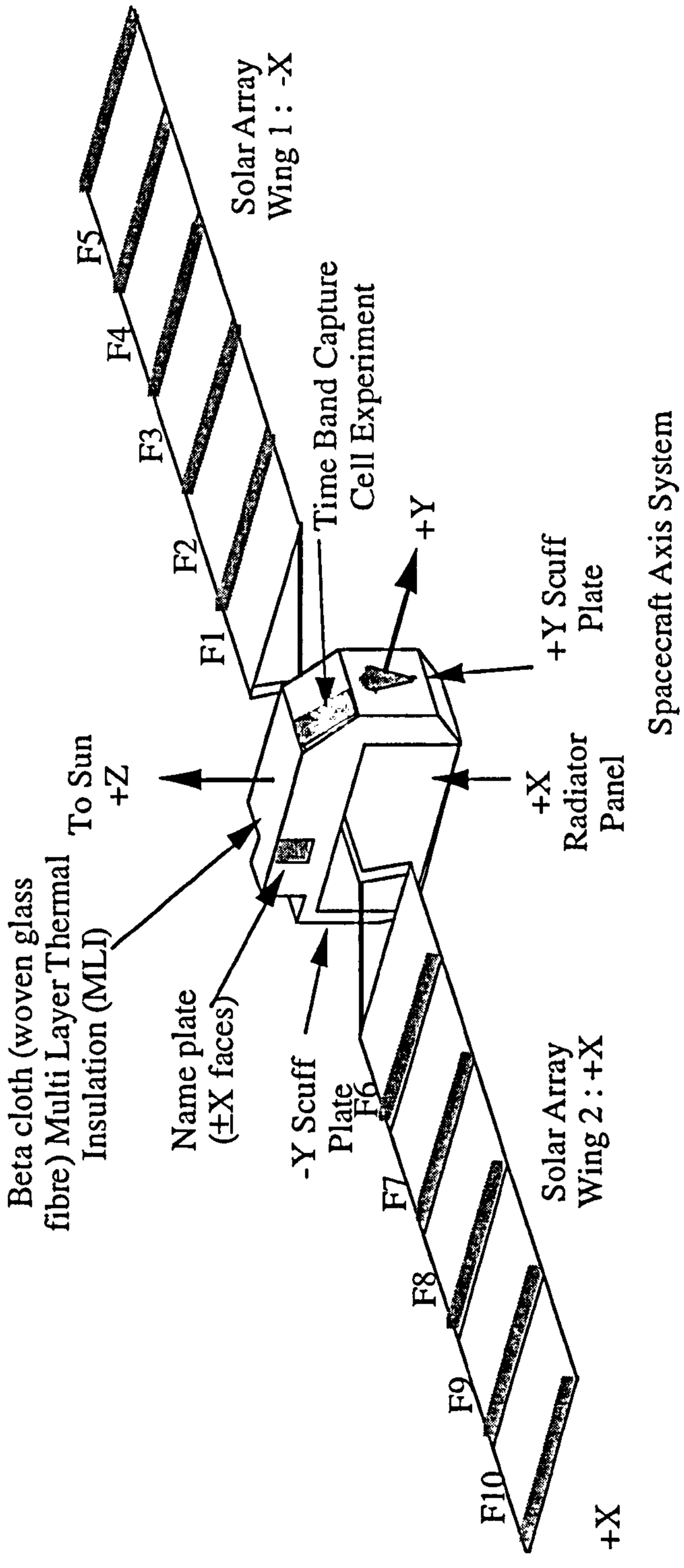

Figure 1-3. The EURECA spacecraft configuration and spacecraft axes definition. All the components identified have been analysed for impact sites. In this thesis, a summary of the results from the impacts onto solar cells is presented. Note the numbering system for the arrays, where F6 and F1 are closest to the spacecraft body (i.e. most likely to be shielded, and to receive secondary ejecta from impacts onto the main body) and F10 and F5 are furthest away. Impact data from F7 is used in this thesis. The grey areas represent the areas scanned to a higher resolution and include the f1 swaths from the solar arrays. Image adapted from Unispace Kent *et al.*, 1994.

EURECA is ESA's platform for microgravity experiments and made its first flight in 1992/93, launched and retrieved by the space shuttle. Figure 1-3 shows the spacecraft configuration and the location of TiCCE (TImeband Capture Cell Experiment), a non-time resolved, dedicated impact instrument. There was no movement of the spacecraft relative to the solar array wings, therefore the shielding of the solar arrays remained constant. One of the Hubble Space Telescope (HST) solar arrays (see Figure 1-4) was returned to Earth after the HST servicing and repair mission, STS-61. The solar arrays were Sun-pointing but, unlike EURECA, HST can rotate 360° about an axis perpendicular to the plane of the solar panels to track astronomical objects. Therefore, variable shielding of the solar arrays by the telescope body was present during the mission.

A schematic of the HST and EURECA solar cells are given in Figure 1-5. Note that the HST cell is approximately 30 times thinner than the EURECA solar cell. Unlike the EURECA PFA, the HST PFA recorded a large number of impacts on the rear surface which also produced visible features on the glass (front) surface. These impact sites had a significantly different morphology to the impacts onto the front glass surface and have recently been calibrated against impacts in the laboratory (Herbert *et al.*, 1997).

Scanning of both the EURECA solar array wings and the HST SPA wing was performed at two levels of resolution to make the most of the limited man-hours available. In one survey ("catch-all" survey), small areas were scanned in detail with every crater visible to the naked eye being located and photographed. In the other survey (main survey) a cut-off size was decided upon such that all craters above this size limit over the entire surface could be located and imaged. This means that the flux of impacts measured down to this size limit is reliable. Table 1-2 gives the number of impacts found in each survey above this threshold and the number found in the catch-all scans. In addition, the smallest feature measured in the full survey is recorded in Table 1-2.

The morphology of the impact sites can be divided into two categories: semi-infinite response, and finite response. At the time of writing, the classifications of the impact sites noted during the PFA (Unispace Kent *et al.*, 1994 and Space Applications Services *et al.*, 1995) have been advanced by Herbert and McDonnell (1997) who note that there are 6 morphological classes covering different (overlapping) impact site size regimes. These classes may be evidence of different impactor parameters. The key features of solar cell craters (common to the majority of impact classes) as identified by the PFAs are shown in Figure 1-6 with a schematic of the measurements made. The definition of D_p and D_{co}, as based on morphology, vary between classes. The main features are listed here:-

- Central pit, diameter D_p. This is believed to be formed early in the impact process in a similar way to hypervelocity craters on ductile materials.

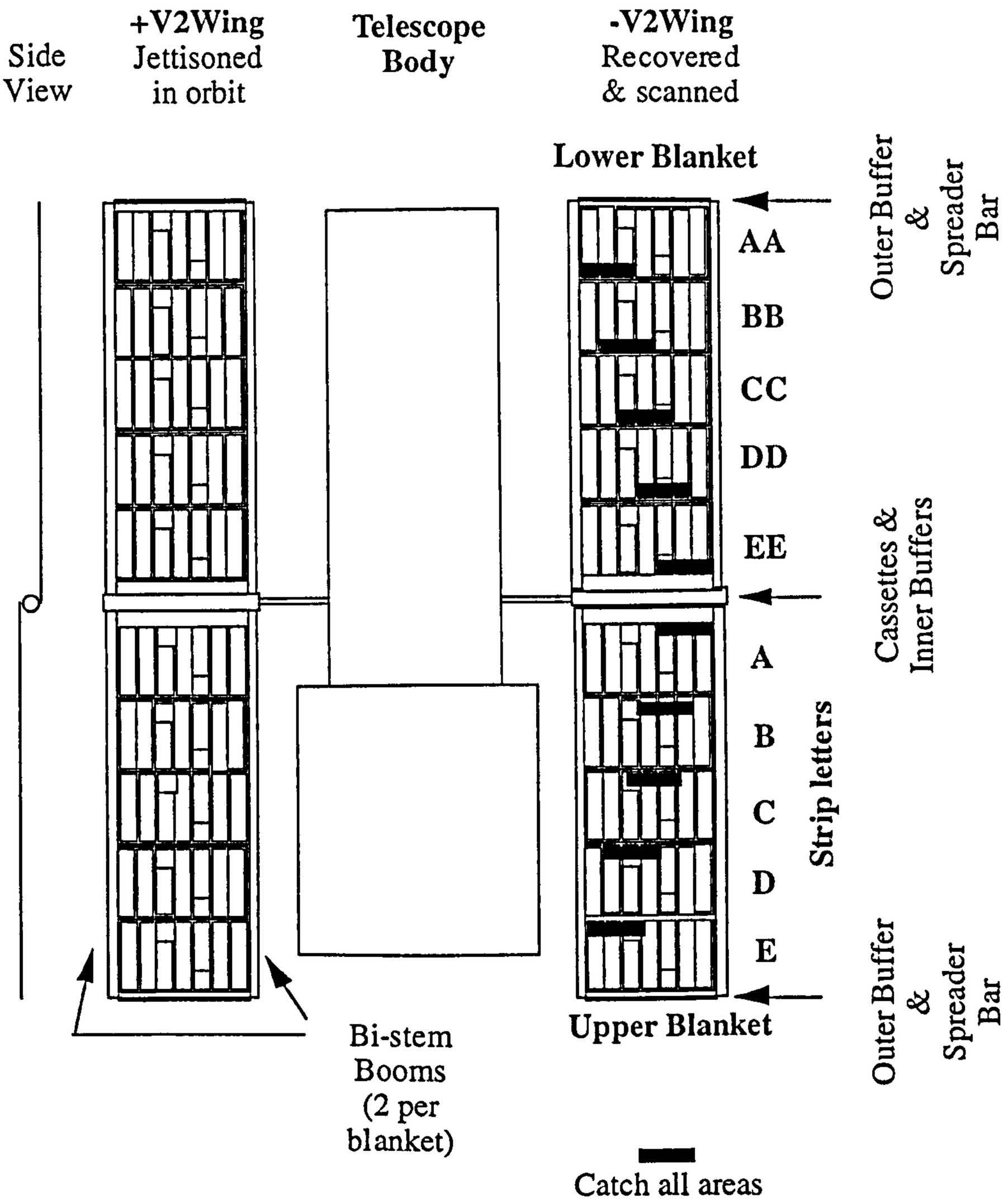

Figure 1-4. The Hubble Space Telescope -V2 blanket has a surface area of 28.92 m^2 including buffers, and 25.92 m^2 without the buffers. The total cell area was 21.27 m^2. The solar panel assembly (SPA) numbering is given by the letters A-E and AA-EE. The solar arrays were shielded to some degree along their full length (SPA E to AA). Data from microscopic / scanning electron microscope (SEM) scans of selected areas of SPAs D and E are used in this thesis. The catch-all scans of selected areas of each SPA picked up all features visible to the naked eye. Image from Space Applications Services *et al.*, 1995.

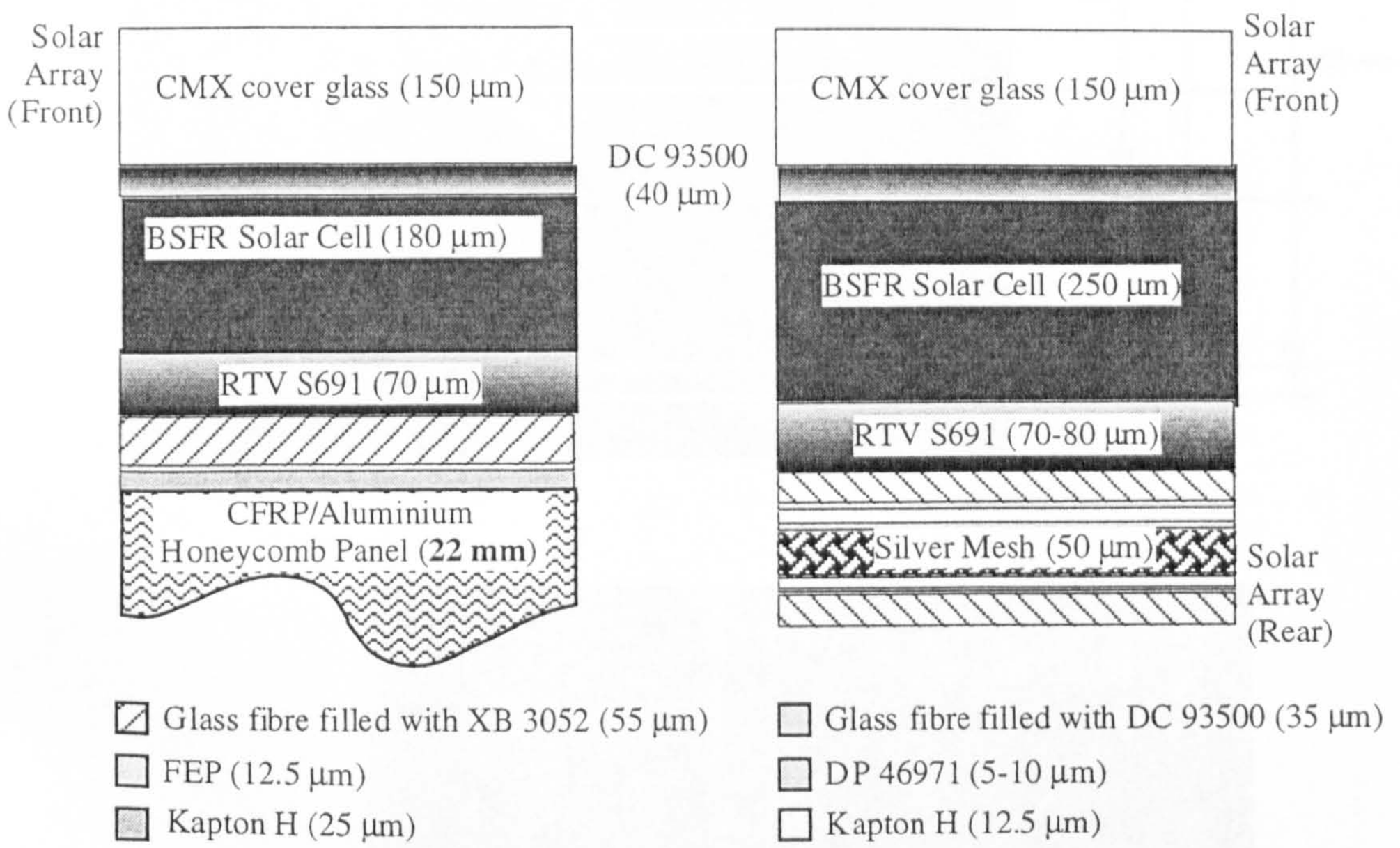

Figure 1-5. Solar cell cross-sectional schematic. The total thickness of the EURECA solar array is some 30 times that of the HST array. CMX glass is a patented glass produced by Pilkingtons U.K. which is designed to let through wavelengths of light for maximum performance of the Back Surface Forward Reflection (BSFR) silicon layer. DC 93500 is a clear adhesive and RTV S691 is a reddish colour adhesive. RTV can be seen in images of deeper impacts on the HST and EuReCa solar cells. HST arrays were based on a flexible substrate, whilst EURECA arrays were attached to a honeycomb panel. The honeycomb consisted of carbon fibre reinforced plastic (CFRP) facesheets and aluminium honeycomb, providing low mass, high stiffness for the solar cells. (Drawing by A. D. Griffiths, based on HST schematic produced by E. A. Taylor.).

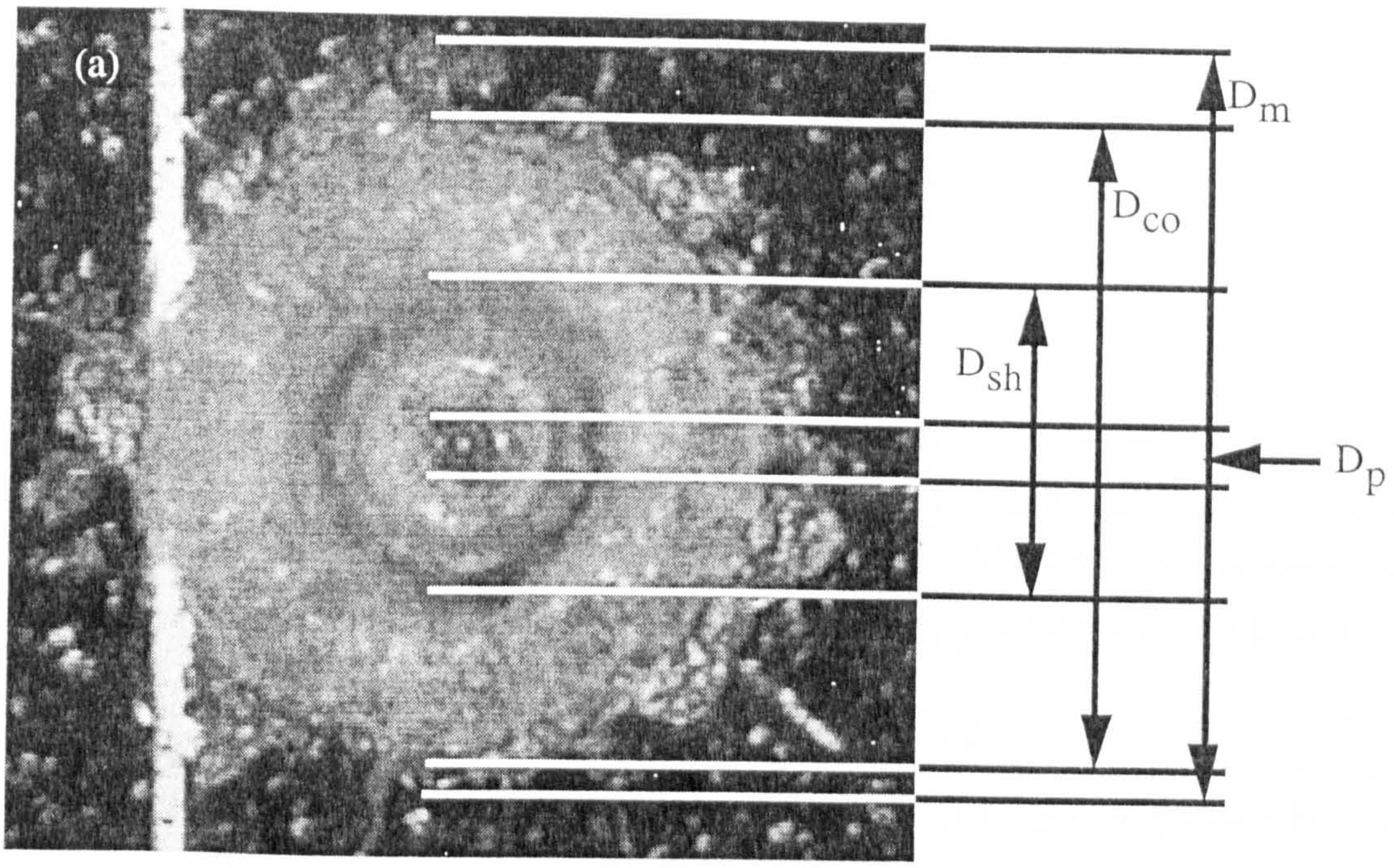

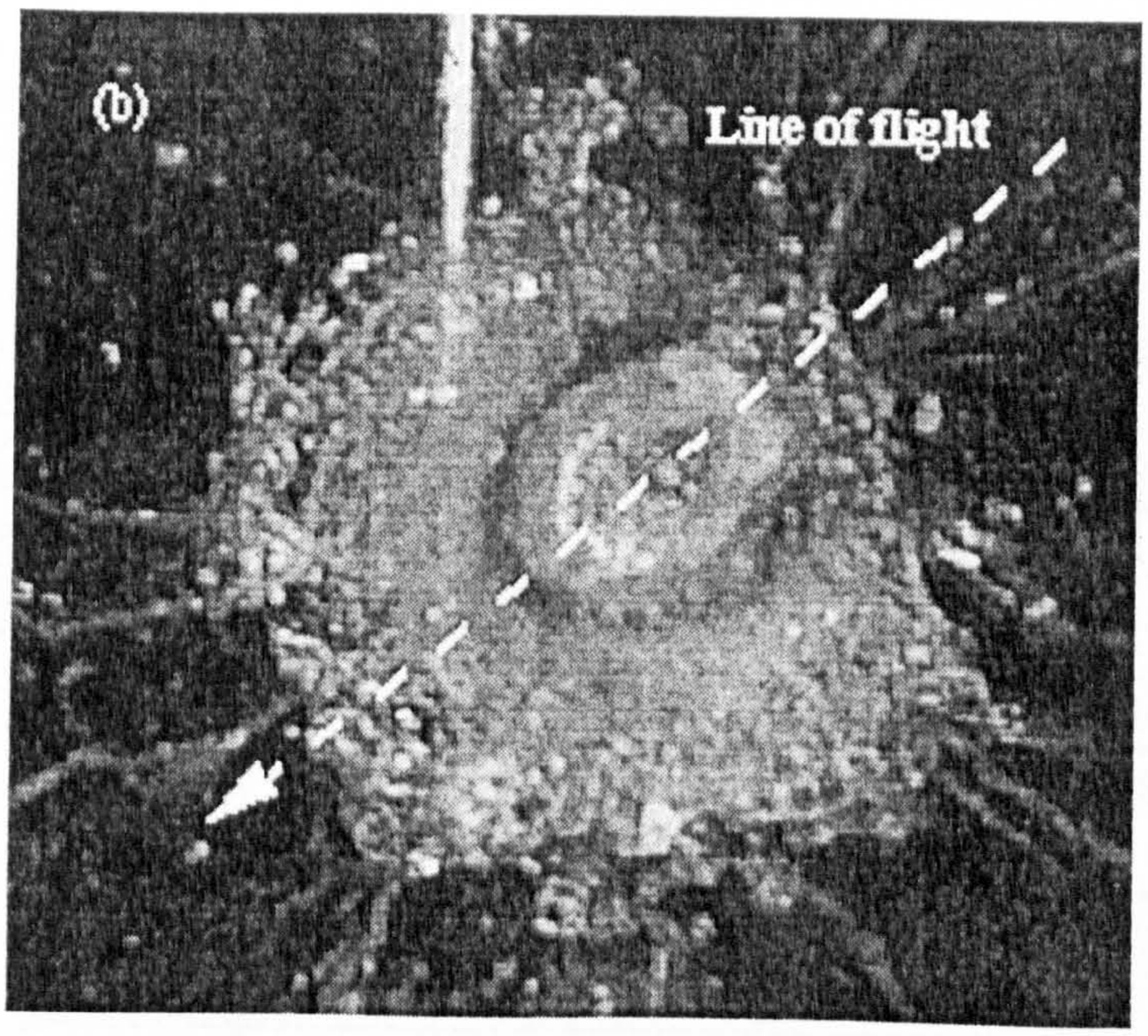

Figure 1-6. (a) A typical impact morphology noted on both HST and EURECA solar arrays. This impact was recorded on HST. It is less than 1 mm in diameter and shows a central pit (D_p), shatter area (D_{sh}), conchoidal diameter (D_{co}). The maximum damage parameter (D_m) is used to identify the largest radius of damage beyond the conchoidal feature. (b) An impact formed by an obliquely impacting particle, identified by the damage morphology. The features noted in (a) are visible here. Measurements were made along the perceived line of flight (based on impact morphology) and perpendicular to it.

- Shatter zone, diameter D_{sh}. This is a region of highly shocked powdered glass surrounding the pit.
- Conchoidal spallation zone, diameter D_{co}. This region is formed by fracturing and subsequent ejection of the surrounding material due to stresses induced by the expansion of the central pit.
- D_m is the maximum extent of damage

The impact morphologies noted during the small size optical scan are very different to those noted during the main and catch-all scans (Figure 1-7). The solar cell glass behaves as a semi-infinite piece of glass and produces a central pit and conchoidal diameter, as seen on lunar rock micro-impacts (Hörz *et al.*, 1971). These impact morphologies are reviewed in detail in chapter 2.

Table 1-2. Area-time product and low resolution scanning details of solar arrays used in this thesis (from Shrine *et al.*, 1996 and M. K. Herbert, personal communication).

Parameter	EURECA	HST
Area (m^2)	40.08	20.73
Time in orbit (10^8s)	2.82	1.14
Cut-off size (μm)	650	1200
No. impacts Survey Catch all /main	168 / 535	137 / 696
Total (impacts)	703	841
Catch all size range (μm)	> 100	> 100
Smallest feature measured in survey (μm)	130	780

Table 1-3. High resolution scans used in this thesis. (The area of one HST or EURECA solar cell is 8.36×10^{-2} cm^2, M. K. Herbert, personal communication)) #: number

Solar array	Method	Area (m^2)/ # cells	Mag.	Threshold (μm)	Reference
EURECA F7	Opt./Video	0.095	×50	not known	Berthoud, 1994
EURECA F7	Opt./Video	0.019	×400	30	Berthoud, 1994
HST SPA D+E	Opt.	0.085(10)	×20	32	Berthoud, 1995
HST SPA D+E	Opt.	0.493(58)	×50	9	Berthoud, 1995
HST SPA D+E	SEM	0.002(7)	×200	2	Berthoud, 1995
HST SPA D+E	SEM	0.0085(1)	×500	2	Berthoud, 1995
HST SPA D+E	Opt.	13 cells	×25	20	Shrine *et al.*, 1996

High resolution surveys of cells from EURECA and HST solar arrays have been carried out (Berthoud, 1994; Berthoud, 1995; Shrine *et al.*, 1996) using optical and scanning electron microscope techniques to obtain a magnification of up to 500×. The size of impact feature observed in these scans is consistent with non-perforations of the solar cell cover-glass, and

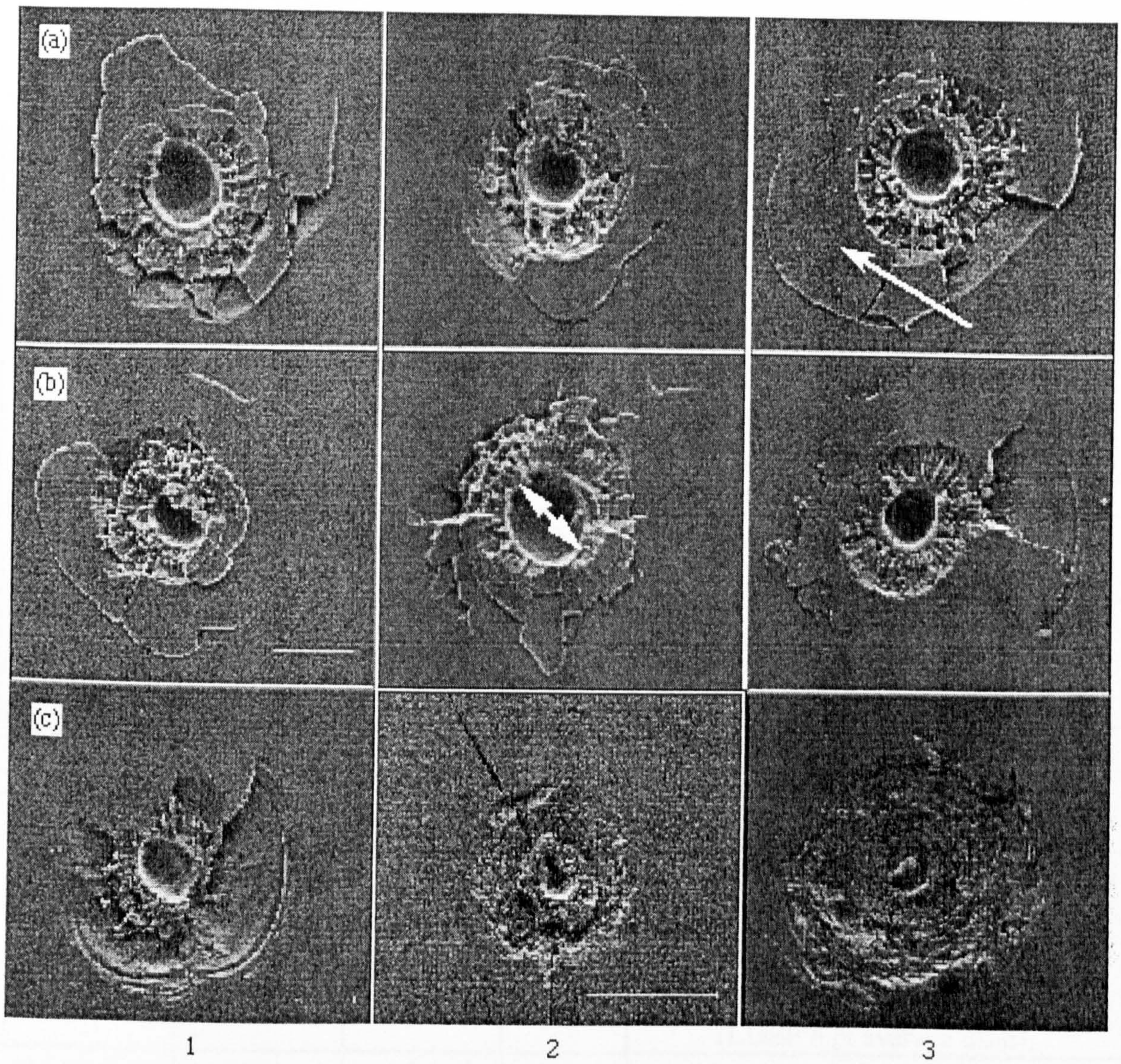

Figure 1-7. Impacts from a scanning electron microscope (SEM) of the Hubble Space Telescope from Shrine *et al.* (1996). (a),(b) Pit sizes between 20-50 μm (c) Pit sizes greater than 100 μm. Note the central pit morphology (identified in image (b)2) and the areas of conchoidal cracking (image (a)3). The majority of impacts onto the space flown surfaces will be at non-normal angles but the pits appear mostly circular. (a)1, (b)1, (c)1, (c)2 could be formed by a spherical oblique incidence impactor. However, such impact features could also be formed by a non-spherical impactor. The arrow identifies a conchoidal fragment on the verge of spallation.

the detection threshold is up to two orders of magnitude better than the main surveys. These data will be more applicable to the calibration experiments with small particles presented in this thesis. A summary of these surveys is shown in Table 1-3 and the flux data are plotted in Figure 1-8.

1.3 Fluxes Decoded from EURECA and HST

Table 1-4. Previous flux analyses of solar arrays

Reference	Solar Array	D_{co} range scanned (m)	D_{co} to F_{max}?	Comment
Berthoud, 1994	EURECA	~10^{-6}-10^{-2}	No	ESABASE d_p, v predictions (meteoroid and debris) compared with D_{co} using damage equations (meteoroids: ρ_p = 1 g cm^{-3}, v=17 km s^{-1}; space debris: ρ_p = 4 g cm^{-3}, v=11 km s^{-1}) to get a projectile diameter
Berthoud, 1995	HST	~10^{-6}-10^{-2}	No	As for Berthoud, 1995.
Berthoud and Paul, 1995	EURECA, HST	N/A	N/A	Summary of results from Berthoud, 1994 and Berthoud, 1995.
McDonnell *et al.*, 1995	HST	10^{-4}-10^{-2}	No	Gravitational enhancement/Earth Shielding factors for LDEF, EURECA and HST presented.
Drolshagen *et al.*, 1996	EURECA	10^{-5}-10^{-1}	Yes	Assume ρ_p = 2 g cm^{-3}, v=10 km s^{-1} and d_p = 0.5 D_{pit} and use F_{max} and $D_{pit} \propto d_p$ relationships to get conversion between ductile and brittle targets (LDEF 6 pt average used).
Drolshagen *et al.*, 1997	HST	10^{-6}-10^{-2}	No	As for Berthoud, 1994.
Shrine *et al.*, 1996	EURECA, HST	10^{-6}-10^{0}	Yes	$D_{co} \propto d_p$ relationship validated against oblique impacts on solar cells. D_{co}/F_{max} relationship developed, applied to small craters in semi-infinite regime.
Paul *et al.*, 1997	EURECA, HST	~10^{-6}-10^{-2}	No	As in Berthoud, 1994 and Berthoud, 1995.

The two high resolution solar array fluxes (i.e. number of impact features per square metre per second) have been plotted in Figure 1-8. The work in Table 1-4 summarises previous publications detailing the fluxes decoded from HST and EURECA, both high resolution (optical and SEM) and low resolution (main survey and catch-all). The fluxes can be compared with impacts recorded on ductile materials (e.g. LDEF) via a conversion factor (Drolshagen *et al.*, 1996 ; Shrine *et al.*, 1996) or to environment modelling programmes

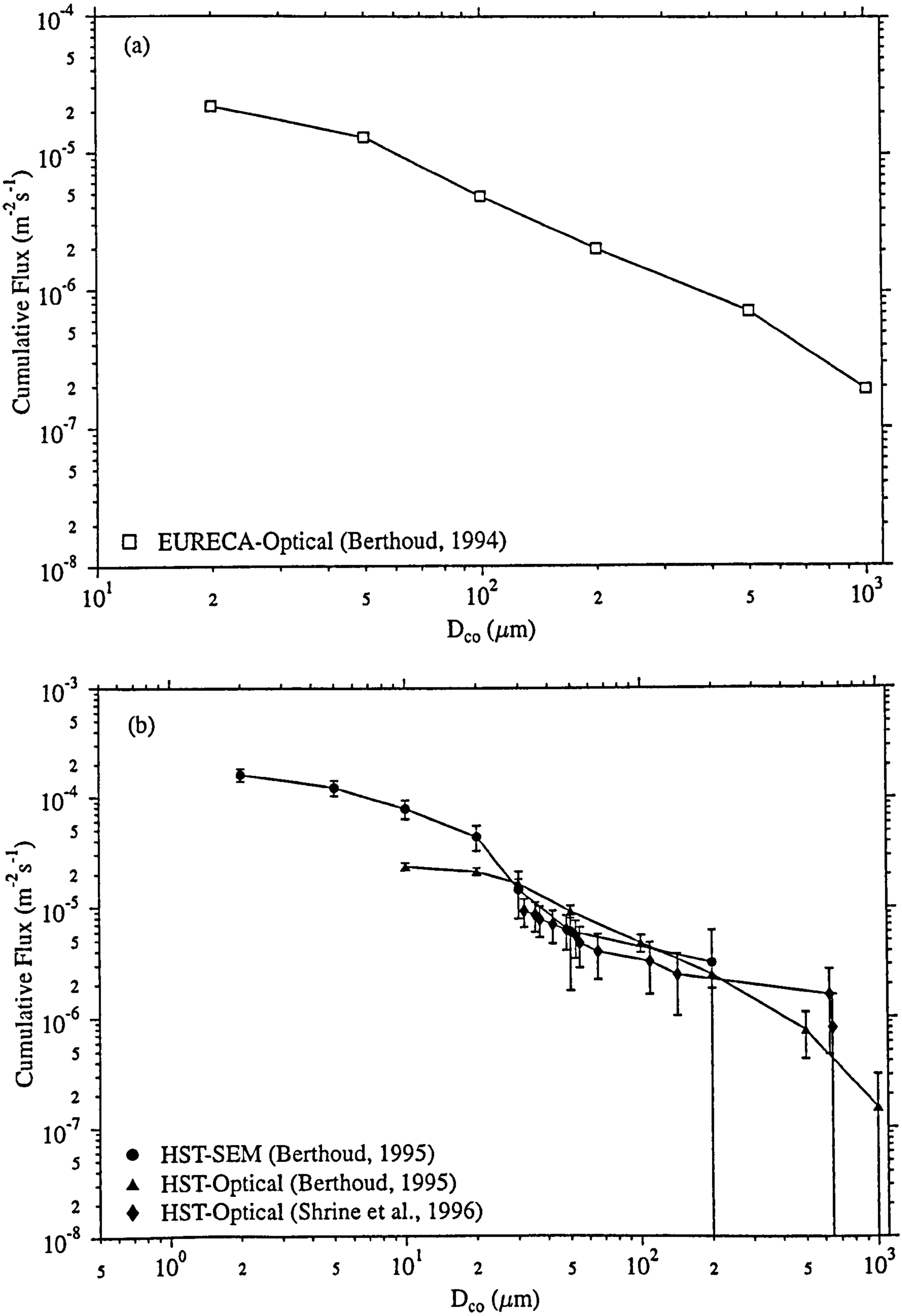

Figure 1-8. High resolution solar array flux data used in this thesis. Error bars have been calculated where the number of counts per bin is published. (a) EURECA (b) HST solar arrays.

(ESABASE, see Griffiths, 1997 for details). The output of ESABASE is the 'damage count' expressed in terms of the projectile diameter, density and impact angle for both the debris and meteoroid populations; this can be compared with impact damage on the solar array (conchoidal or pit diameter) by the use of a damage equation, where impact velocity and density are assumed for the debris and meteoroid populations and the particle diameter derived. The assumption of a single velocity and density for the meteoroid and debris populations is an approximation to the LEO impact environment.

1.4 Summary

The LEO particulate environment, as encountered by an orbiting satellite, has been presented. The influence of spacecraft viewing geometries and pointing histories on the impact flux recorded has been discussed. The impact data from satellites and solar arrays have been presented and previous flux analyses of these surfaces reviewed.

Chapter 2

2. Experimental Programmes

The shot programmes carried out for the purpose of this thesis have been defined so as to investigate impact parameter regimes not covered by previous researchers. At smaller sizes, finely graded soda-lime projectiles (projectile diameter range of 30-300 μm) were accelerated onto semi-infinite soda-lime targets to investigate the dependence of impact features on the projectile diameter, and to provide a data set for the test of a new, fracture based damage equation, presented in Taylor *et al.* (1997d) (12 shots). Projectiles in the diameter range 100-500 μm are under-represented in the literature so this shot programme also added valuable data. At the millimetre-sized impactor range, previously only low and medium density projectiles had been fired at brittle targets. Therefore a programme, consisting of 30 shots and covering a wide range of projectile densities, was executed for this thesis.

Finally, a 35 shot programme onto spacecraft honeycomb material (carbon fibre reinforced plastic facesheets and aluminium honeycomb core) was executed to investigate damage morphologies, ballistic limit and to aid damage equation development. The following were investigated: ejecta production (qualitative and quantitative), hole size (front and rear), internal honeycomb damage and the ballistic limit of the target. The measurement of the impact results was carried out in association with M. K. Herbert, the comparison with aluminium, with D. J. Gardner and the LEO risk modelling, with A. D. Griffiths. R. Thomson assisted in the first part of the shot programme. The X-ray facilities were provided by Dr. J. Hodgkinson at the Centre for Composite Materials (Imperial College London).

The shot programmes are described in this chapter and the measurements made on the targets (and the techniques used) are summarised. A qualitative review of the impact morphology damage is also presented, including some new observations made during this thesis. A more in-depth, quantitative analysis is presented of the honeycomb impact data. The results from the shot programmes are presented in later chapters and have also been published in the following papers: Shrine *et al.*, 1996, Taylor *et al.*, 1997d, Taylor and McDonnell, 1997, Taylor *et al.*, 1996b, Taylor *et al.*, 1997a, Taylor *et al.*, 1997b, and Taylor *et al.*, 1997c.

2.1 Motivation

In order to obtain information about the Low Earth Orbit (LEO) environment from returned spacecraft surfaces, a method for decoding the impact crater parameters (crater diameter, crater depth) to obtain impactor characteristics (projectile diameter, velocity, density, shape and impact angle) must be found. The full range of space impactor parameters found in LEO (as given above) cannot be reproduced in the laboratory. Therefore the space impact craters can either be 'partly' compared with impact craters produced in laboratories (direct calibration) or 'fully' compared with damage equations (empirically determined and based on

the laboratory results) extrapolated to LEO impact conditions. Both require the use of hypervelocity acceleration techniques - typically either a light gas gun (LGG), a Van de Graaff (VdG) or other accelerator (e.g. plasma drag gun or rail gun). In addition, laboratory impact data can be used for hydrocode validation, a computer modelling technique suited for investigation of hypervelocity impact processes.

2.2 Light Gas Gun Operation

A hypervelocity gun's final projectile velocity is dependent on the gas pressure produced by the explosive and the projectile mass. For a projectile driven by a constant gas pressure p, Eq. 2-1 links the length of the barrel (L), the mass of the projectile (M), the cross-sectional area (A) and the muzzle escape velocity, v.

$$v=\sqrt{2p\left(\frac{AL}{M}\right)} \tag{2-1}$$

Therefore, for a given value of A, p must be as high as the gun can stand, the barrel as long as possible, and the mass of a projectile small. However, the pressure exerted by the gas is not constant over the flight of the projectile and, as it expands from the high pressure reservoir, it must use some of the stored energy to accelerate its own mass. The maximum escape velocity of the gas, v_{esc}, is a function of the gas temperature (T_0), molecular mass (M) and the ratio of specific heats (γ) and is given in Eq. 2-2.

$$v_{esc}=\frac{2}{\gamma-1}\sqrt{\left(\frac{\gamma RT_0}{M}\right)} \tag{2-2}$$

It is seen that hot, light gases (hydrogen or helium) provide the best accelerating gas for hypervelocity impacts. The Kent two stage Light Gas Gun (LGG) compresses and heats the gas by using a piston driven by burning rifle powder. If the piston is fast, a strong shock wave (with associated shock wave heating and compression) is formed. A heavy piston cannot be accelerated to suitable velocities, so the piston is made of a lightweight nylon material.

A schematic of the two stage LGG used in this work is given in Figure 2-1. A shotgun cartridge, filled with rifle powder, is ignited when the firing pin hits the cartridge primer (powder chamber). A solid nylon piston is accelerated by the detonation of the rifle powder in the cartridge and travels down the pump tube. The piston compresses a light gas in the pump tube, which is initially at a pressure of 40-45 atmospheres. Hydrogen is used since a lower molecular weight produces higher velocities (The velocity is governed by the Maxwellian distribution.) The resulting pressure peak ruptures a bursting disk which separates the evacuated blast tank, flight tube and target chambers and launch tube from the pump tube. This energetic process is contained by the central breech assembly. Behind the

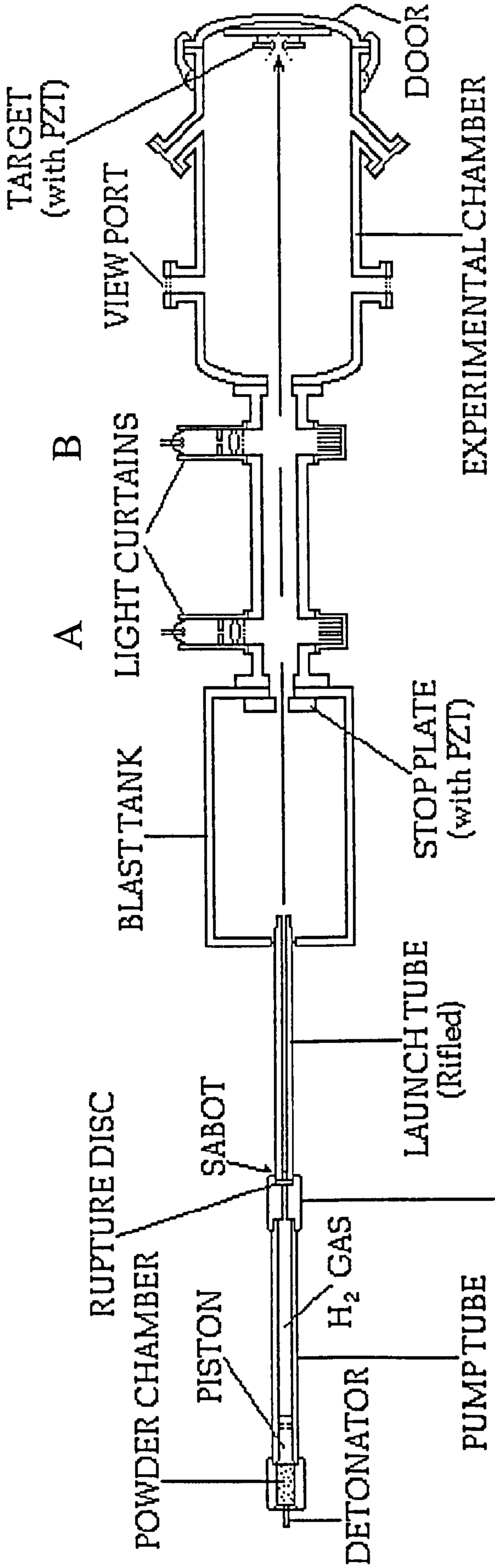

Figure 2-1. The Light Gas Gun.

bursting disk is a projectile 'holder', known as a sabot. The sabot used for the studies described in this thesis consists of four interlocking nylon parts. Individual projectiles are mounted in sabots drilled to fit the projectile diameter. The 30-300 μm diameter projectiles used for this thesis work were handled using aluminium tubing and large numbers of projectiles were placed into the sabot. This multiple projectile firing is known as the buckshot technique. The sabot (and the projectile(s)) are accelerated by the gas pressure once the diaphragm bursts. The launch tube is rifled, so spinning the sabot and causing it to separate into the four component parts (which have a radial outward motion) once it leaves the launch tube. The four sabot pieces (and the bursting disk fragment) are then stopped by a 'stop plate' in the blast tank. The stop plate has a hole which allows passage of the projectile through to the experimental chamber.

Table 2-1. Light Gas Gun operating parameters.

Item	Quantity
Cartridge type	Shotgun
Shotgun Powder	10.00 ± 0.04 g of Hercules R-19 or R-22
Piston	Nylon 66, 82 mm in length
Light Gas	Hydrogen
Initial Pump Tube Pressure	42.0 ± 2.0 bar
Bursting (Rupture) disk	0.45 mm thick 2014-T3P
Sabot	4-way split sabots (4.5 mm diameter)
Stop plate	Mild steel, 13 mm thick
Initial experimental chamber pressure	10^{-1} mbar
Pump tube (bore dia.)	12.7 mm
Launch tube (bore dia.)	4.3 mm

Velocity measurement was performed by a time of flight measurement using piezo-electric transducer (PZT) sensors on the stop plate and target (or aperture plate, for buckshot work). Signal timing was performed using an oscilloscope, recording at 2.5×10^7 samples per second. Corrections for the shock wave path in the stop and aperture plates (by subtracting the signal time) were performed to calculate the time of flight of the buckshot cloud or projectile. Time of flight measurements could also be made more directly using the two lasers mounted at the ports marked A and B in Figure 2-1. As the projectile passes, the laser beam was interrupted and the detector signal recorded by the oscilloscope. The laser technique could not be used for buckshot clouds due to the small projectile size. The laser time of flight technique is more accurate as it involves fewer signal measurements and is a more direct measurement.

Prior to the commencement of this thesis in November 1994, a five year development programme on the LGG (which was assembled in-house) was undertaken (1989-94).

Details of the optimisation of the performance (both in terms of maximum velocity reached, reliability of the firing and improving the safety of the procedures) can be found in Mackay (1994) and Baron (1996). For this thesis, the choice of sabot, piston, pump tube pressure and velocity measurement techniques have been defined by these earlier research programs (see Table 2-1).

2.3 Glass on Glass 'Buckshot' Programme

Multiple projectiles (finely graded glass beads) were loaded into a sabot for this experimental programme. The targets used in this work were 50.8 mm diameter, 10 mm thick soda-lime ("float") glass. Soda-lime glass is sometimes referred to as float glass, which describes its process of manufacture. In order to prevent fracture at the edge of the disk, the targets were purchased as 'ground all around' [1]. An aluminium plate (3 mm thick), with a 20 mm diameter aperture, was mounted ~120 mm in front of the aluminium target holder, as shown in Figure 2-2(a). Also shown, in Figure 2-2(b), is the set-up used to produce oblique impact data onto solar cells and glass simultaneously (Shrine *et al.*, 1996).

Table 2-2. Projectiles used in this work. Asterisk (*) denotes projectiles sorted by sieves; all other projectiles produced by Whitehouse Scientific.

Shot ID	d_p(μm) (mean)	Standard deviation (of projectile diameters)(%)	No. of impact sites	Vel. (km s^{-1})
GBS13	26.7	3.9	29	5.14
GBS12	36.1	2.4	23	4.61
GBS01	49*	8.8	19	5.07
GBS06	53	1.5	25	4.31
GBS11	77.9	1.3	8	4.41
GBS07	105.8	1.9	13	4.10
GBS18	150.9	4.6	22	3.97
GBS17	178.1	3.2	3	5.26
GBS15	195.2	2.8	2	5.63
GBS02	196*	8.8	11	5.17
GBS09	275*	10.0	1	5.26
GBS14	292.7	2.1	2	5.14

Projectiles were either finely graded spherical glass beads[2] (Figure 2-3) or glass ballotini[3] (sphericity not guaranteed) (Figure 2-4), which had been graded using stainless steel mesh sieves. The shot program details are given in Table 2-2. After impact the glass targets were

---

[1] Suppliers, Piper Glass, UK; glass manufacturers Pilkington Glass, UK.

[2] Whitehouse Scientific Ltd, UK.

[3] Potter's Ballotini Ltd, UK.

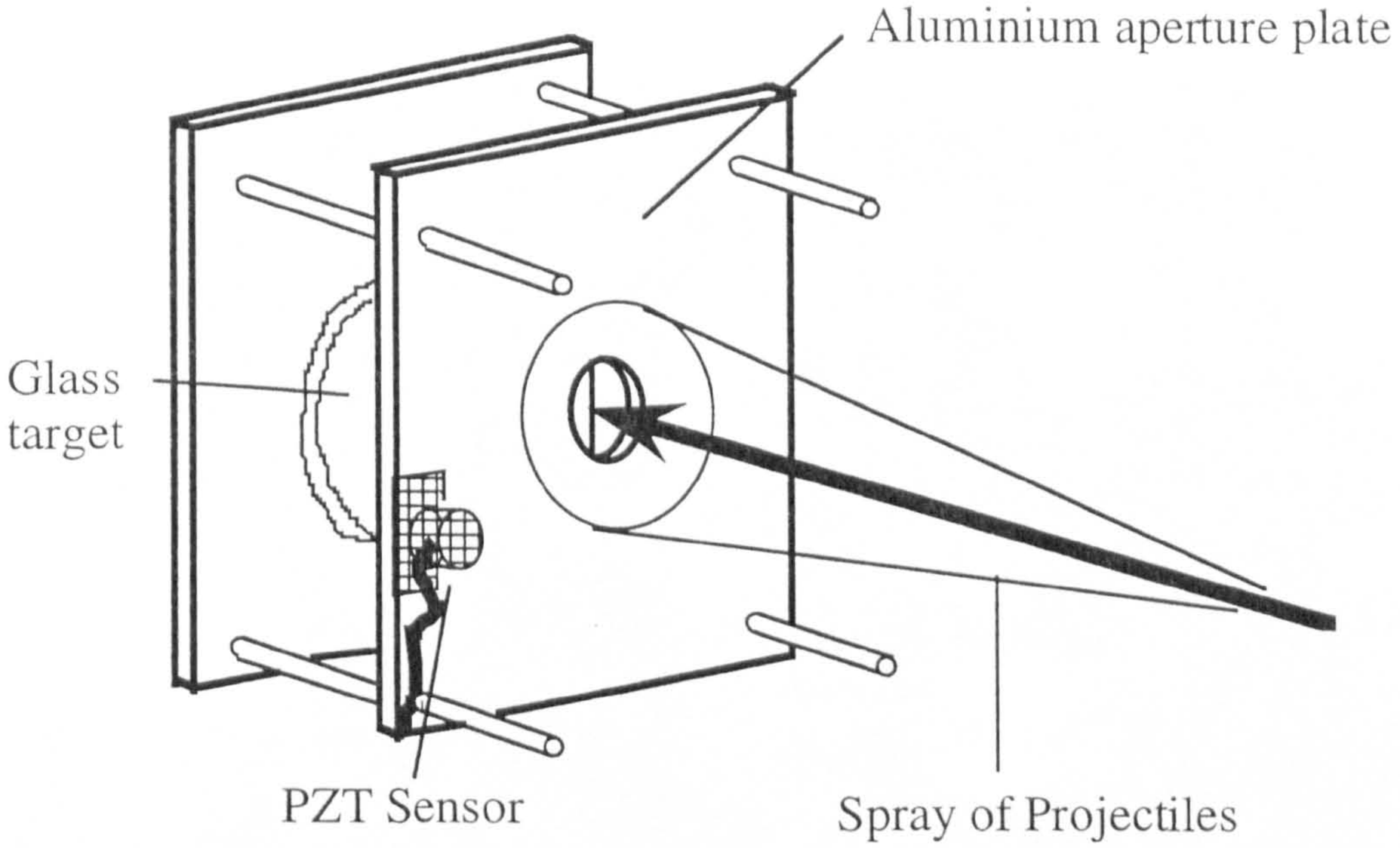

Figure 2-2(a). Experimental set up for LGG buckshot programme. (Taylor *et al.*, 1997d and Shrine *et al.*, 1996).

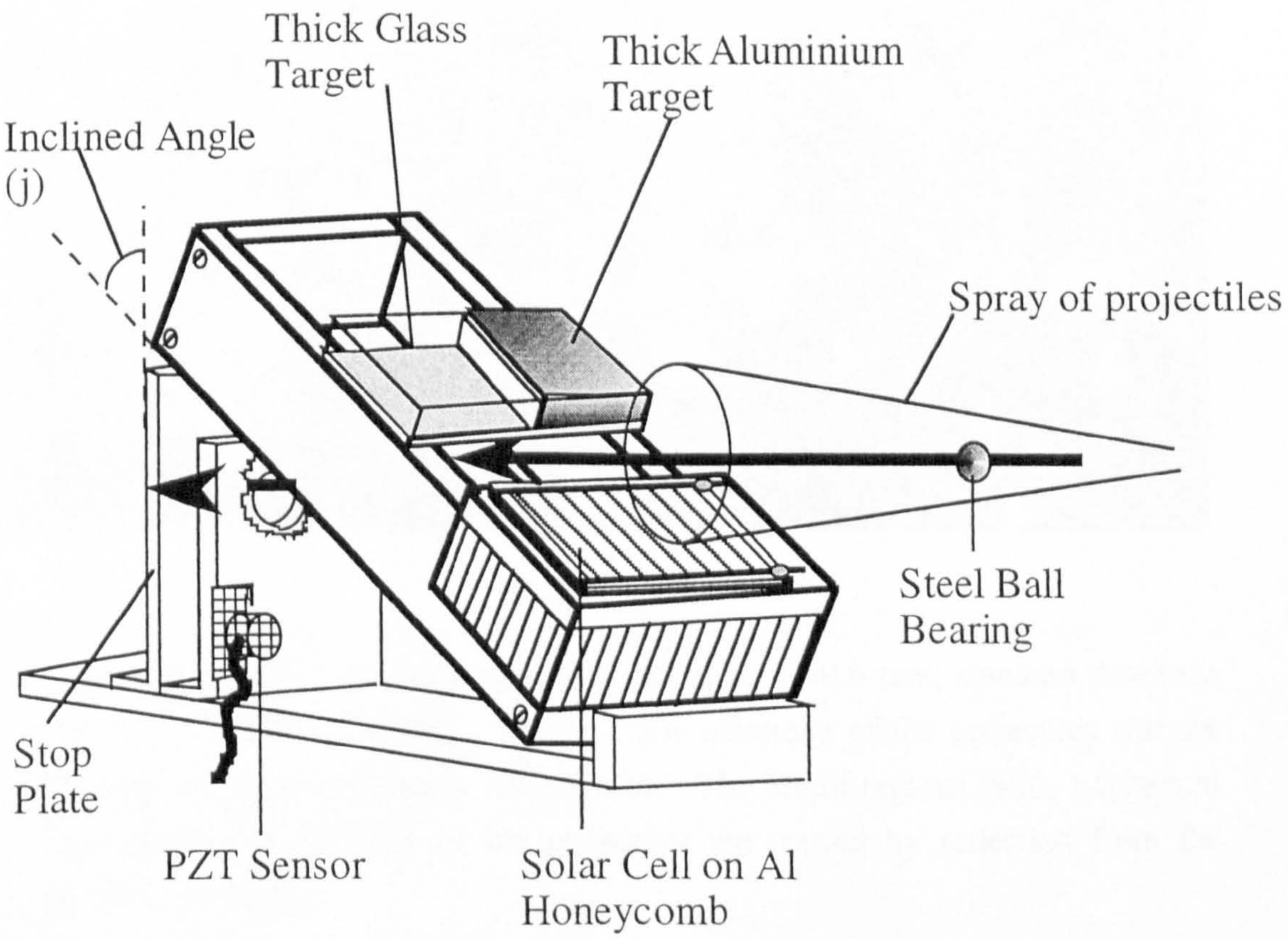

Figure 2.2(b). Experimental set up for solar cell and soda-lime glass impact programme (Shrine *et al.*, 1996)

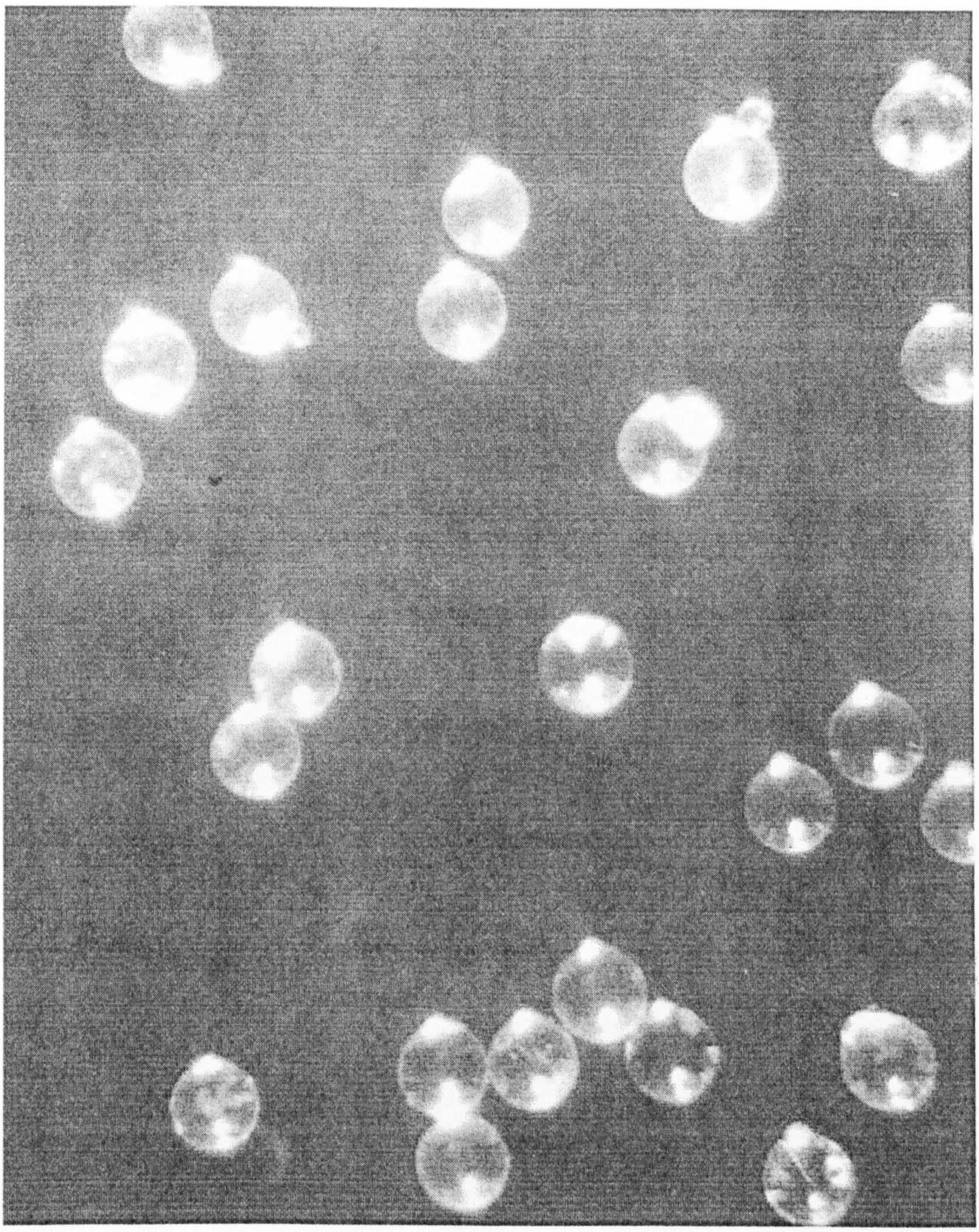

Figure 2-3. Sorted and graded ballotini (mean d_p = 99.6 μm, standard deviation is 2.9 μm). (Baron, 1996). Note the low ellipticity of the projectiles and the absence of large deviations in the diameter. The bright regions (with a spherical appearance) on the edge of the projectiles are caused by reflection from the illuminating source.

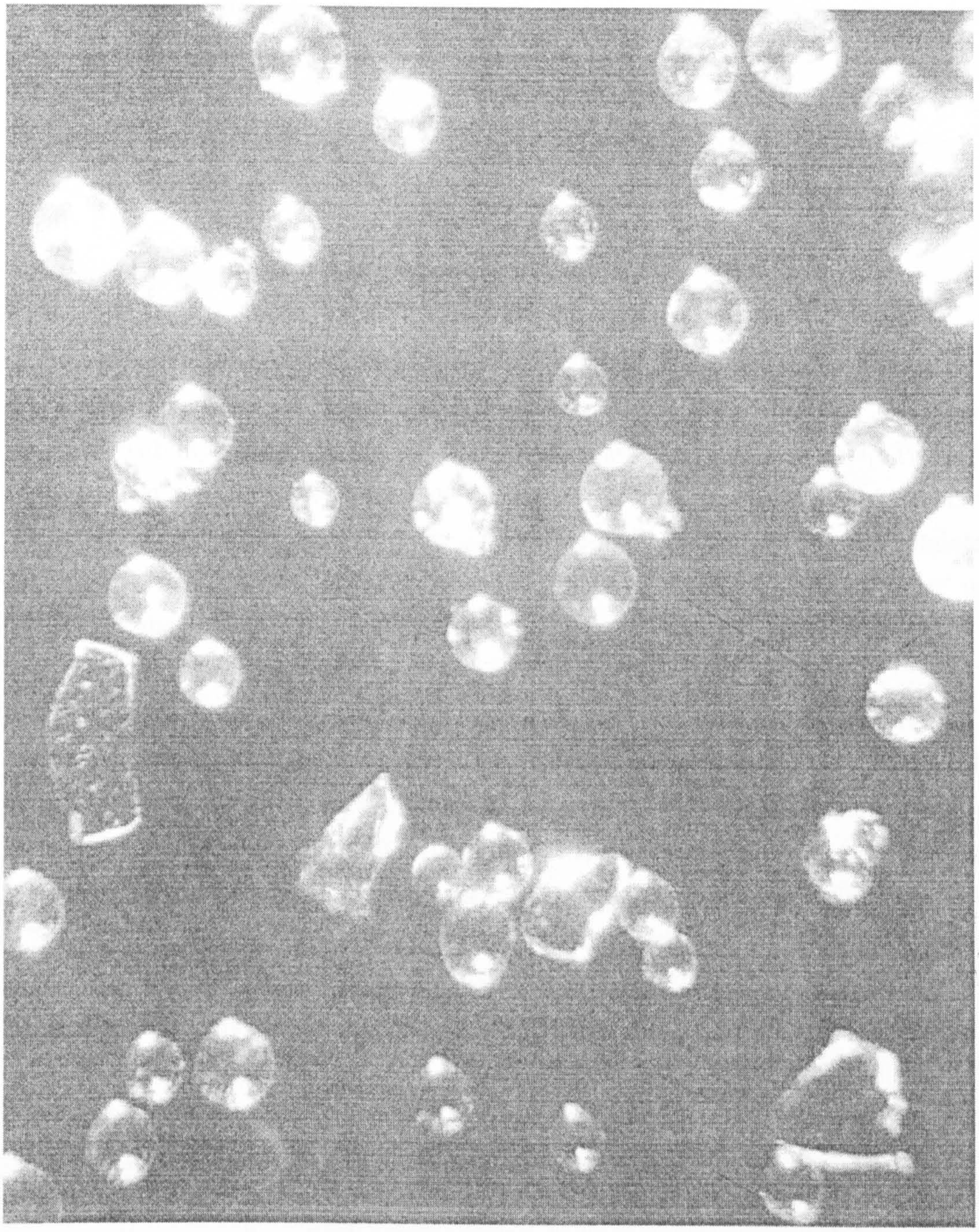

Figure 2-4. Sieved ballotini (sieve diameter range 90 - 106 μm). There is a variation in diameter and ellipticity of the particles. In addition some of the fragments are 'shards' of glass. (Baron, 1996). The bright regions (with a spherical appearance) on the edge of the projectiles are caused by reflection from the illuminating source.

coated with a thin layer of aluminium or gold and the impact sites were imaged using UKC's scanning electron microscope (SEM). The impact site parameters were measured and an average value, plus the standard deviation, was used in the impact database. The diameter of the craters in the aluminium aperture plate were also measured using the SEM. The scatter in the aluminium crater diameters is used as a check on the spread of velocity and projectile diameter within the buckshot cloud. The variation in the aluminium crater diameter values was typically ± 2 %, caused by velocity and particle diameter variation.

A further estimate of the velocity spread in a buckshot cloud can be obtained by studying a high-speed IMACON[4] image, as shown in Figure 2-5. Table 2-3 gives the details of the measurements made from the cloud. A 2 mm stainless steel projectile was used as a 'plug' and 150-180 μm diameter iron projectiles were used. Tests showed that the minimum size for good visibility was above the 90 μm diameter glass projectile threshold. Therefore, 150-180 μm iron projectiles were chosen for better visibility. The measured velocity of the projectile was determined using the laser time-of-flight system on the stainless steel projectile. The iron projectiles were spread out in a cloud behind the main 'plug' projectile. At a time t, the projectile has travelled a distance x m and the rear of the cloud (x-a) m. The distance x is the distance from the launch tube exit to the IMACON camera (2.691 m) The value of a is determined by measurements from the (calibrated) IMACON images. Calibration was performed by measurements made from images of an object of known diameter. Accurate timing between the second laser and the IMACON camera was provided by an oscilloscope. The variation in velocity between the projectile and the rear of the buckshot cloud is very small. In this calculation, the variation in velocity is 0.03 km s^{-1} or 0.7 % of the projectile velocity, which is of the same order as the measurement error for a millimetre sized projectile's velocity measurement via the laser signals (typically 0.5 - 1 %) (M. J. Cole, personal communication).

Table 2-3. Calculation of Δv between front projectile and rear of cloud using IMACON 468 camera images of buckshot cloud in flight.

ID	$v_{measured}$	x (m)	a (m)	t (μs)	v_{proj} (km s^{-1})	$v_{cloudrear}$ (km s^{-1})	Δv (km s^{-1})	%Δv
1104971	4.52	2.691	0.015	245	4.52	4.495	0.025	0.7 %

2.4 'Millimetre-sized' Projectiles onto Glass Programme

The targets used in this programme were made of soda-lime glass; 152.4 mm in diameter and 25.4 mm in height. The targets were mounted so that the rear was not in contact with

[4] IMACON was provided on loan by the EPSRC. Thanks are due to M. Cole, M. J. Burchell and J. C. Zarnecki for the IMACON image and measurements in this thesis.

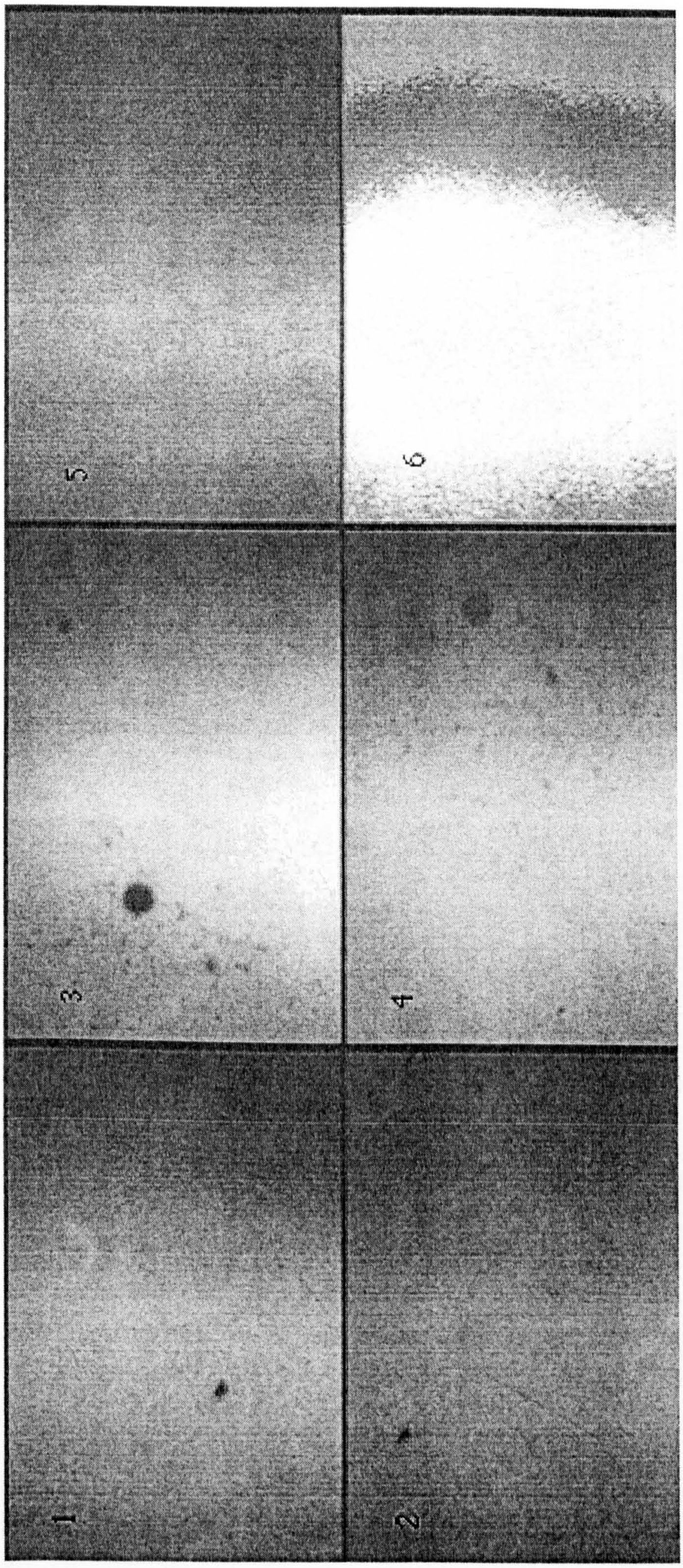

Figure 2-5. IMACON photograph of 2 mm stainless steel projectile and 150 - 180 μm iron buckshot projectiles. The time between each frame (numbered 1 to 6) is 4 μs. The projectile and buckshot cloud can be seen in frames 3 and 4. Frame 6 was taken by a faulty channel of the IMACON.

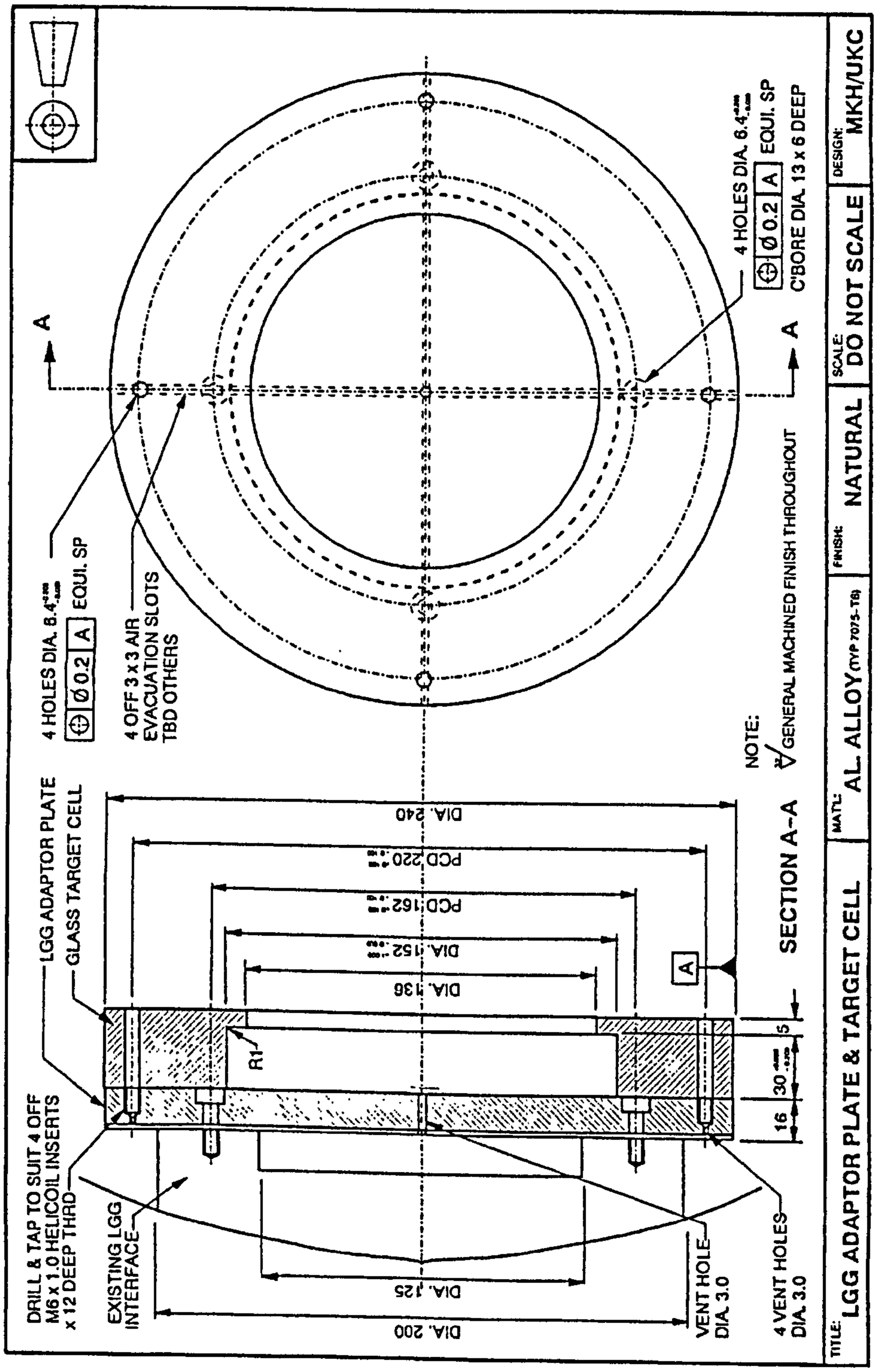

Figure 2-6. Schematic of soda-lime glass holder for section 2.4 shot programme (millimetre-sized impactors). Drawn and designed by M. K. Herbert.

another surface (free rear surface). In order to prevent fracture at the edge of the disk, the targets were purchased as 'ground all around'[5], as for the previous programme.

Table 2-4. mm-sized impact shot programme. (N/A : no data given by manufacturers)

ID	v (km s^{-1})	d_p (mm)	ρ_p (g cm^{-3})	Grade	Projectile type
G02	4.99	1.0	4.51	500	Titanium
G03	5.01	1.0	8.03	100	Stainless Steel AISI 316
G04	4.95	1.0	7.75	100	Stainless Steel AISI 420
G05	5.17	1.0	8.47	1000	Phosphor Bronze
G06	4.79	1.0	14.97	10	Tungsten Carbide
G08	5.44	1.5	1.45	N/A	Cellulose Acetate
G09	5.39	1.2	7.75	100	Stainless Steel AISI 420
G10	5.30	0.8	7.75	100	Stainless Steel AISI 420
G11	5.00	0.8	7.92	100	Stainless Steel AISI 304
G12	5.00	0.8	2.78	200	Aluminium alloy 2017
G14	5.05	1.0	2.78	100	Aluminium alloy 2017
G15	5.37	1.2	1.15	N/A	Nylon
G16	5.20	1.0	7.83	25	Chrome Steel AISI 52100
G17	5.00	0.8	7.83	25	Chrome Steel AISI 52100
G19	5.14	1.2	7.83	25	Chrome Steel AISI 52100
G20	5.07	1.2	2.78	200	Aluminium alloy 2017
G22	4.88	0.8	7.92	100	Stainless Steel AISI 304
G23	4.69	0.8	7.83	25	Chrome Steel AISI 52100
G26	4.44	2.0	2.78	200	Aluminium alloy 2017
G27	5.42	1.0	7.75	100	Stainless Steel AISI 420
G28	5.34	1.5	1.15	N/A	Nylon
G29	4.90	1.5	7.92	100	Stainless Steel AISI 304
G30	4.98	1.5	7.75	100	Stainless Steel AISI 420
G31	5.42	1.2	2.78	200	Aluminium alloy 2017
G32	5.00	0.8	2.78	200	Aluminium alloy 2017
G34	5.49	1.5	3.99	N/A	Synthetic Ruby
G35	5.18	1.5	2.78	200	Aluminium alloy 2017
G39	4.59	1.0	7.75	100	Stainless Steel AISI 420
G40	4.61	1.0	2.78	200	Aluminium alloy 2017

The mounting arrangement is shown in Figure 2-6. Small rubber pads were used to prevent the rear of the glass target making direct contact with the target holder. A semi-cylindrical curved tray, 0.91 m in length, was placed in the main target chamber to catch the ejecta from the impact. The shot programme is given in Table 2-4. The majority of the projectiles used in this thesis were procured from Salem Speciality Balls, U.S.A., Trafalgar Ball Bearings,

[5] Suppliers, Piper Glass, UK, glass manufacturers Pilkington Glass, UK.

U.K. and Goodfellows, U. K.. The projectiles chosen were limited by the availability and cost. The numerical values of the grades given in Table 2-4 are defined in Table 2-5. Note that the variation in diameter and sphericity is always less than 1 %. The density and full material names of the projectiles are given in Table 2-6.

Table 2-5. ANSI/AFMBA definition of ball grade quality.

Grade	Allowable ball diameter variation (μm)	Allowable deviation from spherical form (μm)
10	0.25	0.25
25	0.6	0.6
100	2.5	2.5
200	5	5
500	13	13
1000	25	25

Table 2-6. Projectile names and densities.

Material name	Material specification	Density (g cm^{-3})
Stainless Steel (Martensitic)	AISI 420	7.75
Stainless Steel (Austenitic)	AISI 316	8.03
Stainless Steel (Austenitic)	AISI 302, 304	7.92
Chrome steel	AISI 52100	7.83
Titanium	Ti (pure)	4.51
Phosphor bronze	PB102 (Cu - 92-94% Sn 6-8 %)	8.47
Aluminium alloy	Al 2017	2.78
Cellulose acetate	-	1.45
Tungsten Carbide	-	14.97
Nylon	-	1.15
Ruby	-	3.99

2.5 Composite/Honeycomb Programme

A full range of projectile diameters, densities and impact angles were investigated in this thesis to evaluate the response of the target to hypervelocity impact. The photography, digital analysis of the impact features and further analysis of the ballistic limit was carried out in conjunction with M. K. Herbert (GKN Westland Ltd.). The target material comprised carbon fibre reinforced plastic (CFRP) facesheets with an aluminium honeycomb (Al-HC) core, as typically used for a LEO space platform. The CFRP/Al-HC construction (e.g. CFRP lay-up) and material properties are given in Table 2-7.

An aluminium witness plate (1.6 × 100 × 100 mm) was mounted at a distance of 142 ± 1 mm behind the rear target surface for each shot (Figure 2-7(a)). The error on the velocity measurements is ± 2%. Where both velocity measurement systems failed, a velocity of 5 km

s^{-1} was assumed, based on previous firings with that projectile (denoted by the symbol * in Table 2-8). The set-up for oblique impacts is shown in Figure 2-7(b). A witness plate was only necessary for the highly oblique shots (75°). The shot programme is given in Table 2-8.

Table 2-7. Target material properties

Face sheets	
Prepreg matrix	4 ply satin woven carbon fibre epoxy HMF371-7714B
Fibre Orientation	0°/90°/90°/0°
Thickness	1.62 mm
Density	1800 - 1850 kg m^{-3}
Modulus of Elasticity	69.1 - 69.5 kN mm^{-2}
Honeycomb core	
Section type	Aeroweb
Material	Al Alloy 3003
Core density	83 kg m^{-3} (5.2 lb ft^{-3})
Cell size	6.4 mm (0.25 inches)
Cell foil thickness	0.06 mm (25 x 10^{-4} inches)
Core thickness	45 mm
Film adhesive	Redux 609 or 312

Table 2-8. Composite material impact programme.

Shot ID	d_p(mm)	ρ_p (g cm^{-3})	v(km s^{-1})	θ (°)	E(J)
HC01	2.0	7.8	5.9	0.0	559.3
HC02	1.0	7.8	6.1	0.0	76.5
HC03	1.0	8.5	6.2	0.0	86.1
HC04	1.5	1.5	4.9	0.0	30.6
HC05	1.5	8.5	5.0*	0.0	187.1
HC06	1.5	7.8	5.0	0.0	167.8
HC07	2.0	8.5	4.8	0.0	400.2
HC11	1.2	1.2	4.6	0.0	11.1
HC13	2.0	1.2	5.0*	0.0	60.2
HC15	1.0	2.8	5.4	0.0	21.5
HC16	1.2	2.8	4.9	0.0	29.9
HC17	1.5	2.8	5.9	0.0	87.0
HC18	2.0	2.8	5.1	0.0	151.3
HC19	0.8	2.8	5.0*	0.0	9.32
HC20	1.5	2.8	4.8	46.6	58.0
HC21	1.2	2.8	5.2	44.3	34.6
HC22	1.5	2.8	5.0	74.6	61.6
HC23	1.2	2.8	5.0	74.4	31.2
HC24	1.5	4.0	4.7	74.7	78.8

Table 2-8 cont.

Shot ID	d_p(mm)	ρ_p (g cm^{-3})	v(km s^{-1})	θ (°)	E(J)
HC25	1.5	2.8	5.1	74.7	64.6
HC26	1.2	2.8	5.0	14.3	31.5
HC27	1.5	2.8	4.9	14.7	60.4
HC28	0.8	7.8	5.1	14.4	26.9
HC29	1.0	7.8	5.8	16.0	67.3
HC33	1.2	2.8	5.2	24.5	33.6
HC34	1.2	2.8	5.2	63.5	33.9
HC35	1.2	2.8	5.2	59.7	34.8
HC36	1.0	7.8	5.1	74.4	52.2
HC37	1.0	7.8	5.3	45.0	57.0
HC38	1.5	4.0	4.9	45.0	84.9
HC41	1.2	4.5	5.0	73.4	51.8
HC43	1.2	4.5	5.2	44.5	54.7
HC44	1.2	4.5	5.1	17.0	52.2
HC45	1.2	4.5	5.1	14.8	53.0
HC46	1.2	4.5	5.1	74.1	53.7

2.6 Measurements and Morphology: Glass and Composites

The three shot programmes described in sections 2.3 to 2.5 produced a large number of targets with impact features. Table 2-9 shows the imaging techniques used to characterise the damage for each shot programme. The measurements taken on each sample are defined in this section.

Table 2-9. Imaging techniques used on experimental samples

	Glass (buckshot)	Glass (mm-sized)	Composites
Photography	no	yes	yes
SEM	yes	no	no
X-ray	no	no	yes
Profiling	no	yes	no

2.6.1 Buckshot measurements

The impact craters were too small (typically < 1 mm) to measure except via use of the scanning electron microscope (SEM). The targets were sputtered, as described in the previous section, and imaged. The typical morphology noted is given in Figure 2-8(a)-(d). As multiple impact sites were present on the target due to the buckshot technique, all the impact sites were measured and a mean value of the crater parameters determined. The error bar was defined as the standard error of the mean ($\sigma/\sqrt{(n-1)}$) (σ: standard deviation). The range in the crater diameters measured is due to a combination of uncertainties in crater

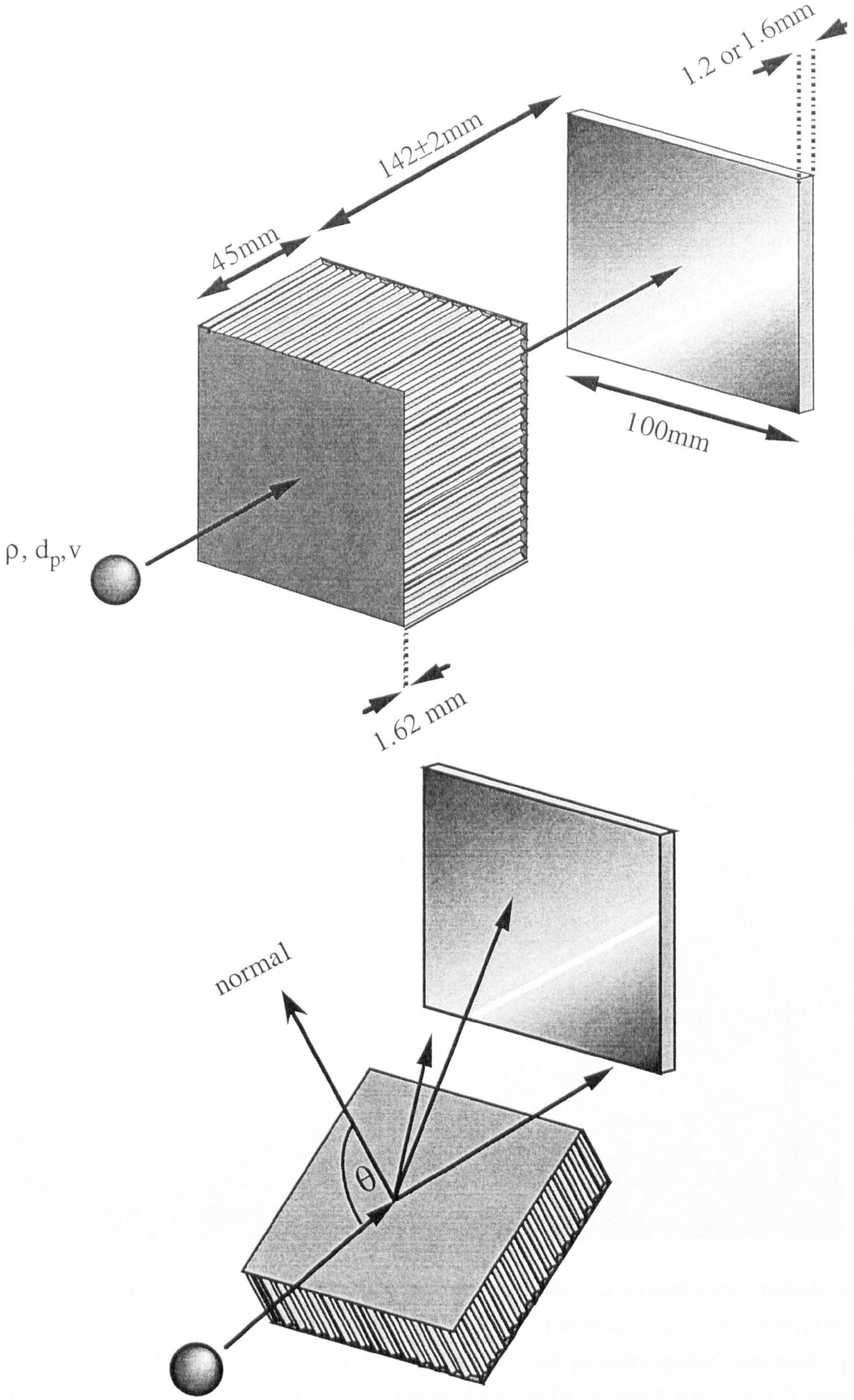

Figure 2.7. Experimental set up for normal and oblique shots onto carbon fibre reinforced plastic / aluminium honeycomb (CFRP / Al-HC). (Image drawn by J. M. Marchant.)

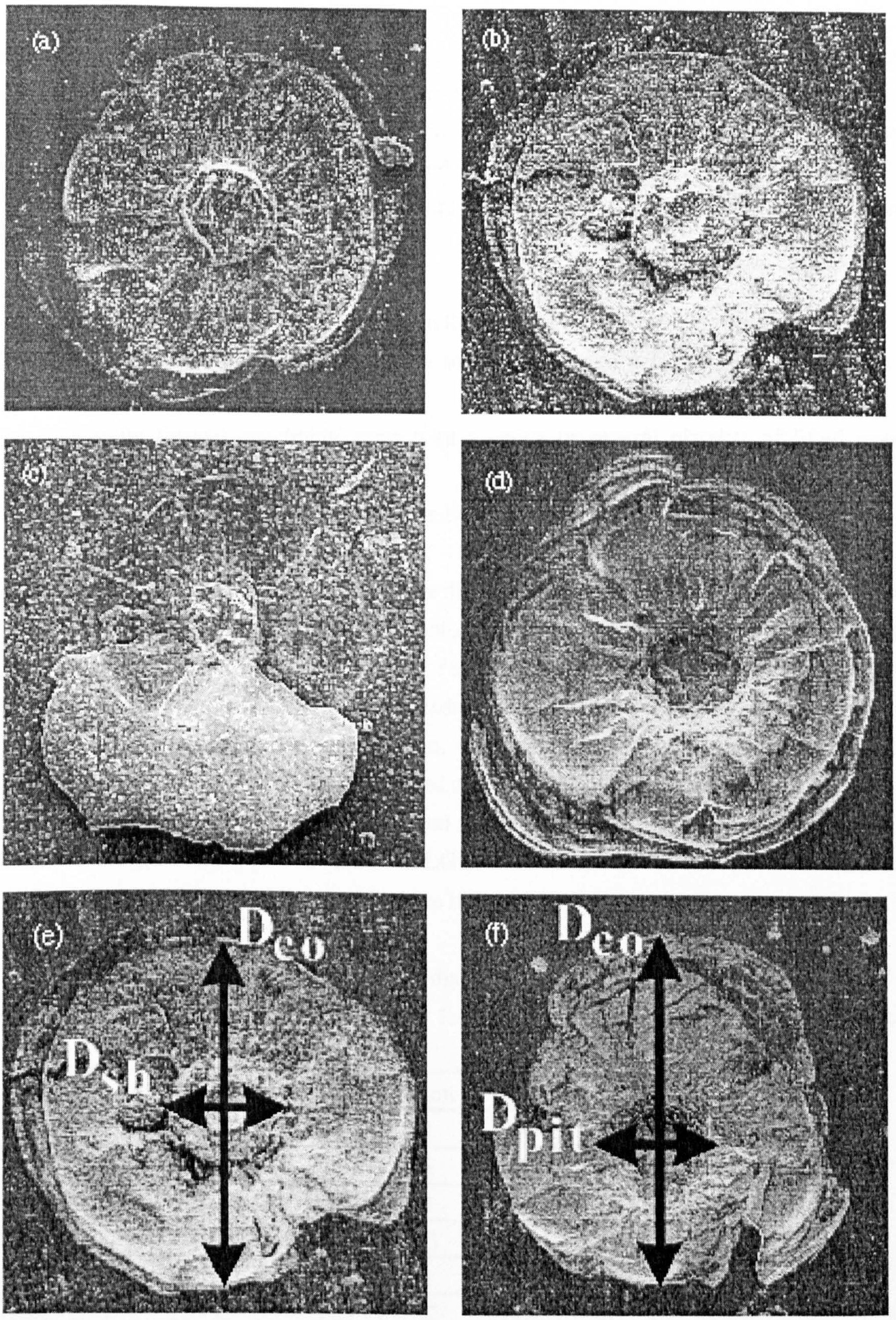

Figure 2-8. (a)-(d) Examples of morphology from the impact programme onto soda-lime glass for this thesis. (a) Central raised plateau plus conchoidal diameter (d_p = 36.1 μm), (b) as (a) but with central pit within central plateau (d_p = 53 μm), (c) partially spalled conchoidal platelet (d_p = 26.7 μm), (d) central pit and conchoidal diameter (d_p = 105.8 μm). (a)-(c) formed by projectiles $d_p < 50$ μm, (d) $d_p > 50$ μm at ~5 km s^{-1}, (e) conchoidal diameter (D_{co}) and raised plateau (D_{sh}), (f) D_{pit}.

measurements and a significant distribution of crater sizes due to variations in properties of the projectiles and target. The error in the measurement technique was insignificant compared with the scatter in the data observed (section 4-5). The parameters measured were the conchoidal diameter (D_{co}) and the raised shatter diameter (D_{sh}) in Figure 2-8(e) and the D_{pit} parameter in Figure 2-8(f). There were 4 main types of craters observed, shown in Figure 2-8:

a) conchoidal zone with a raised plateau in the centre,
b) conchoidal zone with a raised plateau in the centre and a bowl shaped indent in the plateau,
c) a partially formed conchoidal zone with a single or several platelets of lifted material connected to the central plateau, and
d) conchoidal zone with a crater or "pit" in the centre.

Types a, b and c are observed at a projectile diameter of around 75 μm and below, and type d above this size. The change in morphology is summarised in Table 2-10. The plateau region in types a-c is probably the bottom of the original crater formed early on in the impact process. Type c appears to be an intermediate stage where one or some of the platelets, ejected to form the conchoidal zone, remain. These morphologies (pit in the plateau region; unejected platelets) have also been observed on lunar micro-craters (Hörz *et al.*, 1971; Glass, 1972), although glass-lined pits are not seen on our targets. A possible explanation for the absence of glass-lined pits is that, at LGG velocities, the central pit does not reach temperatures as high as achieved with space impacts.

Table 2-10. Number of pit and shatter diameters recorded on glass targets. Bold type signifies that the morphology is dominant for that projectile diameter. * denoted projectiles obtained by sieving glass ballotini.

Shot ID	d_p(μm) (mean)	D_{pit} ?	Count	D_{sh} ?	Count
GBS13	26.7	yes	4	**yes**	29
GBS12	36.1	yes	6	**yes**	22
GBS01	49*	yes	2	**yes**	19
GBS06	53	yes	13	**yes**	25
GBS11	77.9	**yes**	8	no	0
GBS07	105.8	**yes**	12	no	0
GBS18	150.9	**yes**	22	no	0
GBS17	178.1	**yes**	3	no	0
GBS15	195.2	**yes**	2	no	0
GBS02	196*	**yes**	11	yes	1
GBS09	275*	no	0	**yes**	1
GBS14	292.7	**yes**	2	no	0

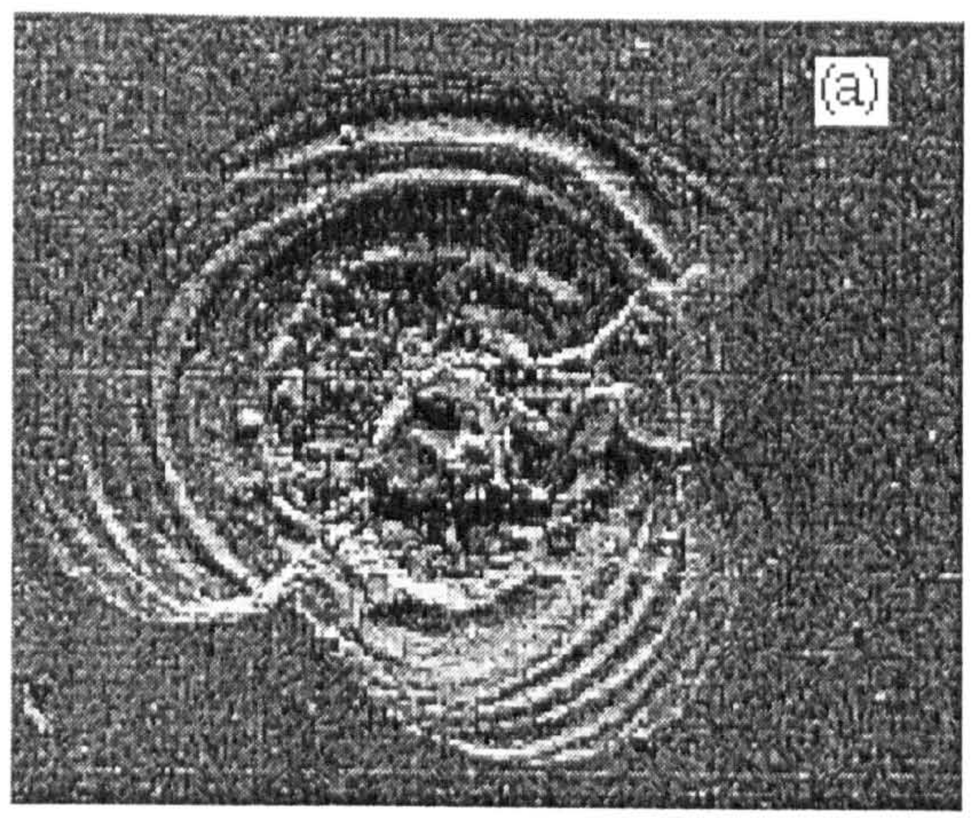

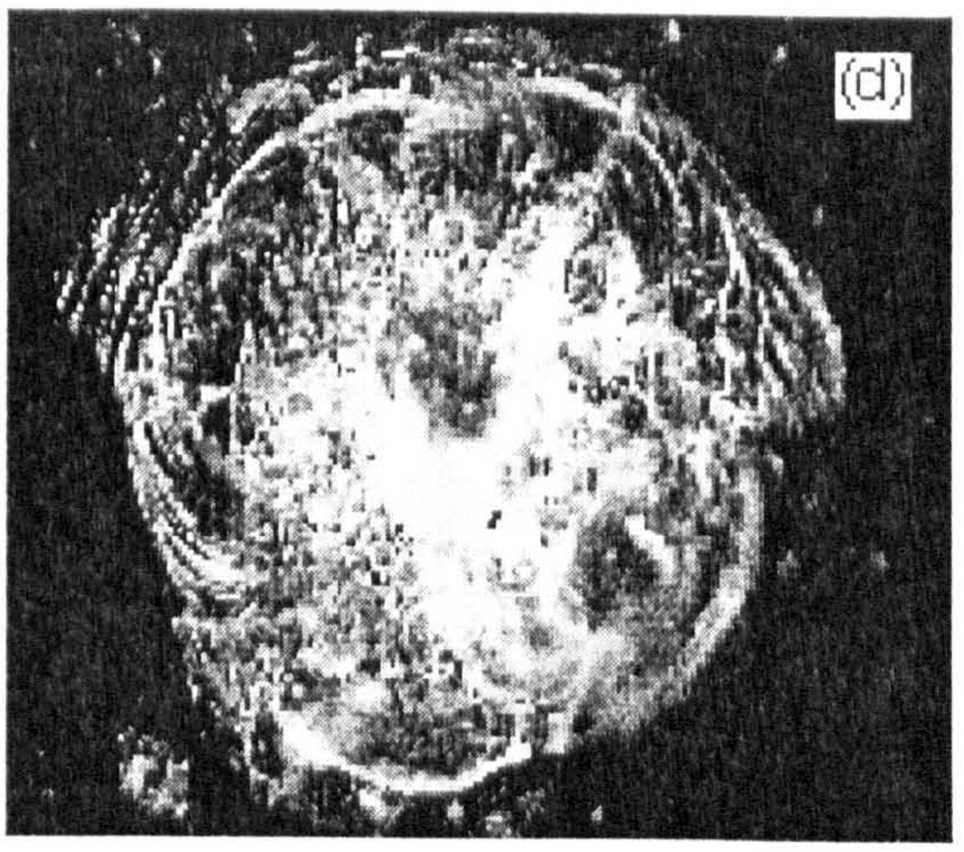

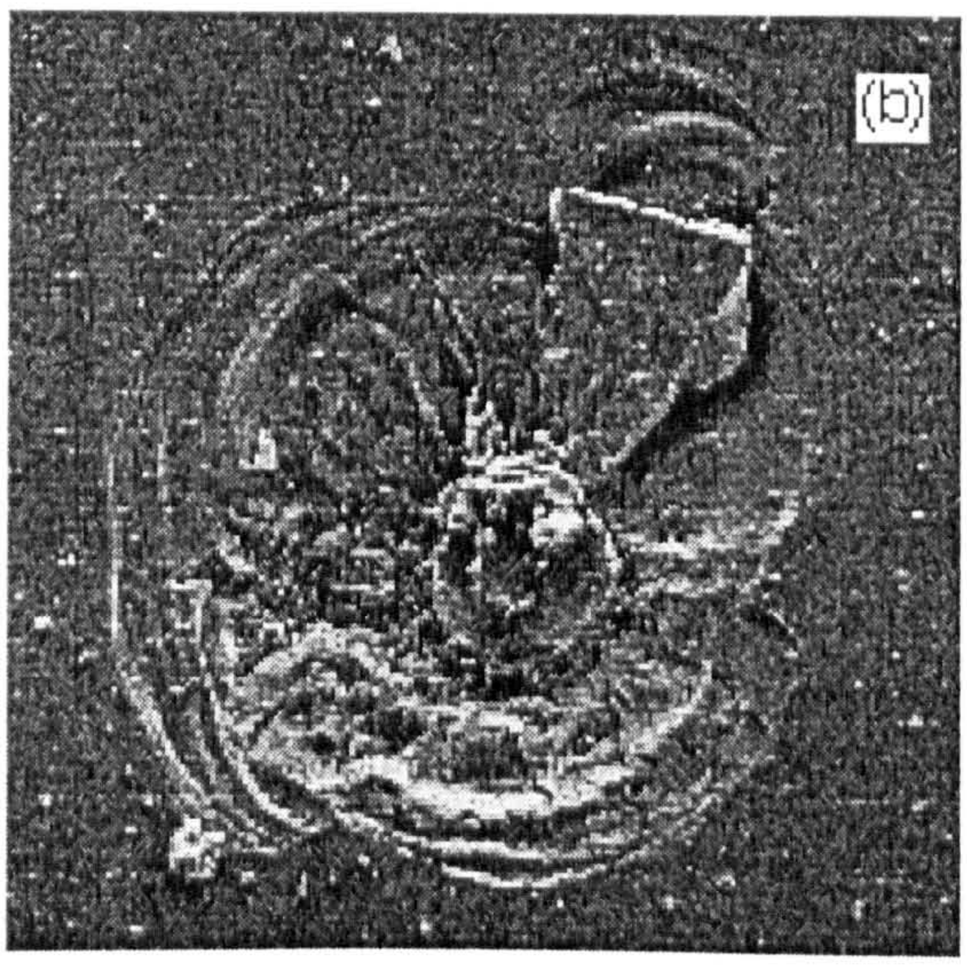

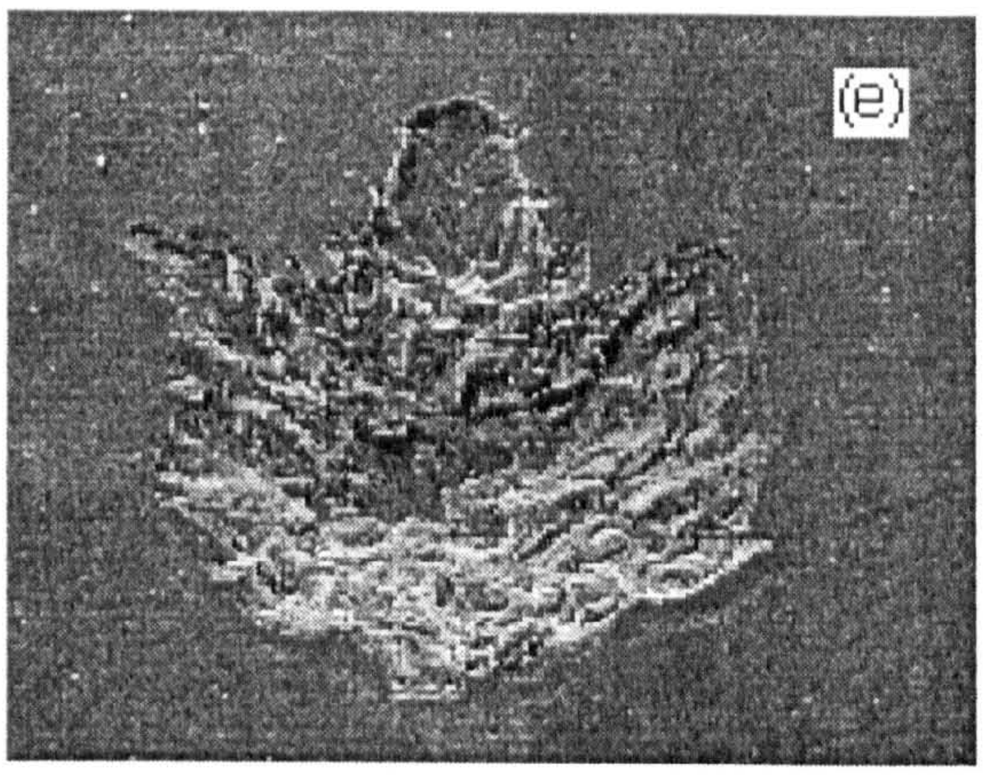

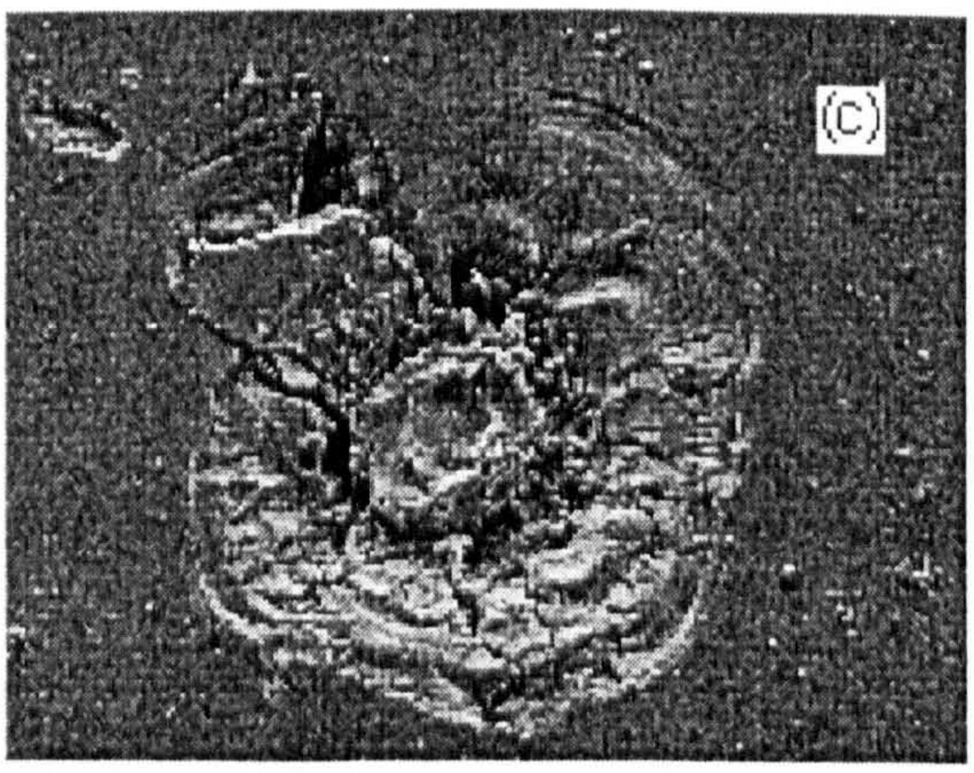

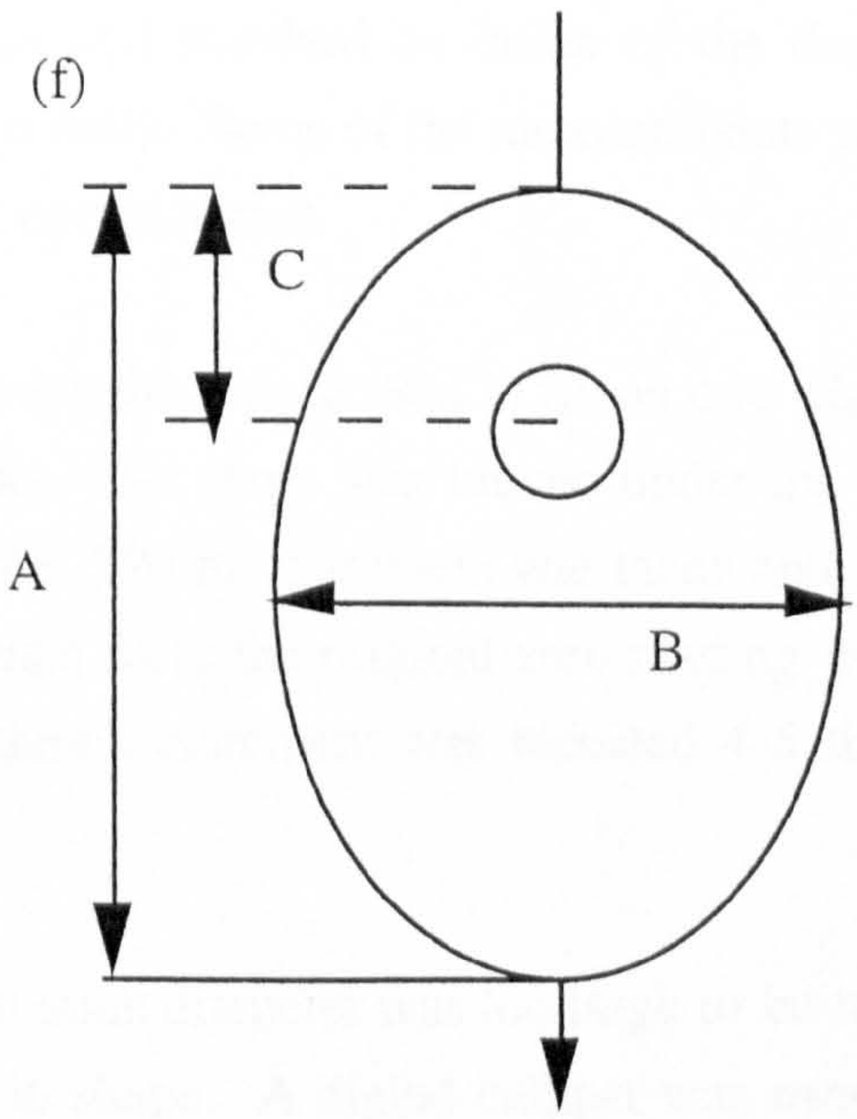

Figure 2-9. Impact morphology for oblique impacts onto solar cell targets (Shrine *et al.*, 1996). (a) 0° (b) 30° (c) 45° (d) 60° (e) 75° (f) measurements made on oblique impacts. The geometric mean of the conchoidal diameter is calculated in the same manner as for 0° impacts. The centroid offset, a parameter used to characterise the impact angle of craters, is given by $1-(2C/D_{co})$. Arrow signifies impact direction.

The maximum and minimum D_{co} values were measured for each impact site, representing along the line of flight (A) and perpendicular to it (B) for oblique impactors. This is shown in Figure 2-9. The conchoidal diameter, D_{co}, was calculated by taking the geometric mean of the A and B measurements ($\sqrt{(AB)}$). The mean values were averaged and the standard deviation obtained.

2.6.2 Millimetre-sized impactors

A schematic of the typical morphology noted on the glass targets is given in Figure 2-10. Different pit profiles are observed for different density projectiles. Examples of the morphology (central crater with raised rim in (a) and (c) and subsurface spallation and spallation diameter in (a)-(c)) are given in Figure 2-11. An optical microscope with clock gauges attached was used to measure the depth and central crater diameter. These gauges (measurement accuracy of 0.01 mm) extended or retracted as the stage (used to move the target from left to right under the microscope) or the microscope itself (up and down) was moved. By focusing on parts of the crater, then moving the microscope or the stage, a measurement could be made of the features. The clock gauges could record movement to ± 0.01 mm.

Depth measurement. A flat, circular black disc with a circular aperture was placed over the impact crater to provide the zero point. The operator focused on the deepest part of the crater then set the clock gauge to zero. The microscope was then adjusted to focus on the top surface of the black disc and the measurement taken. The operator then refocused on the base of the crater and noted the difference from the original zero setting as the error. This measurement was made 4-5 times and the mean and standard deviation of the depth were calculated (subtracting the thickness of the black disc). Some of the measurements were also repeated by R. Thomson to confirm absence of operator bias.

Crater diameter measurement. Graticules on the eyepiece were used to fix on one edge of the central crater. The clock gauges were set to zero. The stage was moved under the eyepiece until the opposite edge lined up with the graticule. The measurement was taken and the stage returned to the original crater edge. The difference from the original zero reading was taken as the individual measurement error. Again, the measurement was repeated 4-5 times and the mean and standard deviation calculated.

Spallation diameter and crater volume. The spallation diameter was too large to be measured by microscope and was only roughly circular in shape. A digital calliper was used to take two spallation diameter measurements (perpendicular to each other) but there was significant user variation in the measurements. An alternative measurement, developed by Burchell (Burchell *et al.*, 1998) for measuring spallation diameter and depth of penetration, was

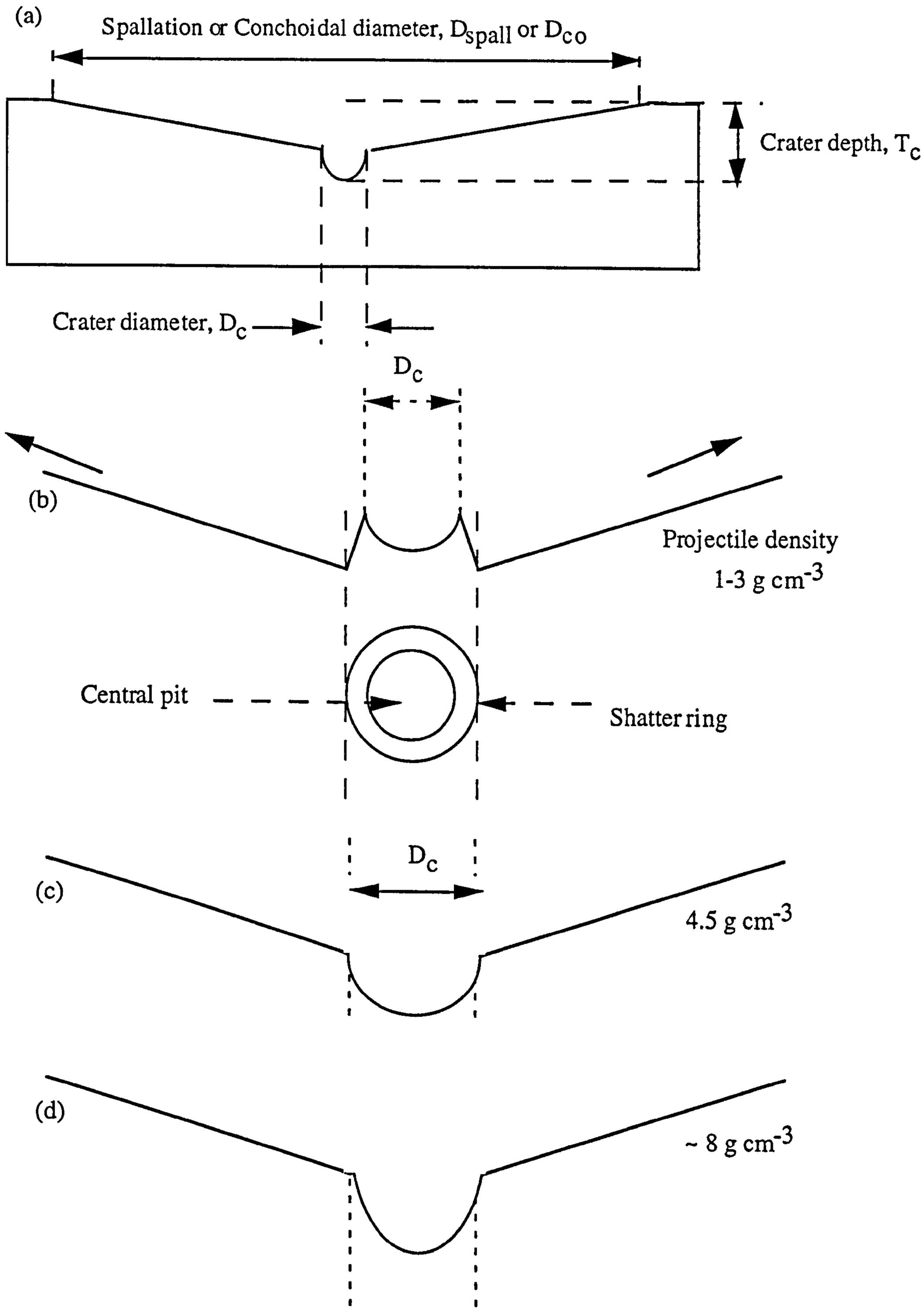

Figure 2-10. (a) Morphology observed on soda-lime glass targets when impacted by mm-sized impactors. (b) Close up central pit profile caused by low density impactors at ~5 km s^{-1}. The central pit is raised and surrounded by a ring of opaque ridged glass, assumed to be shattered. (c) Rounded pit profile from a titanium impactor (d) Deeper pit profile (high density projectiles).

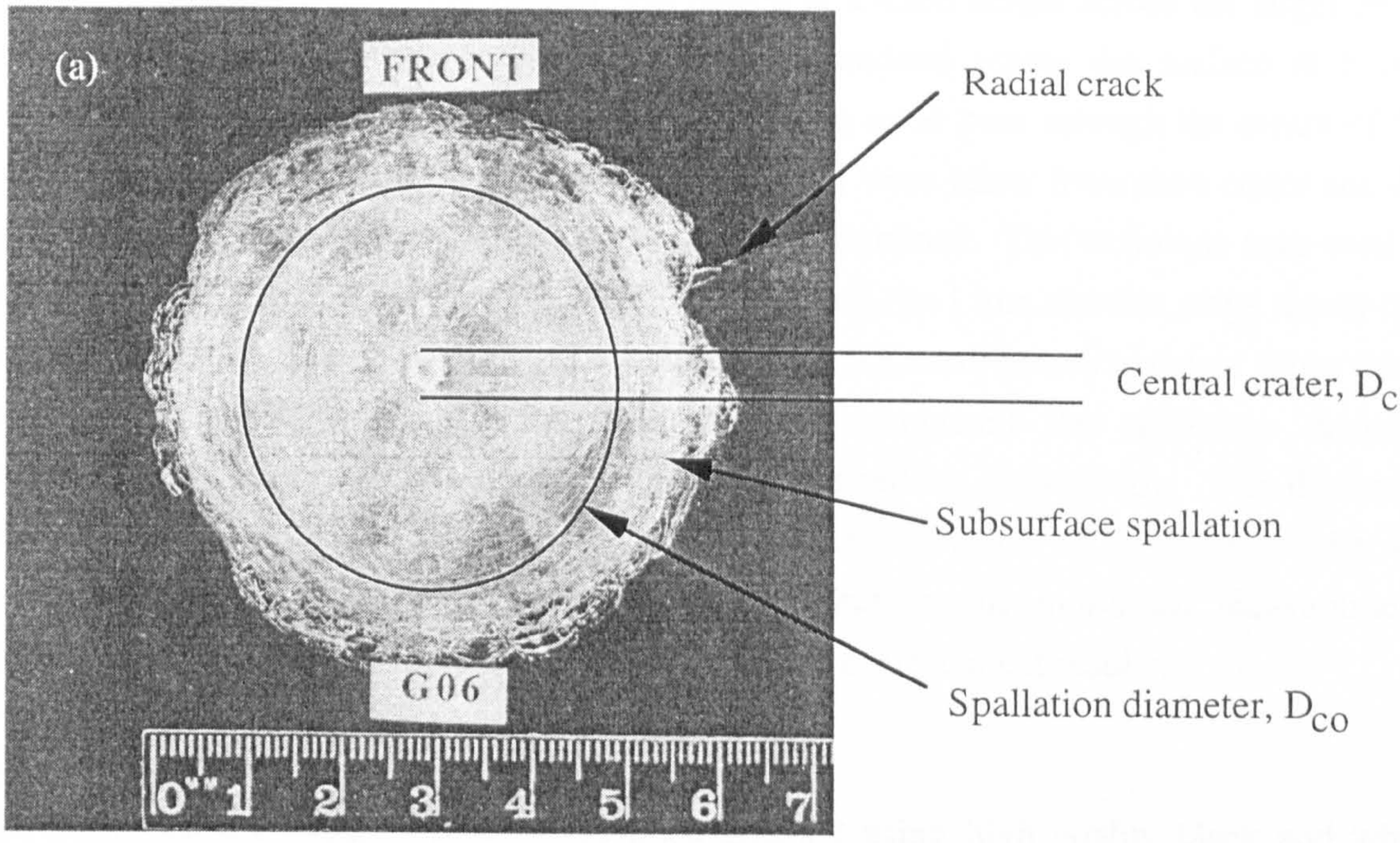

(b) (c)

Figure 2-11. Impact morphology onto soda-lime glass for mm-sized impactors. (a) Tungsten carbide impact showing central pit feature with shatter halo. (b) Stainless steel projectile (deep pit) (c) Aluminium projectile (shallow pit with shatter halo).(b) and (c) have been inverted for clarity. The pit profile changes as a function of impactor density, as given in Figure 2-10.

applied to the glass targets.[6] A support was placed at a fixed height across the target and a depth gauge (converted from a digital calliper) was moved across the surface at 1 mm intervals. The support was placed at such a position so as to pass through the centre of the central impact feature. Several profiles (typically four) were taken from each crater and the average value of the spallation diameter and volume determined. This technique was used to verify the depth measured by optical methods. However, the 1 mm discrete steps meant that the central crater could not be resolved clearly. The depth measurements matched those taken by the optical microscopy so the final data set comprised the spallation diameter measurements and the depth and crater diameters obtained by microscopy. For the crater diameter and depth sets of measurements, the standard deviation of the mean of the 4-5 measurements was greater than the error measurement on the individual measurement. Therefore, the former is used where errors are quoted in subsequent results.

2.6.3 Composites

The front and rear impact features were photographed using high quality black and white film by S. Scott at the University of Kent at Canterbury's Photographic Unit. The general morphology of the impact features is shown in Figure 2-12. These impact features were digitally imaged and the projected area of the holes (A_f and A_r) were calculated using a pixel recognition/counting programme and the appropriate scaling factor. The measurements were made by M. K. Herbert. By equating the hole damage area (A_h) to that for a circle, the equivalent diameter (D_{eq}) was obtained using Eq. 2-3.

$$D_{eq} = (4A_h / \pi)^{0.5} \qquad (2\text{-}3)$$

This diameter value did not include any delamination damage of the surface. (Delamination damage is defined as material removed around the central hole which does not fully penetrate the surface). In addition, for the oblique shots, the hole diameters along (D_a), and perpendicular (D_b) to, the flight axis were measured. The elliptical ratio (circularity index, C. I.) was calculated from the ratio (D_a/D_b). The total hole diameter D_{eq} was defined by replacing A_h with A_t (Eq. 2-4) in Eq. 2-3.

$$A_t = A_f + A_r \qquad (2\text{-}4)$$

The morphology of impacts onto CFRP/Al-HC above the ballistic limit is given in Figure 2-13. The entrance and exit holes are much larger than the projectile diameters for the three high density projectile shots shown. The witness plates (placed behind the targets for the normal incidence shots) show different classes of damage caused by the exiting projectile

---

[6] The measurements were carried out by Dr. M. Burchell for the purpose of determining the crater volumes of the glass as part of a collaborative programme with the author of this thesis.

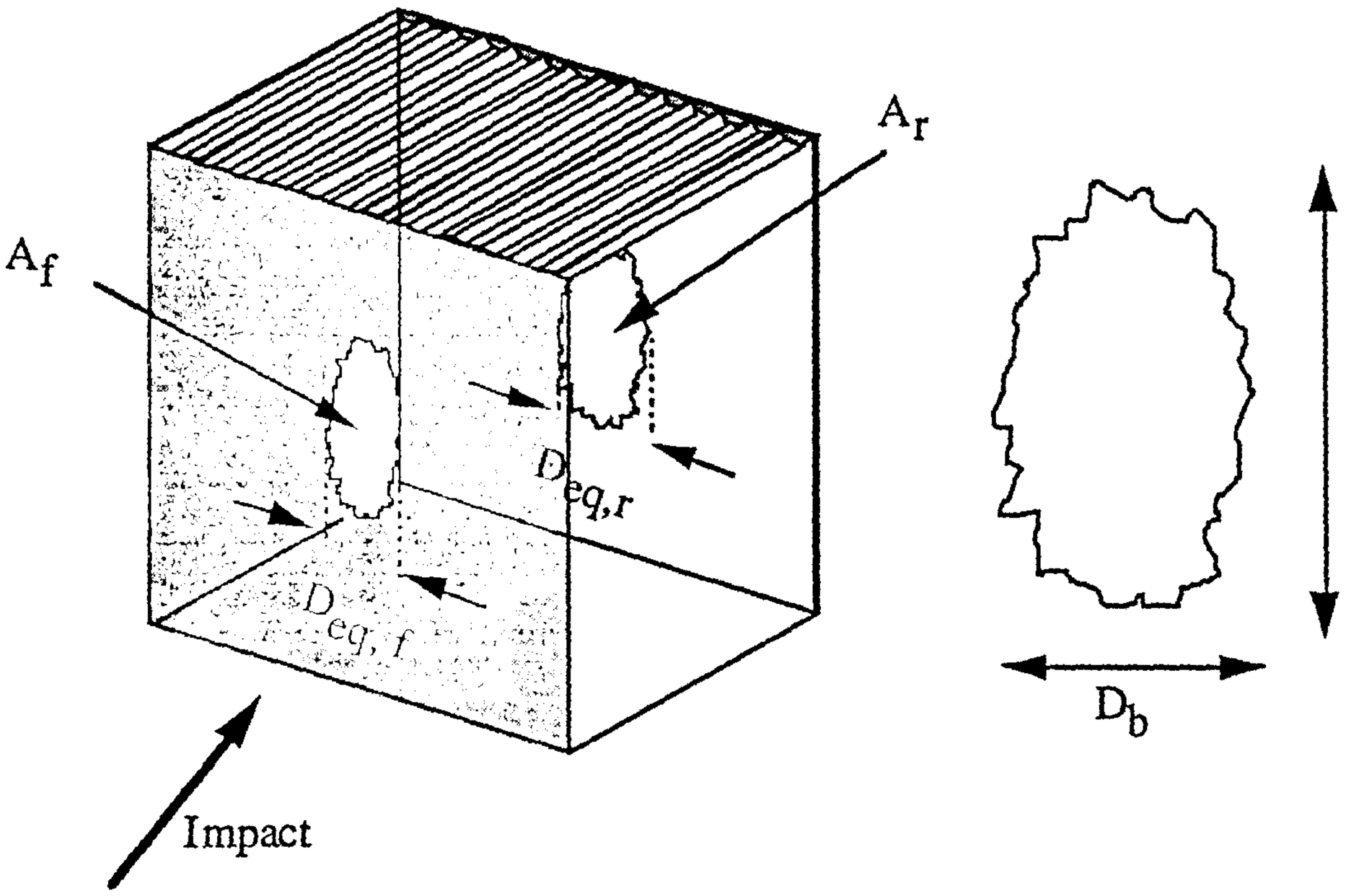

Ellipticity: D_a/D_b

Hole Growth Factor (HGF): $D_{eq,r} / D_{eq,f}$

$$A_t = A_f + A_r$$

Figure 2-12. The measurements made on the exterior surface of the honeycomb. The hole area for the front and rear, and the resulting equivalent diameters were calculated using a digital scanning programme. A hole growth factor (HGF) (the ratio of the rear and front hole equivalent diameters) was defined and used to identify damage trends. The ellipticity of the entrance hole (for oblique impacts) was defined as the ratio of the maximum and minimum hole diameters. (Image drawn by J. M. Marchant.)

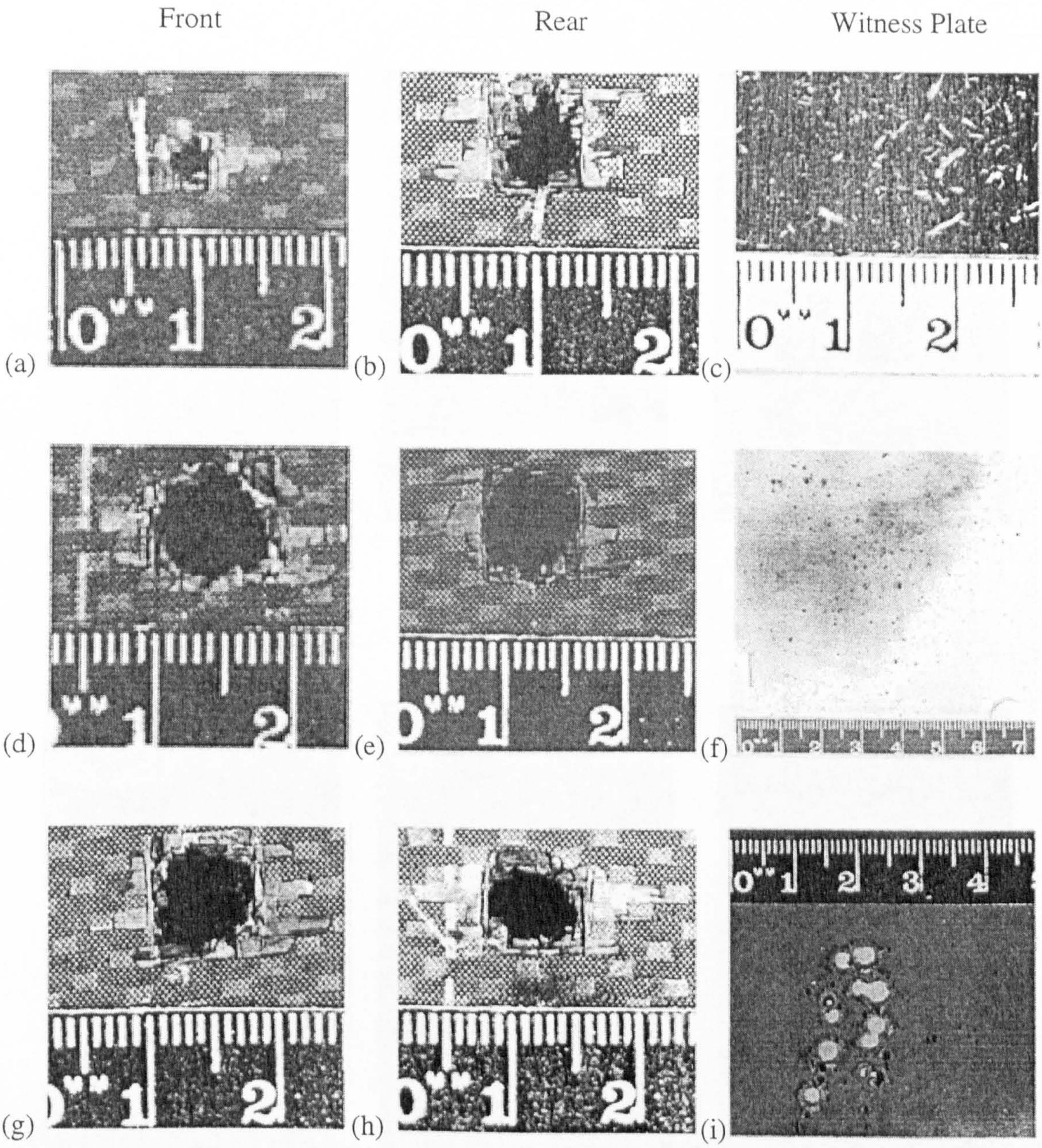

Figure 2-13. The images marked front, rear and witness plate show the entrance and exit holes and the front witness plate damage, respectively. (a) - (c) 1 mm phosphor bronze projectile (HC03). Carbon fibre fragments are stuck to the witness plate in (c). (d) - (f) 1.5 mm stainless steel projectile (HC06). There are a large number of circular impact craters on the witness plate (f). (g) - (i) 2 mm phosphor bronze projectile (HC07). The witness plate has been perforated.

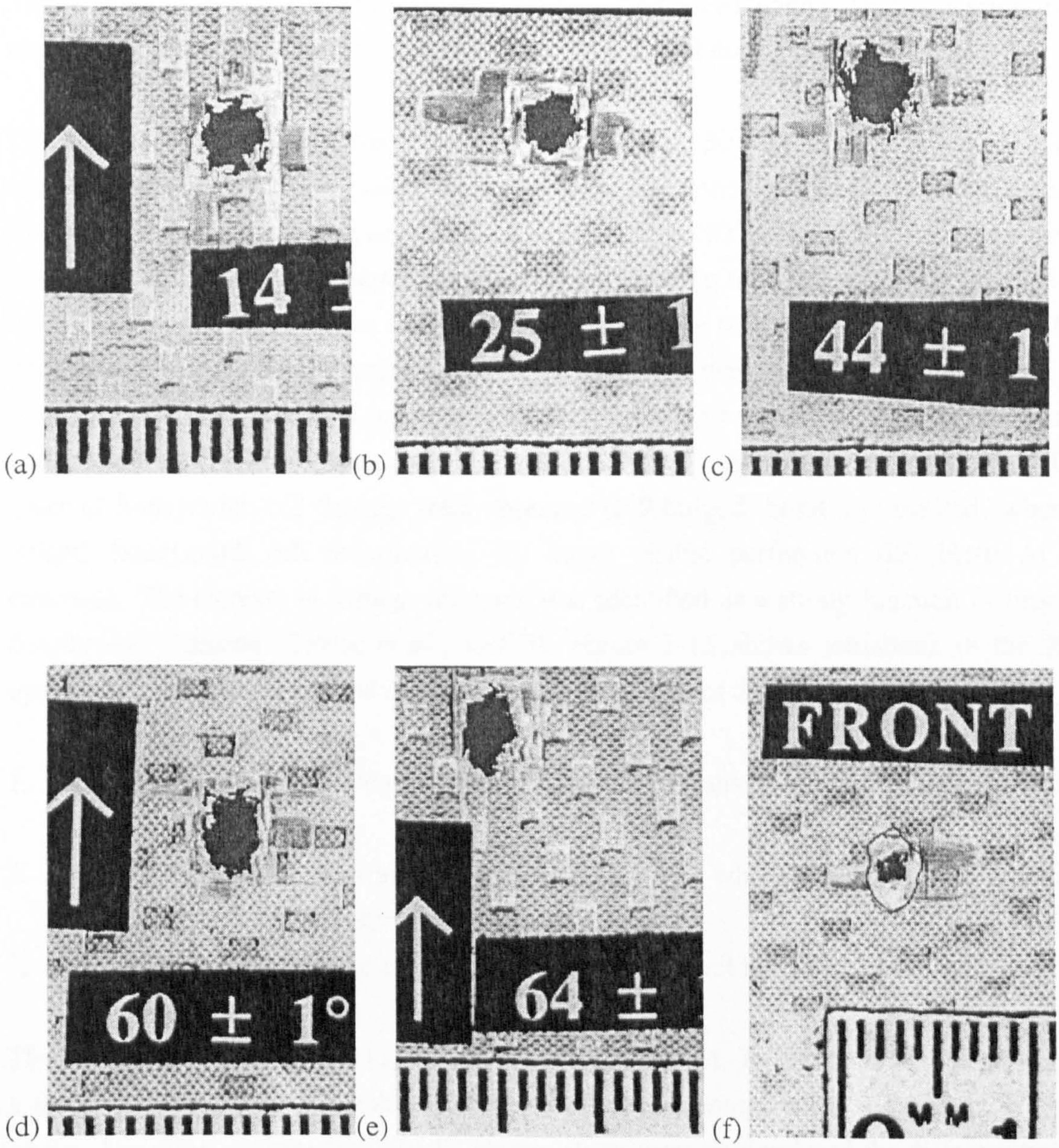

Figure 2-14. Crater morphology on CFRP/Al-HC for a range of impact angles for a 1.2 mm Al 2017 projectile. (a) 15° (b) 25° (c) 44° (d) 60° (e) 64° (f) 75° impacts. In (f) the outline shows the typical crater observed at this highly oblique impact angle. The 1.2 mm projectile was not large enough to produce the crater morphology through the full facesheet thickness. Images have been inverted for clarity.

and target fragments. The crater morphology of impacts onto CFRP/Al-HC as a function of impact angle (for a 1.2 mm aluminium projectile) is given in Figure 2-14. The crater shape becomes more elongated as the impact angle increases. For both the normal and oblique shots, a large quantity of ejecta was produced from the rear target surface (classified in Taylor *et al.*, 1997c). In addition, loose material remained within the target (comprising metal and carbon fibre fragments) which were not retained during target handling.

The internal honeycomb damage was measured using 30 keV X-rays exposed for 30 seconds onto Polaroid film (using the 43804 Faxitron Series at the Centre for Composite Materials, Imperial College, London). The exposed Type 52 Polaroid film recorded the cell damage integrated over the target thickness. The resulting morphology was classified and the maximum damage area was determined using the same technique as for the CFRP hole. An estimate of the random errors in the target response was provided by analysis of two pairs of shots using identical projectiles, impact angles and velocities. The variation in the crater features was used to estimate the 'reproducibility' errors applied to the data. Three types of honeycomb cell damage were observed (cell bulged, burst and blasted, where (i) bulged: honeycomb cell deformation, (ii) burst: visible perforation (iii) blast: Al wall removal). The increase in damage observed was identified as a strong function of projectile density and diameter (Taylor *et al.*, 1997b). Figure 2-15 shows variations in the X-ray opacity of the target for normal impacts. Three categories of damage were identified:-

1. Opaque. Indicative of crumpled / crushed multi-cell walls preventing the transmission of X-rays.
2. Partially transparent. Indicative of foreshortened cells whose walls have been subjected to buckling permitting partial transmission of X-rays.
3. Transparent. Identifies the extent of the entry and/or exit holes.

The honeycomb damage also varied as a function of impact. In Figure 2-16, the damage for a titanium projectile and a stainless steel projectile are compared as a function of impact angle. The witness plates from the 0° impact shots were scanned and the different types of damage were identified and grouped into five classes (given below). To quantify the damage, a swath 2.9 mm wide through the centre of the damage was scanned, and the number of craters in each category above a detection threshold of 300 μm was recorded. At the magnification used, features down to 15-20 μm could be detected, but were not counted due to their large number. The witness plates from the highly oblique shots were not scanned due to time constraints on this thesis.

1. Fibres embedded in the plates, characterised by elongated shape (length to width of 10:1 or larger) and carbon fibre remnants (Figure 2-13(c)).

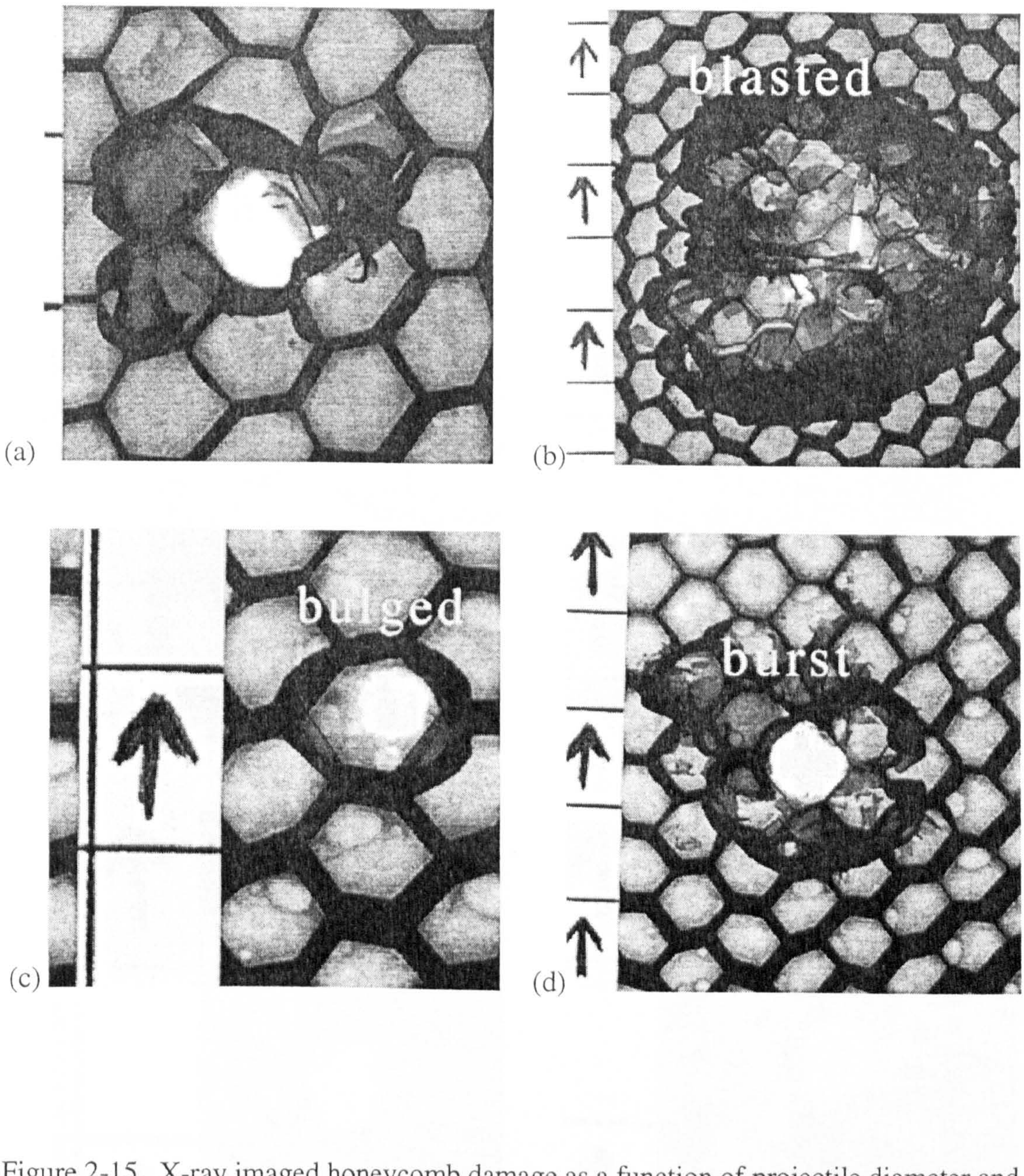

Figure 2-15. X-ray imaged honeycomb damage as a function of projectile diameter and density. (a) 1.0 mm phosphor bronze projectile (b) 2.0 mm phosphor bronze projectile (c) 1.0 mm Al 2017 projectile (d) 2.0 mm Al 2017 projectile. The three types of honeycomb cell damage identified in Taylor *et al.*, 1997c - cell blast, bulge and burst - are shown in (b), (c) and (d). Scale is in centimetres.

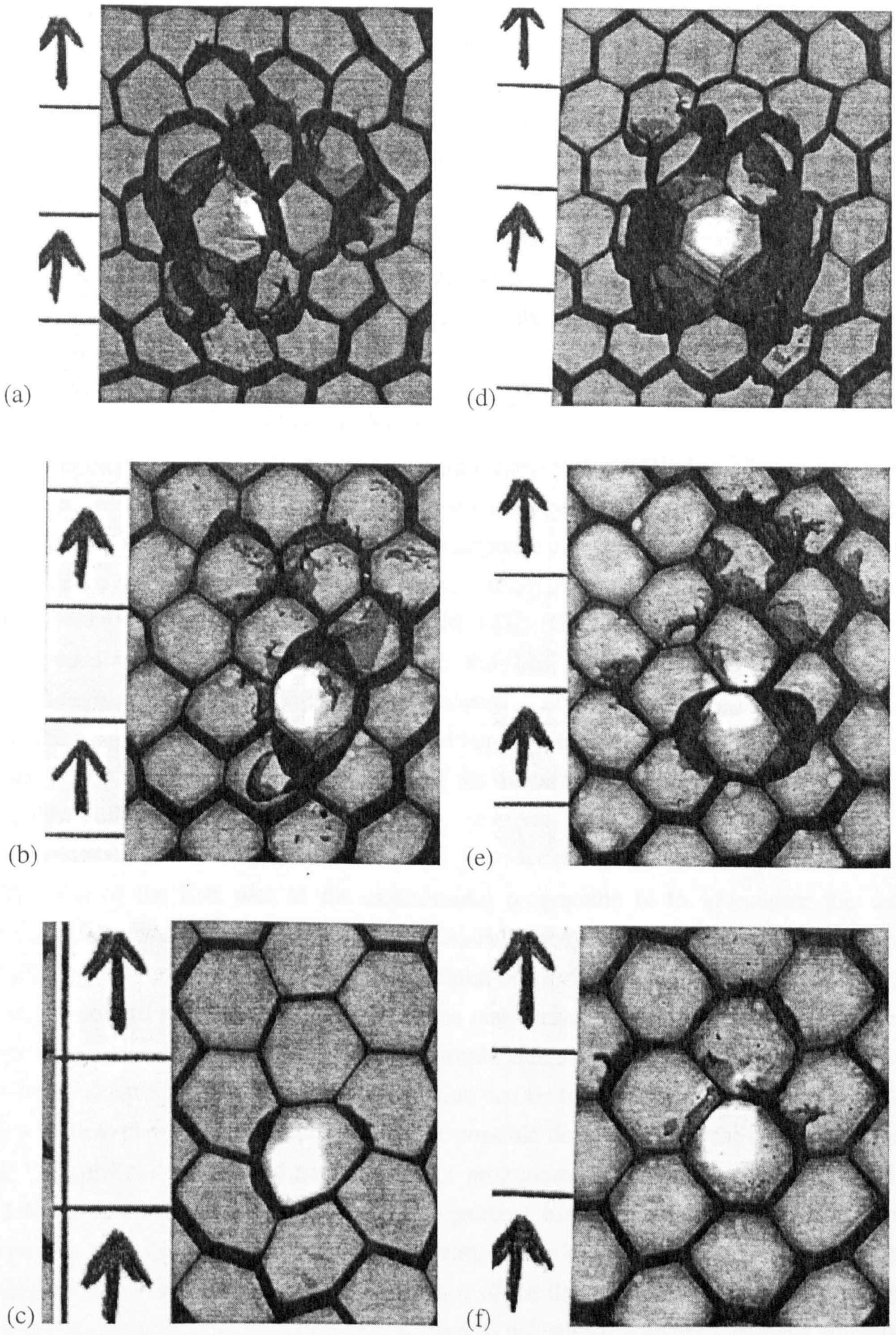

Figure 2-16. X-ray imaged honeycomb damage for a range of impact angles and projectiles. (a) 15° (b) 45° (c) 73° (d) 16° (e) 45° (f) 74° impacts. (a)-(c) 1.2 mm Ti (d) - (f) 1.0 mm S/S 420. The honeycomb damage decreases with increasing impact angle. Scale is in centimetres and arrow signifies direction of impact.

2. Fibre footprints. The crater is elongated (as for category 1) and the interior is ridged in the direction of the long axis. Assumed to be caused by plastic deformation of the witness plates due to fibre impact.
3. Asymmetric craters. These had lips along the long axis and had a length to width ratio of typically 5:1. Presumed to be due to fibres impacting at a higher velocity than category 2.
4. 'Scoop' craters, similar in appearance to a highly oblique impact of a spherical particle. Possibly short fibre sections approaching the hypervelocity regime.
5. Circular craters with lips and perforation of the witness plate. Typically with rough interiors (Figures 2-13 (f) and (i)).

2.7 Composite Materials: A Review

Carbon Fibre Reinforced Plastic / Aluminium Honeycomb (CFRP/Al-HC) is in common use as a spacecraft structural material and provides good performance in terms of high strength, low weight and low thermal distortion. The response of this material to hypervelocity impact has been, until now, poorly characterised, although the channelling behaviour of the honeycomb has been known since at least 1970 (Gehring, 1970). Its increasing use, combined with the projected increase in the LEO debris population, requires better characterisation of its response to both normal and oblique hypervelocity impact. In addition, honeycomb is used as a structural support for solar arrays such as those used on the EURECA spacecraft. Knowledge of its impact performance may help post-flight analyses of future retrieved solar arrays.

The aim of the first part of the experimental programme is to investigate the damage mechanisms and morphology of a CFRP/Al-HC honeycomb spacecraft structure near the ballistic limit, at an impact velocity in the region of 5 km s^{-1} for normal impacts. The ballistic limit is defined as marginal perforation of the rear surface of the target. The dependence of the ballistic limit and impact damage on projectile diameter and density for normal impacts is used to determine whether a damage equation can be formulated. The damage incurred on the witness plates (seen as representative of possible damage to internal spacecraft systems) is categorised. The second part of the shot programme (oblique shots using 0.8-1.5 mm diameter aluminium, titanium and steel projectiles) used projectile diameters and densities selected from the first part of the shot programme in order to investigate the effect of angle of impact on the ballistic limit. The dependence of the damage on projectile diameter, density and impact angle, from both data sets, is used to investigate whether a damage equation can be formulated. X-ray testing of the normal and oblique impact targets from both shot programmes is used to analyse the dependence of honeycomb cell damage on angle of impact, projectile diameter and density.

The body of work describing hypervelocity impact on composite materials is much smaller than that for metallic targets. Previous work is summarised in Table 2-17, identifying results pertinent to the aims of this work. The onset of marginal perforation, and the form of equations governing thin and thick target behaviour, have not yet been fully explored in composites. Therefore, the applicability of scaling between aluminium and composites has not been proved. If a scaling factor between composites and aluminium can be identified, it will allow ductile material damage equations (as implemented in ESABASE) to be applied to composite targets.

Table 2-17. Summary of hypervelocity impact studies pertinent to this work. Impacts on composite plates and tubes and composite and metal honeycombs (The value of d_p/f for honeycomb refers to the front facesheet only). #: number of shots.

Author	#	Target	d_p (mm)	proj. type	v (km s^{-1})	θ(°)	d_p/f	Comm-ents
Christiansen, 1990	58	Tubes	0.6 - 3.2	glass, Al	3.3 - 7.8	0, 45	0.31 - 1.77	$D_{eq,t} \propto E^{1/3}$.
Gehring, 1970	14	Cd/Al HC	3.18	Cd	6.5-7.0	0	2.0-9.6	Chann-elling identified.
Gorshkov et al., 1992	24	F/glass laminate	0.8-2.0	steel, glass	3.0-7.3	0	0.056 - 0.5	Ballistic limit.
Lambert, 1997	3	CFRP plate	0.7-1.2	Al	6.0-6.2	0	0.18-0.3	Ballistic limit reached.
	4	" + MLI	0.9-1.2		5.8-6.6		-	
	3	CFRP/Al-HC	0.9-1.1		5.3-6.6		0.82-1.0	MLI increases limit by factor of 3.
	2	" +MLI	1.1-1.5		6.4-6.5		-	
Taylor et al., 1997c	21	CFRP/Al-HC	0.8-1.5	Al, Ti, steels	4.7-5.8	15-75	0.5-1.0	HC damage identified
Taylor et al., 1997b	15	CFRP/Al-HC	0.8-2.0	nylon, Al, Ti, steels	4.5-6.2	0	0.5-1.25	Ballistic limit f(E, ρ)
Tennyson and Manuelpillai, 1994	14	PEEK GRE	0.1	SiC, Al_2O_3	3.5-10.5	0	0.2	Low v ejecta.

Table 2-17 continued.

Author	#	Target	d_p (mm)	proj. type	v (km s^{-1})	θ(°)	d_p/f	Comments
Terrillon et al., 1991	2 2 1	Al HC Al HC HC	1.0 1.0 1.0	Al	6.9-7.5 7.4-8.1 -	20, 70 20, 70 70	2.44 1.96 -	Channelling. Rear hole damage is larger for 70° impact.
Unda et al., 1994	5	Tubes	0.9-2.0	Al	2.6-7.6	0, 45	0.69 - 1.54	Ballistic limit reached.
Yasaka et al., 1994	11	Tubes	10-20 (cyl)	steel	0.5-0.6	0	3.3-6.7	Dust-like fragments, perforation.
Yew and Kendrick, 1987	38	Graphite plate	1.74 (cyl, L =1.88)	nylon, Al	3-7.5	0	0.13 - 0.77	Ejecta from composite target only. D/d_p = 7 -9

2.8 Results

A qualitative review of the impact morphology has been provided in section 2.6.3. A quantitative analysis of the ejecta, internal honeycomb damage and hole size for oblique impacts is presented as a prelude to an investigation of possible forms for a CFRP/Al-HC damage equation.

2.8.1 Ejecta

Five categories of ejecta were identified in Taylor *et al.* (1997c) and reviewed in section 2.6.3: carbon fibres embedded in the plate (category 1), fibre 'footprints' (2), asymmetric craters (3), 'scoop' craters (4) and circular craters (5). Categories 1, 4 and 5 are shown in Figure 2-13. The velocity of all the ejecta categories was inferred to be sub-hypervelocity due to the rough surface on the inside of the spherical craters. These craters were also deeper than the typically observed depth to diameter ratio of ~0.5 observed for hypervelocity impact craters, again implying sub-hypervelocity impacts (< 4-5 km s^{-1}). The angle subtended by the witness plate was low (Figure 2-7), thus the impactors forming crater categories 3 and 4 (asymmetric and scoop craters) are necessarily non-spherical and near-normal. The source of the 'circular crater' impactors (category 5) may be projectile remnants or aluminium honeycomb material. The orientation of the ejecta (with respect to the witness plate surface) may not be normal (along the long axis of the fibres). The morphology of the craters suggests that the length of the fibre fragments decreases with increasing ejecta velocities.

A scan of the witness plates was carried out (methodology reviewed in section 2.6.3) and summarised in Table 2-18. The exit hole size, from the rear of the CFRP/Al-HC honeycomb structure might be considered to be a predictor of the ejecta category and amount. However, there is no correlation between rear hole diameter and ejecta category. Therefore, even if a damage equation for a two-plate analogue system can be derived, information on the resulting ejecta damage could not be obtained.

Table 2-18. Witness plate ejecta analysis for features >300 μm (Perf: Perforation of the 1.6 mm plate). {number} signifies the number of plate perforations.

ID	Perf ?	Categories 1&2	Categories 3&4	Category 5	Comments (whole plate scan)
HC02	no	2	0	1	Many category 1 and category 5 below 300 μm threshold.
HC03	no	23	5	1	Damage dominated by categories 1&2. Category 5 do not have lips.
HC05	yes {1}	1	4	13	Category 5 dominant over others below 300 μm. At 300 μm 3&4 are dominant over 1&2.
HC06	yes {1}	5	10	24	Many category 2 and 3 below 300 μm. Category 2 at larger cone angles.
HC07	yes {15}	1	5	39	Hundreds of micro category 2 (~20 μm) on plate, very few categories 2-4 above 300 μm.
HC17	no	6	0	0	most damage, category 1 at 15-20 μm threshold.
HC18	no	0	1	0	very little damage, nearly all category 1 at 15-20 μm threshold

2.8.2 Honeycomb

Three categories of honeycomb damage, designated 'blast damage', are defined in section 2.6.3, based on variations in the X-ray opacity of the target :-

1. Opaque. Indicative of crumpled / crushed multi-cell walls preventing the transmission of X-rays.
2. Partially transparent. Indicative of foreshortened cells whose walls have been subjected to buckling permitting partial transmission of X-rays.
3. Transparent. Identifies the extent of the entry and/or exit holes.

The projectile diameter, density and impact angle trends of the damage have been presented in Figures 2-15 and 2-16. The increase in damage has been identified to be a strong function of projectile density and diameter in section 2.6.3. The honeycomb damage trends with impact angle and impact energy are given in Figures 2-17 and 2-18. The damage area can be two orders of magnitude greater than the projectile cross-section. The steep tail-off in damage area at highly oblique impact angles, as shown in Figure 2-17, is due to projectile ricochet. For impacts at 75°, the projectile does not penetrate the aluminium honeycomb. The scattered points in Figure 2-18 below the main trend are again due to highly oblique impacts. The data presented in Figure 2-18 suggest that a damage equation could be developed to predict honeycomb damage area as a function of impact energy. For $\theta > 70$-75°, a different relationship would have to be used.

2.8.3 Oblique impacts: hole sizes

In Figure 2-19, the ellipticity of the targets is plotted against the impact angle (measured from the normal). Impacts at angles greater than 45° show a clear ellipticity. In Figure 2-20, D_a/d_p (the crater diameter along the line of flight, normalised by projectile diameter) is plotted against impact angle. There is a drop in D_a/d_p for low density projectiles at highly oblique impact angles, but not for the higher density projectiles. This work explores the initial dependence of honeycomb to oblique impacts. An understanding of the hole formation process in composites is the first step in developing a damage equation. However, the target response variability (plotted as error bars) results in a wide range of potential curve fits.

2.9 Electrostatic accelerators

Although the Van de Graaff generator at the University of Kent at Canterbury was not used to create new data for this thesis, much of the data used in the derivation of published damage equations is accelerated by electrostatic techniques. This data set is called the 'small' projectile data set, because the projectile diameters are in the range $d_p = 0.1$-10 μm.

An electrostatic accelerator delivers a charged particle (charge q) in an electric field produced by a potential difference, V. The product, qV, is the kinetic energy given to the particle. The velocity of the particle is measured by a time-of-flight system in the accelerator and an amplifier is used to detect a signal from a conducting cylinder measuring the induced particle charge before impact. Therefore, the mass of the particle can be deduced from the relationship $0.5mv^2 = qV$. Analysis of experimental data at the University of Kent has shown that there is not a clear relationship between charge and mass (Cole, 1997).

Figure 2-21 shows a plot of mass versus velocity for all the 'small' data (further defined in chapter 3) used in this thesis. A linear least squares fit was applied to all the data and also to the individual accelerator types. (If mass, m, is proportional to v^b, then $\log m = b \log v + \log a$, where a is a constant and b is the gradient.) The results of the fit are given in Table 2-13 and show that the velocity reached varies with accelerator and projectile type. The

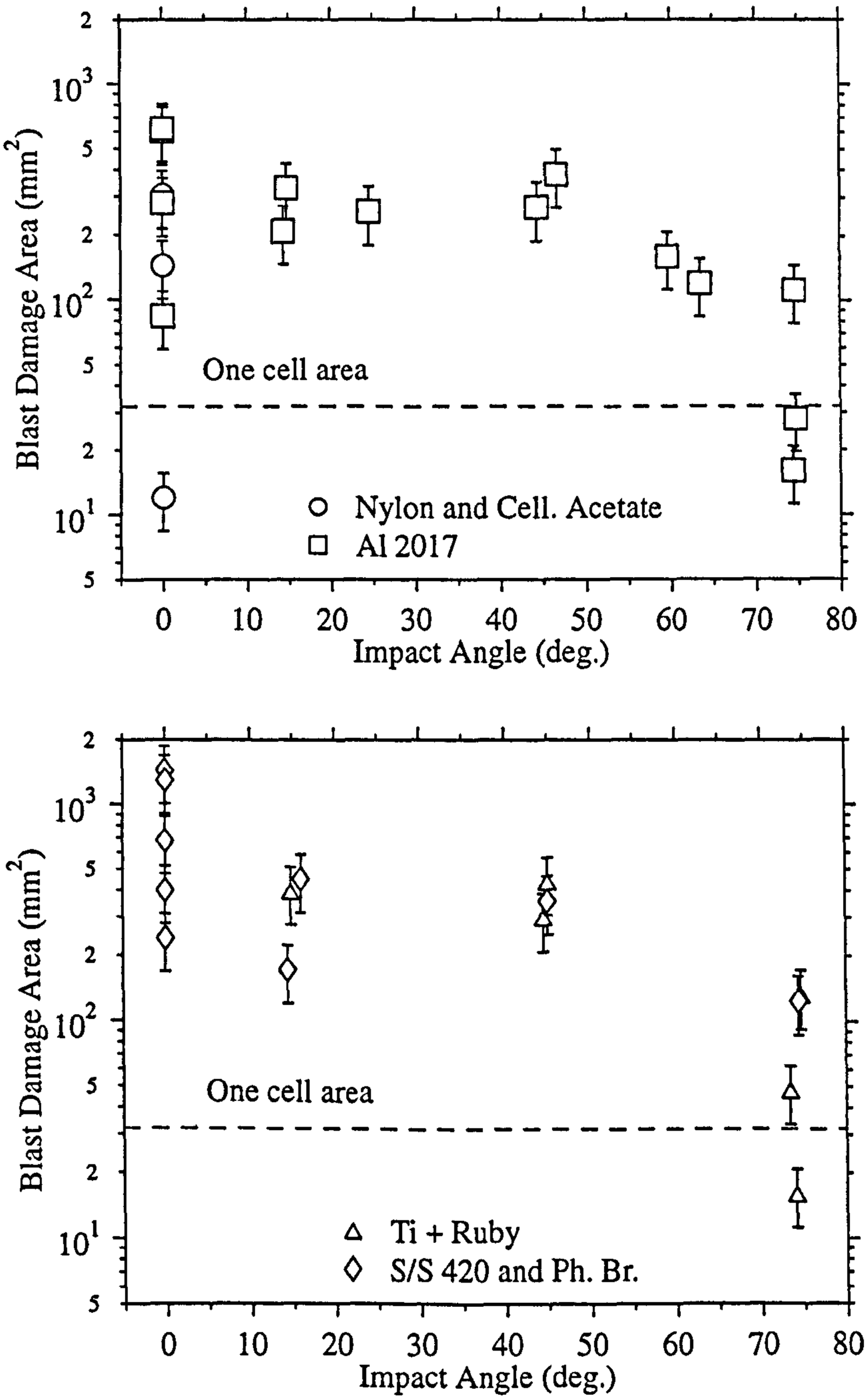

Figure 2-17. Honeycomb blast damage area as a function of impact angle for all data. The damage area encompasses burst, blasted and bulged cells as measured using X-ray photography. The error bars correspond to 30% measurement error (operator bias).

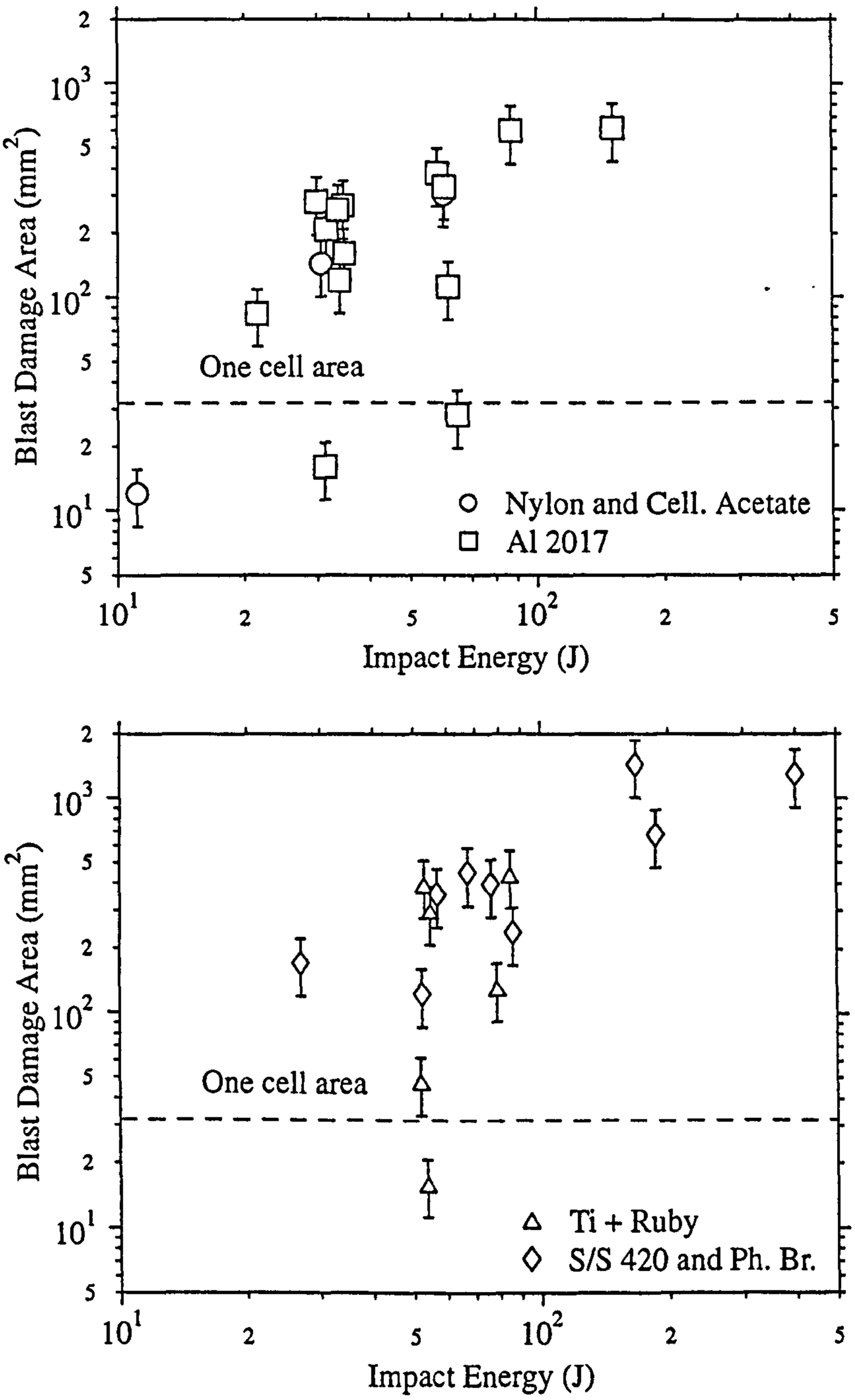

Figure 2-18. Honeycomb damage as a function of impact energy for all data.

The damage area encompasses burst, blasted and bulged cells as measured using

X-ray photography. The error bars correspond to 30% measurement error (operator bias).

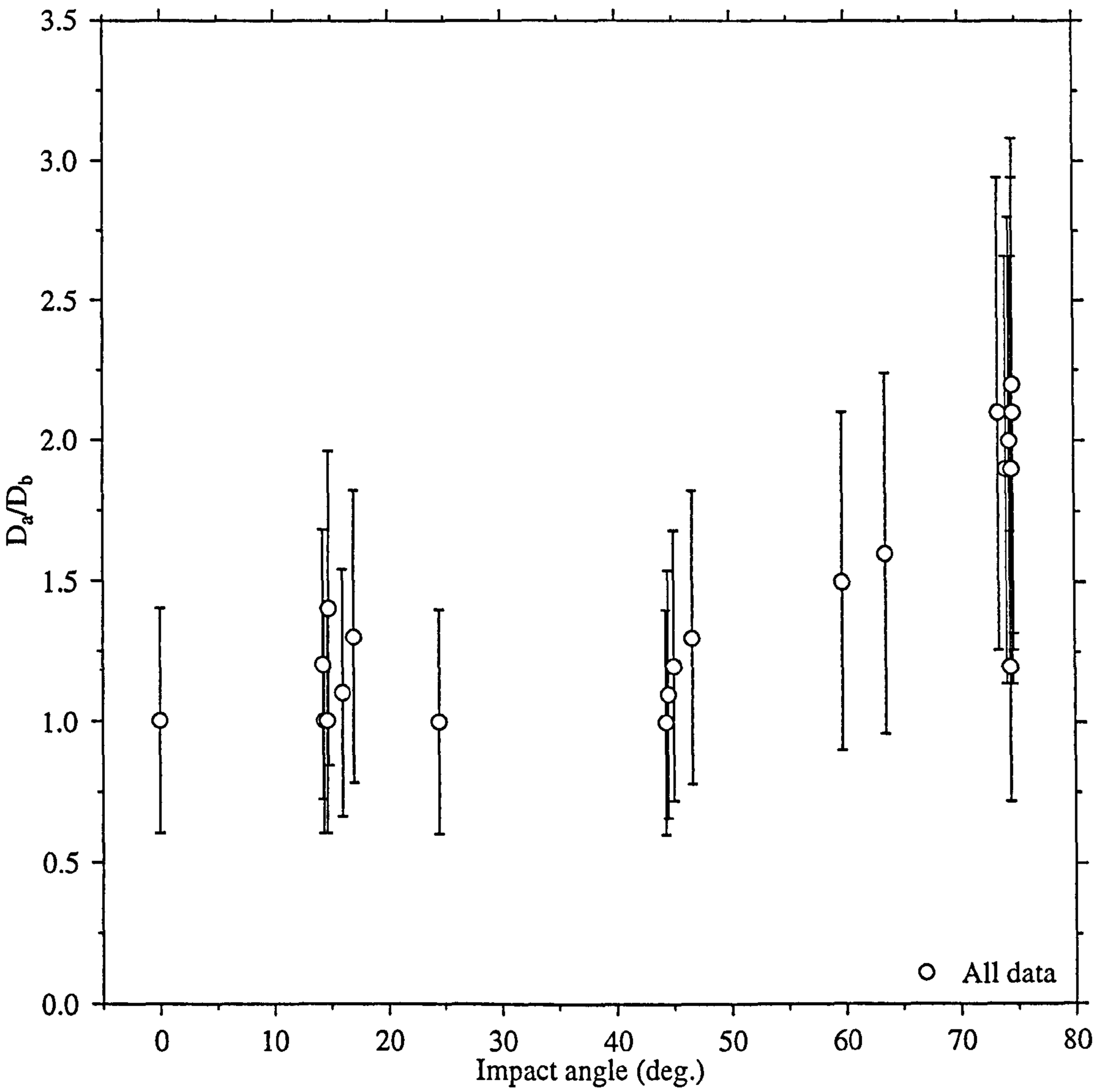

Figure 2-19. Ellipticity as a function of impact angle. The error bars are calculated from two repeated shots (HC22, HC25, HC41 and HC46) and represent variations in the target response, not measurement errors.

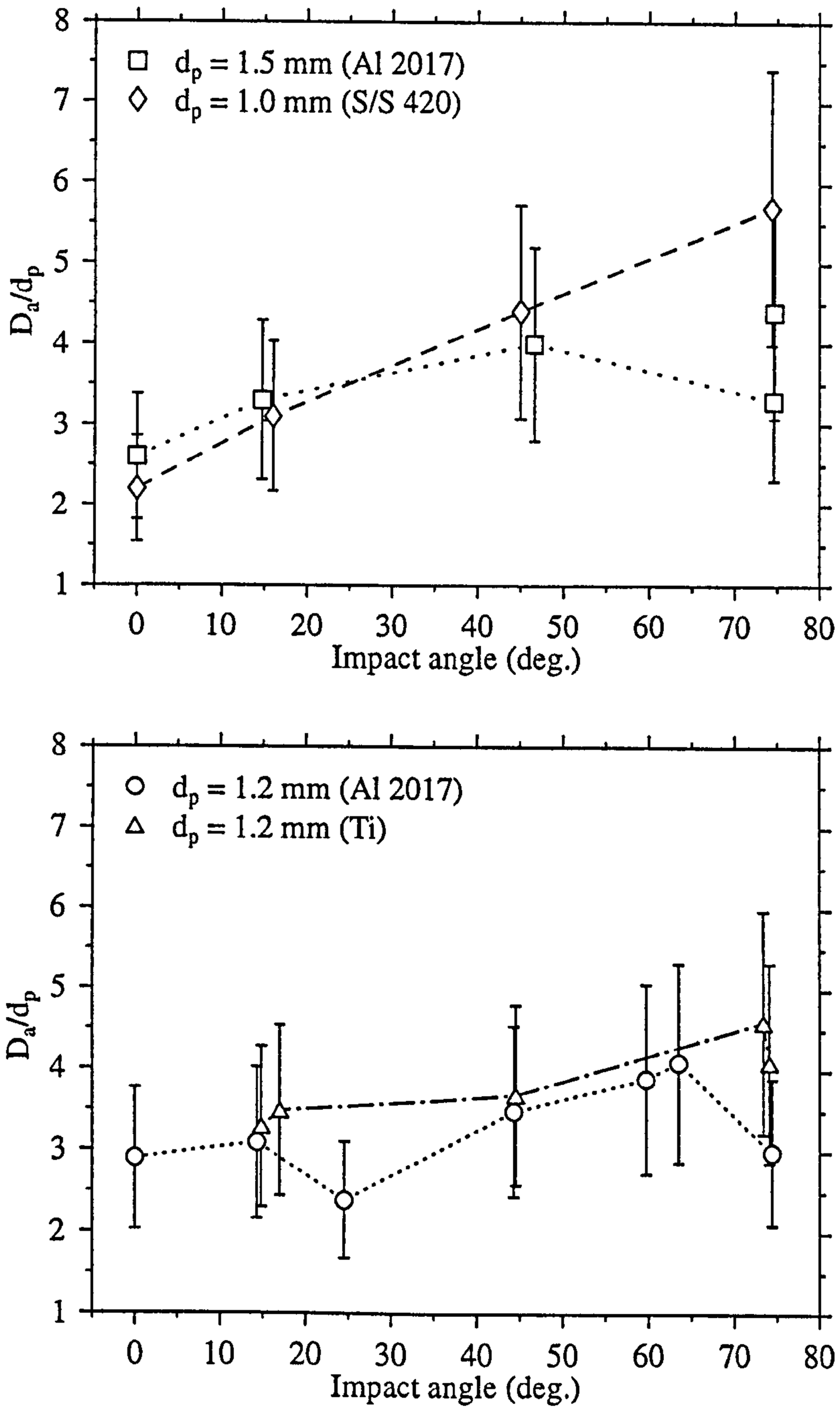

Figure 2-20. D_a/d_p as a function of projectile density for four different projectiles. The errors on D_a are estimated from two repeated shots (HC22, HC25, HC41 and HC46) and represent target variability errors, not measurement errors. The lines are drawn between the four data sets to better identify the trends with impact angle.

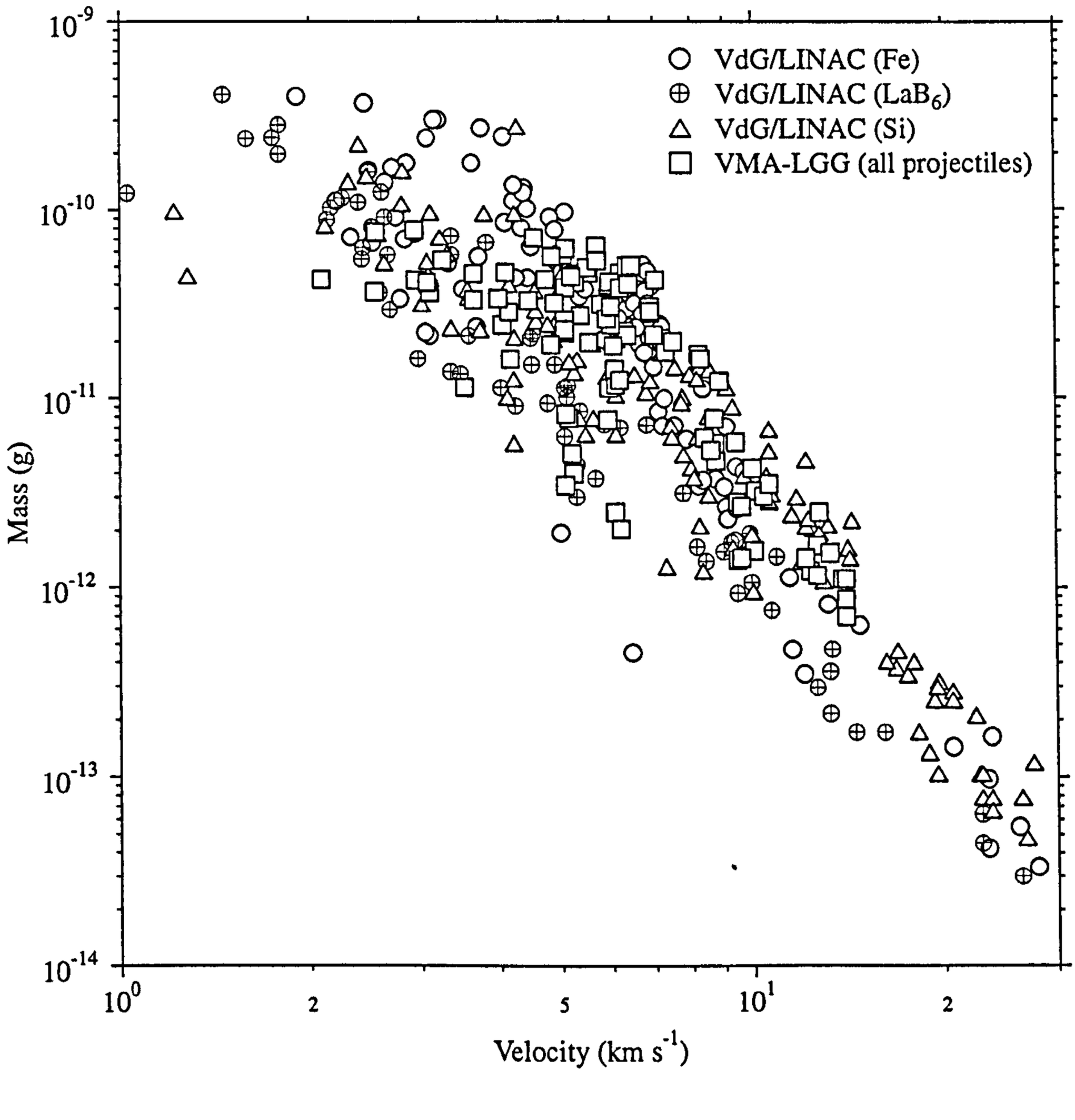

Figure 2-21. Mass versus velocity for electrostatically accelerated projectiles.

(VdG: Van de Graaff; LINAC: Linear Accelerator; VMA-LGG: Vertical Mass Accelerator)

correlation coefficient (discussed in chapter 4) is not high, implying that a range of velocities can be reached for a given particle diameter and accelerating voltage.

Table 2-13. Least squares fits for electrostatically accelerated particles. (VdG: Van de Graaff; LINAC: Linear Accelerator; VMA: Vertical Mass Accelerator)

Accelerator	b	loga	r^2	number	Reference
All	-2.53	-9.09	0.69	551	Mandeville, 1972; Roy *et al.*, 1972; Roy and Slattery, 1973
VdG/LINAC	-2.68	-9.00	0.75	388	Roy *et al.*, 1972; Roy and Slattery, 1973
VMA-LGG	-1.85	-9.54	0.42	163	Mandeville, 1972
Fe (VdG/LINAC)	-2.55	-9.09	0.58	203	Roy *et al.*, 1972; Roy and Slattery, 1973
LaB6 (VdG/LINAC)	-3.07	-8.93	0.94	66	Roy *et al.*, 1972; Roy and Slattery, 1973
Si (VdG/LINAC)	-2.80	-8.80	0.86	37	Roy *et al.*, 1972; Roy and Slattery, 1973

2.10 Summary

The shot programmes onto soda-lime glass and spacecraft honeycomb have been summarised and the measurements made on the target materials described. The morphologies of the target materials under hypervelocity impact, as observed in shot programmes executed for this thesis, have also been reviewed. The key impact results from the honeycomb, as observed in the shot programmes, have been summarised in this chapter.

Chapter 3

3. Experimental Data and Damage Equations

In this chapter an analysis of the experimental data set (some 800 impact data points) and published damage equations is presented. Data from the glass hypervelocity impact programmes described in chapter 2 are included in the data set. Target and impactor parameters are as defined in chapter 2.

Table 3-1. A summary of data sources used in this thesis ('large' projectiles). (gbs: glass buckshot technique used, multiple datapoints per shot. FQ: fused quartz; SLG: soda lime glass; Al: aluminium; Fe: iron; Ti: titanium; Cell.: cellulose; S/Steels: Stainless Steels; TCB: tungsten carbide. # : Number of data points.)

Identifier	d_p (μm)	v (km s^{-1})	θ (°)	#	Projectile	target mat'l	Reference
Edelstein	397-1250	2.5-8.6	0-60	62	Al, garnet, glass	fused silica	Edelstein, 1992
Flaherty	200-396	1.0-7.5	0	12	pyrex, sapphire, tunsgten carbide	fused silica	Flaherty, 1969
Mandeville (b)	780-800	1.4-2.9	0	38	Al, Fe, glass	pyrex granite basalt, basalt glass	Mandeville, 1996
McHugh	48.1, 396-2459	5.8-16.6	0	103	borosilicate glass	quartz, alumino-silicate glass	McHugh and Richardson, 1974
Rott	16-86	4.1-11.6	0	17	glass	SILEX	Rott, 1988
Schneider	1100-2500	4.0-9.1	0-45	6	Al, Ti	FQ	Schneider *et al.*, 1995.
Shrine (gbs)	49	4.9-5.5	45-75	5	SLG	glass	Shrine *et al.*, 1996
Taylor (a) (gbs)	26.7-292.7	4.1-5.6	0	12	SLG	SLG	Taylor *et al.*, 1997d
Taylor (b)	800-2000	4.4-5.5	0	29	Nylon, Cell. acetate, Al, Ti, S/steels, TCB.	SLG	Taylor and McDonnell, 1997

The composites honeycomb impact data are summarised and tested against existing damage equations; the most simple being the ballistic limit as a function of impact energy. The experimental data are also assessed for their impact on spacecraft operations. The motivation for this work is to assess the accuracy of current published damage equations for impacts onto brittle materials. These damage equations can be used to decode the impactor parameters for impacts on brittle surfaces (such as solar cells) and for hydrocode calibration. Hydrocodes, once calibrated, can then be used to explore the hypervelocity impact response beyond the experimental regime used for damage equation development (chapter 5). The range of parameters to be addressed covers both impactor parameters (velocity, density, shape, impact angle, diameter) and target parameters (density, thickness, and, potentially, material parameters not yet determined).

3.1 Experimental Data

Table 3-2. A summary of data sources used in this thesis ('small' projectiles and solar cell impacts). (HST: Hubble Space Telescope solar array; ECS: EURECA solar arrays; ECS-R: impacts onto the rear of EURECA solar arrays; SLG: soda-lime glass; FQ: fused quartz, gbs: glass buckshot technique used, multiple datapoints per shot (the average is used in the spreadsheet). Si: silicon; Fe: iron; LaB_6: lanthanum hexaboride; Al: aluminium; Cu: copper. # : Number of data points.).

Identifier	d_p (μm)	v (km s^{-1})	θ (°)	#	Projectile	target mat'l	Reference
Dirr	7-86	4.4-11.5	0-75	22	glass	HST	Dirr et al., 1995
Kuczera	92-114	7.0-10.0	0	2	glass	ECS	Kuczera, 1985
Mandeville	0.7-9.0	1.5-14.6	0-60	163	Al, Fe, polystyrene	SLG, FQ, vitreosil, spectrosil	Mandeville, 1972
Paul	7-70	5.3-9.0	0-60	10	glass	ECS	Paul, 1994
Roy (a)	0.3-5.6	1.2-26.8	0-60	201	Si, LaB_6, Fe	quartz	Roy et al., 1972
Roy (b)	0.2-5.7	1.9-27.9	0-60	187	Si, LaB_6, Fe	oligoclase	Roy and Slattery, 1973
Schaefer	500-1100	4.9-5.7	0-60	20	Al, plexiglass, Al-cylinder, glass, chrondrule	ECS, ECS-R	Schaefer and Schneider, 1994
Schneider (b)	200-2000	6.0	0	2	Cu	Olympus	Schneider and Stilp, 1985
Shrine(gbs)	49	4.9-5.5	0-75	7	sodalime glass	HST, ECS	Shrine et al., 1996

The data set used in this work is a substantially extended and modified version of that input by the author, K. Paul and L. Berthoud as part of the ESA contract (Berthoud and Taylor, 1996). The thesis data set is the result of a wide ranging literature review of impact data from the late 1960s to the present time and includes data produced for this thesis (some 50 shots), summarised in chapter 2. Due to the large volume of data entered, several checks were made on the accuracy of the data entry. For example, plots were made of (i) velocity versus projectile diameter and (ii) crater and pit profiles (D_{co}/D_{pit}) as a function of velocity. In addition, for micron-sized particles, care was taken not to confuse measurements of the pit and conchoidal diameter during data entry.

In Table 3-1 and Table 3-2, the impactor and target parameters of the data set are summarised. In Figures 3-1 and 3-2 the information is presented as a plot of velocity versus projectile diameter and projectile diameter versus density. The electrostatically accelerated particles (identified by the mass-velocity relationship in Figure 3-1) are called 'small' projectiles, the others 'large' projectiles. There is a good range of projectile densities for the 'small' data set, but not for the solar cell data. Only one type of projectile (and thus one density) has been fired onto solar cell targets. The millimetre-sized shot program carried out for this thesis has extended the density range for the large projectile data set. The tables (3-1 and 3-2) include the data produced by the author during the period of research for this thesis. The target materials are soda-lime glass, borosilicate glass (and solar cells), fused quartz, fused silica, basalts and oligoclase (a lunar analogue material).

3.2 Analysis of Data against Impactor and Target Parameters

The experimental data summarised in Table 3-1 and Table 3-2 can be analysed graphically to display trends in the data. For example, D_{co} and T_c are expected to increase with impact velocity. Published damage equations (reviewed in section 3.3) also predict that the dimensional scaling is small (d_p exponent of 1.1 or less) meaning that the absolute values of T_c/d_p should be similar for both a 1 mm and 1 μm projectile impacting at a given velocity. The data are presented graphically in Figures 3-3 to 3-6. The features and analysis are discussed in following sections.

3.2.1 Conchoidal diameter

A subset of the data in Table 3-1 and Table 3-2, for which the conchoidal diameter, D_{co} was recorded (normal impacts only onto brittle materials, not solar cells), is plotted in Figure 3-3. The data are divided into the 'small' and 'large' classifications described in the previous section. Both non-rear spalling (semi-infinite) and rear spalling ('finite') targets are included. In Figure 3-3(a), the parameter D_{co}/d_p (conchoidal diameter normalised by projectile diameter) is plotted against velocity for a range of projectile densities. The plot shows a clear bifurcation with one branch (marked A, encompassing all 'small' and some 'large' impactors) showing a very shallow increase with velocity compared with branch B,

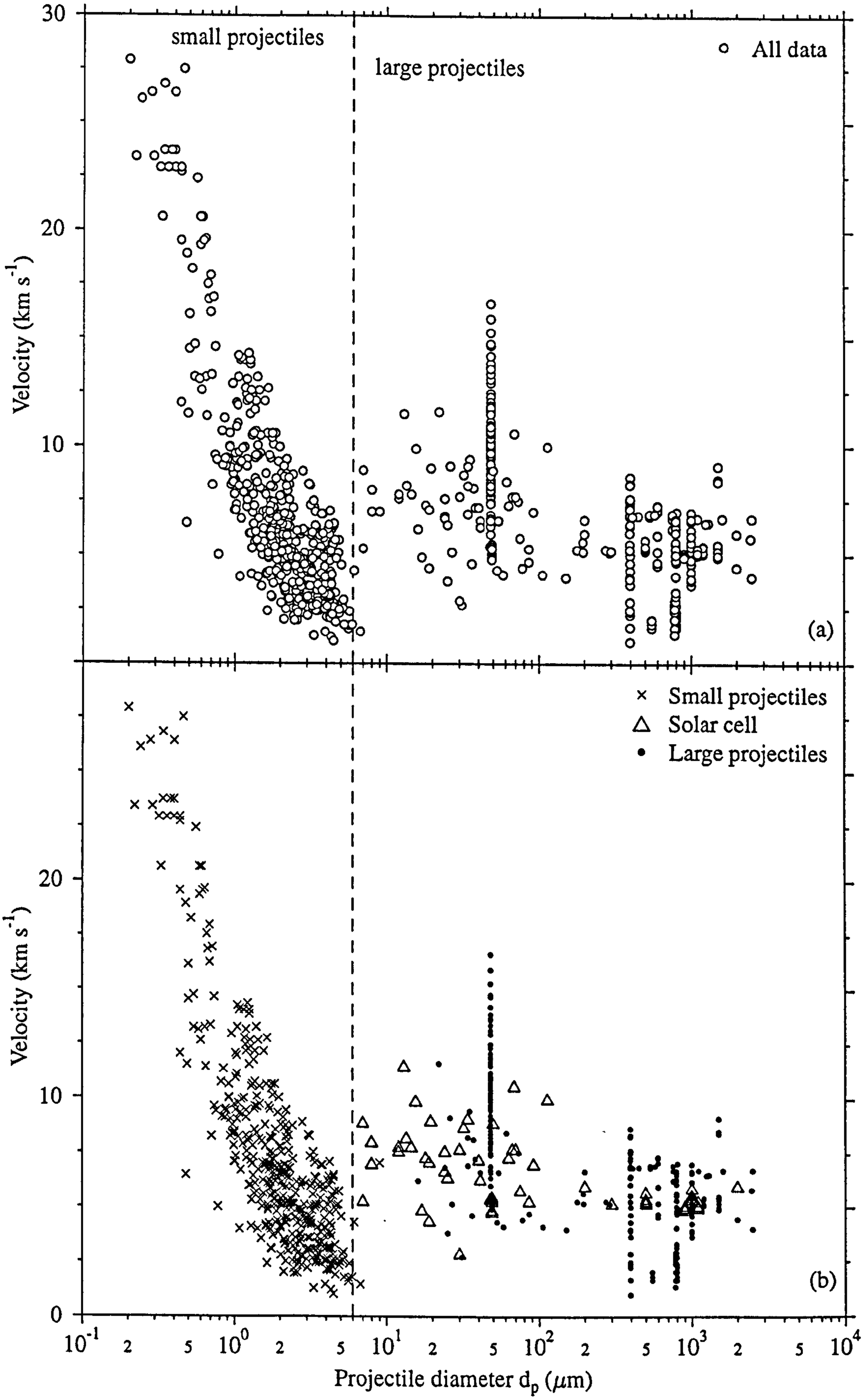

Figure 3-1. Characteristics of the data set used in this thesis. Velocity versus projectile diameter for (a) all data (b) classified into "small", "large" projectiles and impacts onto solar cells. "Small" projectiles are electrostatically accelerated.

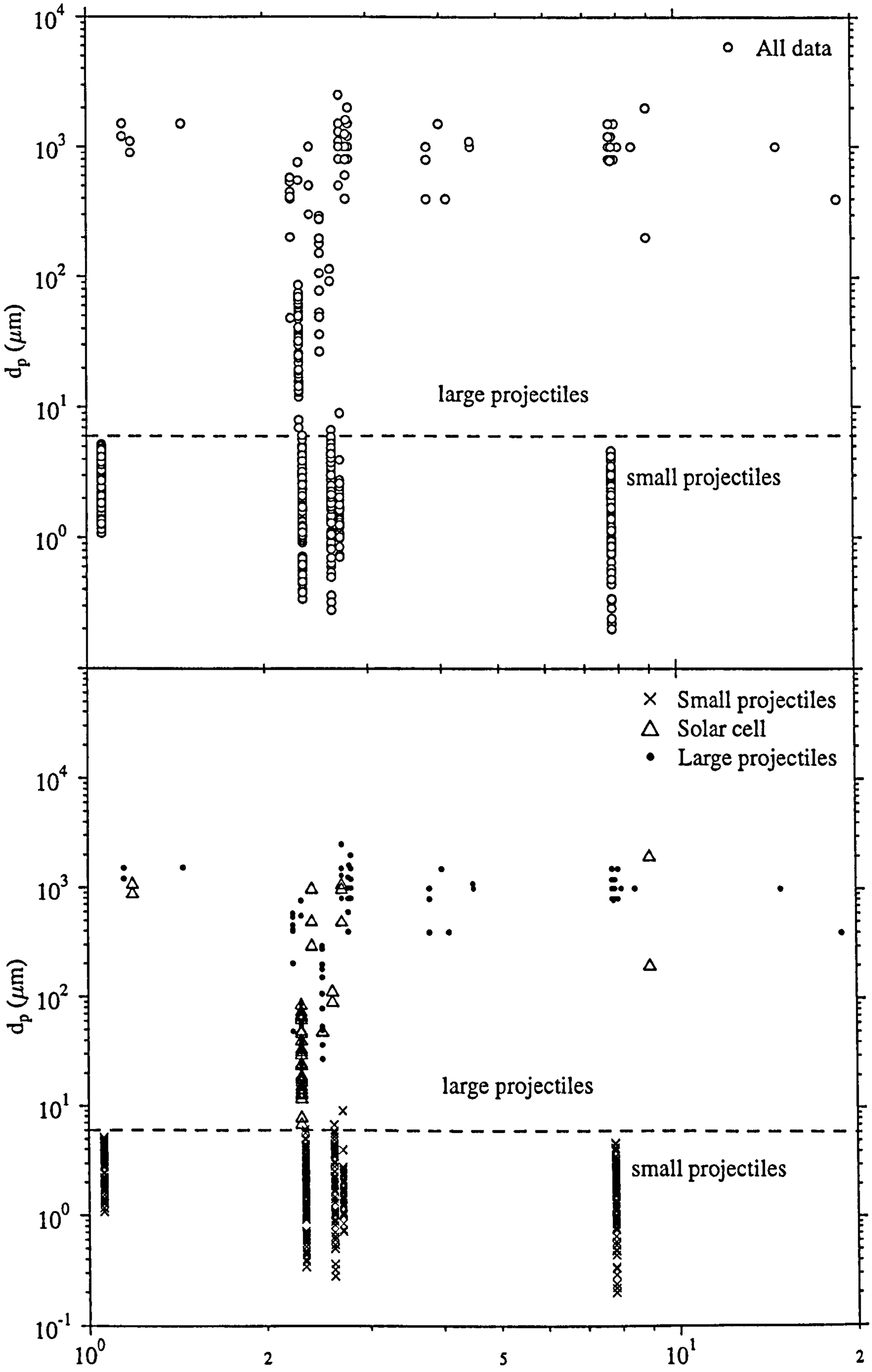

Figure 3-2. Characteristics of the data set used in this thesis. Projectile diameter versus density for (a) all data (b) classified into "small","large" projectiles and solar cell targets. Target materials cover the full range given in Table 3-1.

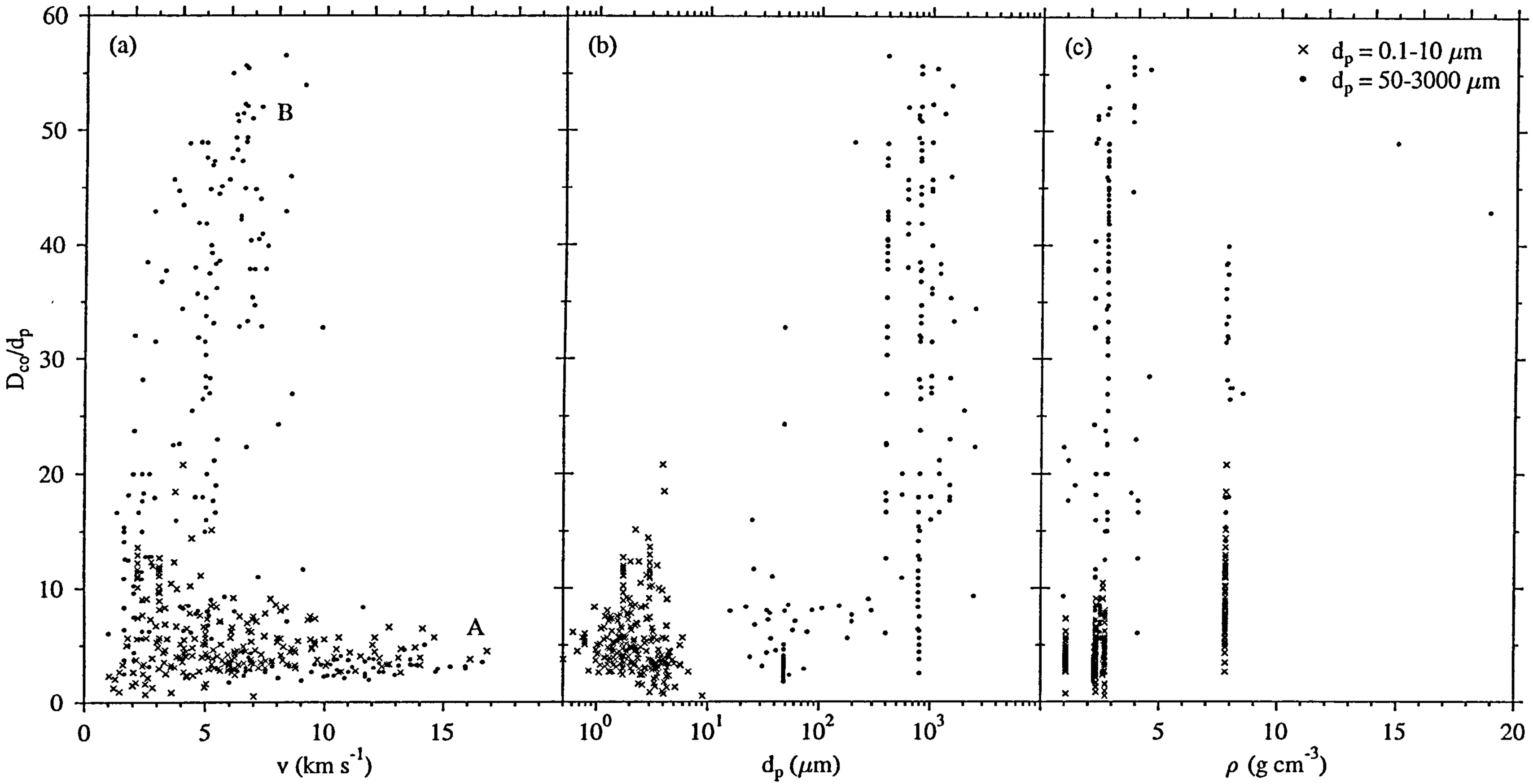

Figure 3-3. D_{co}/d_p (conchoidal diameter / projectile diameter) as a function of (a) velocity (A, B discussed in text) (b) projectile diameter (c) projectile. density. For (a) and (b), the full range of projectile densities is included. In (c) the full velocity range (0-17 km s^{-1}) is included.

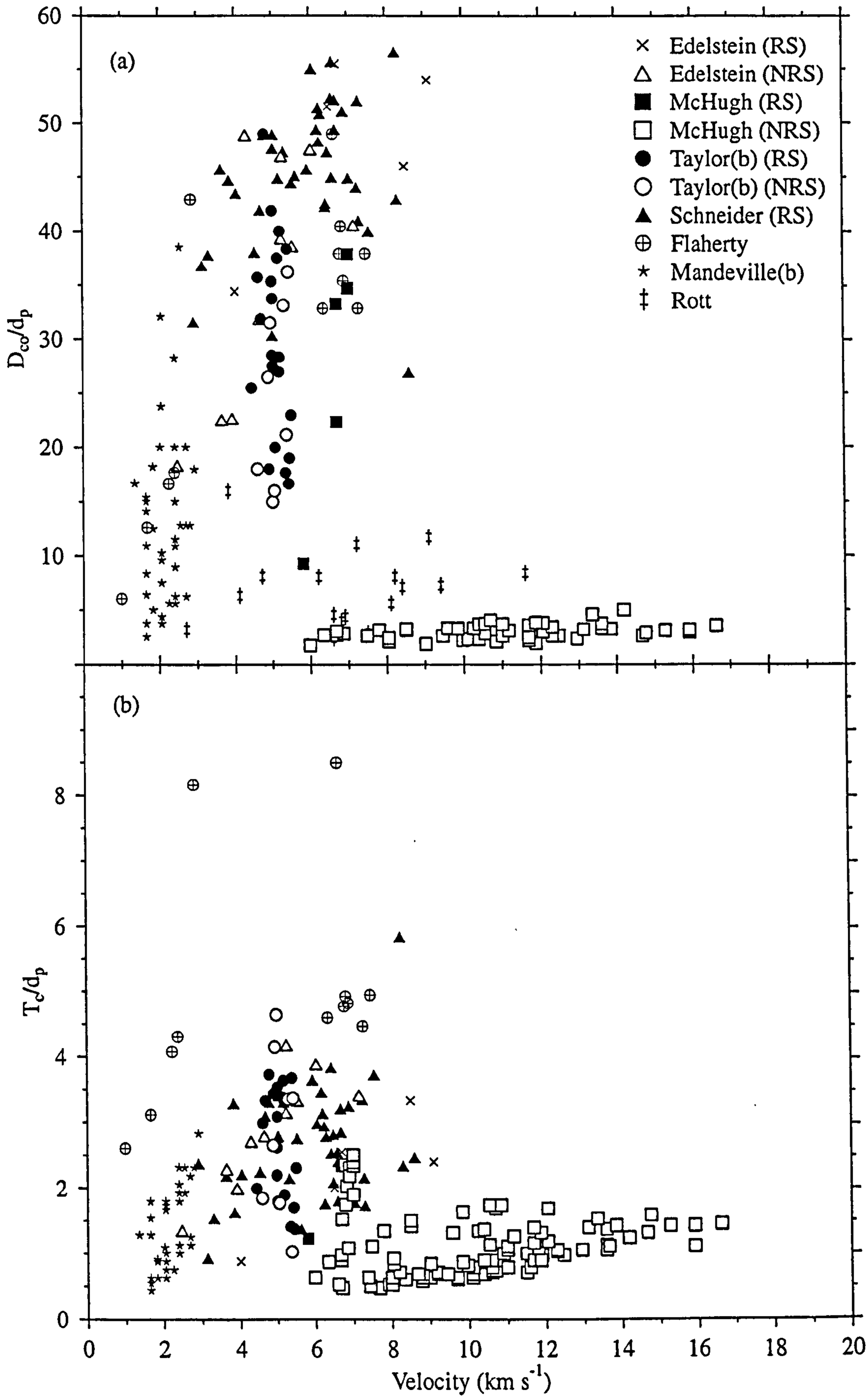

Figure 3-4. (a) D_{co}/d_p (conchoidal diameter normalised by projectile diameter) and (b) T_c/d_p (depth normalised by projectile diameter) versus velocity, sorted by experimental data set (Table 3-1) (NRS: Non-rear spalling, RS: rear spalling)

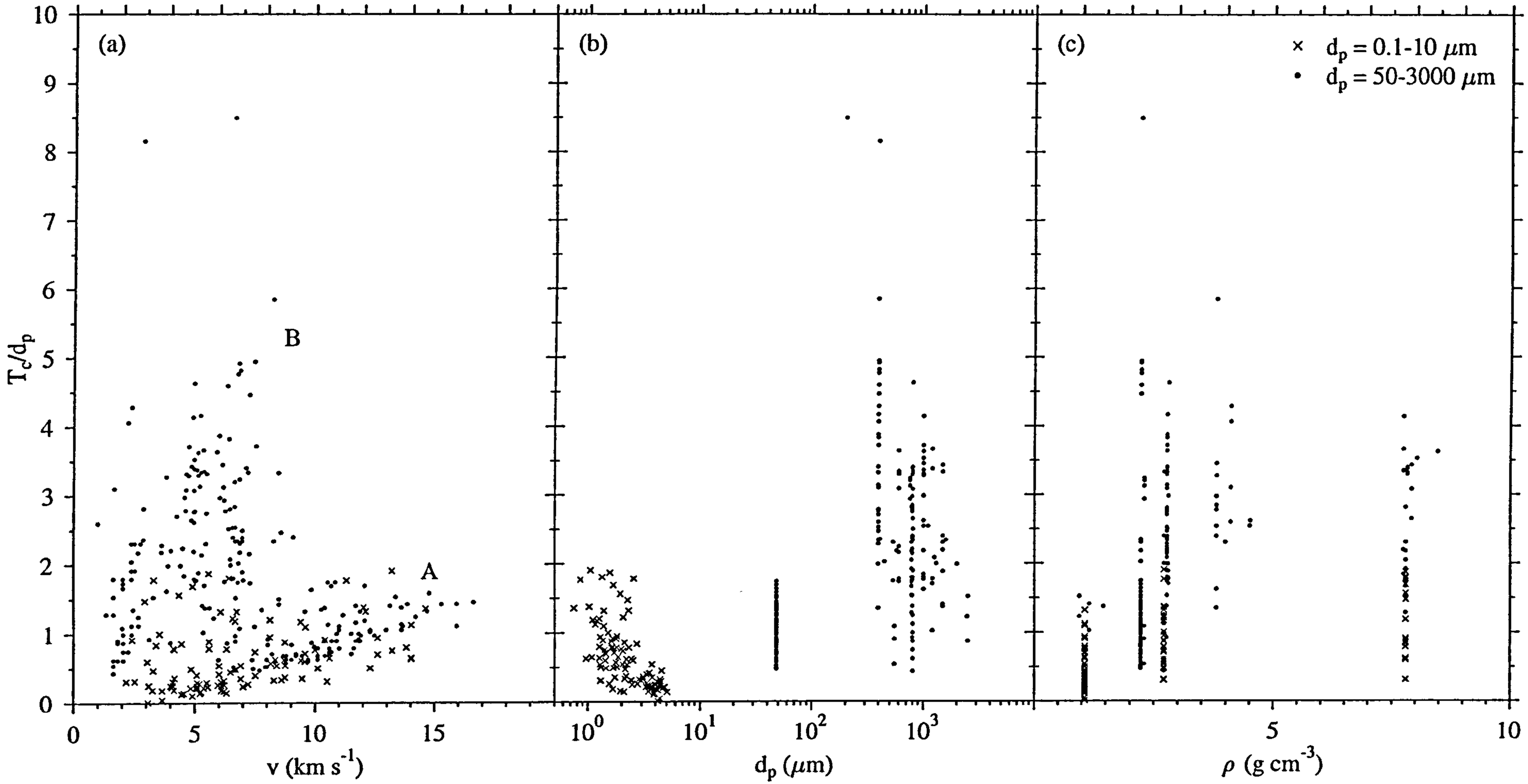

Figure 3-5. T_c/d_p (depth normalised by projectile diameter) as a function of (a) velocity (A, B discussed in text) (b) projectile diameter (c) density. For (a) and (b), the full range of projectile densities is included. In (c) the full velocity range (0-17 km s^{-1}) is included.

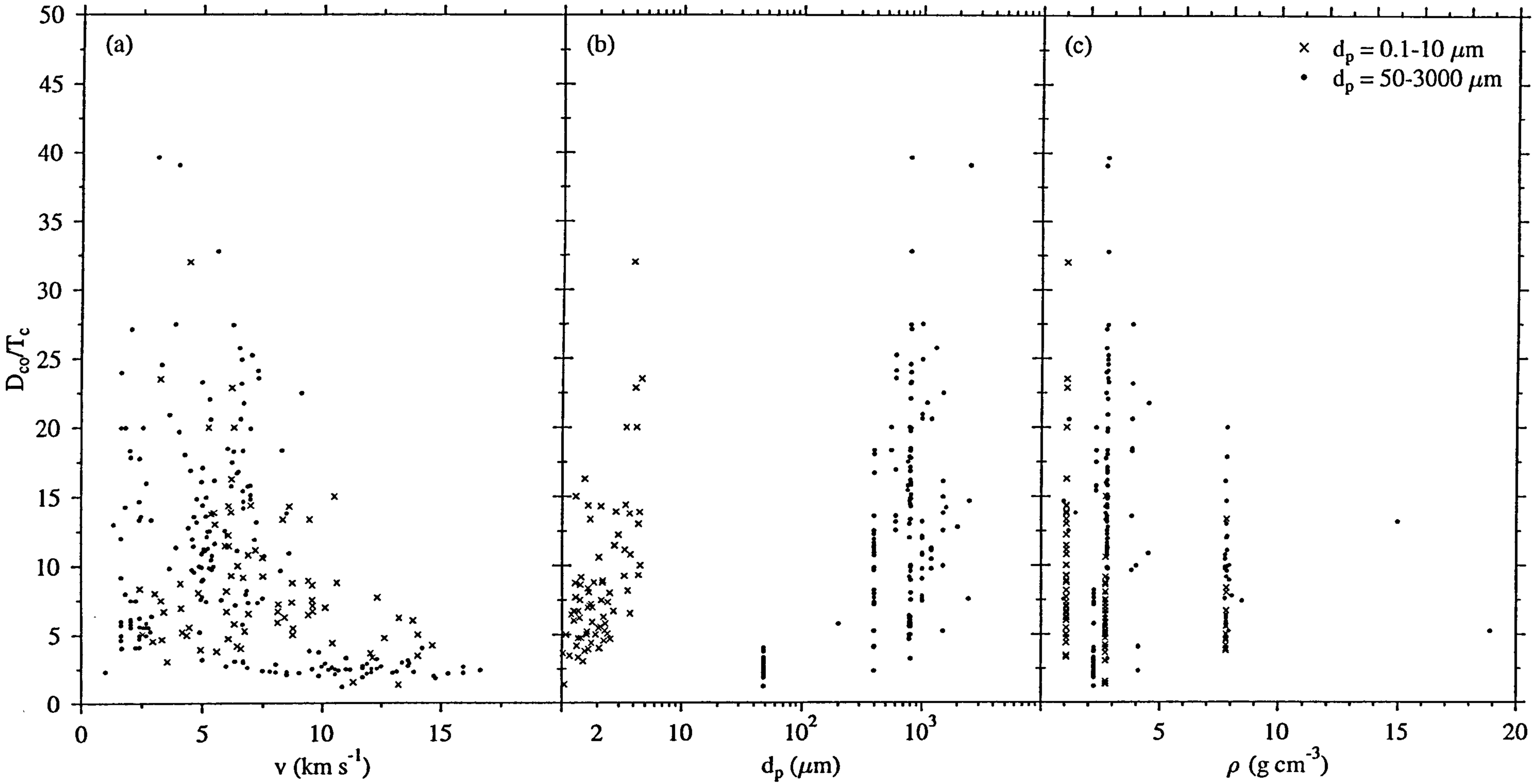

Figure 3-6. D_{co}/T_c (conchoidal diameter normalised by projectile diameter) as a function of (a) velocity, (b) projectile diameter, (c) density

For (a) and (b), the full range of projectile densities is included. In (c) the full velocity range (0-17 km s^{-1}) is included.

which shows a steep increase. The 'large' data set can be subdivided into the source experimenter groups (where one or more impact parameters are tightly constrained). This is shown in Figure 3-4(a). The lower gradient grouping (A) consists of impacts onto semi-infinite targets in the range d_p = 30 - 300 μm. The data are from several experimental programmes. The higher gradient grouping (B) consists of projectile diameters d_p > 400 μm (up to 2500 μm). This much larger value of D_{co} for a mm sized impactor compared with a micron sized impactor was first noted by the author (Taylor and McDonnell, 1997). The B grouping also includes impacts onto finite targets (as defined by rear perforation, see section 3.4). The plots of D_{co}/d_p against d_p and ρ_p (Figures 3-3(b) and (c)) are presented for completeness. The value of D_{co}/d_p is greater for all projectile densities in the large data set, compared with the small data set.

The B trend may be due to edge effects, where the D_{co}/(target diameter) and D_{co}/(target thickness) is large enough to denote that reflection of the shock wave from the edge or rear will affect the formation of the impact feature.

3.2.2 Depth of penetration

A similar, although less defined bifurcation in the depth of penetration (T_c) data can be seen in Figure 3-5(a). Again, the B group is comprised of 'large' projectiles and again the data set is divided into experimenter source (with some impactor parameters tightly constrained). In Figure 3-4(b) the data is divided into experimenters data sets. The A group is produced by 48 μm diameter projectiles and shows no appreciable difference in target type response. The mid-region (between A and B) is occupied by impacts onto finite targets and the B group by d_p > 400 μm projectiles. The mid-region between A and B can be explained by considering the onset of marginal perforation (i.e. rear spallation) in glass as compared with ductile materials. Unlike the ballistic limit in aluminium, say, where the onset is likely to be reproducible, the microstructural flaws which cause the glass to fail are randomly distributed and have a size distribution. Therefore some scatter is to be expected in the values of T_c/d_p for impacts onto rear spalling targets. The reflected rear wave may also influence the formation of the central pit. The value of T_c/d_p is greater for all projectile densities in the large data set, when compared with the small data set.

3.2.3 Crater profile

The crater profile (D_{co}/T_c) for normal impacts over the range 1 - 18 km s^{-1}, d_p = 1 - 2500 μm is shown in Figure 3-6. The crater dependence is plotted against velocity, projectile diameter and density (a, b and c respectively). Note that this is a part of the whole data set (all normal impacts onto brittle materials), as not all experimenters recorded both the conchoidal diameter and the depth of penetration. Plotted against velocity, there is scatter in the data, although a bimodal distribution is suggested for the large data set. The small data are scattered in between the two forks. These results are analysed against the damage equation predictions in section 3.3

3.2.4 Crater and pit profiles

In comparison with the conchoidal diameter and depth of penetration (defined in Figures 2-8, 2-9 and 2-10), the pit diameter can be measured across a range of morphologies. Two different morphologies were identified in Figure 2-8. A range of pit morphologies observed on both laboratory targets (Vedder, 1971; Mandeville and Vedder, 1971; Vedder and Mandeville, 1974; Nagel and Fechtig, 1980), Apollo windows (Cour-Palais, 1974) and lunar rocks (Hörz *et al.*, 1971) is given in Figure 3-7. It should be noted that the pit diameter measured is not the transient pit, but the final pit diameter.

In Figure 3-8, the pit profile (D_{co}/D_{pit}) for three target types (oligoclase, soda-lime glass and quartz/fused silica) versus velocity is presented. The data are from the 'small' data set (Mandeville, Roy(a) and Roy(b)) and the projectiles are in the diameter range 1-7 μm. Two projectile types were fired onto the quartz and oligoclase: silicon and lanthanum hexaboride. Therefore, near-identical impact conditions exist for these two data sets. Similarly, polystyrene and aluminium were fired onto fused quartz (equivalent to fused silica) and soda-lime glass. Above 5 km s^{-1}, soda-lime glass has a pit profile, D_{co}/D_{pit} ~ 2-3, and oligoclase has a slightly more scattered ratio (D_{co}/D_{pit} ~ 2-4). The results for quartz suggest a wider variation in D_{co}/D_{pit}. The data suggest that the response of quartz may be different to that of soda-lime glass and oligoclase. This difference may be due to target variability. The more reliable D_{co}/T_c ratio cannot be investigated for these craters as depth data is not available for these small impact craters.

In Figure 3-9, the pit and crater profiles (D_{co}/D_{pit} and D_{co}/T_c) are plotted using data from the 'large' and 'small' data set. The projectile diameters were in the range 1-4 μm for the 'small' data set, and 1-3 mm for the 'large' data set. The values of D_{co}/D_{pit} and D_{co}/T_c are higher for the 'large' data, but are overlying the 'small' data. The rear spalling (RS) data show increased values of D_{co}/T_c compared with non-rear spalling (NRS) data, but the values of D_{co}/D_{pit} are overlying for the NRS and RS data.

In summary, there is a suggestion that soda-lime glass and oligoclase might provide a different response to quartz for small impactors and that millimetre-sized and micron-sized impactors might produce a different pit profile. The onset of rear spallation does not appear to affect the D_{co}/D_{pit} pit profile.

3.2.5 Conchoidal diameter as a function of impact angle

As space impacts occur at all angles, impact tests have been carried out to investigate the effect of angle (Θ) on the conchoidal diameter, D_{co}. In Figure 3-10 the normalised conchoidal diameter, D_{co}/d_p, is plotted against impact velocity for impacts onto quartz and oligoclase at 30° and 60°. The projectile diameters were in the range 1-4 μm for both data sets. Iron, silicon and lanthanum hexaboride projectiles were used for both shot

(a) Cross-section through microcrater

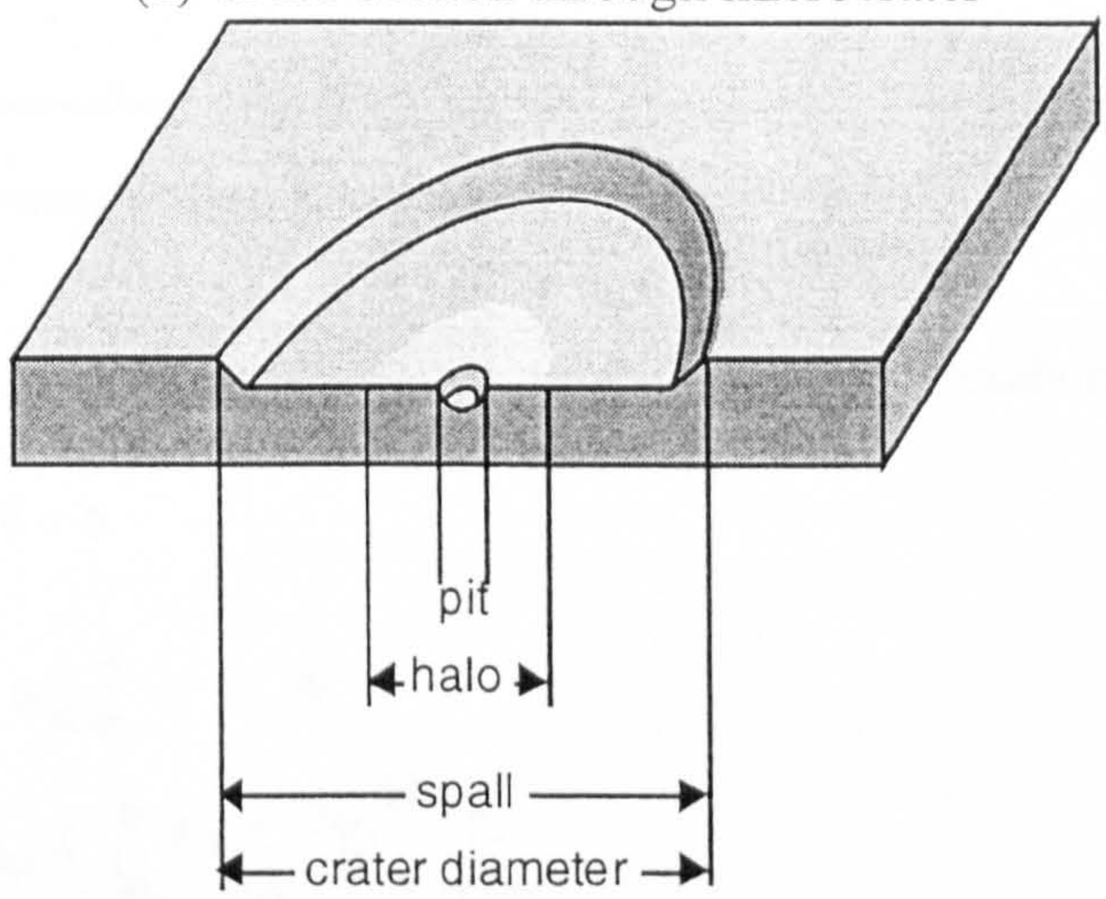

(b) Spall plate geometries

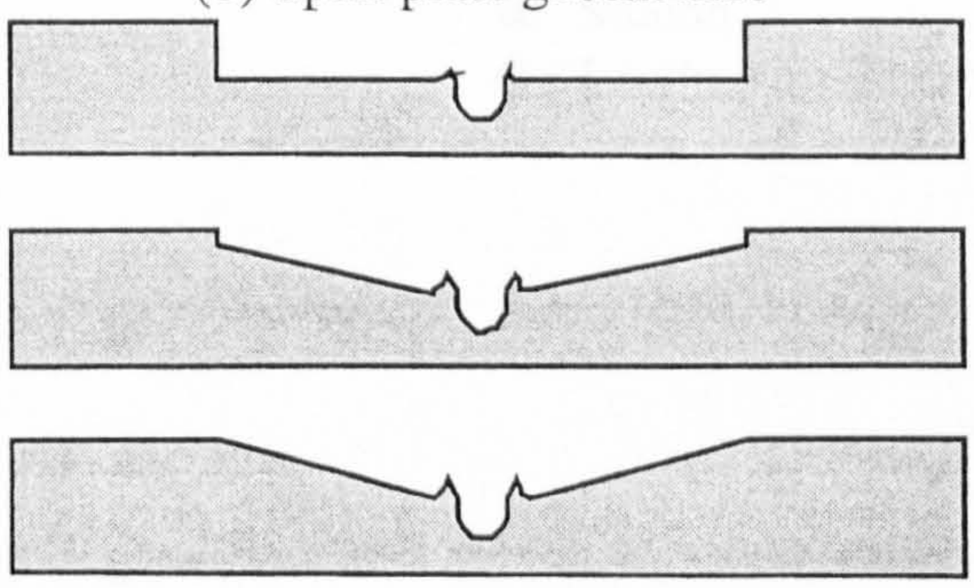

(c) 'Stylus' pit geometries

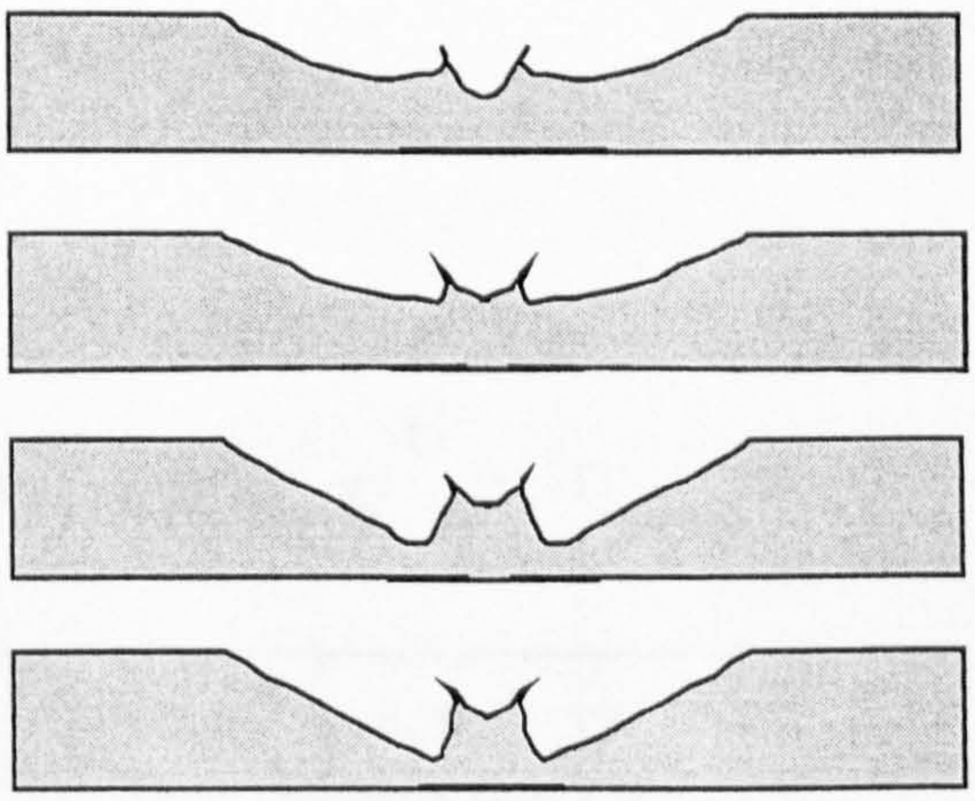

Figure 3-7. Micrometeorite crater morphologies observed on lunar rock surfaces (Image adapted from Hörz *et al.*, 1971, drawn by J. M. Marchant)

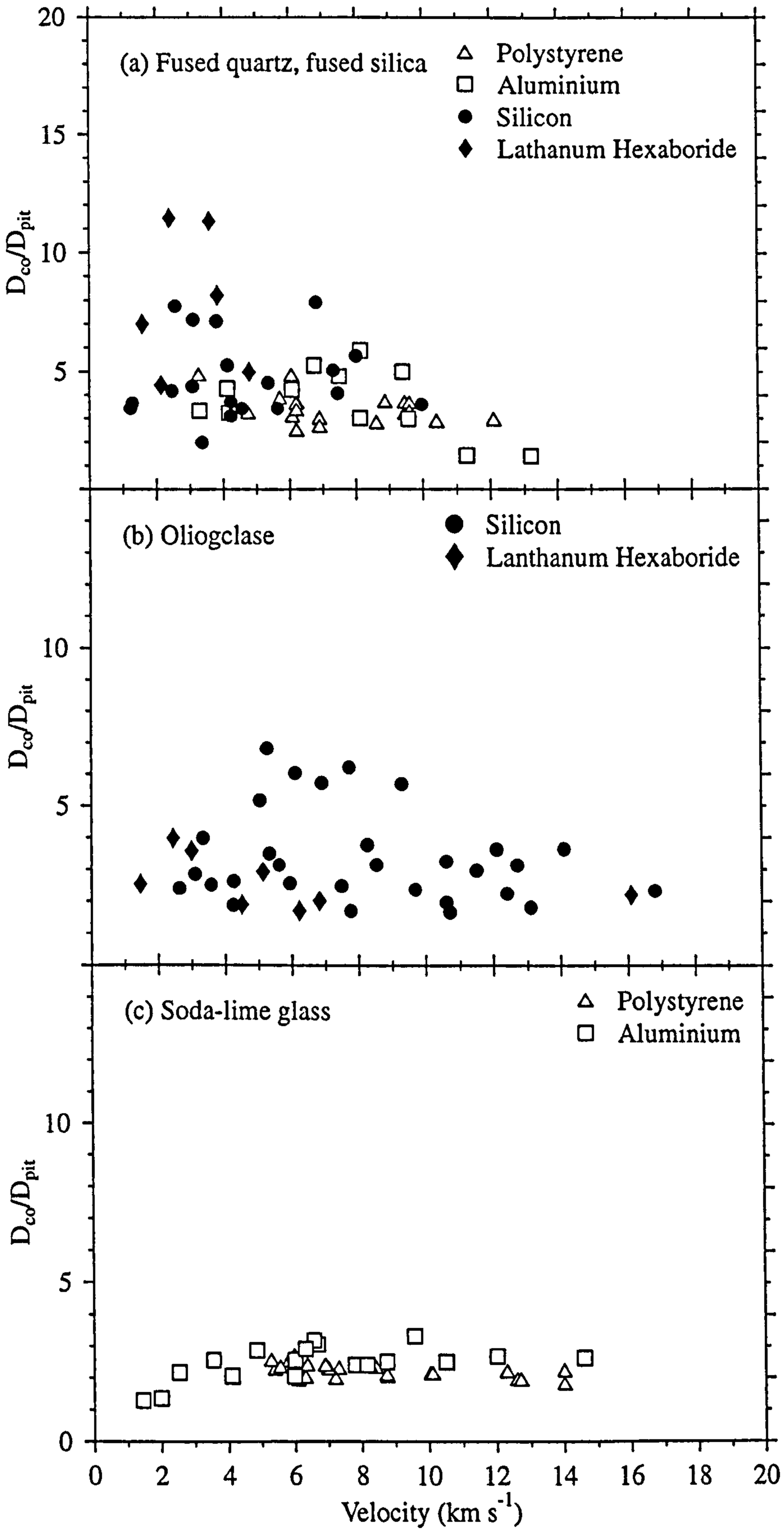

Figure 3-8. D_{co}/D_{pit} versus velocity for (a) fused quartz/silica (b) oligoclase and (c) soda-lime glass targets. The soda-lime glass data have a constant value of D_{co}/D_{pit} of 2-3 above 5 km s^{-1}, whilst the quartz/silica data are more scattered.

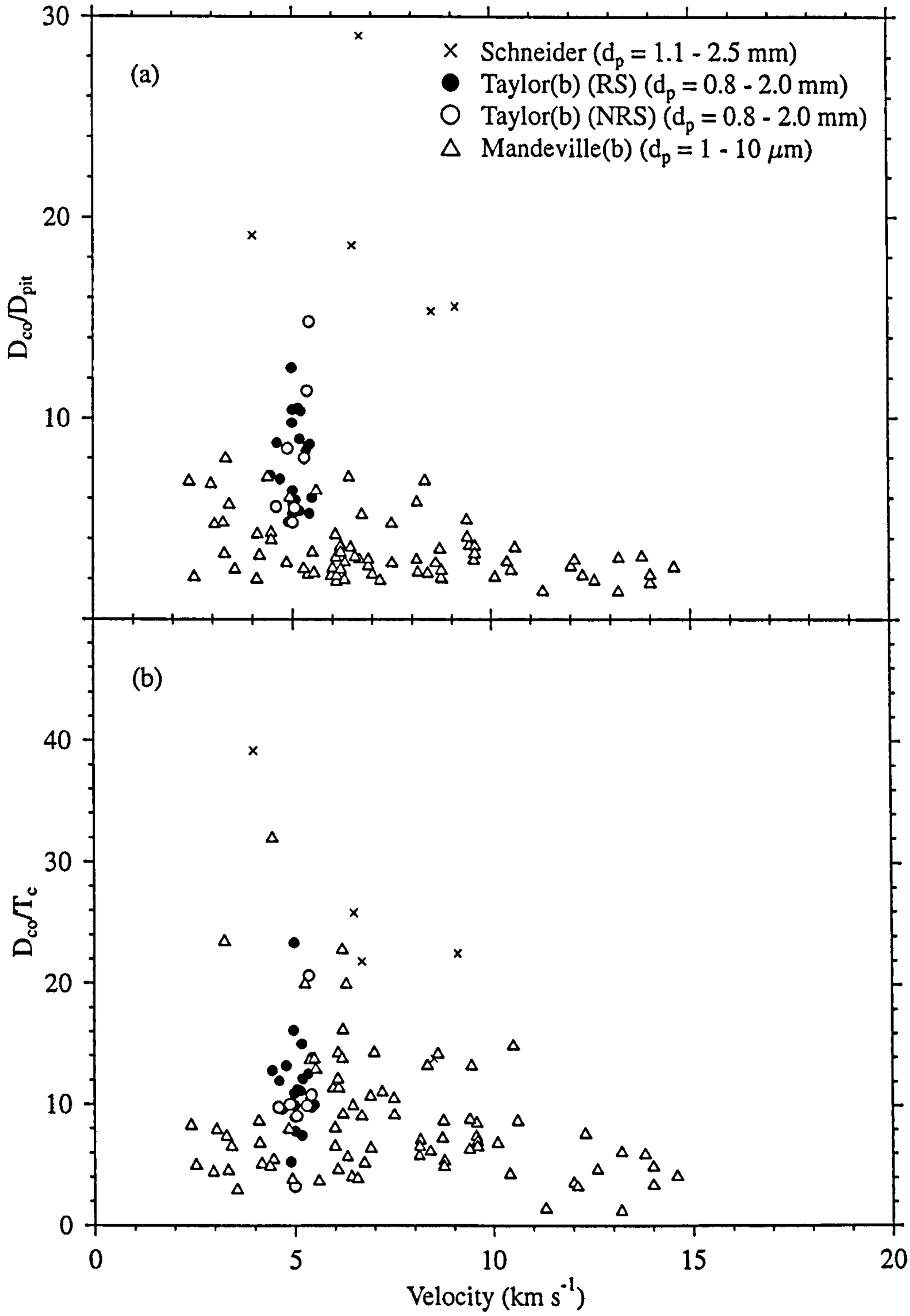

Figure 3-9. Data sets for which full crater profiles have been recorded.(a) D_{co}/D_{pit} and (b) D_{co}/T_c versus velocity. Data from Table 3-1. (RS: rear spalling. NRS: non-rear spalling)

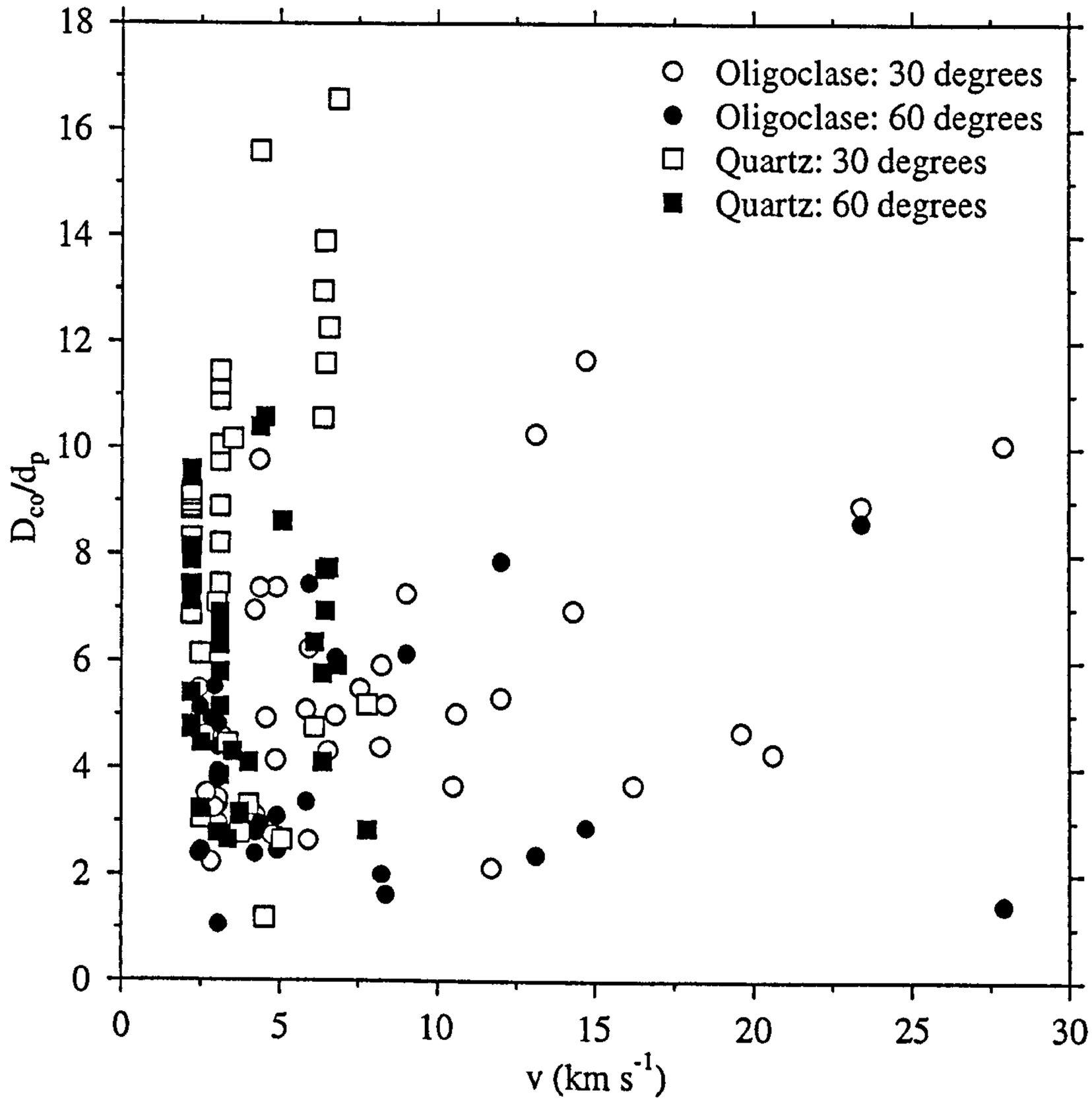

Figure 3-10. D_{co}/d_p as a function of velocity for shots onto oligoclase and quartz at 30 and 60 degrees. The D_{co}/d_p values for quartz show a much stronger dependence with velocity than the values for oligoclase. Fe, Si and LaB6 projectiles were used for shot programmes onto both materials. Note that the quartz data do not extend over the full range of velocities. Data from Table 3-1.

programmes. The values of D_{co}/d_p for quartz at 30° and 60° cover a larger range of values than for the oligoclase. Although the data are scattered, they suggest a steeper increase with velocity than the data for impacts on oligoclase. If both materials provided the same hypervelocity impact response then the values of D_{co}/d_p should be similar. This is not the case. Following on from the differing pit profiles identified in section 3.2.4 for quartz and oligoclase, these data suggest again that quartz may provide a different response to hypervelocity impact than oligoclase and soda-lime glass (further discussed in chapters 4 and 6).

3.3 Damage Equations: Review and Analysis

Power law damage equations are fitted to experimental data then extrapolated to predict damage features at velocities (or other impactor parameters) beyond the calibration data set. Either in LEO or on the lunar surface, the impact velocities go beyond what can be achieved with laboratory accelerators for macroscopic particles. The source data and techniques used to develop them are given in Table 3-1, Table 3-2 and Table 3-3. Note that the depth equations were developed for impacts onto fused quartz and fused silica and that the conchoidal damage equations (including Eq. 3-6, strongly based on Eq. 3-4 and Eq. 3-5) included ductile material data in their data sets. For comparison, the simplest relationship between impactor and target is if crater volume is proportional to kinetic energy. This defines the values of exponents for d_p, v and ρ_p as 1, 0.33 and 0.67 respectively. (The symbols are defined as T_c - depth of penetration, ρ_p - projectile density, v_p - projectile velocity, d_p - projectile diameter, D_{co} - spallation diameter, Θ - impact angle (measured from normal).)

3.3.1 Depth (T_c) equations

<u>McHugh and Richardson, 1974</u>

$$T_c=0.64 d_p^{1.2} \rho_p^{0.5} v_p^{0.67} \qquad \text{(cgs, v in km s}^{-1}\text{)} \qquad (3\text{-}1)$$

<u>Gault, 1973</u>

$$T_c=2.2\times10^{-4} d_p^{1.071} \rho_p^{0.524} \rho_t^{-0.5} v_p^{0.714} \qquad \text{(cgs)}$$

or

$$T_c=0.54 d_p^{1.071} \rho_p^{0.524} v_p^{0.714} \qquad \text{(cgs, v in km s}^{-1}\text{)} \qquad (3\text{-}2)$$

if density is assumed to be 2.3 g cm^{-3} for target density and the units are converted from cm s^{-1} to km s^{-1}.

<u>Cour-Palais, 1982</u>

$$T_c=0.53 d_p^{1.06} \rho_p^{0.5} v_p^{0.67} \qquad \text{(cgs, v in km s}^{-1}\text{)} \qquad (3\text{-}3)$$

3.3.2 Diameter (D_{co}) equations

Gault, 1973

$$D_{co}=5.92\times10^{-4}d_p^{1.11}\rho_p^{0.54}\rho_t^{-0.5}v_p^{0.74}\cos\Theta^{0.86} \quad \text{(cgs)} \quad (3\text{-}4)$$

Fechtig *et al.*, 1974

$$D_{co}=5\times10^{-4}d_p^{1.13}\rho_p^{0.71}\rho_t^{-0.5}v_p^{0.754} \quad \text{(cgs)} \quad (3\text{-}5)$$

Paul and Berthoud, 1995

$$D_{co}=5\times10^{-4}d_p^{1.076}\rho_p^{0.784}\rho_t^{-0.5}v_p^{0.727}\cos\Theta^{0.601} \quad \text{(cgs)} \quad (3\text{-}6)$$

Table 3-3. Source data used to derive damage equations Eqs. 3-1 to 3-6. (PDA: plasma drag accelerator; LGG: light gas gun; EDA: electrostatic dust accelerator; LPG: lithium plasma gun; CDG: capacitor discharge gun; Obl: oblique impacts; Duct: ductile material data; #: number of data; *: no information available; Poly: polystyrene; Fe: iron; Al: aluminium; Boro: borosilicate; S/steel: stainless steel)

	Eq.	Gun	Duct. ?	Obl. ?	Range	v (km s^{-1})	Proj.	Brittle targets	#
T_c	3-1	CDG LGG	no	no	50μm to mm	6-17	Boro glass, Al, Poly	Fused Silica Aluminosili-cate glass	103
T_c, D_{co}	3-2 3-4	*	no	yes	μm to cm	1-7	Fe, Al, Poly, pyrex	basalt, granite	100
T_c	3-3	*	*	*	*	*	*	*	*
D_{co}	3-5	EDA LPG LGG	yes	no	μm to mm	1-60 3-18 1-5	Al, Carbon, Fe, glass, s/steel	glass, norite	*
D_{co}	3-6	3-4, 3-5 + PDA	no	yes	1-100 μm	1.22-26.8	As for 3-4, 3-5 plus glass	quartz glass SILEX	*

By considering the Paul and Berthoud (1995) D_{co} equation and the McHugh and Richardson (1974) T_c damage equations (shown to be the best at predicting the experimental data in the following section 3.3), the dependence of the D_{co}/T_c ratio on impactor parameters can be evaluated. This profile can then be compared with experimental data. The resulting equation, Eq. 3-7, shows little or no dependence on impactor parameters. Therefore, according to the equation predictions, the experimentally determined values of D_{co}/T_c should be nearly constant over the range of experimental parameters.

$$\frac{D_{co}}{T_c}=0.54d_p^{-0.12}\rho_p^{0.28}v_p^{0.06} \quad \text{(cgs)} \quad (3\text{-}7)$$

3.3.3 Damage equations compared with experimental data

In this section, the 0° incidence impact data set is used to test the empirically determined damage equations (Eqs 3-1 to 3-6). In Figures 3-11 and 3-12, the experimental values for T_c and D_{co} are plotted against the equation predictions on log-log graphs. The dotted lines represent $D_{co}(expt) = D_{co}(equation\ prediction)$ and $T_c(expt) = T_c(equation\ prediction)$. Figure 3-11 applies to the D_{co} damage equations and Figure 3-12 to the T_c damage equations. The McHugh and Richardson (1974) equation predicts the data well, but the other equations over-predict at small values of T_c. Of the D_{co} damage equations, the Paul and Berthoud (1995) equation offers the closest correlation to the data over the whole range. For $D_{co}(expt)$ < 100 μm, both the Fechtig *et al.* (1974) and Gault (1973) equations under-predict the experimental values by up to an order of magnitude. The degree of under-prediction is less for the Paul and Berthoud (1995) equation. For D_{co} < 100 μm (microparticle regime), the Paul and Berthoud (1995) equation does not display a strong trend from over-prediction to under-prediction, unlike the Fechtig *et al.* (1974) and Gault (1973) damage equations.

In Figures 3-13 and 3-14 a more quantitative approach to the analysis of damage equations is presented. By plotting the ratio (experiment datum/equation prediction) against velocity for both the 'small' and the 'large' data sets, any size scaling can be identified. Eq. 3-1 (McHugh and Richardson, 1974) shows little dimensional scaling in Figure 3-13(a), unlike Eq. 3-3 (Cour-Palais, 1982), where the large data set is clearly separated from the small data set. The value of the d_p exponent was 1.2 for Eq. 3-1 versus 1.06 and 1.07 for the other two equations. The range of over-, or under-, prediction is kept to within four times that of the experimental data. However, in Figure 3-14, there is a much greater degree of over-prediction and evidence of dimensional effects (Figure 3-14(a) and (b)) for both the small and large data sets. This is less for Eq. 3-6 (Paul and Berthoud, 1995), which has a d_p exponent of 1.08 versus 1.13 and 1.11 for Eqs. 3-4 and 3-5.

The performance of an equation against the data set can be assessed by calculating the ratio by which the calculated value of T_c must be multiplied in order to incorporate a particular percentage of the data (for both for under-prediction and over-prediction). The value of this scaling factor, which includes 75, 90 and 95% of the data for both under-, and over-, prediction (where the equation over- or under-predicts the experimentally measured values), has been calculated for Eq. 3-1 and Eq. 3-6. These equations have shown to provide the best predictive performance over the range of data tested. The results are presented in Table 3-4. These upper and lower bands are typically 0.8 and 2-3 times the equation predicted value for a particular set of impactor parameters. Therefore the damage equations do not predict the depth of penetration and conchoidal diameter to a high degree of accuracy.

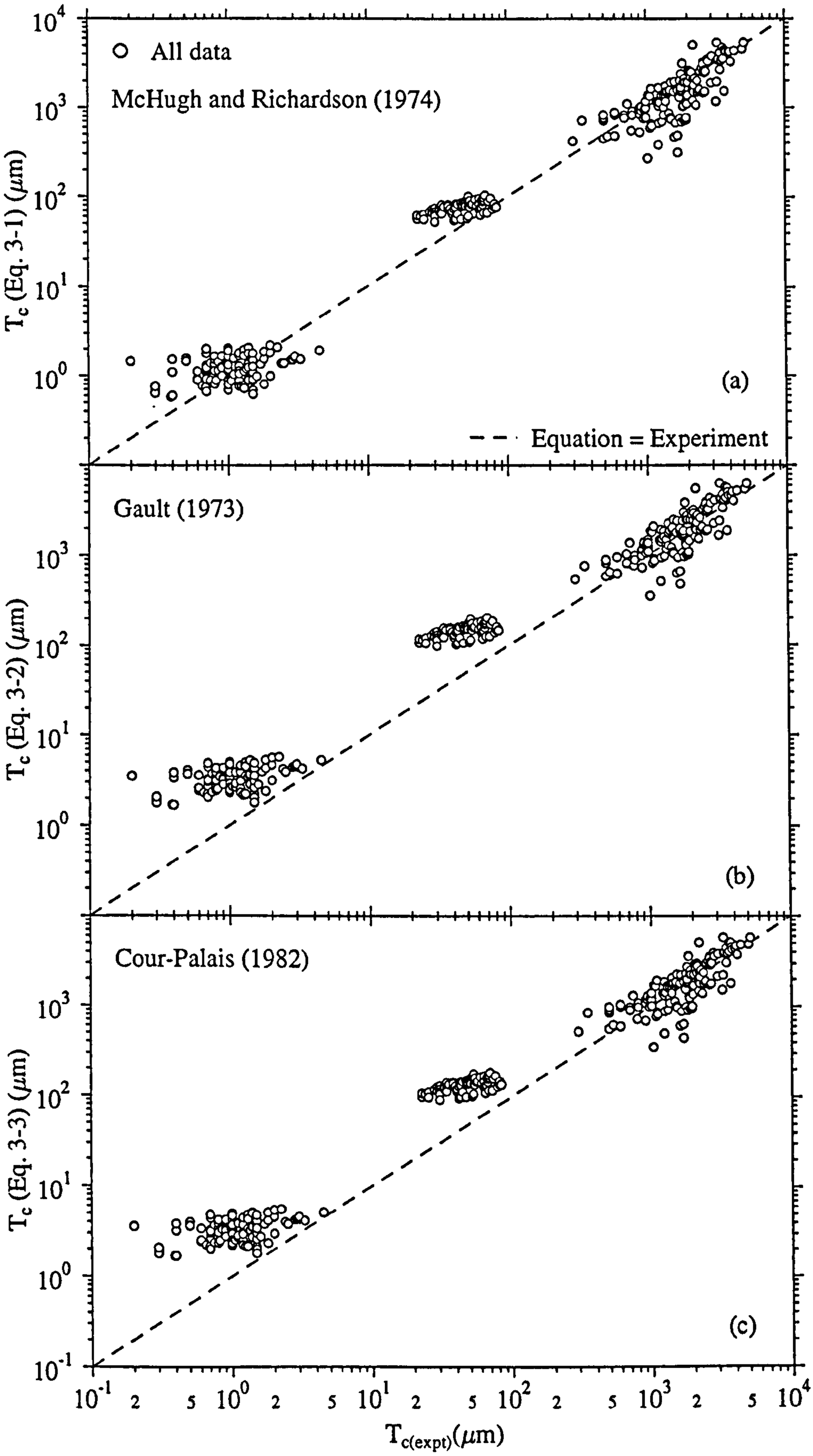

Figure 3-11. Depth equation predictions against experimental data (a) Eq. 3-1 (b) Eq. 3-2 (c) Eq. 3-3. The dotted line signifies when experimental data = equation prediction.

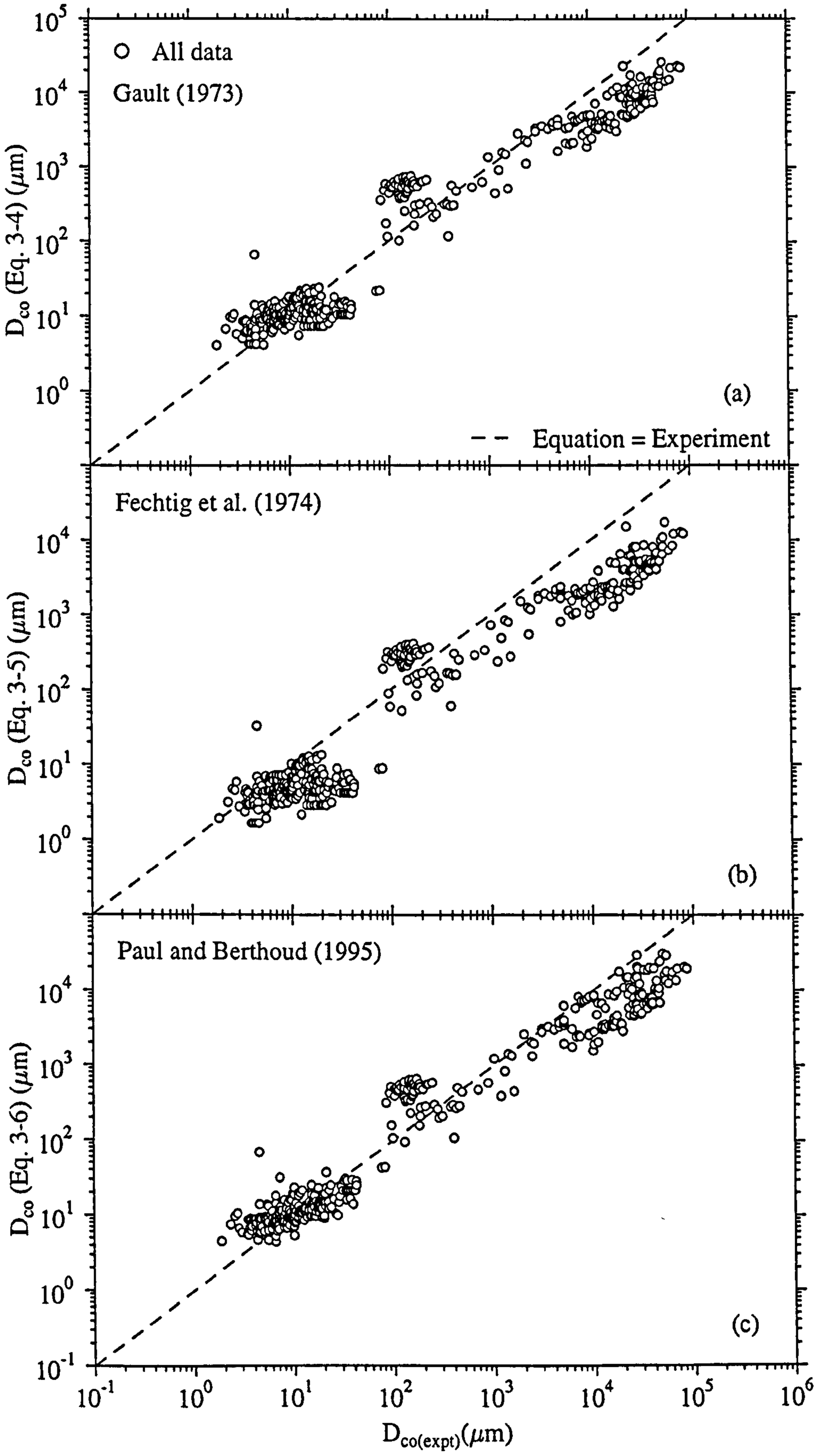

Figure 3-12. Conchoidal damage equation predictions against experimental data.

(a) Eq. 3-4 (b) Eq. 3-5 (c) Eq. 3-6. The dotted line signifies experimental data

equation prediction.

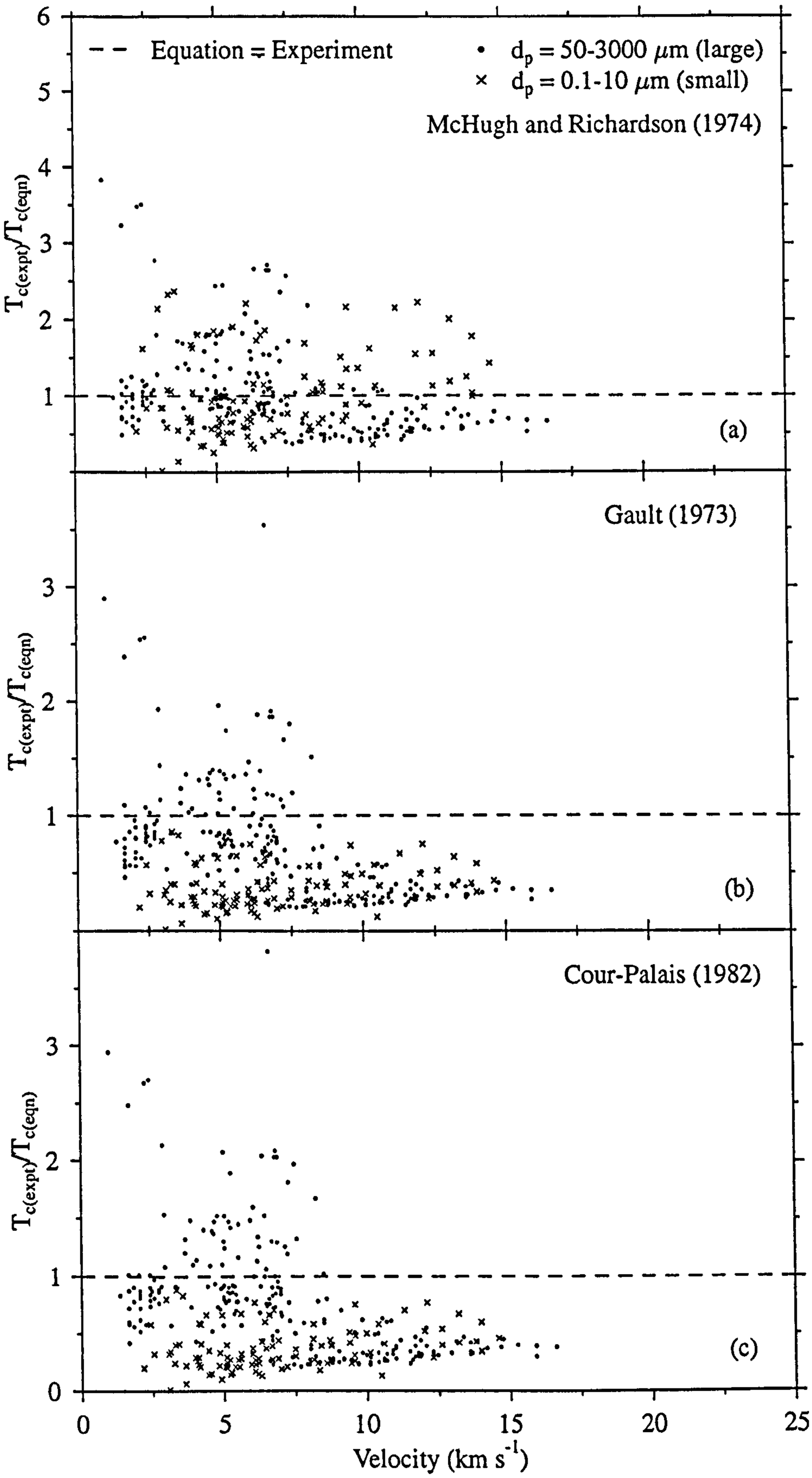

Figure 3-13. Data from Figure 3-11 plotted as a ratio (expt/equation prediction).

(a) Eq. 3-1 (b) Eq. 3-2 (c) Eq. 3-3. The dotted line signifies expt data=equation prediction

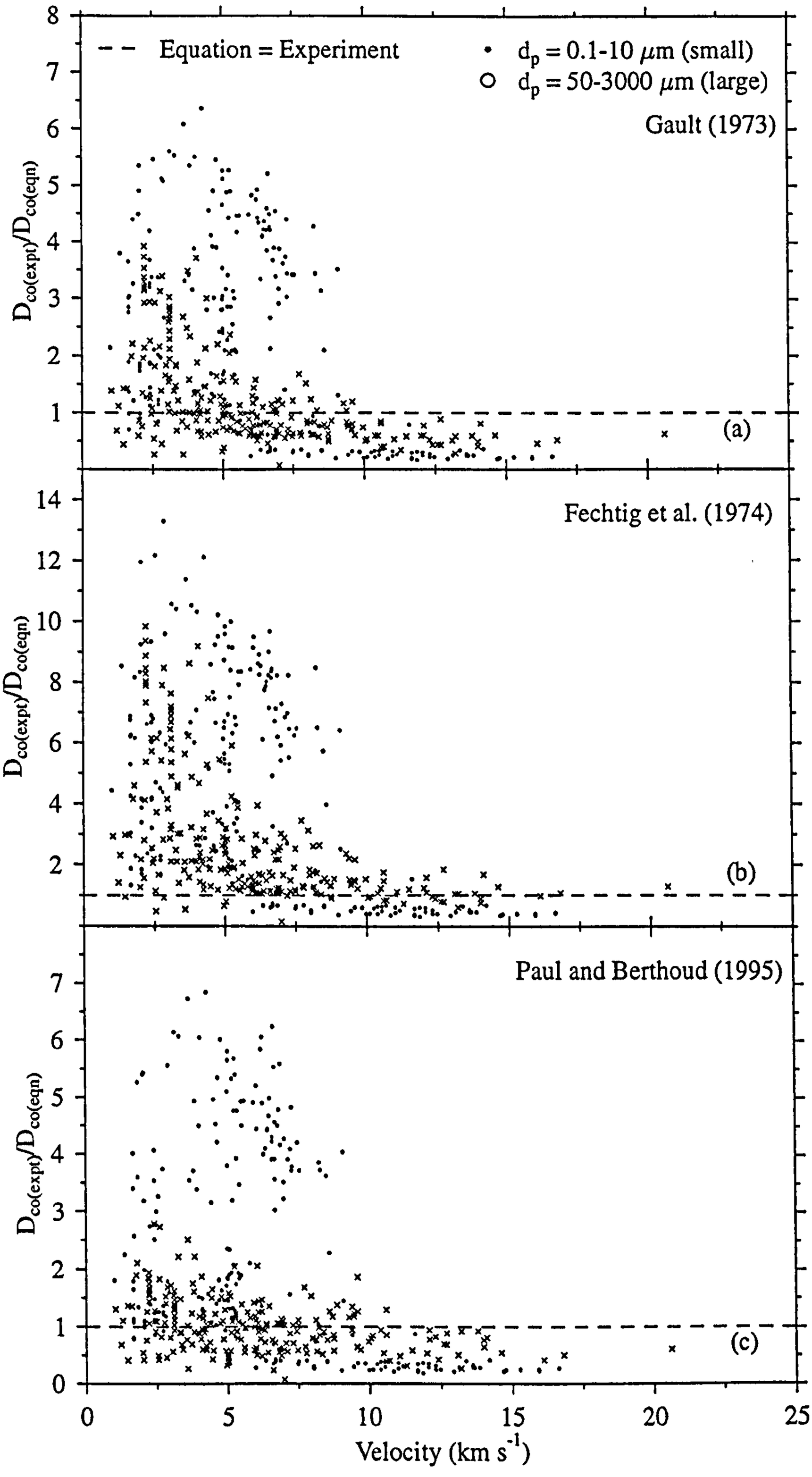

Figure 3-14. Data from Figure 3-12 plotted as a ratio (expt/equation prediction)

(a) Eq. 3-4 (b) Eq. 3-5 (c) Eq. 3-6. The dotted line signifies expt. data = equation prediction

Table 3-4. Statistical analysis of the performance of the damage equations. The lower and upper band values represent the fractional values of the equation predictions which contain 75, 90 and 95 % of the experimental data respectively.

Equation	lower band scaling factor	upper band scaling factor
T_c (McHugh and Richardson equation)		
number of data	212	134
75% of data within bands	$0.97 \times T_c$	$1.81 \times T_c$
90% of data within bands	$0.95 \times T_c$	$2.36 \times T_c$
95% of data within bands	$0.85 \times T_c$	$2.67 \times T_c$
D_{co} (Paul and Berthoud)		
number of data	197	265
75% of data within bands	$0.94 \times T_c$	$3.71 \times T_c$
90% of data within bands	$0.92 \times T_c$	$4.93 \times T_c$
95% of data within bands	$0.80 \times T_c$	$5.56 \times T_c$

3.3.4 Comparison of crater shape profile equation with data

In Figure 3-15, the crater profile (D_{co}/T_c) equation predictions (using Eq. 3-7) are plotted as dashed lines against the experimental data, first shown in section 3.2.3. A density value of 2.7 g cm^{-3} has been assumed for plots a and b and a velocity of 10 km s^{-1} for plot c. Ideally, the data should lie between the upper and lower boundaries of the dashed lines. This is not the case.

3.3.5 Oblique impact data compared with damage equation predictions

The data from Figure 3-10 are compared with the conchoidal diameter predictions from Eqs. 3-4, 3-5 and 3-6 in Figure 3-16. As in Figures 3-11 and 3-12, a log-log plot of experimental data versus equation prediction is presented. The oligoclase data are represented by open symbols and the quartz data by filled symbols. For all three equations, the open symbols and closed symbols do not overlie each other. The data are best predicted by the Gault (1973) damage equation (Eq. 3-4) , whilst the Fechtig *et al.* (1974) damage equation (Eq. 3-5) under-predicts the experimental data. The Paul and Berthoud (1995) damage equation (Eq. 3-6) has an equal balance of under- and over-prediction, but a larger spread (up to an order of magnitude). Conclusions cannot be drawn on the most appropriate value of the $\cos\Theta$ exponent and the equations are not identical in other respects. However, the oligoclase and quartz data suggest a differing response to hypervelocity impact for these two target material types.

3.4 Onset of Rear Spallation

Unlike ductile materials, the onset of rear spallation and perforation in brittle targets has not been studied in detail. The influence of target type has not been quantified, nor has the dependence on impactor parameters and target thickness (T). Understanding the onset of

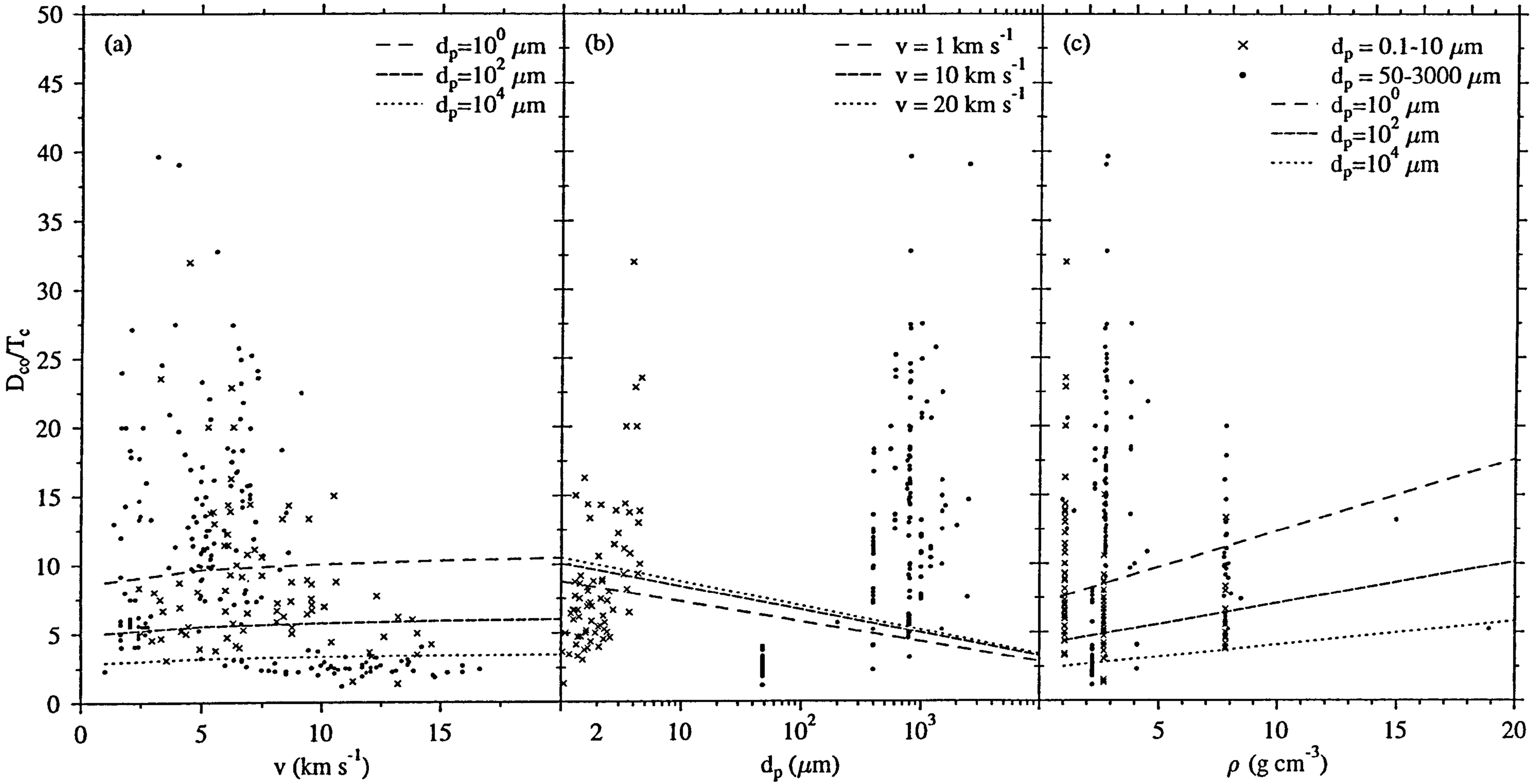

Figure 3-15. Crater shape profile (D_{co}/T_c) as a function of (a) velocity (b) projectile diameter (c) density. Eq. 3-7 predictions are compared to experimental data. Density in (a) and (b) is 2.8 g cm^{-3}, velocity in (c) is 10 km s^{-1}.

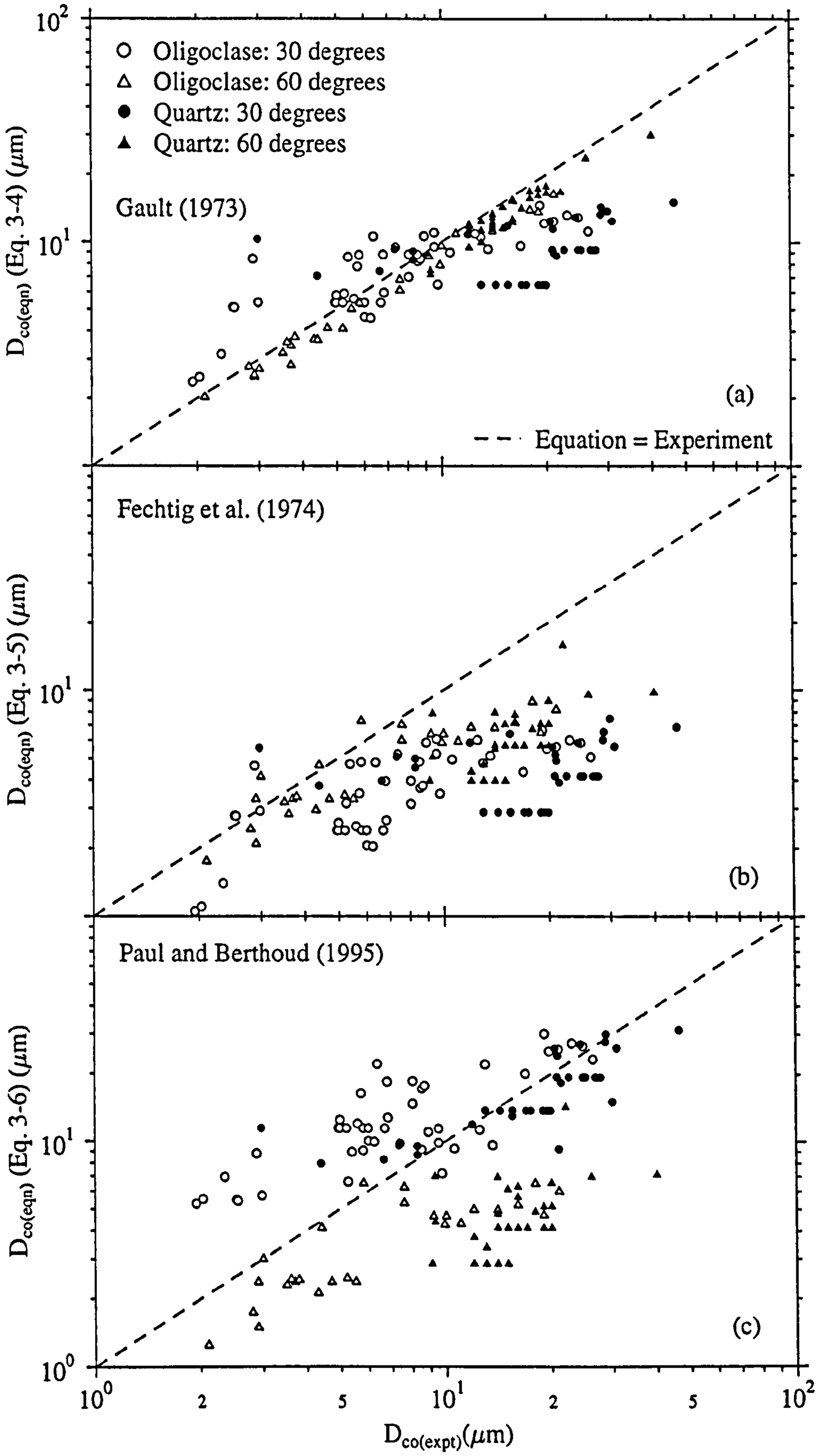

Figure 3-16. Conchoidal damage equation predictions against experimental data. (oblique impacts onto oligoclase and quartz. Data from Table 3-1.) (a) Eq. 3-4 (b) Eq. 3-5 (c) Eq. 3-6. The dotted line signifies experimental data = equation prediction.

rear spallation is important, not only for brittle systems used in space, but also understanding any variation in front target morphology (relevant to decoding the impacts on the HST and EURECA solar cells).

The condition for rear spallation of a finite target has been expressed as a ratio of crater depth divided by target thickness (T_c/T) independent of impact velocity (McHugh and Richardson, 1974). The validity of this criterion can be tested against the McHugh, Edelstein, Schneider and Taylor(b) data sets (Tables 3-1 and 3-2), which incorporate data around the onset of rear spallation. The ratio $T_c/T = 0.143$ was derived from an analysis of four non-perforating shots and three perforating shots over a velocity range by McHugh and Richardson (1974). A further 63 shots from the above data sets, which are classified as rear spalling (RS) or non-rear spalling (NRS), are included in this analysis. The ratio T_c/T is plotted against velocity to test the velocity independent relation defined by McHugh and Richardson (1974). The non-rear spalling points are defined by open symbols and the rear spalling points by closed symbols. In Figure 3-17(a), most of the NRS data points lie below the 0.143 line, as predicted. However, there are many RS shots below the 0.143 line, showing that the division does not strictly hold. The Edelstein data set NRS and RS shots are overlaid within the 3-7 kms^{-1} velocity band, implying that there is not a unique threshold solution for the change in target response from no rear spall to rear spall. The velocity range of the Taylor(b) data is too small to detect any velocity dependence. However, the NRS and RS data overlie on either side of the defined threshold for rear spallation. An alternative definition of the threshold for rear spallation could incorporate a target material parameter and/or a velocity trend. All of the target materials are fused silica, as used for the Space Shuttle/Mir station windows, except for the Taylor(b) data. The data sets for fused silica and soda-lime glass are overlying. Therefore, no obvious target material dependence on the onset of rear spallation is shown. Only the Edelstein NRS data shows a velocity dependence with T_c/T implying that there may not be any significant velocity dependence of the onset of rear spallation.

In summary, the McHugh and Richardson (1974) threshold for the onset of rear spallation is not supported by this data set, although the velocity independence of the threshold is supported by the data. Their prediction for perforation ($T_c/T = 0.5$) cannot be tested against this data set because no perforations have been recorded.

A possible explanation for the results of this analysis may be identified by considering the nature of failure in glass. Microcracks, ~10-50 μm length, open under a propagating shock wave and connect with other cracks and thus cause the material to fail. The size distribution and orientation of these cracks is random, therefore the onset of failure will be variable. However, the stress required for simple cracks to run is several orders of magnitude smaller

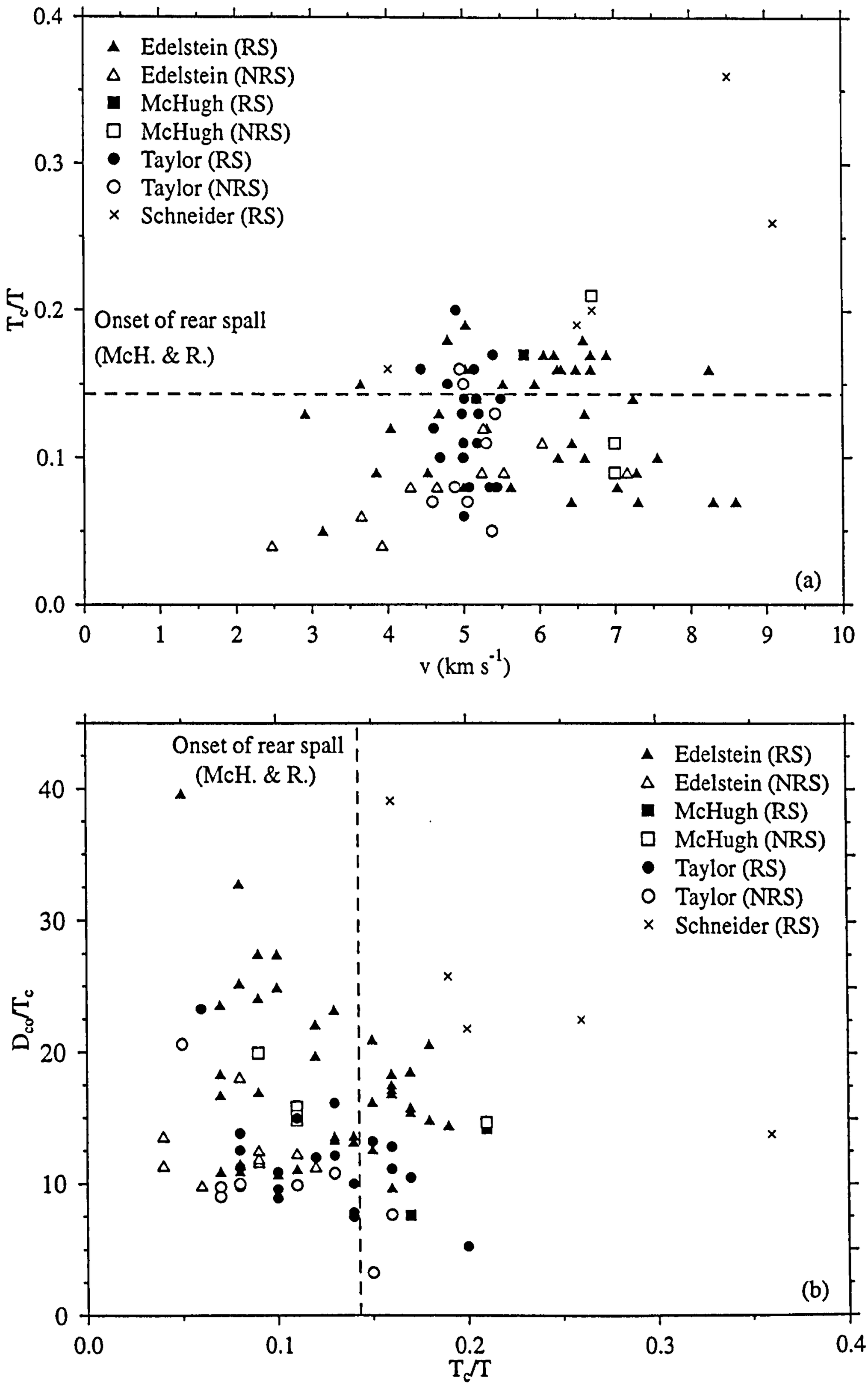

Figure 3-17. Onset of rear spallation. McH&R spallation criterion compared to (a) T_c/T (depth/target thickness) and (b) Crater profile, D_{co}/T_c (conchoidal diameter/depth) versus velocity. (NRS: non-rear spalling; RS: rear spalling)

than a typical stress pulse. It is possible that the speed at which the cracks join up may mean that any distribution in the failure is present for only a short amount of time.

Also of importance for a study of space impacts on solar cell coverglasses is an understanding of how the crater profile, conchoidal diameter and depth vary around the onset of rear spallation. The crater profile (D_{co}/T_c) as a function of T_c/T is shown in Figure 3-17(b). The data do not show a significant variation in crater profile as a function of T_c/T.

Questions arise concerning:

(i) the influence of reflection from the edge or rear of the target on the crater profile, and
(ii) if (i) is demonstrated, at what point does the ratio D_{co}/T_c change as a function of penetration ?

The crater parameters D_{co} and T_c are plotted as a function of T_c/T in Figures 3-18(a) and (b). The D_{co} versus T_c/T plot shows the data sets overlying and the data are clearly scattered. It is difficult to prove whether or not there is a change in conchoidal diameter as a function of T_c/T. The data are bounded by a linear trend between D_{co} and T_c/T. In Figure 3-18(b) the data are less scattered and the different depth responses of soda-lime glass and fused silica/quartz are identified. It should be borne in mind that the data sets represent different impact velocity ranges. There is a change in gradient for the fused silica/quartz data sets at around 0.12-0.13, above which only rear spalling impacts are present. However, below this value, both non-rear spalling and rear spalling points are present. A similar change in gradient for the soda-lime glass data is present at $T_c/T \approx 0.1$. Again, the non-rear spalling points and rear spalling points are distributed below and above this point. In conclusion, a change in gradient is observed at a certain value of T_c/T, different for quartz and soda-lime glass, suggesting a change from semi-infinite to finite (i.e. rear spalling) response. However, the change in gradient does not correlate with the onset of rear spallation which does not occur at a defined threshold.

An alternative definition of the threshold for finite target behaviour may be set up by considering the time for a D_{co} feature to form compared with the time for a shock wave to travel from the impact point to the target rear then back to the front surface. Consider the D_{co} feature to form by radial cracks running outward from the central pit feature. Let the crack running time be the shear wave speed (the maximum failure wave speed is the shear wave speed, Bourne, 1996), 3.5 km s^{-1}. So, for a 25 mm thick target and r_{crack} = 20 mm, the crack formation time is 6 μs and the shock wave travel time is 10 μs. Therefore, the conchoidal feature has formed before the shock wave arrives at the target surface.

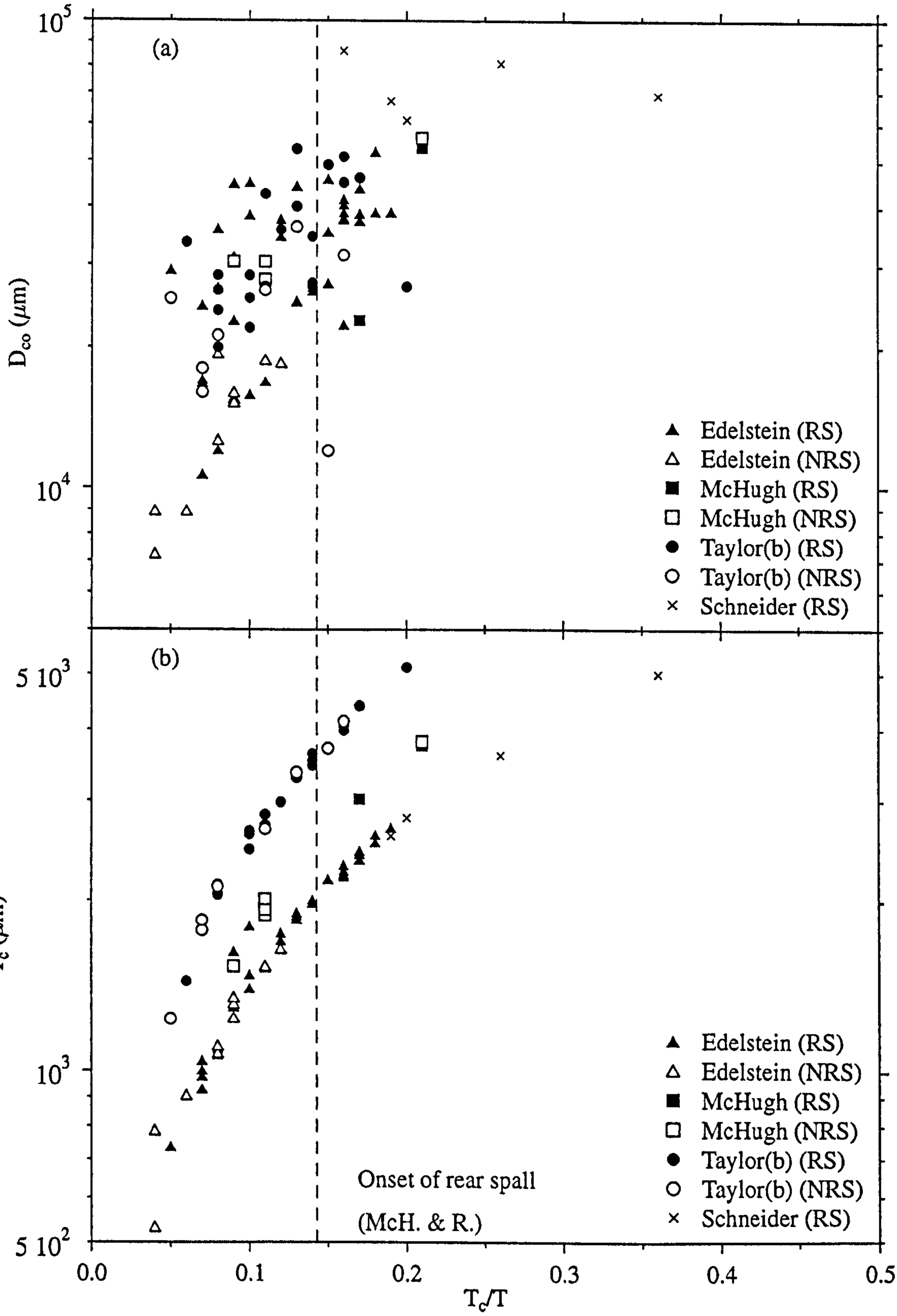

Figure 3-18. (a) D_{co} (conchoidal diameter) and (b) T_c (depth of penetration) as a function of T_c/T (depth/target thickness). RS: rear spallation, NRS: no rear spallation.

3.5 *Solar Cells*

For the impact data onto brittle targets discussed in this chapter to be applicable to the analysis of impacts onto space-exposed solar arrays, the following criteria need to be investigated:-

- The similarity of oligoclase, quartz, fused silica and soda-lime glass targets to the borosilicate glass used in the solar cells (velocity scaling, oblique angle response and crater morphology).
- The cut-off point between semi-infinite and finite behaviour of the brittle material impact database and its applicability to a multi-layer structure.
- The transition point for the change in morphology between simple and complex solar cell craters.

These points are explored in this section.

At the smallest impactor size regime, the solar cell responds as a semi-infinite glass target (see Figure 3-19(a)). At a certain combination of impact parameters (which are probably not unique, see Herbert and McDonnell (1997)), the formation of the surface impact features (e.g. conchoidal diameter) is affected by the rear layers. An example of this morphology is given in Figure 3-19(b). This transition in morphology may or may not be concurrent with the formation of the shatter ring about the central pit (chapter 1).

A threshold (J. C. Mandeville, personal communication) of D_{co} = 200 μm for the transition between semi-infinite and finite coverglass behaviour has been identified. It is calculated using the McHugh and Richardson (1974) criterion in section 3.4, which is derived for impacts onto quartz with a free rear surface. The solar cell is made of borosilicate glass which is backed by other materials, affecting reflection of the shock waves. Therefore the values derived are open to further evaluation. The coverglass thickness is 150 μm so the threshold depth of penetration at which the transition to finite behaviour occurs is at 23 μm, using the McHugh and Richardson criterion. An experimentally observed ratio of D_{co}/T_c of ~ 10 (where T_c is depth of penetration) has been noted on HST solar cells (M. Rival, personal communication). This defines the limit at D_{co} = 230 μm, or more conservatively, 200 μm. Cross-sectioning of a D_{co} = 200 μm impact site, reveals the coverglass / BSFR silicon delamination. But this does not correspond to the diameter at which a morphology change in the craters is observed (from 'simple' to 'complex', as shown in Figure 3-19). A cross section of a D_{co} = 450 μm site also shows the delamination between the coverglass and the silicon. However, there are no fractured regions visible through the coverglass and the

(a)

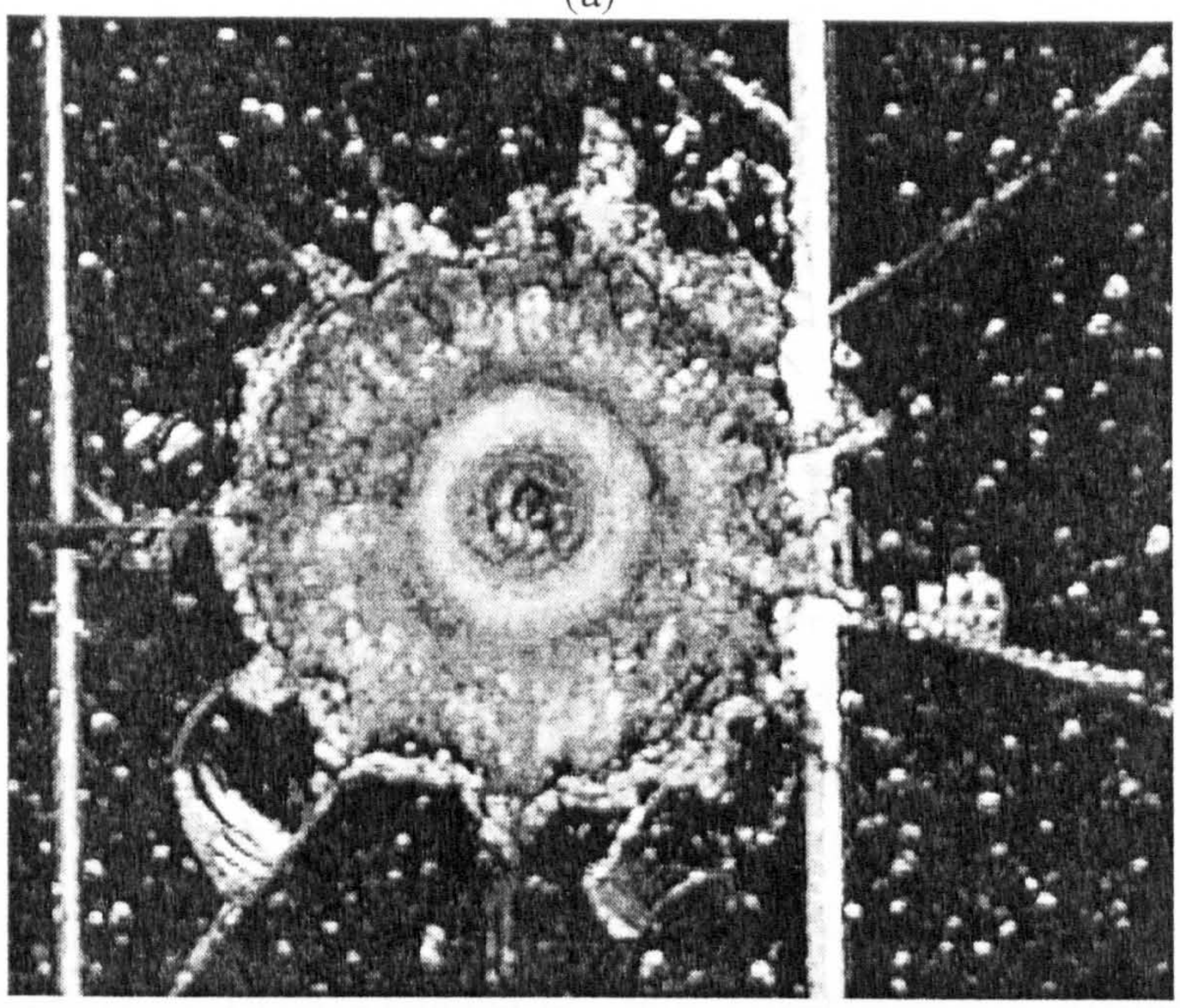

(b)

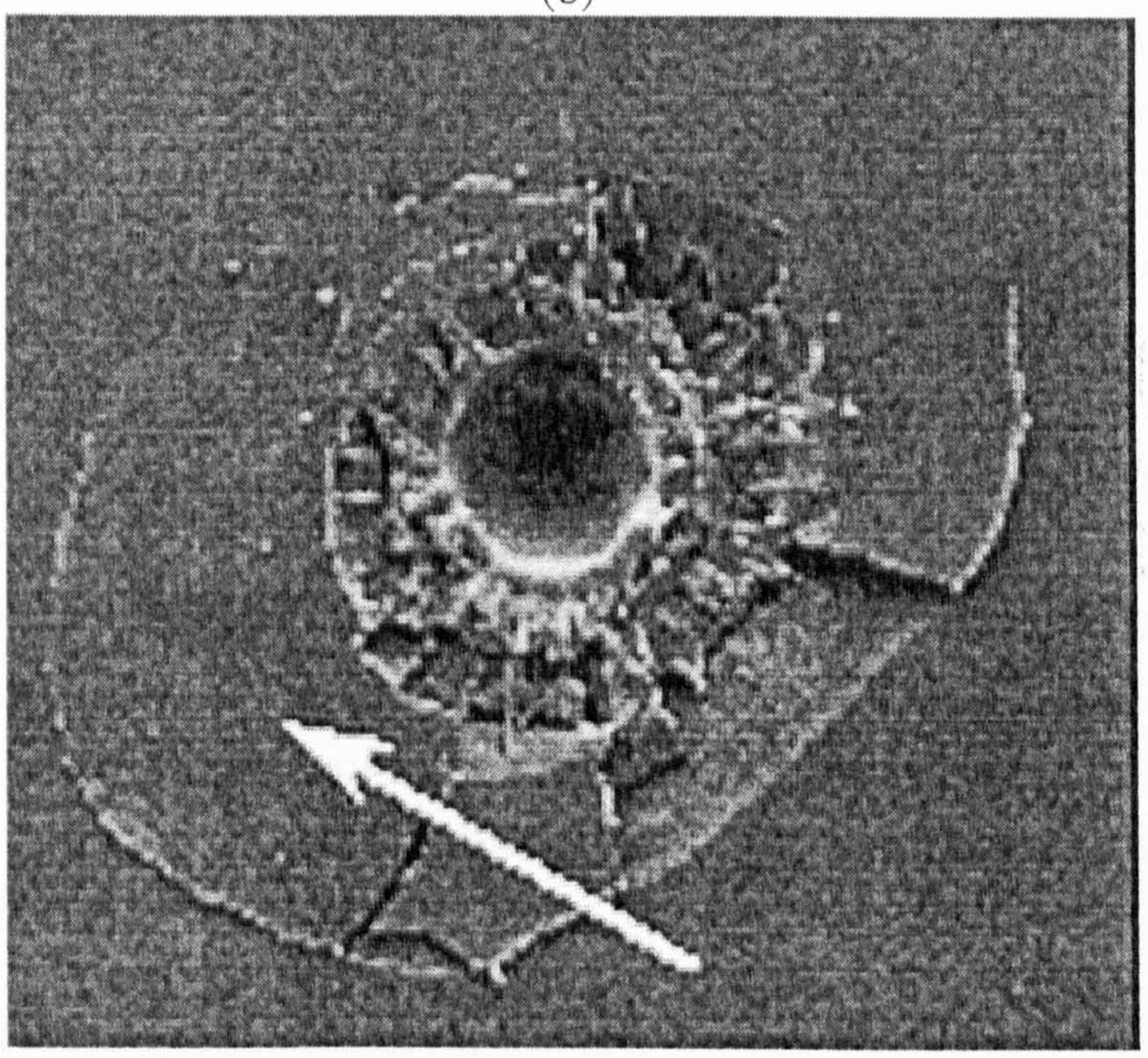

Figure 3-19. Comparison of simple and complex morphology of HST solar array impacts (a) diameter of damage is ~ 1 mm, the morphology of the impact crater is affected by the multi-layer structure of the solar cell (b) Diameter of damage ~ 100 μm. The morphology of the impact crater is similar to an impact on a semi-infinite glass target ∴ only the glass determines the final crater morphology. (Reproduced from Figures 1-6 and 1-7, see captions for more details of impact craters). The arrow identifies a conchoidal fragment on the verge of spallation.

morphology is that shown in Figure 3-19(b); a 'classical' HST impact morphology. In contrast, analysis of a D_{co} = 1570 μm crater shows a modified crater morphology and heavily fractured regions are visible through (and in) the coverglass (Rival, 1997) (Figure 3-19(a)). Therefore, the transition between simple and complex morphology may be at a conchoidal diameter greater than the 200 μm previously quoted.

The dependence of D_{co}/D_{pit} with impact angle is examined in Figure 3-20(a). Apart from the three outliers, the data are overlying for all impact angles. All the projectiles are glass and the particle diameter ranged from 10 to 100 μm. This suggests that the use of the geometric mean obscures impact angle information. The applicability of the oligoclase and soda-lime data to the solar cell impact analysis can be examined by considering the crater profile (D_{co}/D_{pit}) versus impact velocity for normal impacts. The oligoclase and soda-lime data (reproduced from Figure 3-8) are plotted in Figure 3-20(b) with the solar cell data. The D_{co}/D_{pit} values are typically between 2-6 for the solar cell, oligoclase and soda-lime data. The outliers with $D_{co}/D_{pit} > 10$ have smaller D_{pit} values than expected, producing large values of D_{co}/D_{pit}. The quartz data have not been included as they were shown to present a differing crater profile earlier in this chapter. The soda-lime and oligoclase data are mostly within the range D_{co}/D_{pit} = 2-3, but the projectile range was 1-10 μm, compared with the solar cell data's d_p = 10-100 μm. This slight increase in D_{co}/D_{pit} may be due to a dimensional effect.

In Figure 3-21(a) the solar cell impact data are presented, D_{co}/d_p versus velocity, binned by impact angle. All the projectiles are glass and the largest projectile fired was ~ 100 μm. In Figure 3-21(a), the 0°, 30°, 45° and 60° data overlie whilst the 70°-75° shots have slightly lower values of D_{co}/d_p over the velocity range of 5-10 km s^{-1}. Overall, there is not a clear distinction between impact angle and normalised conchoidal diameter (D_{co}/d_p). In Figure 3-21(b) the data from Figure 3-10 (oblique impacts onto oligoclase; no soda-lime glass data is available; quartz data are not included due to the differing response identified in this chapter) are overplotted. The response of oligoclase appears similar to that of the solar cell. Therefore, the utilisation of soda-lime and oligoclase data for this analysis is not disallowed as a result of the comparison with solar cell data.

3.6 Composite Honeycomb Damage Equations

As the full range of space impact conditions cannot be simulated in the laboratory, damage equations based on the available data must be formulated and extrapolated to space impact conditions. The following are explored in this section: (i) ballistic limit of the target as a function of impact energy, (ii) scaling to aluminium hole sizes, (iii) comparison with spaced aluminium shields, and (iv) using damage equations derived from impacts onto composite truss tubes.

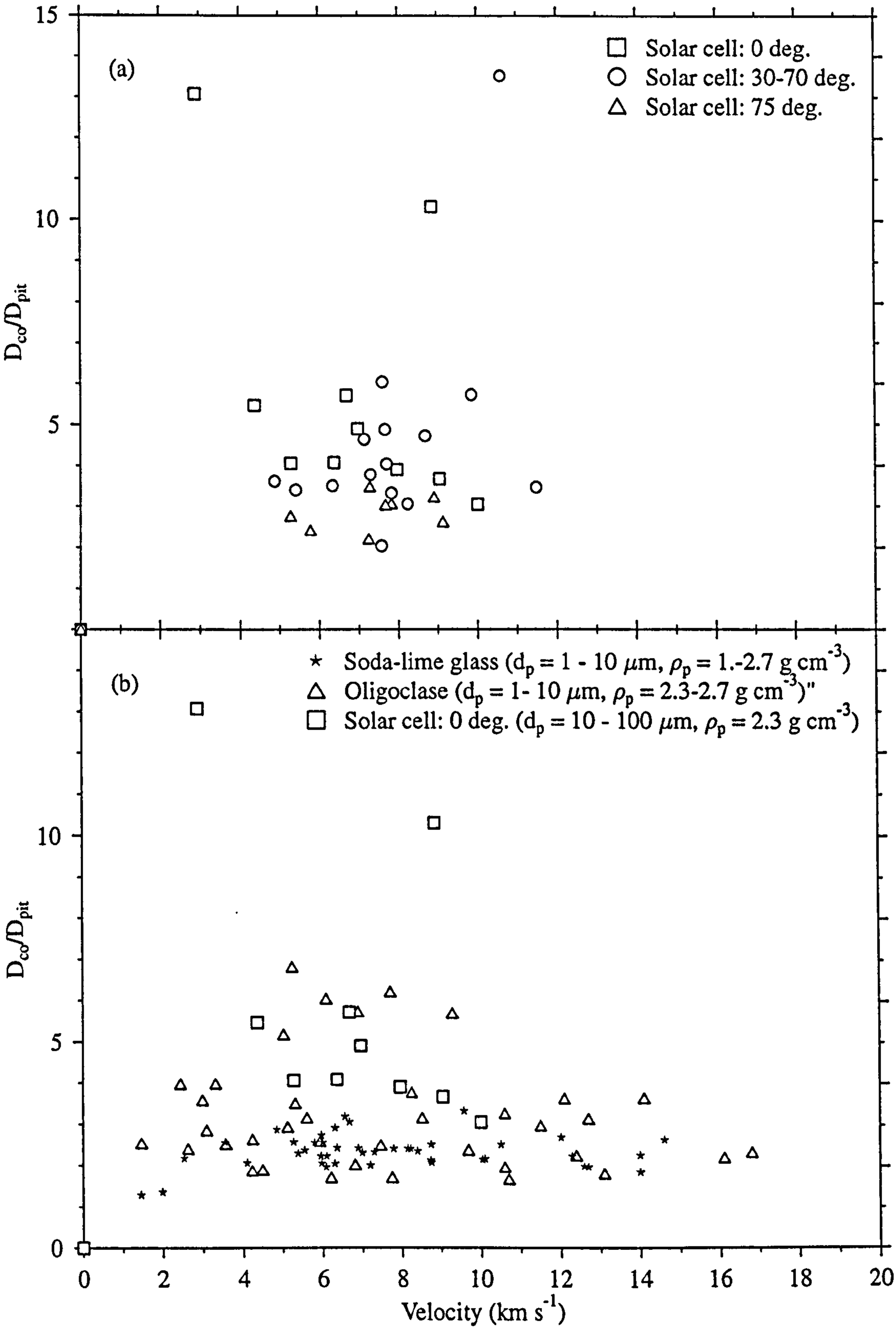

Figure 3-20. D_{co}/D_{pit} versus velocity for (a) solar cell (b) soda-lime glass and oligoclase targets (normal impacts, from Fig. 3-7). (a) The crater profile does not vary significantly with impact angle therefore the whole data set is comparable with the normal impact data in (b). Both data sets have a broadly constant value of D_{co}/D_{pit} in the range 2-6 for 5-10 km s^{-1}

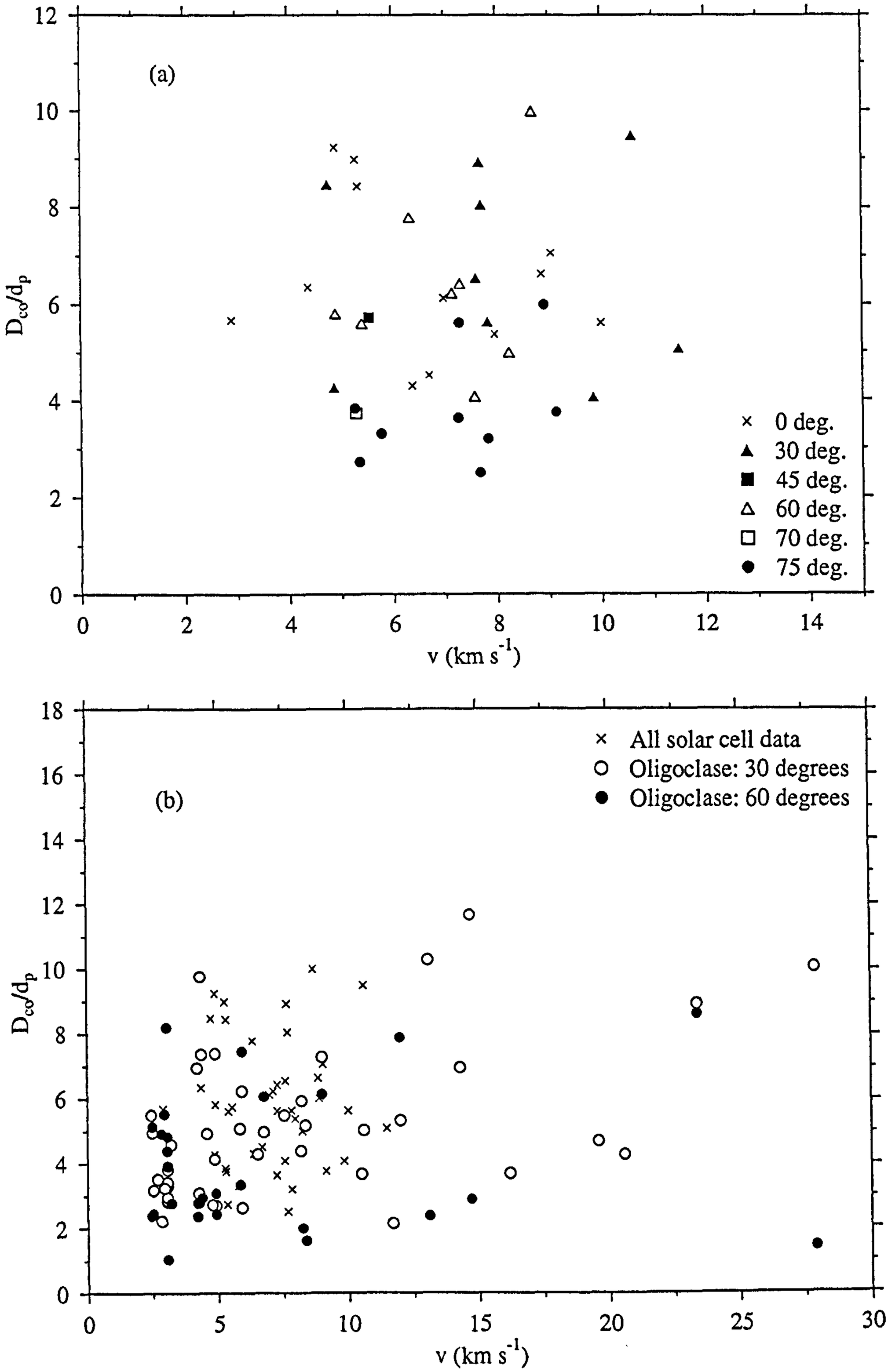

Figure 3-21. (a) D_{co}/d_p versus velocity binned by impact angle for all solar cell data (b) D_{co}/d_p versus velocity for the oligoclase data from Fig. 3-10. The solar cell data and oligoclase data overlie, suggesting that the hypervelocity impact response is comparable.

Table 3-5. Results of LGG shots on CFRP/Al-HC honeycomb (values in bold italic are assumed velocities, see section 2-4)

Shot ID	d_p (mm)	ρ_p (g cm^{-3})	v (km s^{-1})	E(J)	θ(°)	A/B	HGF	E/A_f (Jmm^{-2})	Hole comments
HC01	2.00	7.75	5.87	559	0.0	1.0	1.21	11.0	Rear larger than front
HC02	1.00	7.75	6.14	76.5	0.0	1.0	1.87	20.7	Rear larger than front
HC03	1.00	8.47	6.23	86.1	0.0	1.0	2.22	15.0	Rear larger than front
HC04	1.50	1.45	4.89	30.6	0.0	1.0	n/a	2.45	No rear perforation
HC05	1.50	8.47	5.00	187	0.0	1.0	1.37, 1.24	18.8	Rear larger than front, two exit holes
HC06	1.50	7.75	4.95	168	0.0	1.0	1.00	3.56	Rear equal to front
HC07	2.00	8.47	4.75	400	0.0	1.0	0.74	7.37	Rear smaller than front
HC08	1.00	4.50	4.46	23.4	0.0	1.0	n/a	2.58	No rear perforation
HC11	1.20	1.15	4.62	11.1	0.0	1.0	n/a	1.85	No rear perforation
HC13	2.00	1.15	5.00	60.2	0.0	1.0	n/a	4.10	No rear perforation
HC15	1.00	2.78	5.42	21.4	0.0	1.0	n/a	3.72	No rear perforation
HC16	1.20	2.78	4.86	29.7	0.0	1.0	0.51	3.07	Rear smaller than front
HC17	1.50	2.78	5.93	86.4	0.0	1.0	1.22	7.16	Rear larger than front
HC18	2.00	2.78	5.08	150	0.0	1.0	1.41	9.20	Rear larger than front
HC19	0.80	2.78	5.00	9.32	0.0	n/a	n/a	0.58	Side strike, HC torn apart
HC20	1.50	2.78	4.84	58.0	46.6	1.3	n/a	2.49	No rear perforation
HC21	1.20	2.78	5.23	34.6	44.3	1.0	n/a	2.54	No rear perforation
HC22	1.50	2.78	4.99	61.6	74.6	1.9	n/a	14.7	No rear perforation
HC23	1.20	2.78	4.96	31.2	74.4	1.2	n/a	4.05	No rear perforation

Table 3-5 Continued.

Shot ID	d_p (mm)	ρ_p (g cm^{-3})	v (km s^{-1})	E(J)	θ(°)	A/B	HGF	E/A_f (Jmm^{-2})	Hole comments
HC24	1.50	3.99	4.73	78.8	74.7	2.2	n/a	5.51	No rear perforation
HC25	1.50	2.78	5.11	64.6	74.7	2.1	n/a	4.25	No rear perforation
HC26	1.20	2.78	4.99	31.5	14.3	1.2	n/a	2.89	No rear perforation
HC27	1.50	2.78	4.94	60.4	14.7	1.0	1.1	3.02	Rear larger than front
HC28	0.80	7.75	5.09	26.9	14.4	1.0	n/a	2.61	No rear perforation
HC29	1.00	7.75	5.76	67.3	16.0	1.1	0.5	8.52	Rear smaller than front
HC33	1.20	2.78	5.15	33.6	24.5	1.0	n/a	5.89	No rear perforation
HC34	1.20	2.78	5.17	33.9	63.5	1.6	n/a	3.65	No rear perforation
HC35	1.20	2.78	5.24	34.8	59.7	1.5	n/a	2.97	No rear perforation
HC36	1.00	7.75	5.07	52.2	74.4	2.0	n/a	4.46	No rear perforation
HC37	1.00	7.75	5.30	57.0	45.0	1.2	n/a	3.68	No rear perforation
HC38	1.50	3.99	4.91	84.9	45.0	1.2	n/a	5.11	No rear perforation
HC41	1.20	4.51	5.04	51.8	73.4	2.1	n/a	5.82	No rear perforation
HC43	1.20	4.51	5.18	54.7	44.5	1.1	n/a	4.45	No rear perforation
HC44	1.20	4.51	5.06	52.2	17.0	1.3	n/a	4.92	No rear perforation
HC45	1.20	4.51	5.10	53.0	14.8	1.4	n/a	6.24	No rear perforation
HC46	1.20	4.51	5.13	53.7	74.1	1.9	n/a	4.44	No rear perforation

3.6.1 Ballistic limit: normal and oblique incidence

In Table 3-5, the shot results are presented, showing front hole parameters and rear perforation as a function of impact energy. An example of a shot near the ballistic limit of the system is HC16. No ejecta were recorded on the witness plate, implying that they were not produced and/or were moving very slowly. If the number of category 1 ejecta is

dominant over other categories it implies that the primary ejecta from the rear wall is low velocity carbon fibre and that the projectile material (molten, vaporised or solid) has not penetrated the structure. HC17 and HC18 witness plates show very little ejecta damage above the 300 μm detection threshold, but category 1 is dominant at smaller sizes. These projectiles are aluminium and the impact energies of HC16, HC17 and HC18 are seen to exceed the value of 37 J defined as the ballistic limit of a similar structure (Lambert, 1997). The non-perforating impacts (HC04, HC08, HC11, HC13[1] and HC15) are all low density impactors of lower impact energy. However, it appears that impact energy alone cannot be used as a predictor of the ballistic limit as particles of equal impact energy (HC04 and HC16) produce different damage morphologies. At a given energy, penetration is determined by projectile density for normal incidence shots. Of the 13 normal incidence shots, all the projectiles with a density > 4.5 g cm^{-3} and Al 2017 projectiles with $d_p > 1.2$ mm were found to perforate the rear target (Taylor *et al.*, 1996b; Taylor *et al.*, 1997c). Only two projectiles from the oblique series of shots presented here exceeded the ballistic limit. (At 15°, the ballistic limit is in the range $1.2 < d_p < 1.5$ mm for Al projectiles and dp > 1 mm for S/S 420 projectiles). The honeycomb is effective at improving the hypervelocity impact shielding performance for oblique impacts. The results from the shot programme are plotted in Figure 3-22 with the data from Lambert (1997). It is noted that only perforating impacts are recorded over 100 J of impactor energy for normal impacts. However, the dependence of impact angle on the ballistic limit can only be assessed for impacts below 100 J. The simplest form of damage equation is one based on the ballistic limit. The response has been shown to be not only a function of the projectile impact energy, but also of the impactor density. Therefore the ballistic limit cannot be quoted solely as a function of impact energy. Further studies to determine the ballistic limit dependence will require tests over a range of impact velocities.

3.6.2 Hole growth in composites

In order to formulate a damage equation for composites it will be necessary to consider all damage regimes. The metal response to hypervelocity impact has been well characterised and can be used as a framework for this discussion. Gardner *et al.* (1997) have defined the following regimes of hypervelocity impact damage to metals:

1. $D_h = 0$: cratering regime (no perforation)
2. $0 < D_h < D_c$: marginal perforation
3. $D_h \approx D_c >> d_p$: near-marginal perforation (particle severely disrupted)
4. $D_h > d_p > f$: penetration (particle disturbed)
5. $D_h \approx d_p >> f$: undisturbed penetration

---

[1] The impact energy for HC13 is greater than the ballistic limit but was not experimentally determined.

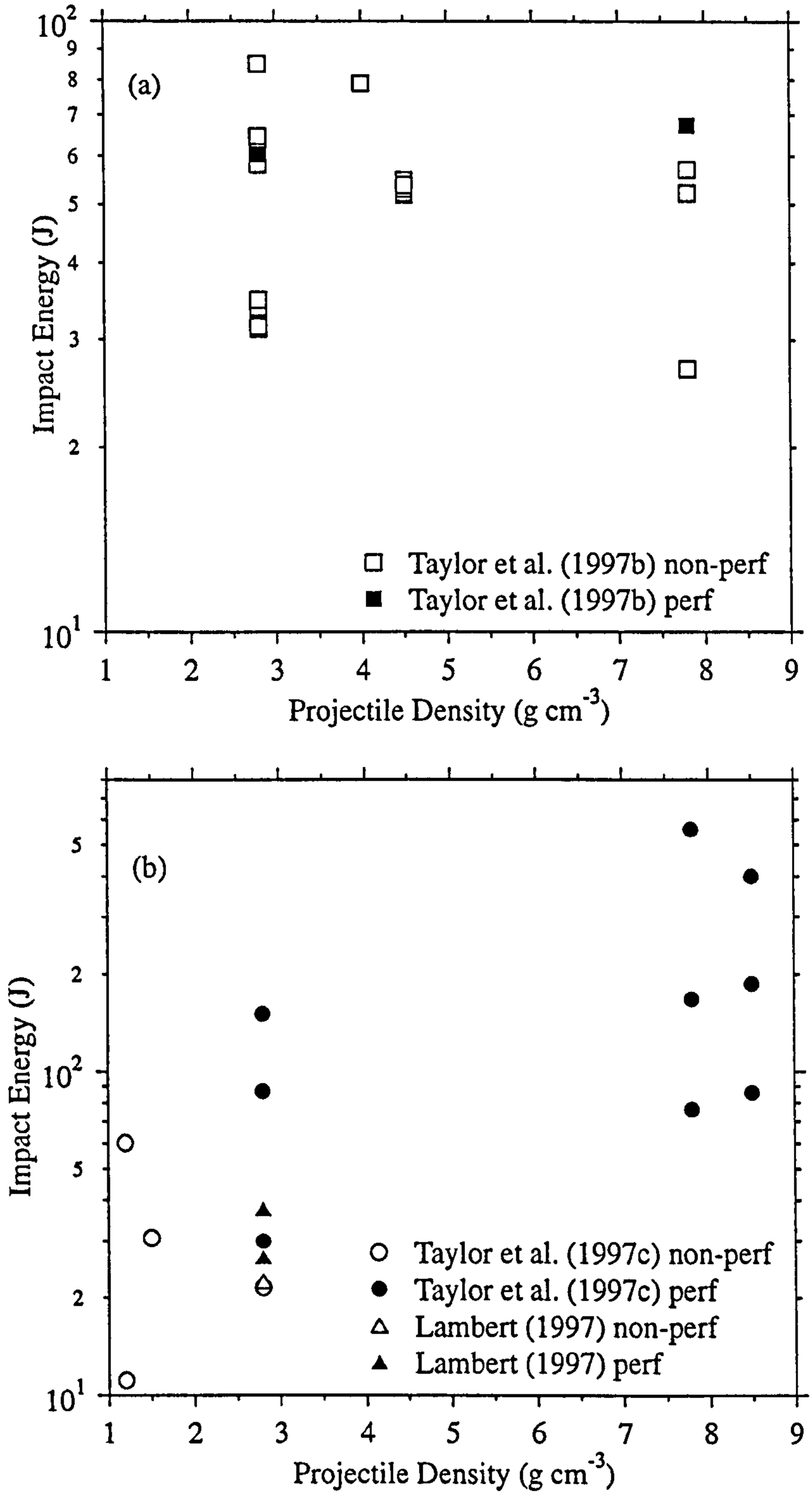

Figure 3-22. The dependence of ballistic limit on particle density and impact energy

(a) Oblique incidence impacts (b) Normal incidence impacts

Filled symbols signify perforating impacts, empty symbols signify non-perforating impacts.

If impact energy could be used as a indicator of penetration then all the perforating impacts would lie above a certain energy value for normal incidence impacts. This is not the case. Non perforating impacts occur at higher impact energies for oblique incidence shots.

Treating the top facesheet as a target in its own right, the hole size in composites ($D_{eq,f}$) is compared with the hole size in ductile materials (D_h). This will allow investigation of the hole growth in composites and also to determine whether a simple composite material scaling factor can be applied to ductile material damage equations. The hole size in a ductile material is derived using the empirically derived Gardner-McDonnell-Collier (GMC) hole growth equation (Gardner *et al.*, 1997), given in Eqs. 3-8 and 3-9.

$$d_p' = A\left(\frac{10}{9+e^{D_h'/B}}\right) + D_h'\left(1-e^{-D_h'/B}\right) \qquad (3\text{-}8)$$

where $d_p' = d_p/f$, $D_h' = D_h/f$,

$$A = 6.97\left(\frac{v\rho_p}{\sqrt{\sigma_t\rho_t}}\right)^{-0.723}\left(\frac{\sigma_t}{\sigma_{Al}}\right)^{-0.217} f^{-0.053} \qquad (3\text{-}9)$$

(and for v<6000 m s^{-1} and an aluminium target, B=(1.85 x 10^{-3}v) - 0.004. All units are SI except f (foil thickness) which is measured in microns.)

For this work, D_h is in the range 2.7-8.3 mm, d_p is between 0.8 and 2.0 mm and f is 1.6 mm, which gives a d_p/f range of 0.5-1.25. This ratio can be compared with the results in Table 9-1, and for similar ranges of d_p/f, penetration was achieved. The experimental tests have a foil thickness $f < d_p < f$ (partially in regime 4) and a hole size, $D_h > d_p$ (regime 4). Therefore, if a comparison with impacts on ductile materials can be made, the impact damage should fall into the 'marginal perforation category'. However, the ejecta plate damage shows signs of severe particle disruption (regime 3). It is thus clear that a direct analogy with ductile material response will not be possible. However, it is expected that, for large enough values of d_p/f, the projectile will behave in a manner analogous to metal-on-metal impacts, punching out the projectile diameter without disturbing the rest of the target.

For composites, cratering (Tennyson and Manuelpillai, 1994) and marginal perforation (Yew and Kendrick, 1987) have been observed, albeit with entirely different morphologies to metals. Due to the structure of composites, the craters are not smooth and there is typically more spallation damage to the rear surface than is observed in metallic surfaces (Cour-Palais, 1987). In this work, the projectile is severely disrupted by the top facesheet, but approaches penetration, as defined above. In Figure 3-23, the GMC equation is plotted for aluminium targets of equivalent density to the CFRP facesheet (using Eq. 3-8) to investigate hole growth in composites with respect to aluminium. Whilst the GMC predicted value is reasonably close for nylon projectiles, for high density projectiles the equation does not predict the hole size for high density impacts. Therefore, the variation in D_h with density is much more pronounced in CFRP than for an Al target (GMC prediction). This implies that a direct conversion factor cannot be applied for impacts onto composite sheets. However, it should be noted that the honeycomb may impede the hole growth in composites. Impact data

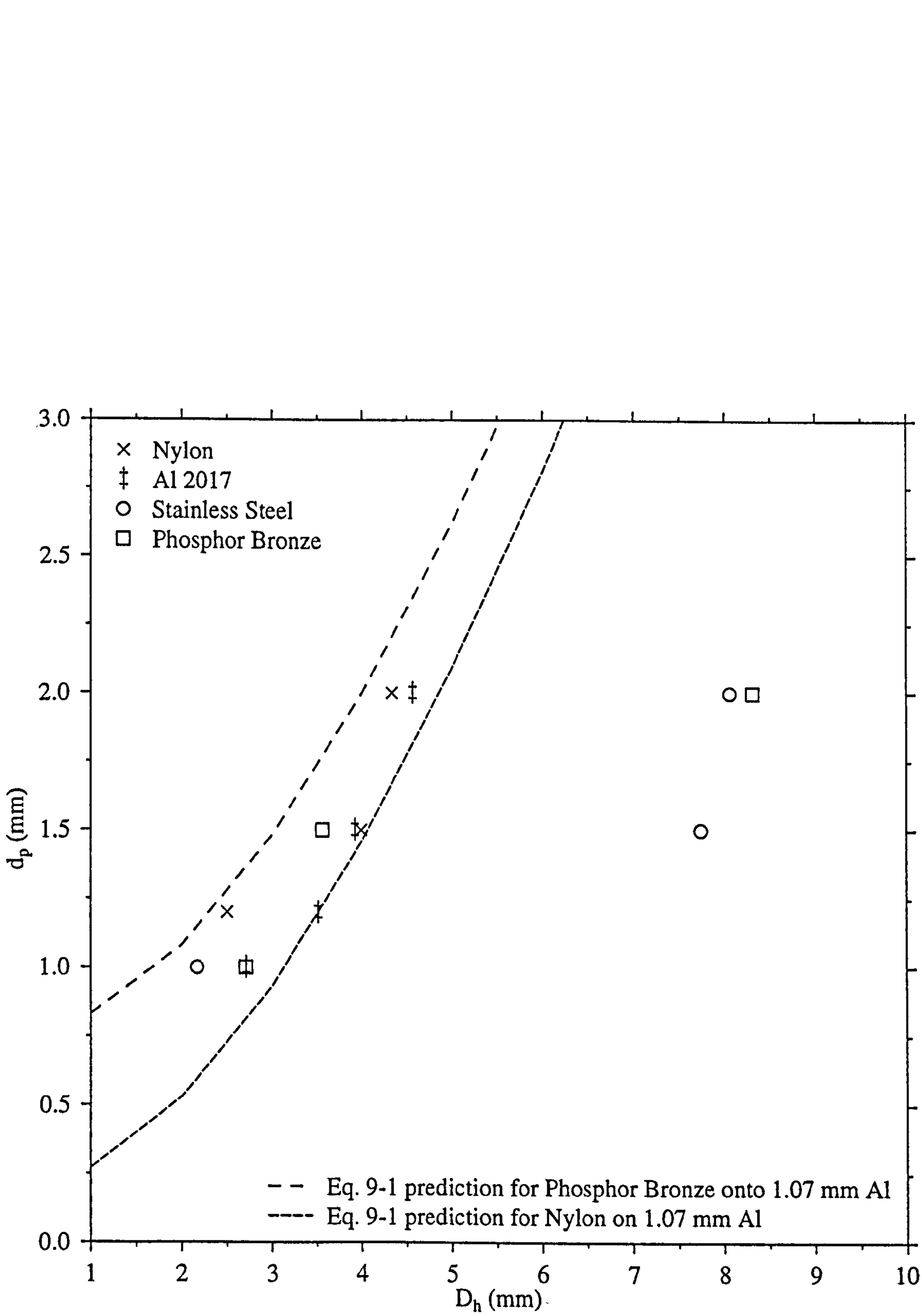

Figure 3-23. The hole size in composites (normal impacts) is compared to the hole size in ductile targets, as predicted by the Gardner-McDonnell-Collier equation (Eq. 3-8) for upper and lower projectile density bounds.

will be required over a large parameter range (velocity range = 1-20 km s^{-1} and d_p = 10-1000 μm) to determine the functional form over the different d_p/f regimes. However, the mechanisms governing hole expansion in CFRP plates (and thus the definition of a hole) will be different to the five regimes defined by Gardner *et al.* (1997).

3.6.3 Comparison with Al shields

Previous authors have published equations which can be used to define the optimum thickness for a dual wall, spaced Al shield. A dual wall equation (Christiansen, 1992) gives a d_p=1.2 mm at 5 km s^{-1} (aluminium projectile) to be the critical projectile diameter for rear wall perforation of a dual wall target with a 45 mm gap and wall thickness of 1.2 mm. 1.2 mm is the thickness of aluminium equivalent to the CFRP sheet density. Marginal perforation of the aluminium shield is in good agreement with CFRP experiment here (HC16, d_p=1.2 mm), but the work presented in the previous section suggests the CFRP hole growth above marginal perforation is not equivalent to aluminium. The possibility of an equivalence between CFRP/Al-HC honeycomb and spaced aluminium plates has previously been suggested, although only in the most general terms (Drolshagen and Borde, 1992). The form of the dual wall equation is such that a direct conversion cannot be attempted for our experimental data (above and below the ballistic limit) to an equivalent thickness of aluminium. No quantitative relationships have been tested for scaling between CFRP and aluminium. In view of the results presented here, the concept of scaling to an equivalent thickness aluminium bumper shield will require further investigation over a wide velocity range for composite/honeycomb structures, such as those studied here.

Considering the above points, the development of a damage equation as a function of impact energy is limited by the response of the honeycomb. Equating a CFRP/Al-HC system to two spaced Al plates cannot yet be achieved, and may not be possible due to: (1) honeycomb channelling, (2) differing hole growth for composites at hypervelocity impact, and (3) differing rear wall failure modes, once the ballistic limit has been reached.

3.6.4 Damage equations for CFRP/Al-HC

The impacts onto honeycomb can also be compared and scaled against impacts onto truss tubes (Christiansen, 1990). Truss tubes present a spaced composite 'plate' profile to impactors with diameters much less than the tube diameter. Eq. 3-10 was derived from an empirical fit to truss tube data. The total area A_t is defined by Eq. 3-11. The total equivalent hole diameter ($D_{eq,t}$) is then calculated using Eqs. 3-10 and 3-11.

$$A_t=A_f+A_r \tag{3-10}$$

$$D_{eq,t}\propto E^{1/3} \tag{3-11}$$

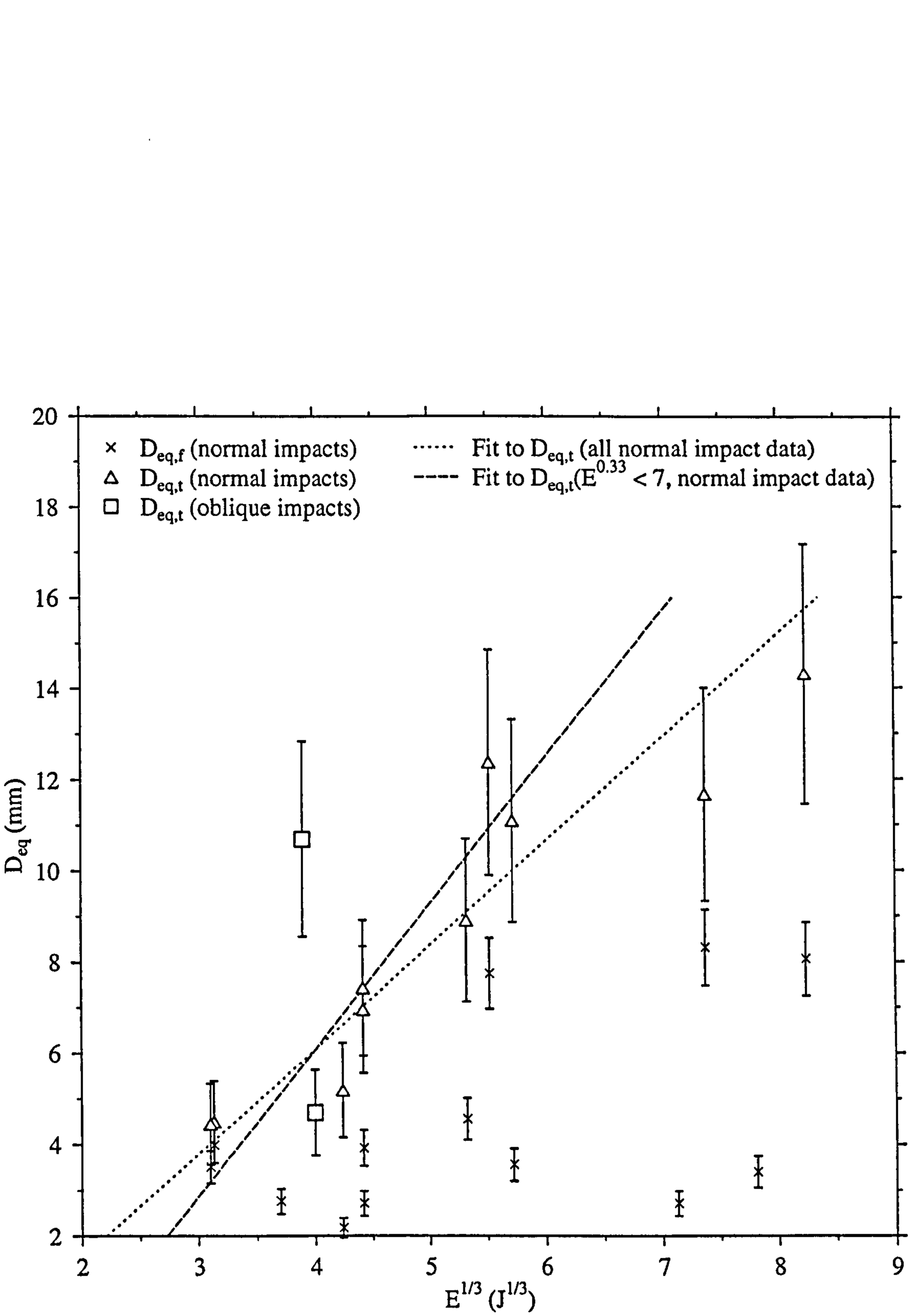

Figure 3-24. The relationship $D_{eq,t} \propto E^{0.33}$ (Eq. 3-11) is tested against honeycomb impact data for normal and oblique perforating impacts. In addition, $D_{eq,f} \propto E^{0.33}$ is tested against the front hole impact data for normal impacts. The least squares fits (Table 3-6) are plotted for normal impact data for a fit to all data and to data $E^{0.33} < 7$

This is shown in Figure 3-24, plotted against $\sqrt[3]{E}$, and a clear relationship can be seen in accordance with the predictions of Eq. 3-10. Eq. 3-11 can be applied to spaced composite plates and thus to the honeycomb targets used in this work. In Figure 3-24, a linear relationship is suggested for perforating impacts. There may also be a bimodal fit with the intersection occurring at impact energies of ~340 J. This result is similar to that derived from impacts onto truss tubes, where a bimodal fit to the data was also noted (Christiansen, 1990). A linear regression fit has been carried out to determine the value of the coefficients (y=mx+c) and the correlation coefficient (r^2) for (a) $D_{eq,t}$ (all normal impact data) (b) all impact data, including the two oblique shots) (c) $D_{eq,t}$($E < 340$ J) (d) $D_{eq,f}$ (normal shots). The results are given in Table 3-6. There is no clear evidence for a bimodal fit across this energy range as there is very little difference between the (a) and (b) fit results. However, there is no similar clear fit for $D_{eq,f}$. The channelling effect of the honeycomb (Gehring, 1970) may limit the scope of this scaling. Fits were carried out with equal weighting as the errors on the velocity measurement were the same for each shot and the equivalent diameter (D_{eq}) is a derived parameter therefore no measurement errors can be attributed to it, ruling out a weighted fit. A fit was not carried out including the oblique impact data due to time constraints on this thesis.

Table 3-6. Linear regression analysis of data in Figure 3-24

	gradient (m)	intercept (c)	r^2
(a) $D_{eq,t}$ (all data)	0.44 ± 0.06	1.33 ± 0.58	0.86
(b) $D_{eq,t}$ ($E^{0.33} < 7$ J)	0.31 ± 0.05	2.10 ± 0.42	0.96
(c) $D_{eq,f}$	0.40 ± 0.58	4.70 ± 2.82	0.04

3.7 Spacecraft Subsystems: Design Considerations

Three types of damage were observed on the target material:-

1. Primary damage (point of particle impact, usually marked by a hole which is often delaminated around the periphery).
2. Secondary damage (resulting from either primary damage or the secondary effects of the impactor(s) passage through the structure- honeycomb damage).
3. Tertiary damage (ejecta damage or freely suspended particles/contaminants resulting from primary and secondary damage. Observed on witness plates and from post-impact handling of the targets).

These three categories of damage can affect spacecraft subsystems in the following ways:-

Primary damage:-

1. Propulsion. Propulsion tanks are usually shrouded behind a second CFRP/Al-HC wall, therefore a penetrative strike with projectile remaining intact (high density projectile, d_p = 2 mm at 5 km s^{-1}) will not cause failure. However, the pipework is less well shielded.
2. Electromagnetic Compatability (EMC). A penetrative hole above a critical size (typically > 5 mm) may reduce the EMC. A reduction of the EMC may induce equipment performance degradation over spacecraft lifetime.
3. Thermal. No significant implications result.
4. Structure. Impacts are not likely to compromise the structural integrity in orbit.

Secondary damage:-

1. Structure. The damage to the HC core is unlikely to pose significant structural implications on-orbit. However, if the localised honeycomb damage is severe, distortion stresses initiated by thermal cycling effects over an orbital period may give rise to pointing inaccuracies for critical instrumentation.
2. Thermal. The honeycomb damage void potentially reduces the efficiency of the conductive heat flow path if the damage area is large enough.

Tertiary damage:-

A large number of contaminants are produced by hypervelocity impact. Non-vaporised debris could enter internal compartments or become ejected from the spacecraft. Internal contamination could potentially disrupt operation of unshielded electronics or harness. External contamination could result in suspended particulates around the spacecraft which may affect exposed optical surfaces and unshielded mechanisms.

In summary, two features of the ejecta, namely the wide spectrum of ejecta categories and the large total quantity of ejecta, are particularly relevant to spacecraft design. The generation of secondary or tertiary ejecta from impacts within the spacecraft interior is not considered to be a problem as the impact products appear to travel at sub-hypervelocity speeds. Direct contamination by ejecta is not considered a probable hazard as many spacecraft components tend to be mechanically shielded for thermal and electrical purposes. However, the generation of expanding clouds of low-velocity carbon fibre fragments may cause problems for unshielded electronics or mechanisms. There could also be a synergistic damage effect for combined perforation and fibre contamination.

3.8 Summary

A large data base of impact data on brittle materials has been presented and analysed (including data produced for this thesis). Plots of D_{co}/d_p and T_c/d_p versus velocity show a bifurcation in the data, where a steeper increase of the normalised conchoidal diameter or depth parameter with velocity is linked to a larger projectile diameter. This may be due to target size effects or a different mechanism operating for millimetre sized projectiles onto

brittle targets. A review of the pit profiles suggests that the response of quartz may be different to that of soda-lime glass and oligoclase. Also, millimetre-sized impactors may provide a different pit profile to micron-sized impactors. The onset of rear spallation does not appear to affect the D_{co}/D_{pit} pit profile for millimetre-sized impactors. For oblique impacts, the D_{co}/D_{pit} pit profiles for quartz at 30° and 60° show a much larger increase with velocity than the data for impacts on oligoclase. If both materials provided the same hypervelocity impact response then the values of D_{co}/d_p should be similar. This is not the case. Therefore, the response of quartz again may be different to that of soda-lime glass and oligoclase. Power law damage equations for both conchoidal diameter and depth of penetration are reviewed. The depth equations were developed for impacts onto fused quartz and fused silica, not borosilicate glass, and the conchoidal damage equations were identified to have included ductile materials in their data sets. The equations were compared against the data set. The McHugh and Richardson (1974) damage equation does not show any trends with size of over-prediction to under-prediction, unlike the Gault (1973) and Cour-Palais (1982) depth equations. Of the D_{co} damage equations, the Paul and Berthoud (1995) equation offers the closest correlation to the data over the whole range. The Fechtig *et al.* (1974) and Gault (1973) equations under-predict the experimental values by up to an order of magnitude for $D_{co} < 100$ μm. Bands, inclusive of 75, 90 and 95% of the data were calculated for the McHugh and Richardson (1974) and the Paul and Berthoud (1995) damage equations. These upper and lower bands are typically 0.8 and 2-3 times the equation predicted value for a particular set of impactor parameters. Therefore the damage equations do not predict the depth of penetration and conchoidal diameter to a high degree of accuracy. A review of the oblique impact data for oligoclase and quartz targets suggests a differing response to hypervelocity impact for the two target material types. The onset of rear spallation was found not to correlate with a published value, although a change in the gradient of T_c versus T_c/T suggests that there is a threshold for finite behaviour. Finally, the analysis of solar cell data showed that the impact data are similar for solar cell, soda-lime glass and oligoclase targets for pit profile (D_{co}/D_{pit}) and normalised conchoidal diameter (D_{co}/d_p) versus velocity.

In summary, the analysis presented in this chapter suggests that the use of quartz may not be appropriate for the development of a damage equation for use on solar cells. Oligoclase and soda-lime glass show a similar hypervelocity impact response (pit profile, oblique angle response) to solar cell impact data. Systematic trends with T_c and D_{co} were also identified in the damage equations, suggesting that further development might be required for application to solar cells. This will be presented in chapter 4.

Analysis of simple damage equations for composite materials show that the total equivalent hole diameter (for perforating impacts) shows a linear dependence on the cubed root of impact energy. The ballistic limit cannot be defined solely in terms of impact energy and

appears to be a more complex function of projectile diameter, density and velocity. The use of 'equivalent thicknesses' of aluminium may not be appropriate as a general conversion factor for CFRP facesheets to ductile target damage equations. The ejecta type and amount, characterised in terms of its subsequent damage potential, is a strong function of density, and a less strong function of projectile diameter. Ejecta production cannot be linked with rear hole diameter, limiting the development of a predictive ejecta type and amount equation.

The honeycomb increases the ballistic limit of the target for oblique impacts > 15°. The honeycomb damage area (cell bulge, burst and blast) is significantly larger than the projectile cross-section and is a function of impact energy. For highly oblique impacts, projectile ricochet occurs and the honeycomb cell damage is negligible. The development of a damage equation may be rendered difficult by the target repeatability under hypervelocity impact and will probably require several equations to predict the damage. The greatest risk to spacecraft operations will probably result from the significant ejecta production, both inside and outside the spacecraft. The total data set will be used to continue the search for a CFRP/Al-HC damage equation.

Chapter 4

4. Damage Equation Development

In chapter 3, the current suite of damage equations were assessed for their accuracy in predicting the impacted target parameters. The equations were found to predict the experimental data moderately well, but showed systematic over-prediction or under-prediction trends with projectile diameter. In this chapter, a number of assumptions used in the derivation of the published damage equations are examined closely, including:

(i) all brittle materials are considered to provide the same hypervelocity impact response to a set of impactor parameters,
(ii) the appropriateness of the least squares fitting technique for deriving power-law damage equations,
(iii) the damage equation parameters (D_{co}, T_c) have a similar definition across the range of impactor parameters, and
(iv) the simple scaling law form applied to ductile target damage equations can be used for brittle materials.

In this chapter, a range of possible explanations for the current conchoidal diameter damage equation performance are presented and, based on the results, a new soda-lime/borosilicate glass damage equation is presented for use on the HST and EURECA solar cells in the semi-infinite regime. The depth of penetration equations are also investigated.

4.1 Least Squares Fitting

The least squares fitting technique has been described by Lyons (1991). The method of least squares fitting is general and can be applied to a range of functions (linear and parabolic functions, harmonics and Fourier series and exponentials). Here, it is applied to a straight line derived by taking logarithms of Eq. 4-1, shown in Eq. 4-2. (D_{co}: conchoidal diameter, d_p: projectile diameter, v: velocity and Θ: impact angle taken from normal. α, β, γ, δ: constants)

$$D_{co}=Kd_p^{\alpha}\rho_p^{\beta}v^{\gamma}(\cos^{\delta}\Theta) \tag{4-1}$$

$$\log(D_{co})=\log K+\alpha\log(d_p)+\beta\log(\rho_p)+\gamma\log(v)+\delta\log(\cos\Theta) \tag{4-2}$$

$$S=\sum_i\left(\frac{a+bx_i-y_i}{\sigma_i}\right)^2 \tag{4-3}$$

The weighted sum of squares (Eq. 4-3) is the numerical quality factor for all the data points compared with the line. For a straight line fit ($y = a + b \times x$), a fitting program will minimise S and produce values for a and b. x_i, y_i are the observed values and σ_i, the standard deviation of the y_i value. The 'quality' of the fitted equation to the experimental data can be ascertained by a range of statistical techniques. The chi-squared test (χ^2) (Eq. 4-4) gives a measure of the goodness of fit between the experimentally recorded value and the predicted value (determined by using the parameters from the least squares fit). Another way of describing the chi-squared test is that it determines how well two parameters are correlated, in this case the experimental value and the equation-derived value. If the two are equal then the parameters are well correlated. (y_i: observed values, σ_i: standard deviation associated with y_i and $\bar{y}$ (y_{bar}) is the mean value over the whole data set.)

$$\chi^2 = \sum_i \frac{(y_i - \bar{y})^2}{\sigma_i^2} \qquad (4\text{-}4)$$

The Pearson product-moment formula (Croxton, 1953) (also known as the linear correlation coefficient, Press *et al.*, 1994) is given in Eq. 4-5, where x_i, y_i represent, in this case, the experimental and equation values respectively. The mean values (over the whole data set) are represented by $\bar{x}$ (x_{bar}) and $\bar{y}$ (y_{bar}). The formula returns values between -1 and +1, where 0 signifies that the values are uncorrelated, -1, negative correlation and +1 that there is perfect correlation between the two columns of data. A high (positive) value of r is a useful way of determining the strength of a correlation but is a poor statistic for determining whether there is a good correlation between two variables. The chi-squared test is used in addition to Eq. 4-5 to determine whether the variables are correlated. One most commonly used variant of Eq. 4-5 is the coefficient of determination (regression coefficient), r^2, which is the square of the Pearson product-moment formula. It varies between 0 and +1 and is generally a measure of how well the equation explains the relationship between the variables.

$$r = \frac{\sum_i (x_i - \bar{x})(y_i - \bar{y})}{\sqrt{\sum_i (x_i - \bar{x})^2} * \sqrt{\sum_i (y_i - \bar{y})^2}} \qquad (4\text{-}5)$$

4.2 Velocity Exponent (v^γ)

At the start of hypervelocity impact research in the 1960s it was not clear whether crater volume was a function of impact momentum or kinetic energy. Experimental tests determined that crater volume was proportional to kinetic energy. Therefore crater diameter (D_c) and crater depth (T_c) (assuming a hemispherical crater) were proportional to $v^{0.67}$. The

2/3 velocity exponent derived from this simple equation forms the basis for the depth equations and the starting point for D_{co} equation development.

The predicted values of the velocity exponents for D_{co} damage equation can be calculated using the McHugh data set (Table 3-1). This data set covers a wide range of velocities (6-16 km s^{-1}) for one projectile type (borosilicate glass, d_p = 48.1 μm) onto two target types (quartz and aluminosilicate glass). Therefore, it is ideal for an investigation of the velocity exponent and the influence of target type. Unfortunately, the conchoidal diameters were only recorded for impacts onto the quartz targets. The velocity dependence of the depth of penetration for both quartz and aluminosilicate glass is presented in chapter 5. Following the power-law formulation used by McHugh and Richardson (1974) and others for damage equation determination, there should be a linear dependence between $\log D_{co}$ and logv ($D_{co}=av^b$, $\log(D_{co})=\log a + b\log v$) which shows no dependence on target type.

In Figure 4-1(a), a log-log plot is presented of the velocity versus conchoidal diameter. A linear trend, with scatter is evident for impacts onto quartz. The linear trend for impacts onto quartz is not well defined (Figure 4-1(b)) and this is reflected in the correlation coefficient for the returned velocity exponent value of 0.32. The value of 0.67 is not supported by this result.

Table 4-1. Results of least squares fits to the McHugh data set. B/S : borosilicate glass. The experimental data are compared with the equation predictions in Figure 4-2.

Parameter	Data set	log a	b	r^2	number of data
D_{co}	B/S onto quartz	1.82	0.32	0.13	53

4.3 Projectile Diameter Exponent (d_p^{β})

The experimental shot programme reviewed in section 2.3 produced a data set which can be used to test the dependence of the conchoidal diameter, D_{co}, on the projectile diameter (d_p). The only variables that require consideration are the impact velocity (not all the impacts were at exactly the same velocity), the projectile diameter, the average value of D_{co} measured and the standard deviations of the conchoidal diameter data. The variation of the buckshot cloud impact velocity has been analysed in section 2.4 and, due to the negligible contribution to experimental error, does not need to be considered. Similarly, the variance in particle diameter (given in Table 2-2) is negligible, due to the low standard deviation of the size within the group of projectiles.

To carry out a least squares fit between projectile diameter and the conchoidal diameter, a velocity scaling has to be applied to the data. This is done by dividing the conchoidal diameter by an appropriate velocity scaling factor, v^{γ}. As the appropriate value of γ has not yet been confirmed, a value of γ = 0.7 has been chosen, based on previous damage

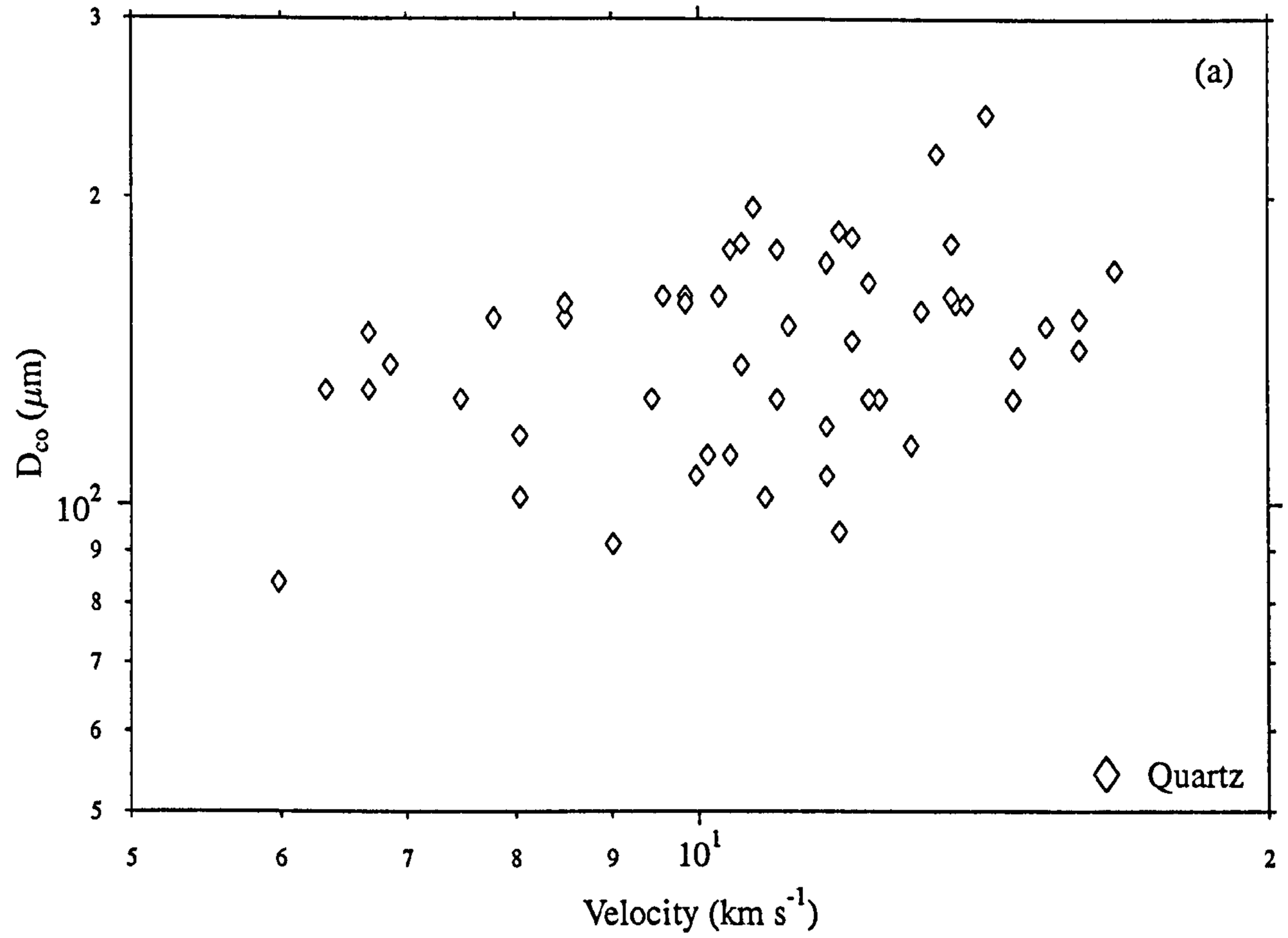

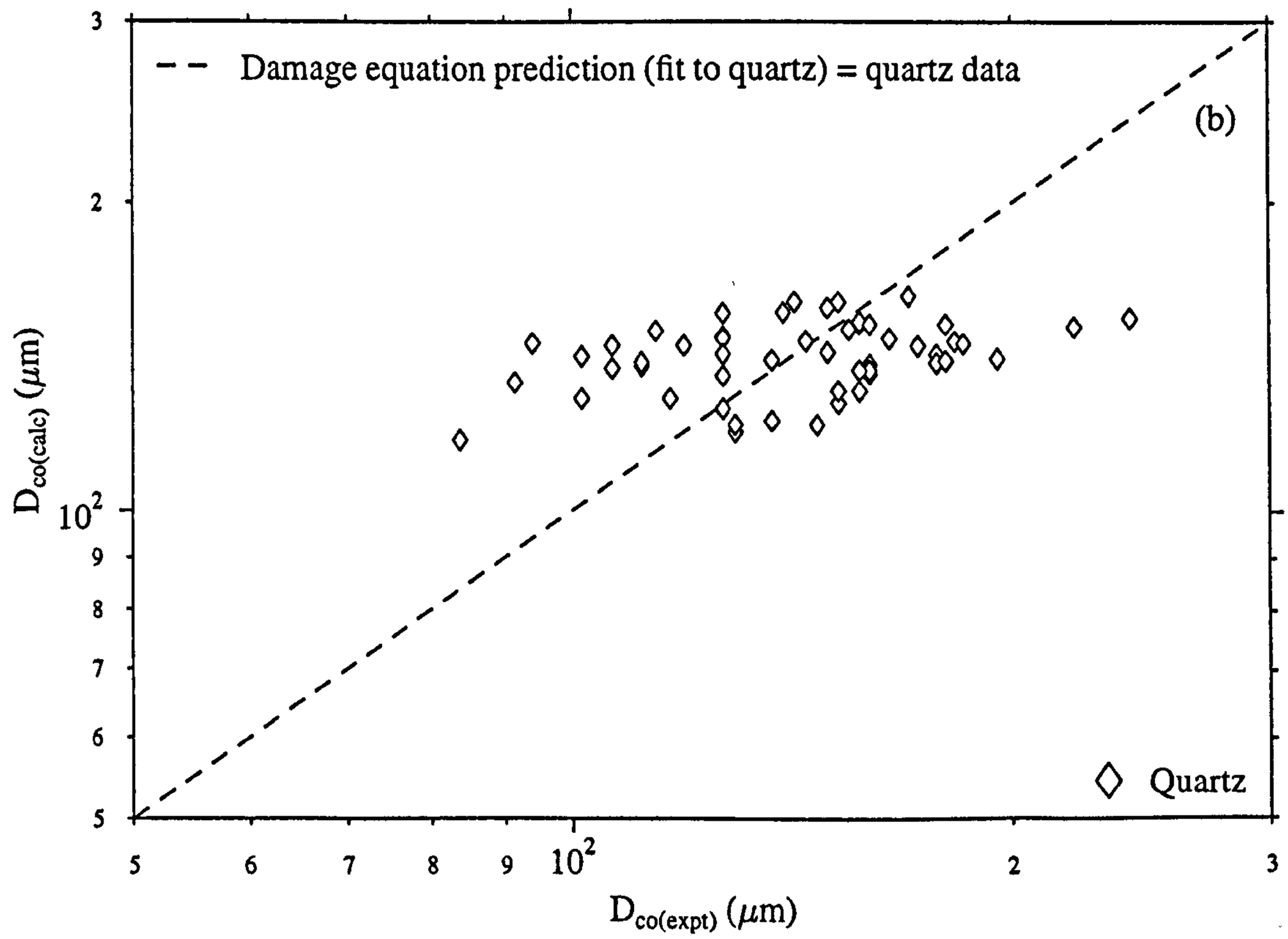

Figure 4-1. (a) D_{co} versus velocity for quartz (McHugh dataset) (b) Log-log plot of the least squares fit to quartz D_{co} measurements (Table 4-1). The dashed line corresponds to $D_{co(calc)} = D_{co(expt)}$

equations. There should be a linear dependence between log (D_{co}) and log (d_p) ($D_{co} = a(d_p)^b$, $\log D_{co} = \log a + b \log d_p$).

Table 4-2. The fits to data using weighted and unweighted data sets and four different fitting programmes. There is no difference between the weighted and unweighted fits using GNUPLOT. LINEST is in EXCEL. FITLS is from CGLE.

Fitting Programme	Normalised by $v^{0.7}$?	Weighted fit ?	log a	standard error	b	standard error	χ^2/ν	r^2
LINEST	yes	no	0.44	0.14	0.99	0.07	1.34	0.95
FITLS	yes	no	0.40	N/A	1.00	N/A	1.33	0.95
GNUPLOT	yes	yes	0.42	0.13	0.99	0.06	1.34	0.95
GNUPLOT	yes	no	0.42	0.13	0.99	0.06	1.34	0.95
LINEST	no	no	0.84	0.11	1.02	0.05	0.99	0.97
FITLS	no	no	0.84	N/A	1.02	N/A	0.99	0.97
GNUPLOT	no	yes	0.84	0.10	1.02	0.05	0.99	0.97
GNUPLOT	no	no	0.84	0.10	1.02	0.05	0.99	0.97

The results of four different fits (using different software) were carried out and are shown in Table 4-2 for both normalised and non-normalised data. The weighting applied was the reciprocal of the standard deviation of the distribution ($\sigma/\sqrt{(n-1)}$). The χ^2 statistics per degree of freedom ν (χ^2/ν) are lower than 1.5, showing a good correlation between the predicted and the experimental values of D_{co}. The values of r^2 (from Eq. 4-5) also show a good fit (r values are not presented because of the high correlation shown by χ^2/ν.

In Figure 4-2, the results of the least square fits given in Table 4-2 are plotted and compared with the experimental data. In Figure 4-2(a), the unnormalised values of D_{co} are plotted against d_p and the four fits are plotted. There is very little difference between the results of the four fits, whether weighted or not. In Figure 4-2(b) (D_{co} is normalised by $v^{0.7}$). The error bars are the standard errors.

The fit results in Table 4-2 show that the inclusion of the velocity exponent in the fit results does not produce a significant difference in the quality of the fit, confirming that, for a narrow band of velocities, the effect of velocity can be ignored. The standard errors produced for the values of log a and b range between approximately 5 and 25 % of the fitted value. This suggests that there is a limitation on how many decimal places the fitted equation predictions can be quoted to. Indeed, the use of more than one or two significant figures for log a and b is not appropriate.

4.4 Impact Angle Exponent ($\cos\Theta^{\delta}$)

The majority of space impacts are oblique and, when taking into account the pointing history of the spacecraft, analysis of the distribution of impact angles can be used to help in

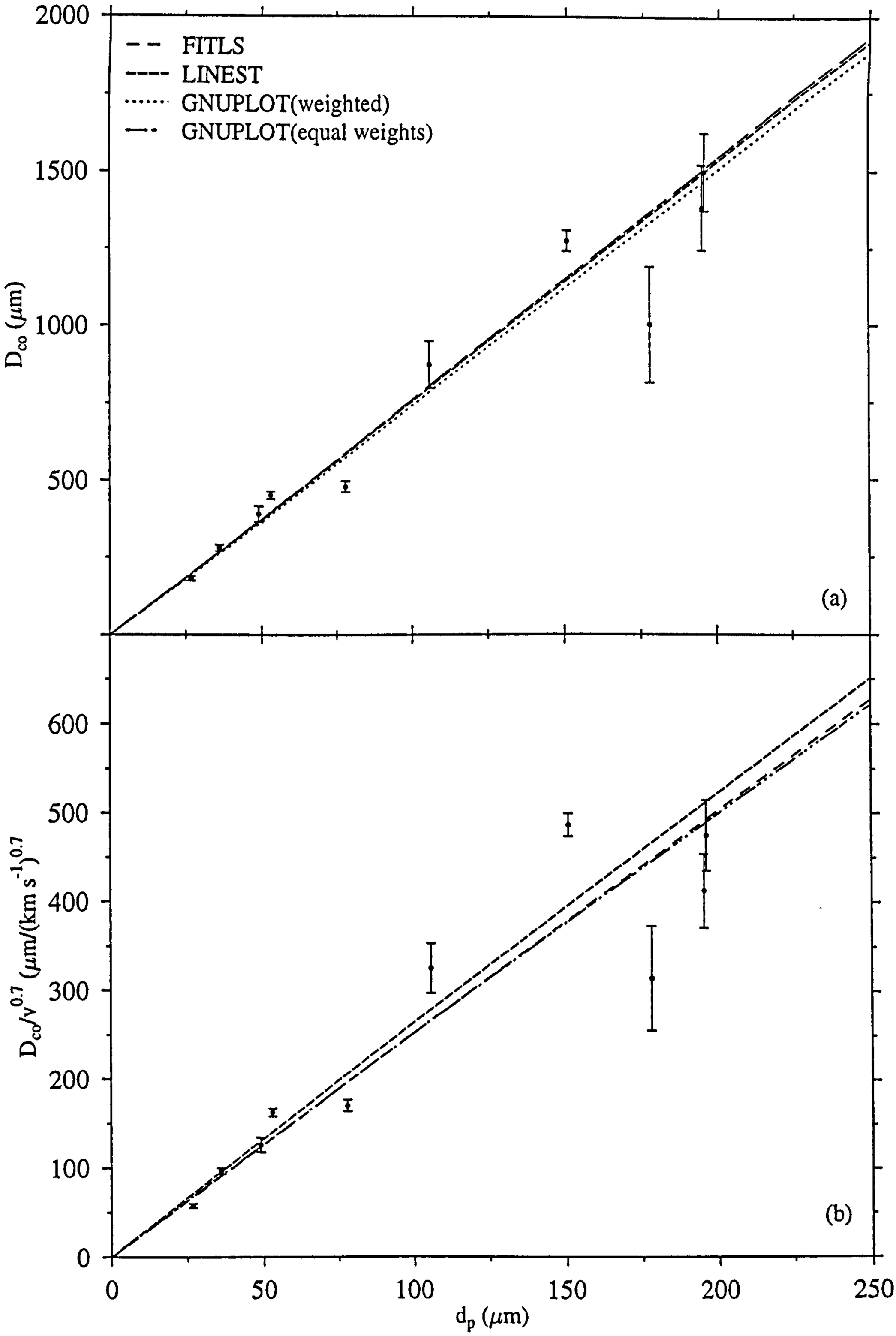

Figure 4-2. (a) D_{co} plotted against d_p compared to least squares fit results (Table 4-2)

(b) D_{co} plotted against d_p (normalised by $v^{0.7}$) , again compared to Table 4-2 fits.

The GNUPLOT weighted and equal weights fits are equal to 2 decimal places.

separating the natural and space debris populations, and the source of the natural populations (sporadics or stream meteoroids). D_{co} has been assumed to vary with cosΘ in the functional form, $D_{co}=a(\cos\Theta)^b$, where Θ is the angle from the normal, in previously published damage equations (section 3.3). An analysis of the change in morphology with impact angle was shown in Figure 2-9. The development of a cosΘ term is necessary for empirical damage equations. By taking logarithms of both sides, a linear dependence between $\log(D_{co})$ and log(cosΘ) is obtained ($\log D_{co} = \log a + b \log(\cos\Theta)$). A least squares fitting programme is applied to determine values of log a and b. A cosΘ exponent of 0.73 was derived by Shrine *et al.* (1996) (based on a fit to the combined data sets of glass and solar cells as the target response was the same within one standard deviation of each point) but no detailed statistical analysis was presented on the quality of the fit or the appropriateness of the cosΘ term.

The impact data used are given in Table 4-3. Not all the impact angles were covered for all the target materials (identified by 'no' and 'yes' in Table 4-3). Two additional shots from the glass buckshot programme (49 μm glass bead projectiles) described in section 2.3 were added to the data set. The impact velocities were contained within a narrow band 5.11±0.34 km s^{-1}, so all the shots were considered to have an identical impact velocity for the purposes of the least squares fit. The large number of impact sites per data point may be used to calculate a standard deviation from the spread in measured values. Therefore a weighted fit (using the reciprocal of the standard deviation to weight the data) can be carried out on the data sets. Three data sets were defined for fitting, incorporating (i) glass and solar cells, plus glass buckshot data, (ii) solar cells and glass, and (iii) solar cells only.

Table 4-3. Impact data used in the investigation of the cos Θ exponent. 'yes': data available. 'no': data not available.

Target	Data first published in	Θ=0°	30°	45°	60°	70°	75°
solar cell	Shrine *et al.*, 1996	yes	yes	yes	yes	yes	yes
glass	Shrine *et al.*, 1996	no	no	yes	yes	yes	yes
soda-lime glass	Taylor *et al.*, 1997d	yes	no	no	no	no	no

A morphological analysis of oblique impact shots onto glass shows that there is a change in crater shape at highly oblique impacts (Figure 2-9(a) compared with Figure 2-9(e)). This is probably due to the low value of the normal component of the impact velocity in the tests, resulting in a different mechanism of formation and thus, a different morphology. A survey of space impacts (typically impact velocities in the range 7-20 km s^{-1}) does not show the change in morphology (Shrine, 1997). Therefore, for the three classes of data, a fit was carried out for both the full range of impact angles (0-75°), and a reduced range (0-70°) based on the onset of the anomalous morphology.

Table 4-4. Least squares fits (weighted) to determine the value of the exponent for oblique impacts. (Units are microns and degrees for projectile diameter and impact angle respectively.)

Target	Θ (°)	log a	standard error	b	standard error	χ^2/ν	r	r^2	number of data
soda-lime+glass+ solar cell	0-75	2.65	0.03	0.92	0.09	0.66	0.94	0.89	14
soda-lime+glass+ solar cell	0-70	2.64	0.03	0.85	0.12	0.59	0.92	0.84	12
glass+solar cell	0-75	2.66	0.04	0.95	0.11	0.75	0.93	0.87	12
glass+solar cell	0-70	2.65	0.04	0.88	0.15	0.67	0.92	0.85	10
solar cell	0-75	2.64	0.02	0.83	0.07	0.20	0.97	0.94	7
solar cell	0-70	2.63	0.02	0.77	0.10	0.21	0.95	0.91	6

The values of the log a parameter were equal to within 1-2 % of the parameter value whilst the values of the b parameter ranged between 0.77 and 0.92. However, the error on the value of b was typically 10-15% and the highest and lowest values (0.92 and 0.77) overlapped within their error bars. The cosΘ exponent of 0.73 (Shrine *et al.*, 1996) was not determined from a linear fit based on logarithms of the data but from a power law fit ($D_{co} \propto \cos^b\Theta$) to the 0-70° data. The difference between 0.73 (Shrine *et al.*, 1996) and 0.77, determined from the same data set but via a different fitting route, suggests that the second and third decimal places, as given in Eq. 3-6, are not justified, given the variation in values produced by the different least squares fits.

The values of the linear correlation coefficient (r) are approaching 1 and indicate positive correlation between the equation prediction and the experimentally recorded value. The r^2 value is quoted as it is often used as a first assessment of the quality of the fit. As mentioned in section 4.1, r is a rather poor statistical parameter for determining whether an observed correlation is statistically significant. The χ^2/ν statistic provides a measure of the goodness of fit. All the values of χ^2/ν are below the threshold of 1.5 (discussed in section 4.1), but it is noted that, for the combined data sets that the 0-70° shots have a better correlation than the 0-75° shots. The values of χ^2/ν are very similar for both the 0-70° and 0-75° solar cell shots, and are the lowest of the six shots, suggesting that there may be a slight difference in target material response for the glass and the solar cells. In conclusion, it appears that solar cell and soda-lime glass can be grouped together for the purpose of least squares fitting. Also, the values returned for the cosΘ exponent range between 0.77 and 0.92 and, typically, have

a standard error of 0.10. Therefore, 1 significant figure is appropriate for use in a damage equation (0.80), with the option of applying an error of 0.10.

The experimental data, plus standard deviation error bars are plotted in Figure 4-3, along with the fits to data from Table 4-4, grouped by target type as described. In Figure 4-3(a) the data and fits to the full angle range of 0-75° are shown. The fits do not go through the 45° ($\cos\Theta = 0.7$) and 60° ($\cos\Theta = 0.5$) impact data points and the fit to the solar cell data passes within the error bars of four data points (compared with three points for the other fits). The glass data only cover the angle range 30-60° and generally overlie the solar cell data, except at 45°. In comparison, Figure 4-3(b) shows the fits to the reduced data range of 0-70°. Here, the three fits are very similar. The χ^2/ν values are the lowest for the fits to the solar cell data alone.

However, a further look at the data plotted in Figure 4-3, suggests that, instead of a power-law dependence between D_{co} and $\cos\Theta$, a linear relationship between the two variables may be appropriate. This is not inconsistent with the values of b returned from four of the six fits in Table 4-4 (0.92 ± 0.09, 0.85 ± 0.12, 0.95 ± 0.11 and 0.88 ± 0.15). The use of $\cos\Theta$ does appear to be currently the best approximation to the trends displayed by the value of D_{co}. Note however, that the value of D_{co} used is the geometric mean. It is possible that the value of D_{co}, along or perpendicular to the projected axis of flight, may yield more information or be more suited to a power-law derivation.

4.5 The Conchoidal Diameter D_{co}: A Unique Parameter ?

The D_{co} parameter has been assumed to be a single valued solution to a set of impactor parameters. Put simply, any variation in the measured value of D_{co} over a series of identical impact tests could be attributed to slight variations in experimental measurements of velocity, projectile diameter, or other parameters. The buckshot programme described in section 2.3 provides an opportunity to explore this. A distribution in D_{co} per shot has been identified and the mean and standard deviation have been calculated for each shot. In this calculation, only those data points produced by the spherical glass beads are used. The spread in velocity due to the buckshot cloud has been identified to be negligible (section 2.3), so only the standard deviation of the projectile diameter and the (average) measurement error on the impact velocity are used. The data and results are summarised in Table 4-5. The calculated standard deviation is always smaller than the measured standard deviation of the D_{co} impact sites. The measured standard deviation is between 2 and 12 times that of the calculated version, therefore an additional contribution to the random distribution of projectile diameters must be present.

Further confirmation of the spread in the impactor parameters can be obtained by considering the impact sites in the aluminium aperture plate placed in front of the glass target. The

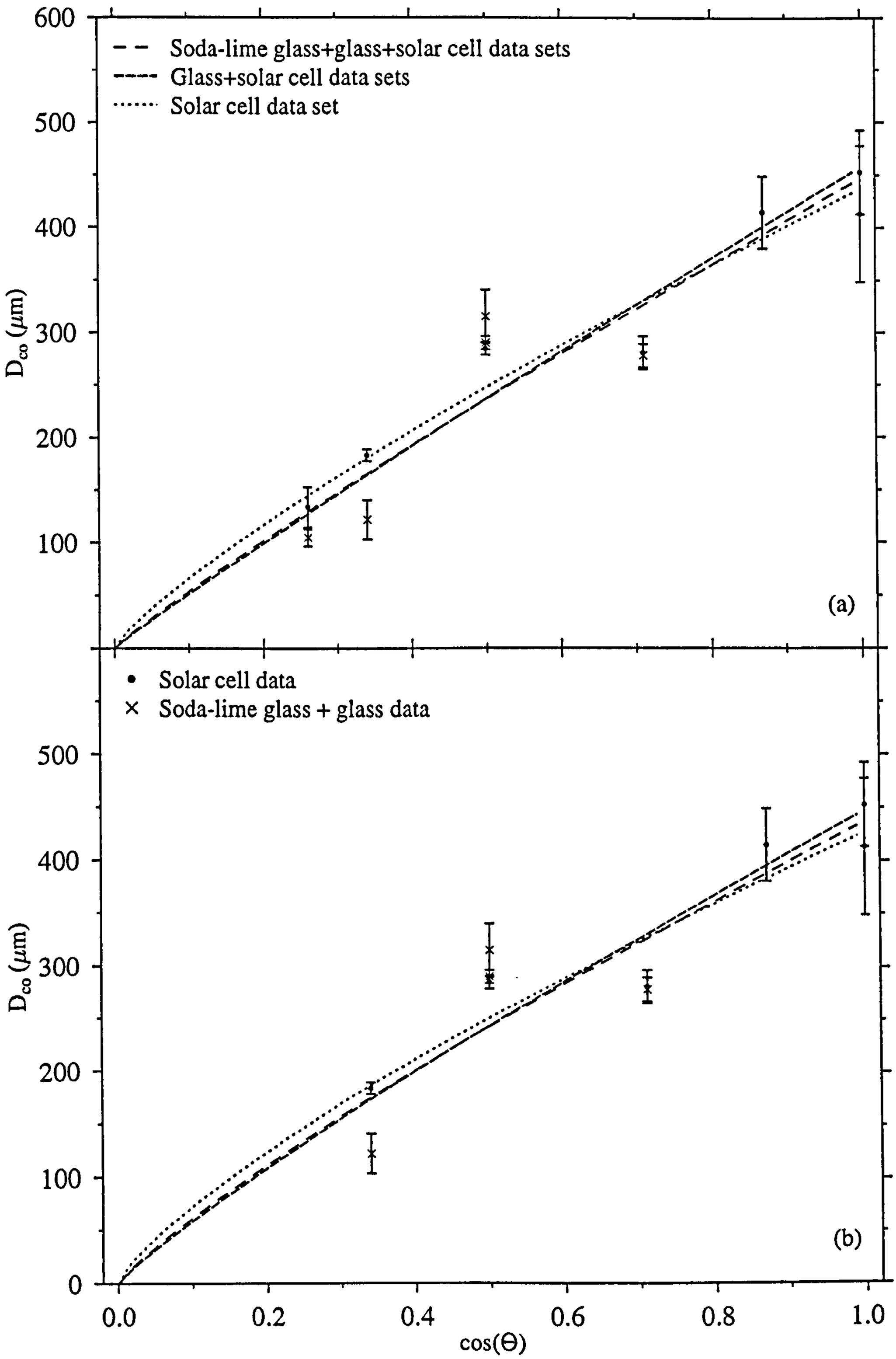

Figure 4-3. D_{co} plotted against cos(Θ) compared to fit results for three data sets for (a) 0-75 degrees (b) 0-70 degrees. Data sets: solar cell only, solar cell +glass and solar cell + glass + soda-lime glass. Data from Shrine et al., 1996 and Taylor et al., 1997d.

hypervelocity impact cratering of aluminium has been well characterised (Gardner, 1995). In Figure 4-4 a plot of the D_c (aluminium crater diameters) and D_{co} (glass conchoidal diameters) is presented. For each shot (at a particular projectile diameter), the width of the distribution is much greater for D_{co} than for D_c, again suggesting the more variable response of glass to hypervelocity impact. The error bars here are the standard deviation normalised by ($\sqrt{(n-1)}$); different numbers of impact craters were recorded on the aluminium plates compared with the glass targets. The greater width of distribution for glass may be due to the presence of microcracks (noted in section 3.4) which govern the direction which a radial crack grows (and thus the petaloid fragment which is spalled off to produce the conchoidal diameter, as noted by Glass (1972). The standard deviation varies between 7 and 30 % of the mean D_{co} value. The average is 20% of the mean D_{co}.

Table 4-5. Comparison of the impactor errors (standard deviation) with the error (standard deviation) calculated from the measured buckshot sites.

Shot ID	Vel. (km s^{-1})	Error (%)	d_p (mean) (μm)	d_p (st.dev.) (%)	D_{co} (mean) (μm)	D_{co} (st.dev.) (calc) (μm)	D_{co} (st.dev.) (expt) (μm)	expt/ calc
GBS13	5.14	2	26.7	3.9	181.4	8.2	37.7	4.61
GBS12	4.61	2	36.1	2.4	280.6	8.4	47.2	5.63
GBS06	4.31	2	53.0	1.5	451.0	9.8	60.6	6.21
GBS11	4.41	2	77.9	1.3	479.1	9.6	48.4	5.04
GBS07	4.10	2	105.8	1.9	871.8	21.9	263.5	12.02
GBS18	3.97	2	150.9	4.6	1273.9	66.9	155.7	2.33
GBS17	5.26	2	178.1	3.2	1002.8	38.0	266.3	7.01
GBS15	5.63	2	195.2	2.8	1381.9	46.8	N/A	N/A
GBS14	5.14	2	292.7	2.1	2354.9	63.6	165.5	2.60

A more quantitative assessment of the variability can be obtained by plotting the glass standard deviation divided by the mean of the measurement against the same ratio for the aluminium. Note that both the mean D_c or D_{co} and the standard deviation have errors attached to them. These errors are calculated by noting that the error of the mean is simply the standard error ($\sigma/\sqrt{(n-1)}$) and the fractional error on the standard deviation is ($1/\sqrt{(2n-2)}$) (Lyons, 1991). The results are plotted in Figure 4-5 and show that for all the data, the variability of glass is greater than or equal to the aluminium. A more detailed analysis is presented in Taylor *et al.* (1998).

4.6 Target Type-Dependent D_{co} Damage Equation

The assumption that all brittle materials provide an identical response to hypervelocity impact is implicit in the published brittle material damage equations (section 3.3). The review of brittle material (i) pit profiles, (ii) oblique impact response, (iii) depth of penetration and

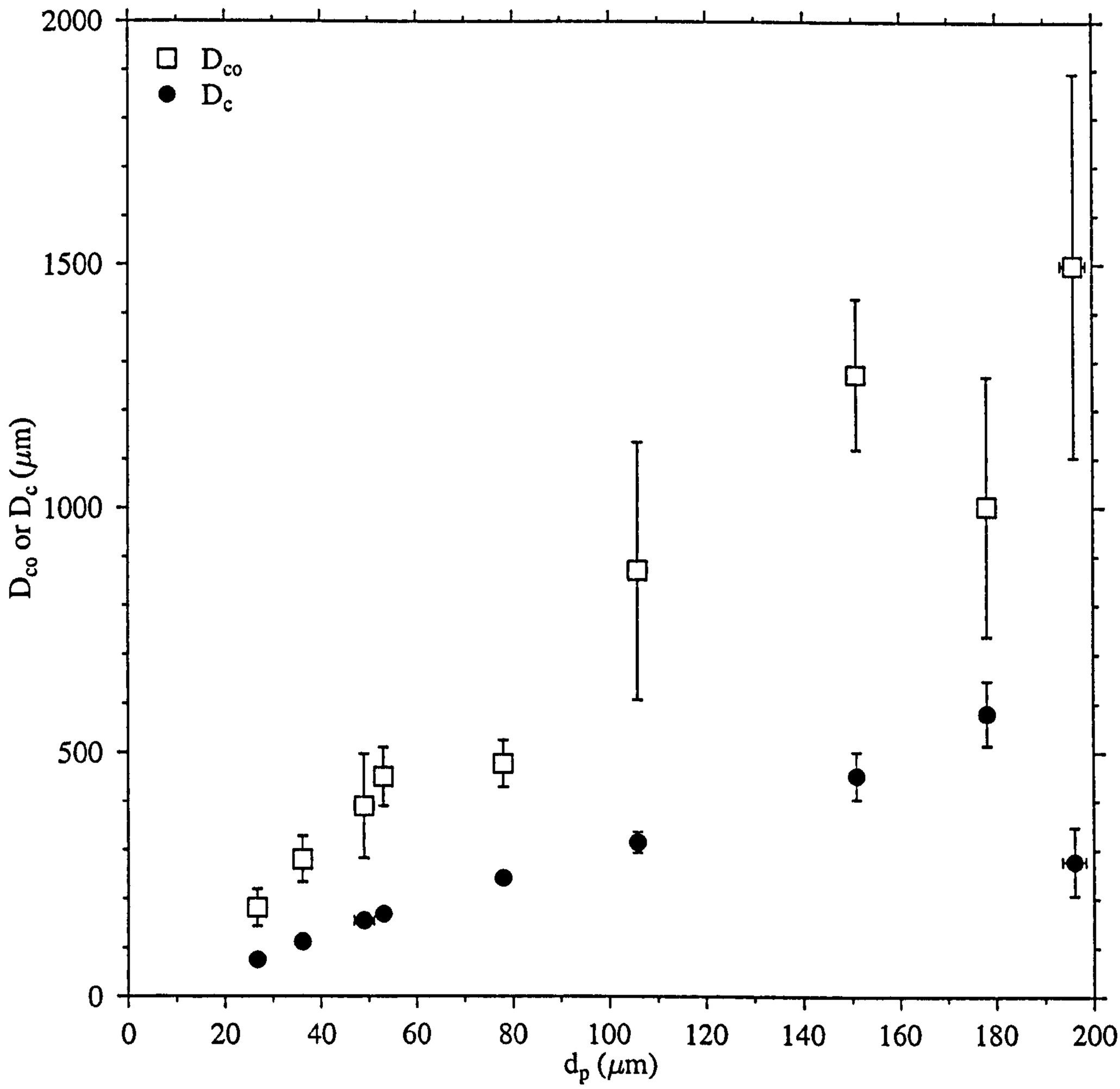

Figure 4-4. D_{co} (glass) and D_c (aluminium) buckshot data plotted against d_p. Errors shown are the standard deviations of the observed crater/conchoidal diameters and projectile diameters.

onset of rear spallation, and (iv) damage equation prediction as a function of target type in chapter 3 suggested that not all brittle materials provide the same response to hypervelocity impact. Also, the variability of the target material may prevent a good fit to the least squares fitting programme, as suggested in section 4.2 (for quartz) and investigated in section 4.5 (for soda-lime glass).

The suggested difference in brittle material hypervelocity impact response can be tested by carrying out least squares fits to the data from Tables 3-1 and 3-2. Firstly, a least squares fit to determine the conchoidal diameter as a function of projectile velocity, impact angle, diameter and density (Eq. 4-1) is carried out. A combined data set is used, comprising lunar rock, quartz, soda-lime glass and solar cell targets. The results are shown in Figure 4-6 and Eq. 4-6. The values of the coefficients are not in agreement with those of Eqs. 3-4 to 3-6 (also summarised in Table 4-6), despite the high value of r^2 (0.96). The results of this least squares fit may be due to the different brittle material target types included in the data set. Therefore, in this section, the data are divided into target types and the least squares fit technique applied to determine the values of the exponents in Eq. 4-1. Rewriting Eq. 4-1 with the numerical values of the exponents obtained by the fit to the combined data set results in Eq. 4-6.

$$D_{co}=10^{0.12}d_p^{1.24}\rho_p^{0.57}v^{0.25}(\cos^{0.45}\Theta) \qquad (4\text{-}6)$$

Four target types are defined (i) lunar rock analogue material e.g. oligoclase (ii) quartz and fused silica (iii) soda-lime glass targets and (iv) soda-lime glass and solar cell (borosilicate glass) targets. The results of section 4.4 suggest that soda-lime glass and borosilicate coverglass provide similar responses to hypervelocity impact. The results of the least squares fits to (i), (iii) and (iv) are shown in Table 4-6 and show good agreement with Eqs. 3-4, 3-5 and 3-6. The results of the fits are numbered as Eq. 4-7, 4-8 and 4-9 (units are: km s^{-1} (velocity), g cm^{-3} (density) and μm (projectile diameter and conchoidal diameter)). Note also the exponent value of cosΘ produced by the least squares fit to soda-lime glass. It is in good agreement with the exponent value given in section 4.4, which was derived from impacts onto soda-lime glass and borosilicate glass (solar cells).

In contrast to the results of the least squares fit to all the brittle material data, producing Eq. 4-6, the results of the least squares fits to categories (i), (iii) and (iv) are similar to the values published in Eqs. 3-4 to 3-6. Therefore, the least squares fitting method can produce 'reasonable' exponent values, when given an appropriate data set as input. In particular, the Eq. 3-4 exponents are broadly reproduced by the values of Eq. 4-7. Differences can be explained by the use of ductile materials in the original data set for Eq. 3-4.

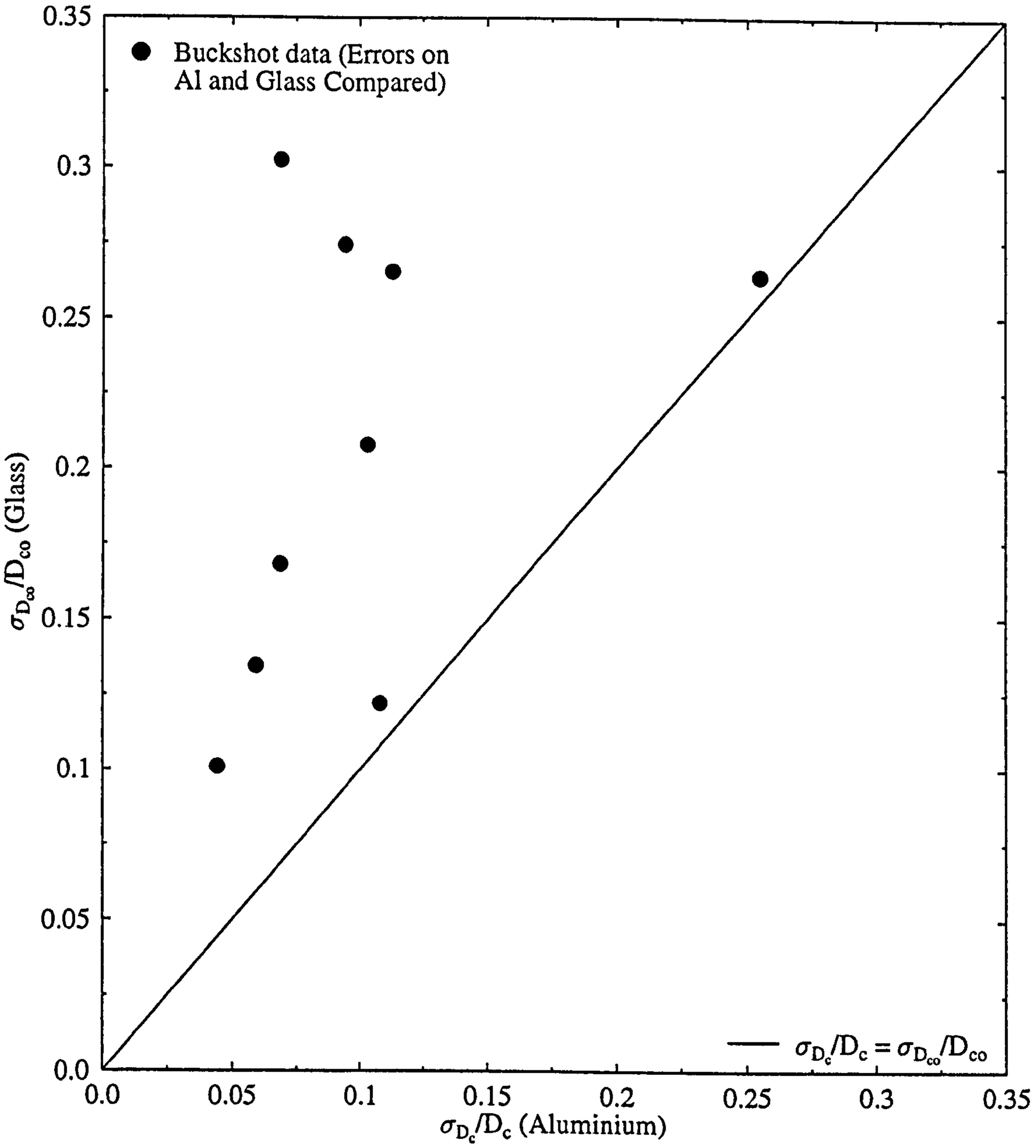

Figure 4-5. The ratio standard deviation/crater mean is plotted for each shot onto glass and aluminium. The line signifies that the crater variability is equal for glass and aluminium. Above this line, glass is more variable. Below, the aluminium is more variable.

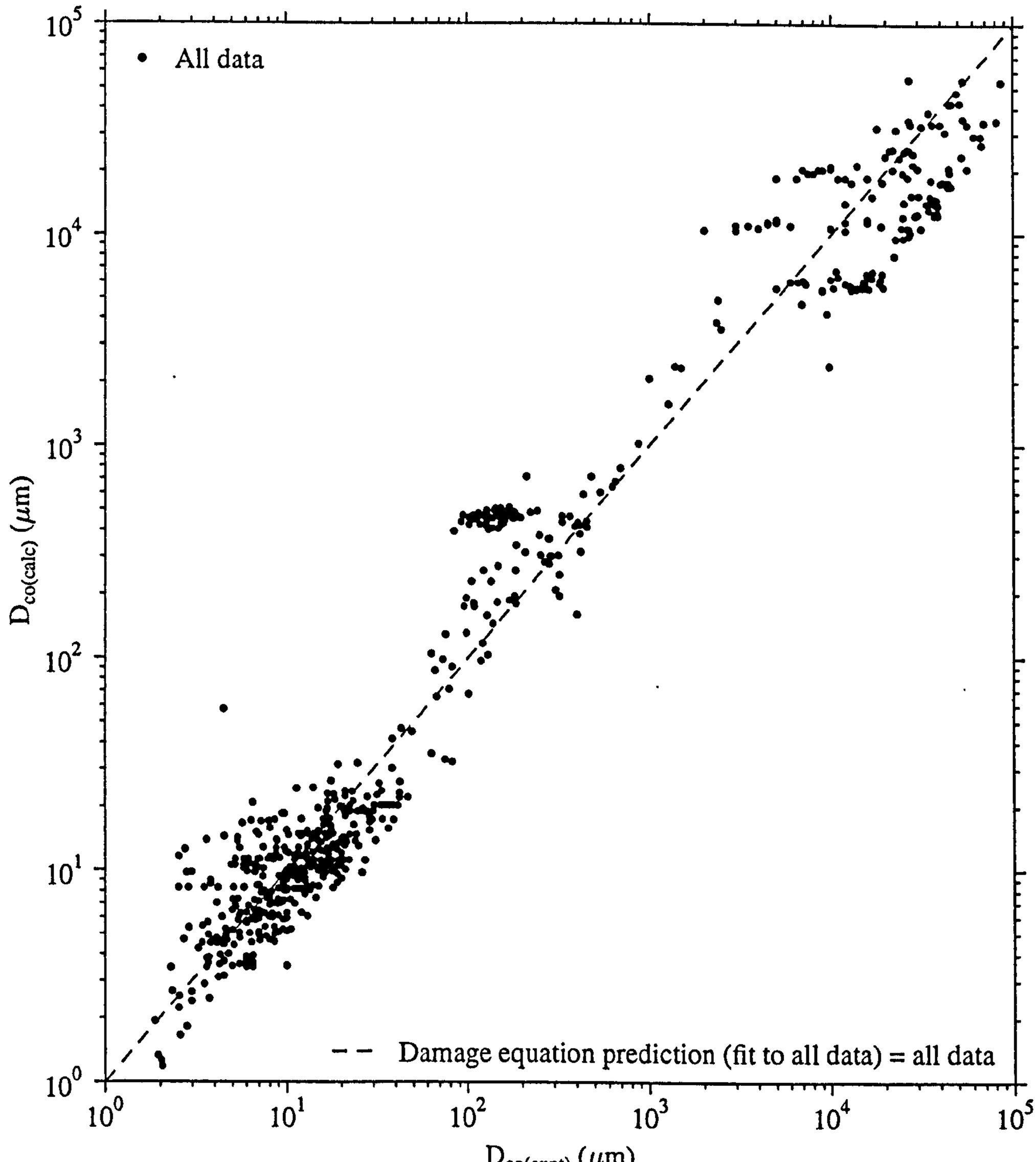

Figure 4-6. Log-log plots of the brittle material damage equation (Eq. 4-6) derived from a least squares fit to all brittle data. The dashed line corresponds to $D_{co(calc)} = D_{co(expt)}$

However, the results of the fits to quartz (summarised in Table 4-7) do not show similar exponent values to the equation described in chapter 3. Different dimensional regimes were chosen to investigate whether there might be some dimensional effect in the quartz response to hypervelocity impact. From the results of the least squares fits given in Table 4-7, it appears that the hypervelocity impact response of quartz is different to that of soda-lime glass and shows a great deal more scatter.

A log-log plot of experimental data versus the equation prediction provides a first glance at the results of the least squares fit. In Figure 4-7, the experimental data (quartz and lunar rock analogues) are plotted against the equations derived from a least squares fit to the lunar rock and quartz (full projectile range) data sets. The two further fits over a reduced projectile diameter range (Table 4-7) are shown in Figure 4-8. Figure 4-9(a) shows the soda-lime glass data set against the soda-lime glass damage equation. In Figure 4-9(b) the solar cell data are overlaid, and it can be seen that they also correspond well with the equation predictions. Similarly, Figure 4-10(a) plots the soda-lime glass and solar cell damage equation against the source data set, and in Figure 4-10(b) the solar cell data set is highlighted, again showing good correlation with the experimental damage equation.

Table 4-6. Results of least squares fit to lunar rock (Eq. 4-7), soda-lime glass targets (Eq. 4-8) and the soda-lime glass and solar cell combined data set (Eq. 4-9) compared with published damage equations (Eqs. 3-4, 3-5 and 3-6).

Exponent value (Eq. 4-1)	Eq. 3-4	Eq. 3-5	Eq. 3-6	Lunar rock (Eq. 4-7)	Soda-lime glass (Eq. 4-8)	Solar cell +SLG (Eq. 4-9)
γ (v, velocity)	0.74	0.754	0.727	0.63±0.06	0.75±0.07	0.66±0.07
β (ρ_p, projectile density)	0.54	0.71	0.784	0.57±0.06	0.44±0.04	0.44±0.05
α (d_p, projectile diameter)	1.11	1.13	1.076	1.18±0.02	1.28±0.01	1.28±0.01
δ (cosΘ, impact angle)	0.86	-	0.601	0.75±0.13	0.87±0.13	0.62±0.06
log(K)	0.03	-0.05	0.03	-0.21±0.07	-0.29±0.07	-0.21±0.07

Table 4-7. Fits to quartz over three projectile size ranges. The equation predictions are compared with the experimental data in Figures 4-8 and 4-9.

projectile size range (μm)	α	β	γ	δ	r^2
1-1250	-0.24	0.65	1.31	0.37	0.96
1-50	0.08	0.52	0.82	0.50	0.90
1-10	0.44	0.68	1.35	0.60	0.69

A check on the statistical significance on the fit can be determined by calculating χ^2 and the ratio χ^2/ν, as well as r and r^2. The usefulness of these statistical measures has already been

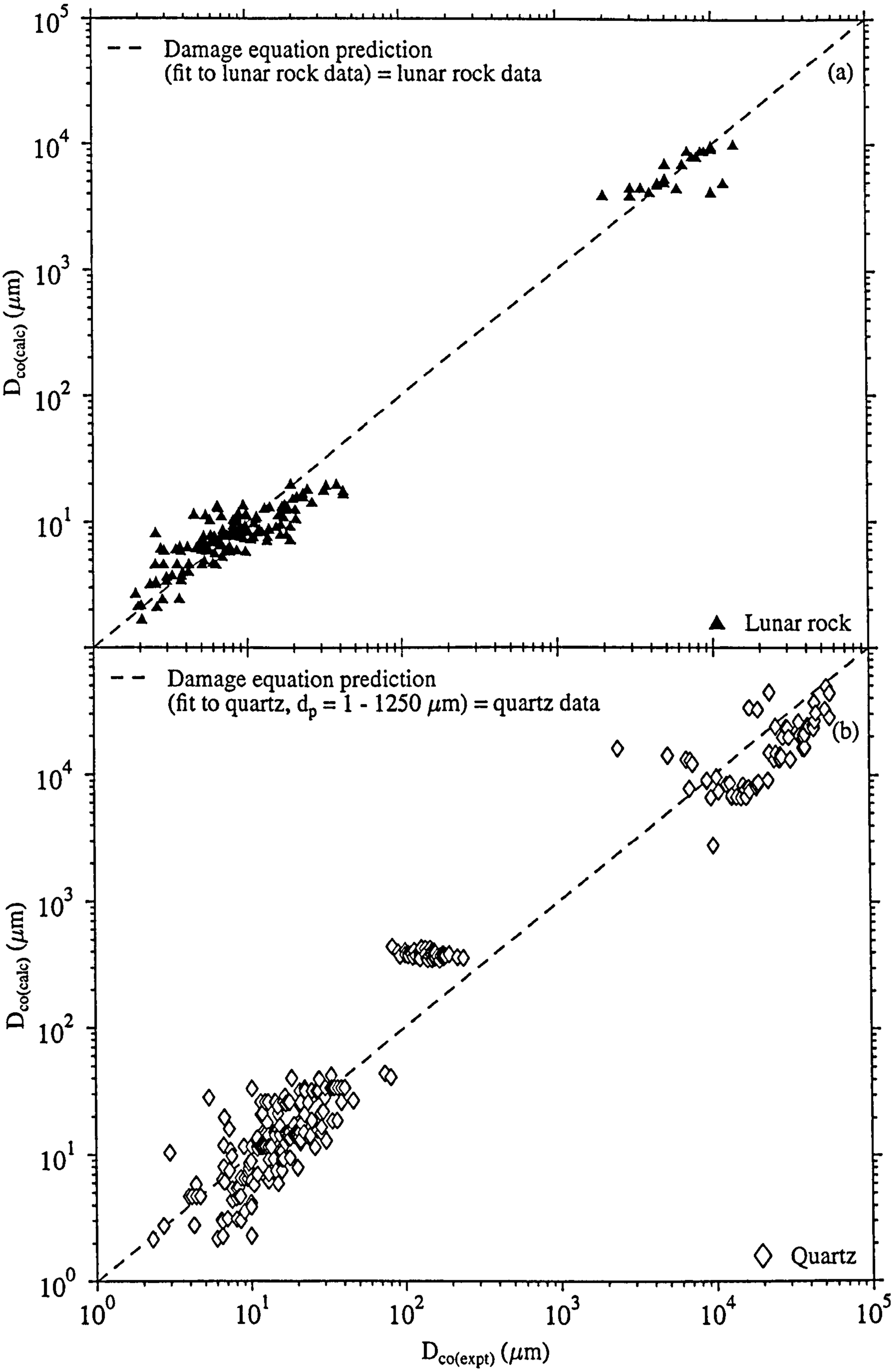

Figure 4-7. Log-log plots of (a) lunar rock (Eq. 4-7) (b) quartz damage (Table 4-7) equations (d_p = 1 - 1250 μm) versus experimental data for lunar rock and quartz, respectively.

The dashed line corresponds to $D_{co(calc)} = D_{co(expt)}$.

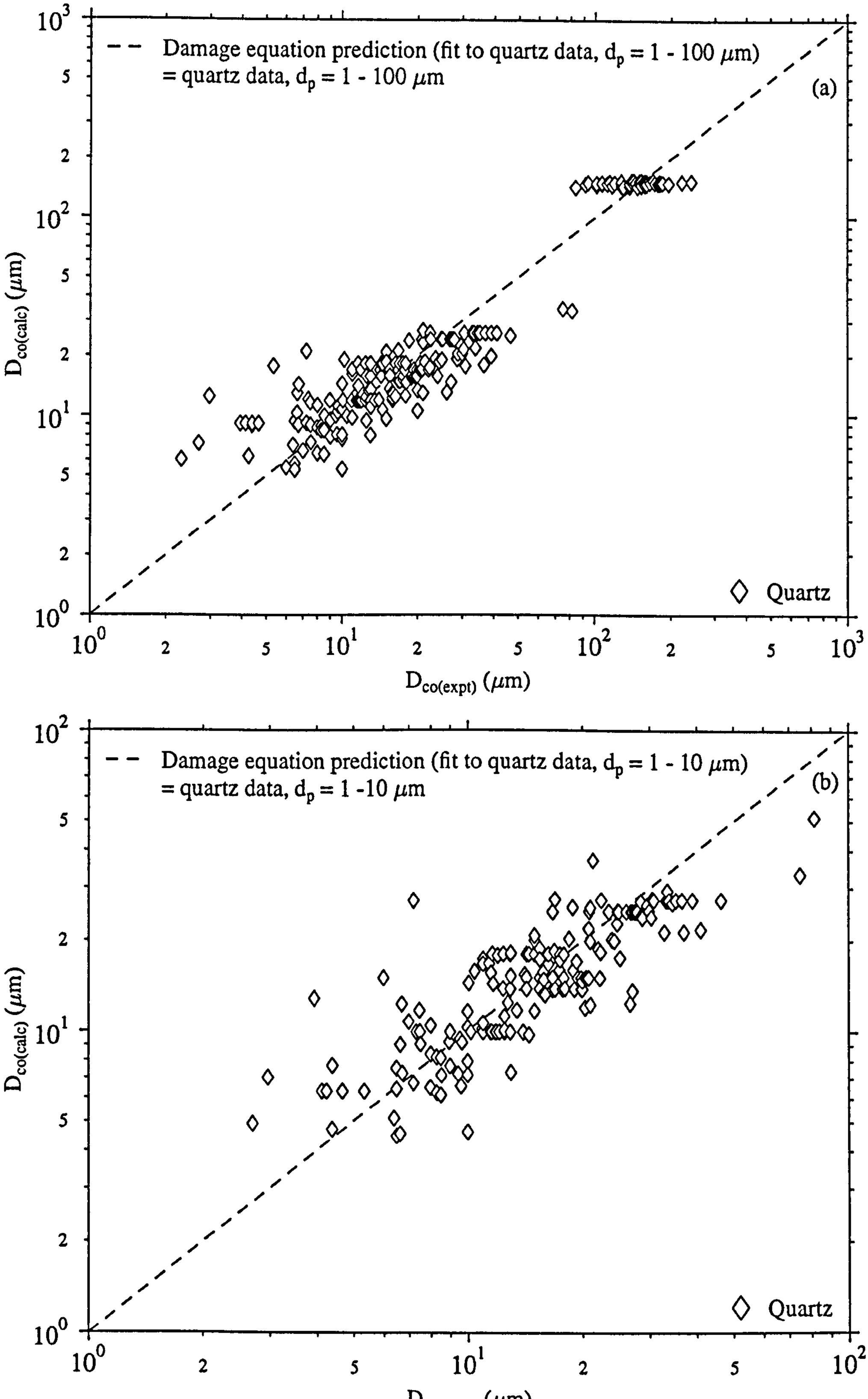

Figure 4-8. Log-log plots of empirically fitted quartz damage equations versus their source data sets (a) d_p = 1 - 100 μm (b) d_p = 1 - 10 μm (Table 4-7). The dashed line corresponds to $D_{co(calc)} = D_{co(expt)}$.

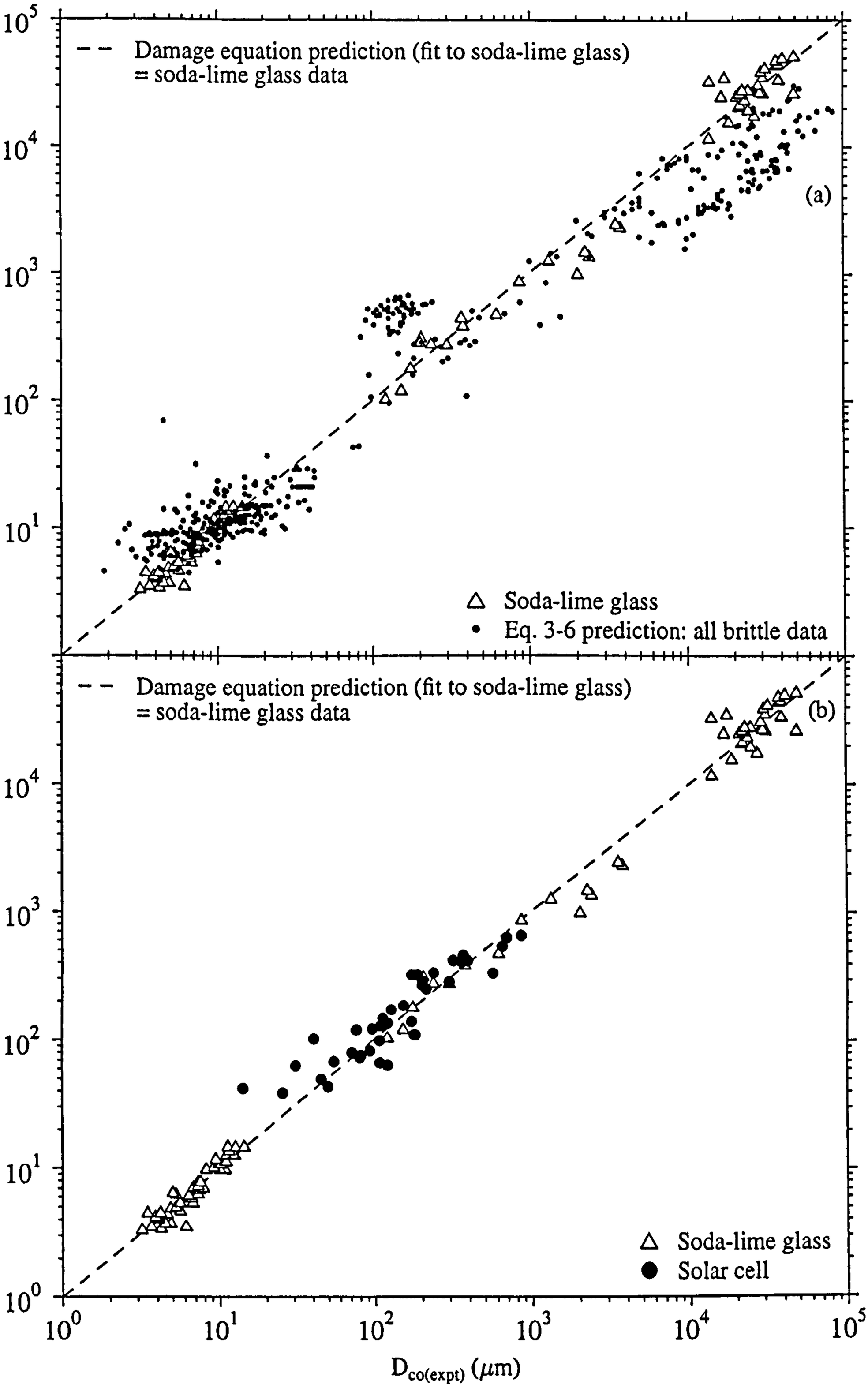

Figure 4-9. Log-log plots of the soda-lime glass damage equation (Eq. 4-8)(a) compared to the soda-lime glass data set and (b) compared to the solar cell (borosilicate coverglass) data. (a) Eq. 3-6 is plotted for comparison. The dashed line corresponds to $D_{co(calc)} = D_{co(expt)}$

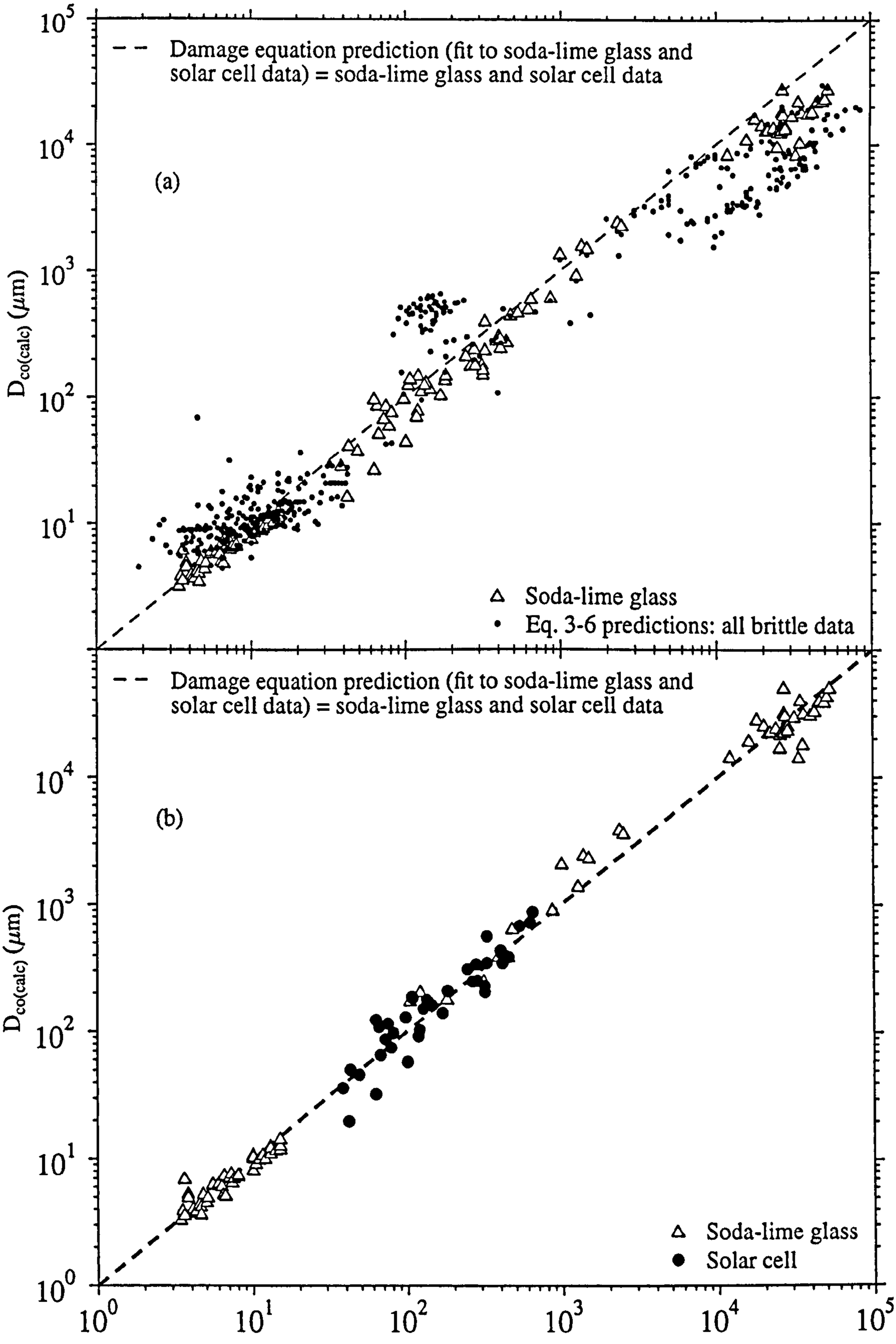

Figure 4-10. Log-log plots of the soda-lime glass damage equation (Eq. 4-9), (a) compared to the soda-lime glass data set and (b) compared to the solar cell (borosilicate coverglass) data. In the upper figure, the Eq. 3-6 predictions are plotted for comparison. The dashed line corresponds to $D_{co(calc)} = D_{co(expt)}$.

outlined in section 4.1. The analysis is carried out for (i) lunar rock analogue materials (Eq. 4-7), (ii) soda-lime glass (Eq. 4-8), (iii) soda-lime+solar cell (Eq. 4-9), (iv) Eq. 3-6 (based on solar cell, soda-lime glass, lunar rock analogues and quartz), (v) solar cell data predicted by Eq. 4-8 (vi) solar cell data, predicted by Eq. 4-9, and (vii) solar cell data predicted by Eq. 3-6. The results are given in Table 4-8. The average value of the standard deviation of 20% (section 4.5) is applied to all the data, to produce values for the χ^2/ν test. Eq. 4-8 better reproduces the full range of soda-lime glass D_{co} values than Eq. 3-6. Eq. 3-6 used quartz in its data set and quartz has been shown to have a different response to hypervelocity impact. However, Eq. 3-6 produces a better fit to the solar cell data than Eq. 4-8. Eq. 4-9 provides the best fit to solar cell data and will be the new soda-lime glass/solar cell damage equation.

$$D_{co}=10^{-0.21}d_p^{1.18}\rho_p^{0.57}v^{0.63}(\cos^{0.75}\Theta) \qquad (4\text{-}7)$$

$$D_{co}=10^{-0.29}d_p^{1.28}\rho_p^{0.44}v^{0.75}(\cos^{0.87}\Theta) \qquad (4\text{-}8)$$

$$D_{co}=10^{-0.21}d_p^{1.28}\rho_p^{0.44}v^{0.66}(\cos^{0.62}\Theta) \qquad (4\text{-}9)$$

Table 4-8. Statistical analysis of the lunar rock and soda-lime glass damage equations against the lunar rock, solar cell and soda-lime glass data sets.

Fit	χ^2/ν	count	r	r^2
Lunar rock (Eq 4-7)	4.62	167	0.950	0.903
Soda-lime glass (Eq. 4-8)	1.71	94	0.954	0.911
Soda-lime plus (Eq. 4-9)	2.42	133	0.960	0.921
Soda-lime glass (Eq. 3-6)	7.75	94	0.919	0.844
Solar cell fit (Eq. 4-8)	3.56	39	0.921	0.849
Solar cell fit (Eq. 4-9)	2.48	39	0.941	0.886
Solar cell fit (Eq. 3-6)	2.75	39	0.934	0.873

4.7 Discussion

4.7.1 The new damage equations

In section 3.2.1 a clear bifurcation in the experimental values of D_{co} was noted. The cause of this (possibly target edge effects or a microstructural response) was discussed and the data seemed to suggest that a different damage equation might be required to describe the response. The different morphology suggested a different mechanism of formation. However, in section 4.6, a least squares fit is presented for the whole soda-lime glass data set with a very good statistical correlation. This is an anomaly because, if the large D_{co} data set were formed by a different mechanism, then such a good fit for the damage equation (Eq. 4-9) would not be expected. Here, a good fit is defined as a fit which returns

exponents similar to the original published brittle material damage equations (Eq. 3-4) and which also has good statistics. The results of the least squares fit to the lunar rock data set (similar in content to that used to derive Eq. 3-4) also reproduces exponents similar to those given for Eq. 3-4. One explanation for the similarity of the fitted exponents to damage equations (Table 4-5), despite the use of the large glass data set with its differing crater profile, may be that the original shots onto the lunar rock material may also have included impacts with a different crater profile. In order to ensure that edge effects do not influence the crater profile the target must be sufficiently large. No quantitative technique exists for trading off the time of formation of spallation diameter against the time of shock wave propagation to the edge of the material and back again. However, when the spallation diameter is of the order of 100 mm a target diameter of 500-1000 mm might be considered large enough. Such a target would most probably be too large and heavy for mounting inside a gun target chamber. Therefore it is likely that shots onto lunar rock material were constrained in diameter and might have produced the altered crater profile. In comparison, the onset of rear spallation (section 3.3.5) does not affect the D_{co} parameter (within the experimental data range shown here) and thus will not affect the development of a damage equation including those data.

4.7.2 The cosΘ exponent

The value of the exponent varies between 0.77 and 0.98 depending on what target data sets were used and whether the full angle range (0-75°) or a restricted angle range, based on morphology (0-70°) was used. In addition, there is not a strong statistical confirmation that a power law form of cosΘ is appropriate for damage equations. Therefore, any application of the cosΘ exponent to retrieved solar cells will be subject to an uncertainty on the angle exponent, e.g. 0.85 ± 0.10. The centroid offset (defined in Figure 2-9), which is a more predictable indicator of impact angle, has not been studied in this thesis, due to paucity of data.

4.7.3 The variability of D_{co}

Typically, the value of D_{co} varies by 20 % for identical impact conditions on soda-lime glass. Similar variability has been noted for solar cell impacts (Taylor *et al.*, 1998). When a value is measured on a brittle material retrieved spacecraft surface (e.g. a solar array) the value will have assigned to it an uncertainty to account for the variable response of the brittle material under hypervelocity impact. Based on the results of the analysis presented in this chapter, such a value might be 20 %. This average value will be used to place limits on the accuracy of flux decoding from solar cell arrays.

4.7.4 Accuracy of the exponent values

Four different fitting programmes have been used and the range in values returned explored. Also, the values obtained depend on whether a fit is carried out to a power-law form, or the linear version (obtained by taking logarithms). The fitting programme would either minimise

the sum of squares of residuals or the sum of squares of the logarithmic residuals. These two factors combined, suggest that only one (possibly two) significant figures should be used for any parameters employed in damage equations. The three decimal places employed in Eq. 3-6 are not supported by the analysis of the damage equations.

4.7.5 Implications for flux decoding from space-exposed brittle materials

The use of power-law damage equations for decoding the lunar microflux (Eq. 3-4) is supported by the analysis here, some 25 years later (Eq. 4-7). The suitability of Eq. 3-6 for use in decoding the impact flux on solar arrays is limited by the use of different brittle (and ductile) target materials in its derivation and the (possibly connected) large error bars which would have to be applied. By comparison, the similarity between impacts onto soda-lime glass and borosilicate glass has been illustrated (section 4.4). New power-law damage equations have been derived for analysis of impacts onto soda-lime and solar cell glasses (Eqs. 4-8 and 4-9). These equations can be applied to the HST and EURECA fluxes given in Figure 1-8. However, the new damage equations also have errors associated with the impactor parameter exponents. These will have to be incorporated into the analysis of the HST and EURECA solar cells. Another factor that must be considered is the variability of the conchoidal diameter, as discussed in section 4.5. This variability means that, for a particular set of impact parameters, the resulting conchoidal diameter can vary in size by typically 20%.

4.8 Further Evaluation of a Depth of Penetration Equation

The published empirically determined power-law depth of penetration brittle material damage equations were reviewed in chapter 3. Systematic trends with size were found. Therefore, a further analysis of these damage equations is presented, using data from shot programmes carried out for this thesis. In addition, data from several other shot programmes (reviewed in Tables 3-1 and 3-2) are used. The velocity dependence of depth of penetration is particularly important as it is used to provide calibration data for computer simulations of hypervelocity impacts (using hydrocodes) in chapter 5.

4.8.1 Velocity exponent (v^{γ})

As discussed earlier in chapter 4, crater diameter (D_c) and crater depth (T_c) (assuming a hemispherical crater) were found to be proportional to $V^{0.67}$, from experimental results. The predicted values of the velocity exponents for T_c damage equations can be calculated using the McHugh and Richardson data set. This data set covers a wide range of velocities (6-16 km s^{-1}) for one projectile type (borosilicate glass, d_p = 48.1 μm) onto two target types (quartz and aluminosilicate glass). Therefore, it is ideal for an investigation of the velocity exponent and the influence of target type. There should be a linear dependence between log T_c and log v ($T_c = a\ v^b$, log $(T_c) =$ log a + b log v) which shows no dependence on target type.

Table 4-9. Results of least squares fits to the McHugh data set. B/S : borosilicate glass, A/S : aluminosilicate glass. The experimental data are compared with the equation predictions in Figure 4-11.

Parameter	Data set	log a	b	r^2	number of data
T_c	B/S onto A/S glass	0.46	1.10	0.75	39
T_c	B/S onto quartz	1.30	0.43	0.18	53
T_c	B/S onto A/S glass and quartz	0.80	0.84	0.32	91
D_{cc}	B/S onto quartz	1.82	0.32	0.13	53

First, in Figure 4-11, a log-log plot of depth of penetration versus velocity is presented for the (a) aluminosilicate glass and (b) quartz. Least squares fits to the data are presented in Table 4-9. The quartz data are much more scattered than the aluminosilicate data. . The correlation coefficients for the fits represent the scatter in the data. This is reflected in the log-log plots of data versus equation prediction given in Figure 4-12. In addition, the values of the velocity exponents returned are not as predicted by the simple 'crater volume ∝ kinetic energy' formulation. Therefore, there is no clear evidence that aluminosilicate glass and quartz can be described by the same damage equation nor that the velocity exponent of 0.67 is appropriate. However, due to the scatter in the data and the consequent problems for the fitting programme, a different velocity exponent cannot be identified with confidence. The data sets are grouped together and a fit performed. Although a velocity exponent of 0.84 was produced, the r^2 value is extremely low.

This data set was used in the derivation of the depth equation reviewed in chapter 3, Eq. 3-1. Eq. 3-1 has a velocity exponent of 0.67 which does not agree with the results of this least squares fit. Although over 90% of the data set consisted of a single projectile diameter over a wide range of velocities, the authors assumed a velocity exponent of 0.67, then selected less than ten data points to be representative of the whole. Half the data were from impacts with a projectile diameter of ~50 μm, the others in the range 400-800 μm. A least squares fit was carried out to determine the projectile diameter exponent (the density exponent was assumed to be 0.5).

4.8.2 Experimental data compared with damage equations

In Figure 4-13, the performance of the damage equations is reviewed, in graphs first published in Taylor *et al.* (1997a). The ratio R (equation prediction to experimental data) is plotted against velocity using data from Edelstein (1992) (impacts onto fused quartz), McHugh and Richardson (1974) (quartz and aluminosilicate glass), Mandeville (unpublished) (granite, basalt, basalt glass and pyrex) and Flaherty (1969) (fused silica). Eqs. 3-1 and 3-3 (the McHugh and Richardson and Cour-Palais damage equations) are used to calculate R. The experimental data are summarised in Tables 3-1 and 3-2.

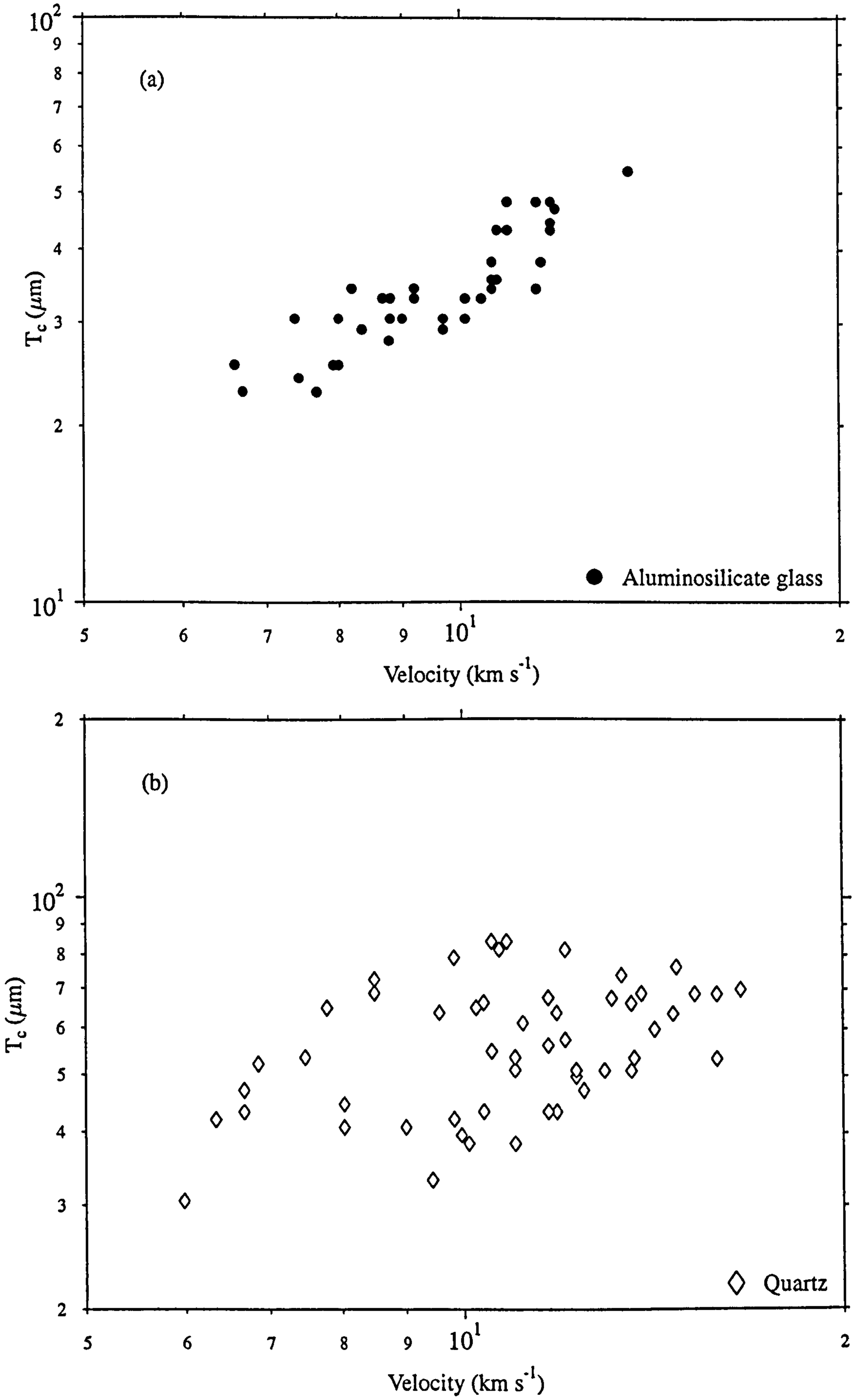

Figure 4-11. (a) T_c versus velocity for quartz (McHugh dataset) (b) T_c versus velocity for aluminosilicate glass (McHugh dataset).

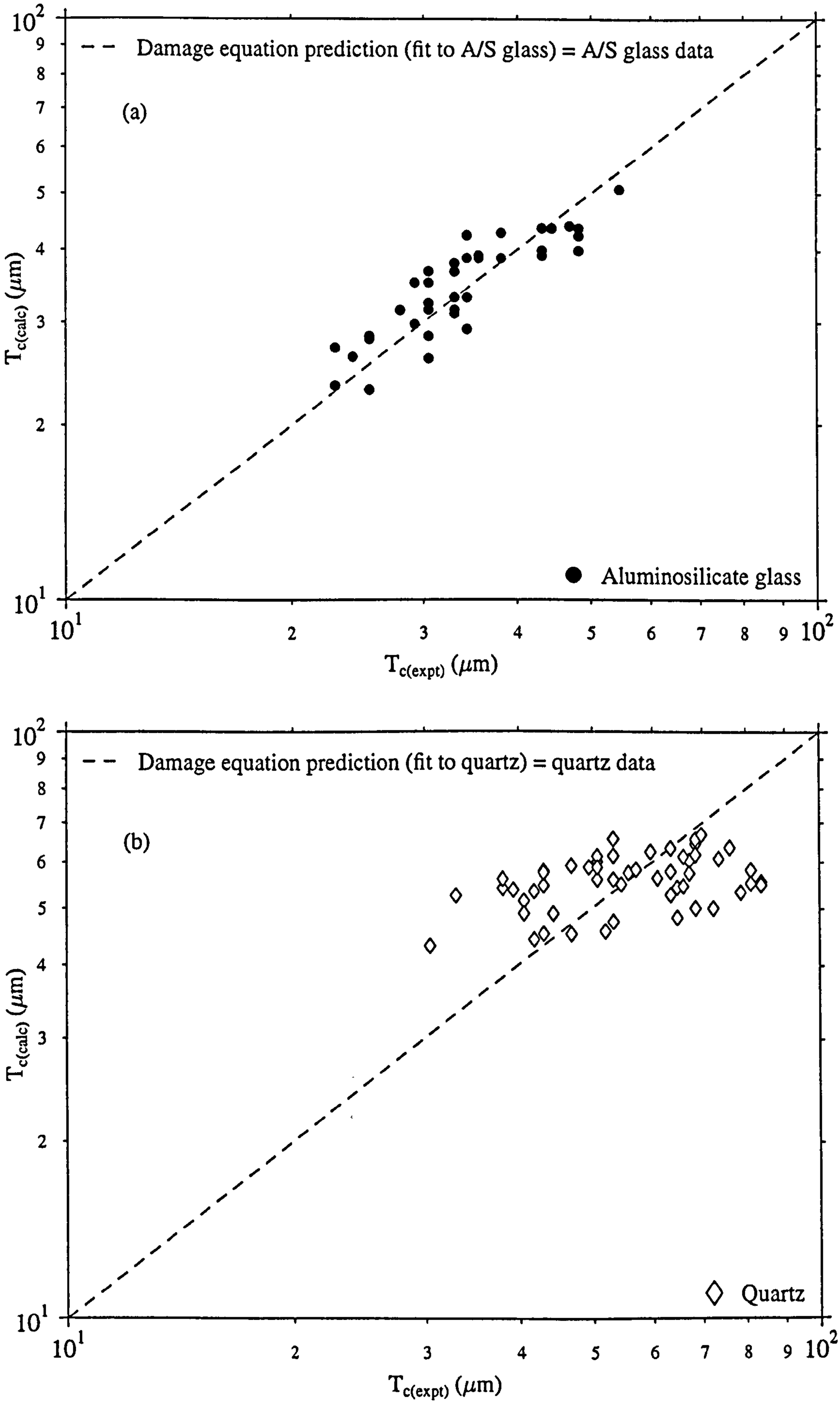

Figure 4-12. Log-log plots of the least squares fits to (a) aluminosilicate glass T_c (b) quartz T_c data sets (Table 4-9). The dashed line corresponds to $T_{c(calc)} = T_{c(expt)}$

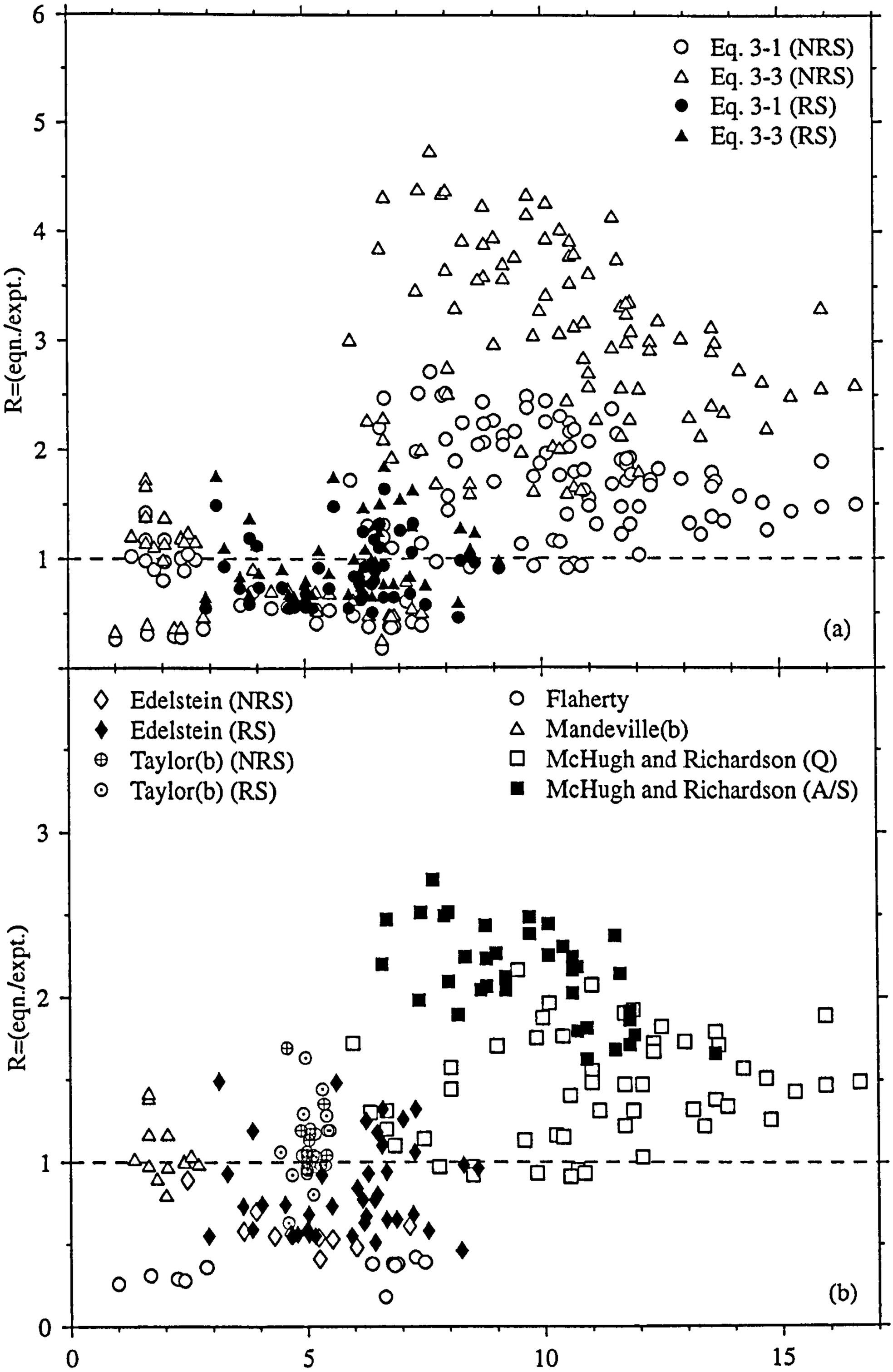

Figure 4-13. (a) The ratio R (eqn prediction:expt data) is plotted for Eq. 3-1 (McHugh and Richardson, 1974) and Eq. 3-3 (Cour-Palais, 1982) for NRS and RS targets shown in (b). (b) R is plotted for Eq. 3-1 for data sets sorted by target type and material. (Q: Quartz, A/S: Aluminosilicate Glass, NRS: non-rear spalling, RS: rear spalling))

Table 4-10. Data sets used in the development of the brittle material depth of penetration equation. The numbers in the columns headed NRS and RS refer to the number of data. More details of the projectile diameter, density and velocity range fired and the target type can be found in Tables 3-1 and 3-2. Data set 1: All brittle data; 2: 'Soda-lime' glass; 3: 'Quartz'. RS: rear spalling; NRS: non-rear spalling.

ID	Target	NRS	RS	1	2	3
McHugh	A/S glass	38	0	y	n	n
Mandeville(b)	Basalt, Basalt Glass	15	0	y	y	n
Mandeville	FQ	49	0	y	n	y
Schneider(c)	FQ-RS	0	5	y	n	y
Edelstein	FS-RS	0	42	y	n	y
Flaherty	FS	12	0	y	n	y
Edelstein	FS-NRS	10	0	y	n	y
Mandeville	Granite, Pyrex	23	0	y	y	n
McHugh	Quartz	63	0	y	n	y
Mandeville	SLG	40	0	y	y	n
Mandeville	Vitreosil	13	0	y	n	n
Taylor(b)	SLG-NRS	8	0	y	y	n
Taylor(b)	SLG-RS	0	21	y	y	n

Both damage equations show a systematic trend from under-prediction to over-prediction with velocity for both non-rear spalling and rear spalling targets. In Figure 4-13(b) the data are plotted by target type, for Eq. 3-1 only. The R ratio is different between soda-lime glass and fused quartz at ~5 km s^{-1} and for quartz and aluminosilicate glass at 7-16 km s^{-1}. Therefore, the damage equations may not have the correct velocity exponent and may also give a different response depending on the target type.

The data set given in Table 4-10 is used for an investigation and development of depth of penetration damage equations for this thesis. It includes micron-sized to millimetre-sized projectiles as well as non-rear spalling and rear spalling targets. The data are summarised in Figure 4-14, where a clear size dependency of $T_{c(expt)}/T_{c(calc)}$ versus $T_{c(expt)}$ is observed.

4.8.3 A new depth of penetration equation ?

The functional form of Eq. 4-1 and the statistical techniques described in section 4.1 are used in this analysis. The results of section 4.8.1 suggest that aluminosilicate glass and quartz have differing responses to hypervelocity impact, as evidenced by the depth of penetration data and the velocity exponents obtained from the fits ($\gamma = 1.10$, $r^2 = 0.75$ and $\gamma = 0.43$, $r^2 = 0.18$ respectively). In order to investigate this discrepancy between fit results and the theory predictions, least squares fits were carried out for the three data sets using velocity as a fitting parameter, in addition to projectile density and diameter. The fits were carried out to the data grouped by target type and rear spalling and non-rear spalling targets. A wide range

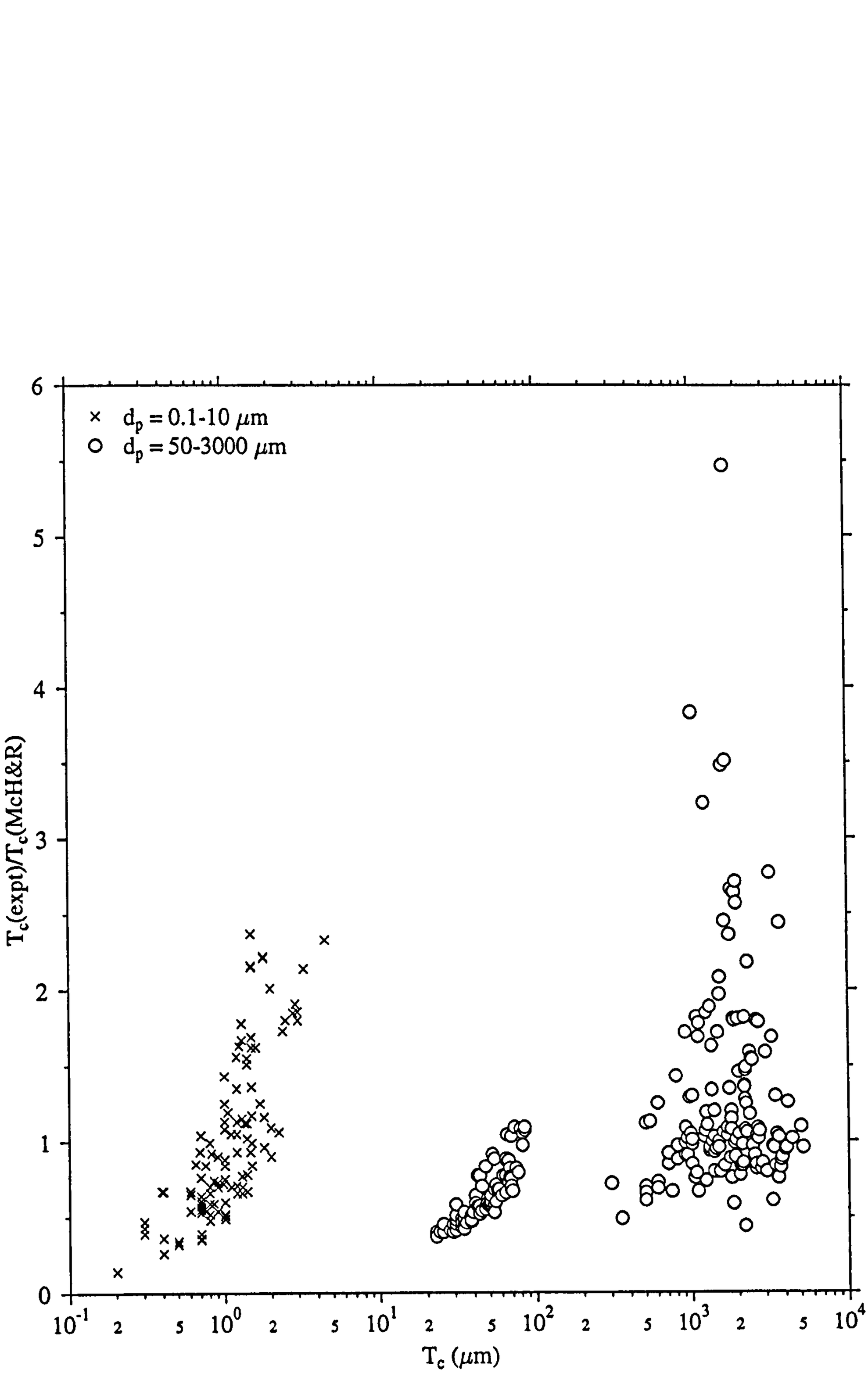

Figure 4-14. T_{expt}/T_{calc} versus T_c for all brittle impact data. The McHugh and Richardson (1974) damage equation (Eq. 3-1) was used. The data show systematic trends with depth of penetration, suggesting that the velocity or projectile diameter exponent may be incorrect for Eq. 3-1.

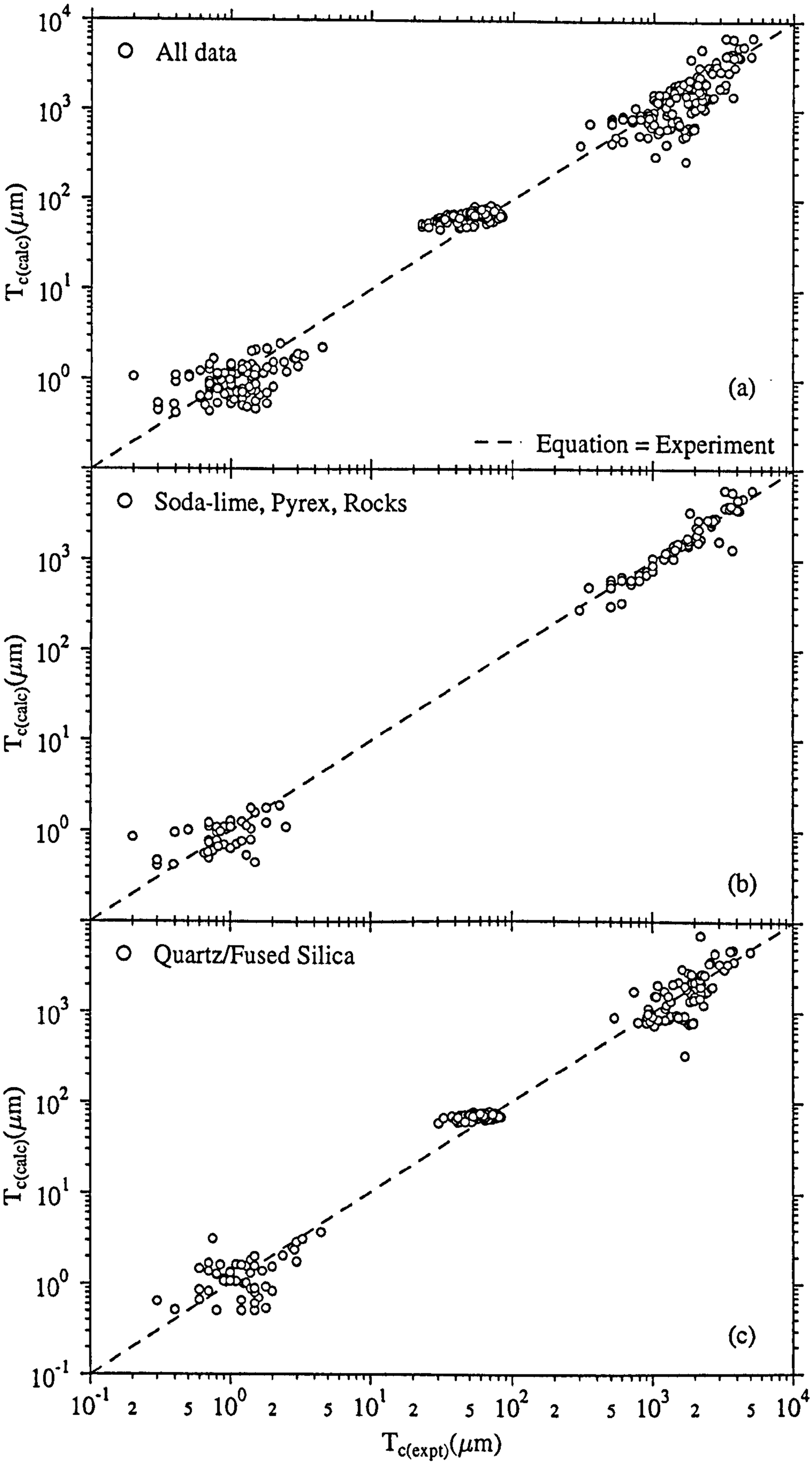

Figure 4-15. Equation predictions (Table 4-11) compared to source experimental data for (a) all brittle data (b) soda-lime glass, pyrex and rocks (c) quartz/fused silica.

of velocity exponents were returned with good values of r^2 (Table 4-11). The velocity exponent varies between 0.31 and 0.86 and there is little difference between the data sets that include the rear spalling data or are based on non-rear spalling data only. The 0.6 exponent (derived from all the brittle data) would appear to be an 'average' of the quartz and borosilicate glass/soda-lime glass/lunar rock analogue data sets and thus should be treated with caution.

Table 4-11. Results of least squares fits to the three data sets in Table 4-10 for velocity (γ) , projectile diameter (α) and density exponents (β)(NRS: non-rear spalling). α, β, γ defined in Eq. 4-1.

	γ	β	α	logK	r^2	χ^2/ν
Data set 1	0.61	0.74	1.21	-1.11	0.97	7.153
Data set 1(NRS only)	0.61	0.79	1.19	-1.11	0.97	8.567
Data set 2	0.86	0.73	1.22	-1.35	0.99	6.297
Data set 2 (NRS only)	0.99	0.80	1.24	-1.475	0.99	6.217
Data set 3	0.31	0.77	1.21	-0.77	0.98	11.479
Data set 3 (NRS only)	0.28	0.78	1.23	-0.78	0.97	13.052

The equation predictions based on the exponents given in Table 4-11 are plotted against the source experimental data in Figure 4-15. The results on the least squares fits do not support the $v^{0.67}$ exponent usually assumed for the depth of penetration equations and suggest, additionally, that target type dependence may need to be considered for future damage equations.

4.9 Summary

The comparison of the least squares fits to the quartz data and the lunar rock + soda-lime glass combined data suggests that these data sets should be kept separate for the development of D_{co} brittle material damage equations. Three damage equations, derived from these data sets, have been presented. Two are appropriate for use on solar cell impact surfaces. An examination of the values for the $\cos\Theta$ and d_p exponents show that such values should not be quoted to more than one or two significant figures, due to the differences in least squares fitting techniques and programmes. Also, the D_{co} parameter has been shown to be variable for constrained impactor parameters. Diameters measured on solar cell surfaces will need to have this error applied. Least squares fits to depth of penetration data show that a wide range of velocity exponents are returned, not supporting the commonly-used 0.67 exponent. Target type dependence is also indicated by the data.

Chapter 5

5. Hydrocode Modelling

5.1 Introduction

In chapters 3 and 4 the empirically determined brittle material damage equations were compared with the data set collected for this thesis. Different brittle materials were found to present a different response to hypervelocity impact. In particular, quartz does not appear to respond in the same way as soda-lime glass and borosilicate glass. The three published conchoidal damage equations (Eqs. 3-4, 3-5 and 3-6) are based on a data set which includes a wide range of brittle materials. Target type-dependent conchoidal diameter equations have been developed (Eqs. 4-8 and 4-9). The three published depth of penetration equations have also been compared with experimental data (Eqs. 3-1 to 3-3). The results show that, although the data are broadly predicted by Eq. 3-1, the 2/3 velocity dependence shown in the damage equuations is not reproduced by a least squares fit to the data used to derive Eq. 3-1. Therefore, although the equation predictions are compared with the hydrocode simulations, they cannot be used to refine the hydrocode models due to uncertainties in their derivation.

Experimental tests are able to access only a small fraction of the impactor parameters in space (velocity, diameter, density, shape and impact angle). However, the empirically determined damage equations can be extrapolated to these conditions. A technique for understanding the response of materials at hypervelocity impact beyond the laboratory calibration regime is the use of hydrocodes (non-linear computer software for modelling dynamic problems).

In this chapter the results of a brittle material hydrocode modelling programme, including the implementation of the Johnson-Holmquist brittle material model (Johnson and Holmquist, 1995; Holmquist *et al.*, 1995) into the AUTODYN-2D hydrocode (Birnbaum *et al.*, 1987), are presented. The modelling programme was carried out by a team consisting of (i) the author (joint implementation of, and simulations using, the Johnson-Holmquist model) (ii) K. Tsembelis, University of Kent at Canterbury (development and test of an alternative Glass Analogue Model (GAM) (Tsembelis, 1998) and (iii) C. Hayhurst, Century Dynamics Ltd. (joint implementation of the Johnson-Holmquist model).

Any modelling technique must be suited to the high strains (material deformations) and strain rates and phase changes that occur during hypervelocity impact. The computational schemes and empirical or semi-empirical strength and failure models and equations of state currently used are examined in this chapter for their suitability for the task. The simulation results from both modelling programmes are examined and compared with the damage equation predictions and experimental data analysed in chapters 3 and 4.

5.2 An Introduction to Hydrocodes

Anderson (1987) defines hydrocodes to be computer programmes (codes) that can be used to perform numerical simulations of highly dynamic events, particularly those including shocks. Hydrocode numerical simulations are based on solving discrete approximations to the continuum equations of mass, momentum and energy balance. Phenomena can be highly non-linear and fields can be discontinuous. Models can be complex, encompassing strain history-dependent plasticity, internal voids or anisotropic response. The term 'hydrocode' originally referred to hydrodynamic simulations but the current codes incorporate strength and failure models that allow realistic simulation of non-fluid materials.

5.2.1 Finite element versus finite difference codes

Finite difference schemes are used in hydrocodes, in preference to the commonly used finite element techniques. Finite element simulations are based on calculations between nodes at equilibrium. However, equilibrium is unlikely to be reached over any significant size scale in hypervelocity impact processes. The finite difference technique, as employed in hydrocodes, is able to deal with non-equilibrium situations. Each calculation point (cell or node) in the simulation has parameter values associated with it (e.g. density) and the code interpolates between these. A shock front observed in an experiment is a discontinuity. Computationally, this discontinuity is smoothed over a few cells.

"Finite difference techniques are an approximate solution to an exact problem and finite element techniques are an exact solution of an approximate problem" G. Johnson, in Anderson , 1987

5.2.2 Lagrange/Euler/Smoothed Particle Hydrodynamics

The target and projectile are computationally represented by a grid in a hydrocode simulation. All grids are constructed from a set of nodes, a set of rules for connecting the nodes and a set of rules for interpolating the data. This is done to discretise the differential equations of the continuum mass, momentum and energy balance and to allow their solution within the code. The cell size of the grid must be small to allow solution of the differential equations.

In a Lagrangian scheme, the grid moves and distorts with the material motion. The technique is computationally efficient as the grid is only as large as required to simulate the particle and target. However, as the grid distorts, large deformations may result which could cause computational errors. These distortions will occur during simulations of hypervelocity impact onto thin plates. Similarly, the propagation of a debris cloud resulting from such an impact is very difficult to model as it calls for the separation of the cells and their propagation. The re-zoning of distorted grids has been used to circumvent the problem. This involves the removal of distorted cells, but also entails the removal of information (pressure, energy etc.) that the cell(s) represent. An artificial computational technique, called

erosion (but not based on the physical process), is used to remove highly distorted cells on the premise that the material which it represents is no longer contributing to the material strength (i.e. it has eroded). An alternative to the erosion parameter is a technique called manual rezoning. It involves (frequent) human intervention during the hydrocode simulation. The parameters associated with a highly distorted cell are noted, then the cell is rezoned to a more appropriate form. The technique is not accurate and is operator dependent.

In contrast, for an Eulerian calculation, the mesh is fixed in space and the material moves through it. Therefore, cells can contain more than one material and be partially filled. There are thus no problems with grid distortion but the cell size must be small enough to 'resolve' the smallest feature (crater lips or debris fragments). In addition, problems arise when a cell contains more than one material. Complex algorithms are required to define the edge of features when the feature is smaller than a cell. The Eulerian technique is much more computationally expensive than the Lagrangian technique.

The Smoothed Particle Hydrodynamics (SPH) technique combines the advantages of the Lagrangian technique (numerically efficient) and the Eulerian scheme (able to cope with extreme material deformation). SPH is a gridless Lagrangian particle method originally derived for astrophysical problems. It has been in use for nearly two decades, and was first used for modelling of interstellar medium shocks (by Lucy, 1977; Gingold and Monaghan, 1977). It is a gridless technique whereby computational nodes (interpolation points, known as 'particles') replace the traditional mesh of Lagrange and Euler methods. In SPH the concept of a cell is replaced by a particle with fixed mass and a given smoothing function that spreads the mass over a 'smoothing length'. When adjusted properly, each particle extends to just touch its neighbours. The conceptual advantages are simplicity, robustness, accuracy and computational efficiency, although the development of robust algorithms for implementation in hydrocodes is on-going. SPH interpolation points (particles) are not bound to a grid so can handle extreme material deformations. Unlike the Lagrangian processor, the grid-free nature of the SPH processor removes the need for unphysical erosion algorithms. SPH is a Lagrangian technique, so empty cells are avoided and resolution naturally increases near high density features. However, there are problems with stability, consistency and, most importantly, with energy conservation for SPH simulations. At the time of writing this thesis, the SPH processor has become available as a beta-release for the AUTODYN hydrocode.

5.2.3 Artificial viscosity and modelling shock waves

Artificial viscosity is used to resolve the computational problems associated with a discontinuity, as in a shock front. It does not represent any physical parameter. The

artificial viscosity algorithm spreads the shock across a small number of cells. In order to represent the shock front, the grid must be sized appropriately.

5.2.4 Validation of hydrocodes, including AUTODYN

Hydrocode simulation of flyer plate impact experiments (which approximate to a one dimensional geometry) can be used for the development and verification of material models for eventual incorporation in multi-dimensional codes. These are the most conclusive data sets for validation. However, the stresses attained in flyer plate experiments are not high enough to reproduce in full the conditions experienced during a hypervelocity impact. This is due to the maximum velocity attained by the majority of guns in use. Historically, in the absence of suitable flyer plate data, hydrocodes used in the space science field have been validated by comparison of crater morphology (i.e. depth, diameter, crater lip formation). Where available, debris cloud propagation resulting from impacts onto thin plates can also be used.

Table 5-1. HVI brittle material hydrocode modelling. (J-H: Johnson-Holmquist, E-PP: elastic-perfectly plastic, Lin.: linear, M-C: Mohr-Coulomb, Lag.: Lagrangian, Eul.: Eulerian, EOS: Equation of State). Ballistic regime is typically 1-1.5km s^{-1}.

Reference	Code	Sch-eme	Strength +EOS	Ball. regime ?	Comment
Alwes, 1990	EFHYD	Lag.	E-PP, M-G	N	Al onto laminated glass, penetration depths compared with modelling results
Anderson *et al.*, 1993	CTH	Eul.	E-PP, M-C, J-H	Y	W rods onto glass, problems with mixed cell in Euler
Loupias *et al.*, 1997	OURANOS	Eul.	POREST	N	Porous silica fibres + resin model
Lundberg *et al.*, 1996	AUTODYN	Lag.	J-H	Y	W rods onto ceramic
Mandell *et al.*, 1996	SPHINX	SPH	E-PP, Lin.	Y	W rods onto ceramic, cracking patterns
McSherry, 1996	AUTODYN	Lag.	M-C, Lin.	N	Simulation of impacts onto thin solar cells
Medina *et al.*, 1996	CTH	Eul.	M-G, SESAME	N	Impacts onto quartz (5-15 km s^{-1})
Meyer Jr., 1995	CTH	Eul.	J-H	Y	W rods onto ceramic, J-H parameter study.
Rosenberg *et al.*, 1997	PISCES	Eul.	J-H (*)	-	Derivation of simple model, by fitting to expt results
Taylor *et al.*, 1997a	AUTODYN	Lag.	J-H	N	HVI onto soda-lime glass

The validity of such modelling is dependent on the hydrocode material models and equations of state used (reviewed in section 5.4), as well as the computational scheme (discussed in section 5.2.2). Validated and tested damage equations (such as those presented in this thesis) can also be extrapolated to provide calibration points for hydrocode simulations, although care must be taken with prior analysis of the damage equations to ensure their suitability for extrapolation. Once the code (and material models and equations of state) has been validated, it can provide a cost-effective approach to the development of damage equations and shielding systems and can be used in parallel with an experimental programme.

5.3 Brittle Material Hydrocode Modelling

The majority of hypervelocity hydrocode modelling results published refer to ballistic hypervelocity impact simulations; a common simulation might be a long tungsten rod onto a confined ceramic at 1.2-1.5 km s^{-1}. The Johnson-Holmquist model was derived primarily for this purpose. Previous hypervelocity impact brittle material hydrocode modelling at typical space (low earth orbit) velocities (Alwes, 1990; McSherry, 1996; Medina *et al.*, 1996) have used simple models (e.g. the linear EOS, section 5.4.3; Mohr-Coulomb strength model, section 5.4.7) to model the strength of the material. A summary of the recently published hydrocode modelling results of impacts onto brittle materials is presented in Table 5-1.

5.4 Equations of State, Material Strength and Failure Models

In a hydrocode, an equation of state (EOS) material model (constitutive relations) and failure model are required. The continuum equations (mass, momentum and energy) are implemented in a hydrocode. However, in order to describe the response of a particular material to a computed shock, an equation of state (EOS) is also required in addition to mass, momentum and energy continuum equations. In addition, the strength and failure models, although optional to model material response to a shock, are necessary to describe the materials of interest for a hypervelocity impact. Anderson (1987) defines these three areas as:

- Volumetric response, or resistance to compression (equation of state)
- Resistance to distortion (constitutive), and
- Reduction in ability to carry stress as damage accumulates (failure).

All the EOS and material/failure models reviewed below are used in the hydrocode simulations in this thesis. Although the target material is brittle (and thus the Johnson-Holmquist model is appropriate), the projectiles in the simulation are mostly ductile. The parameters used in the simulations, except where stated, are from the AUTODYN material library, which is collated from published literature.

An equation of state describes the material with pressure, P, specific volume, V, and internal energy, E (a P-V-E surface). The equations of state reviewed below are typically semi-empirical. (The simplest equation of state is PV=nRT, for an ideal gas). The yield strength of a material is related to the deviatoric stress (and thus the shear stress). It is typically a function of strain (ε), strain rate (∂\∂t(ε)) and temperature (T), and also sometimes of pressure (P)(Eq. 5-1). Failure models are required to adjust the material modelling when the computed local tensile stress exceeds a value which the real material would not be able to withstand.

$$Y=Y(\varepsilon, \dot{\varepsilon}, T, P) \tag{5-1}$$

5.4.1 Mie-Gruneisen equation of state

The Mie-Gruneisen EOS is based on the theory of solids, but can be extended to cover the response of liquids. It cannot be used to describe the vapour phase and thus is sometimes inappropriate for hypervelocity impacts (where, due to the very high pressures, a solid-vapour phase change is possible). It also underestimates the expansion of the material at high velocities, when compared with the Tillotson EOS (section 5.4.4). Both polynomial equations of state and shock equations of state belong to the Mie-Gruneisen family. It is defined by Eq. 5-2 which is based on a reference curve (denoted by the subscript r) and the Gruneisen coefficient, Γ (Eq. 5-3). The Gruneisen coefficient is used to calculate values of pressure away from the reference curve (P_r) analytically. Normally, P is the Hugoniot pressure. However, for isentropic release, P_r is taken to be the Hugoniot pressure (see chapter 6 for discussion of Hugoniots).

$$P=P_r+\Gamma\rho(E-E_r) \tag{5-2}$$

$$\Gamma=v\left(\frac{\partial p}{\partial e}\right)_e \tag{5-3}$$

(Symbols are P (pressure), E (internal energy), ρ (density) and Γ (Gruneisen coefficient). p and e are used to denote values at which the Gruneisen Gamma is calculated. v = 1/ρ.)

5.4.2 Polynomial equation of state

The polynomial EOS is a general form of the Mie-Gruneisen EOS and has two analytic forms, for compression and tension (Eqs. 5-4 and 5-5). The compression, μ, is defined in Eq. 5-6. The form represented here is 'energy dependent' but the polynomial equation of state can also be formulated in an energy independent form (e=0). An energy dependent form of Eqs. 5-4 and 5-5 allows the modelling of different phases of matter. The values of B_0 and B_1 are functions of the Gruneisen coefficient, defined in Eq. 5-3. The polynomial EOS forms the basis for the Johnson-Holmquist EOS.

$$p=A_1\mu+A_2\mu^2+A_3\mu^3+(B_0+B_1\mu)\rho_0 e \quad (5\text{-}4)$$

$$p=T_1\mu+T_2\mu^2+(B_0)\rho_0 e \quad (5\text{-}5)$$

$$\mu=\left(\frac{\rho}{\rho_0}\right)-1 \quad (5\text{-}6)$$

(Symbols are e (energy), ρ (density), μ (compression), A_i, B_i and T_j (i=1, 2, 3, j=1, 2)(constants) and the subscript 0 signifies initial conditions)

5.4.3 Shock equation of state

The Shock EOS is a Mie-Gruniesen (Eq. 5-2) formulation which uses the experimentally determined linear shock Hugoniot parameters c_o and S, linked by the linear relationship $U_s = c_o + Su_p$ (discussed more fully in section 6.3) (assuming $\Gamma\rho = \Gamma_0\rho_0$). In Eq. 5-2, the subscript r is replaced by H to signify the Hugoniot reference curve. P_H, E_H and μ are defined in Eqs. 5-8, 5-9 and 5-6. The shock equation of state is used to model nylon, stainless steel 304 and soda-lime glass in this thesis.

$$P_H=\frac{\rho_0 c_0^2\mu(1+\mu)}{(1-(S-1)\mu)^2} \quad (5\text{-}8)$$

$$E_H=\frac{\rho_0 P_H\mu}{2(1+\mu)} \quad (5\text{-}9)$$

Symbols are P (pressure), E (energy), ρ (density) μ (compression), c_o and S (Hugoniot parameters), subscript 0 (initial conditions) and subscript H (Hugoniot reference curve).

5.4.4 Tillotson equation of state

The Tillotson EOS (Tillotson, 1962) is the most appropriate, available (non-defence) equation for description of the response of metallic material in multi-phases of matter. It incorporates 'low pressure' experimental data with the theoretically derived Thomas-Fermi-Dirac data at pressures above 0.005 GPa. The p-v plane is divided into four regions of interest given by Eqs. 5-10 to 5-14 (illustrated in Figure 5-1). The constants a, b and A are derived from shock experiments. e_o and B are adjusted to give the best fit for the EOS surface. e_o is not the initial energy density of the material, but is a parameter which is often close in value to the vaporisation energy. The following materials are modelled using the Tillotson EOS in this thesis: aluminium 2024, and titanium.

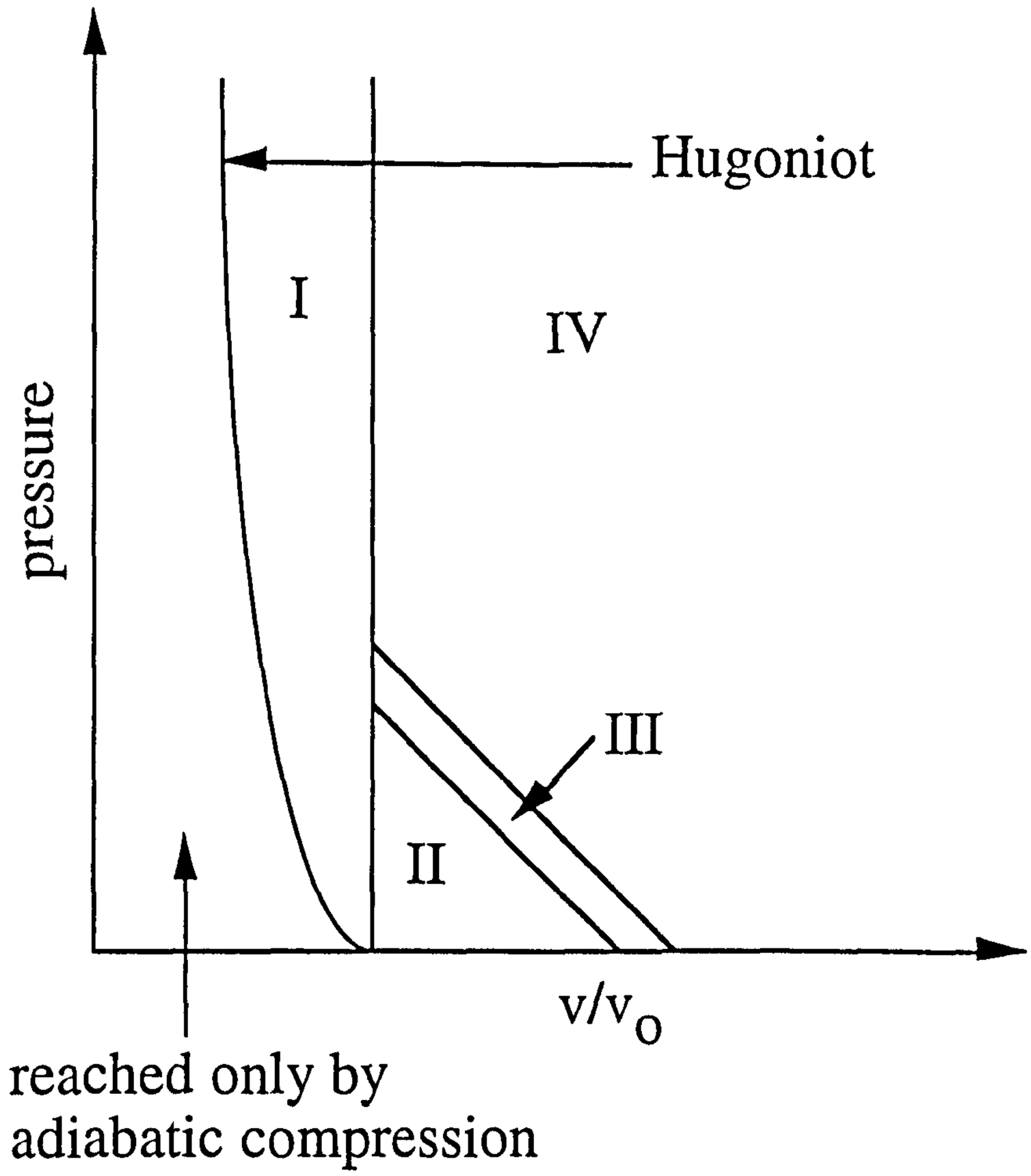

Figure 5-1. The four regions of the Tillotson equation of state.

Region 1 : Compressed phase of material, extends to shock pressures of 0.1 GPa.

$$p_1=\left(a+\frac{b}{\omega_0}\right)\eta\rho_0+A\mu+B\mu^2 \tag{5-10}$$

Region 2 : Material shocked to less than the sublimation energy, e_s.

$$p_2=\left(a+\frac{b}{\omega_0}\right)\eta\rho_0+A\mu \tag{5-11}$$

Region 3 : Region where $e_s < e < e_s'$ ($e_s'= e_s+k\, e_v$)

$$p_3=p_2+\frac{(p_4-p_2)(e-e_s)}{(e_s'-e_s)} \tag{5-12}$$

Region 4 : Expansion phase of the material which has been shocked to energy e_s'

$$p_4=a\eta\rho_0 e+\left(\frac{b\eta\rho_o}{\omega_0}+A\mu\exp(\beta x)\right)\exp(-\alpha x) \tag{5-13}$$

(The symbols m, ω_o, x and η are defined by equations Eqs. 5-14 to 5-17:

$$\eta=\frac{\rho}{\rho_0} \tag{5-14}$$

$$\mu=\eta-1 \tag{5-15}$$

$$\omega_0=1+\frac{e}{e_0}\eta^2 \tag{5-16}$$

$$x=1-\frac{1}{\eta} \tag{5-17}$$

(Symbols: p (pressure), e (internal energy), e_s, (sublimation energy), e_v, (vaporisation energy), ρ (density), subscript 0 (initial conditions).)

5.4.5 Johnson-Cook strength model

The Johnson-Cook strength model (Johnson and Cook, 1983) is used for metals subjected to large strains, high strain rates and high temperatures. The yield strength (Eq. 5-18) is expressed as a function of the effective plastic strain rate, the normalised effective plastic strain rate and the homologous temperature (Eq. 5-19). Eq. 5-19 describes the thermal softening, which is the reduction of the yield strength as the temperature increases. Note that, when $T = T_{melt}$, the yield strength is zero. At high strains and strain rates, strain and strain rate hardening occur, whereby the yield strength of the material increases with respect to the zero strain condition. This is governed by the B and n constants. The C parameter governs the effects of increasing strain rate whilst the A parameter represents the yield stress at low strains.

$$Y=\left(A+B\varepsilon_p^n\right)\left(1+C\log\dot{\varepsilon}_p\right)\left(1-T_H^m\right) \tag{5-18}$$

$$T_H=\frac{(T-T_{room})}{(T_{melt}-T_{room})} \tag{5-19}$$

(Symbols are Y (yield strength), ε_p (effective plastic strain rate), $\partial\backslash\partial t(\varepsilon_p)$ (normalised effective plastic strain rate), T, T_H (temperature and homologous temperature) and A, B, C, n, m, T_{melt}, T_{room} (constants).)

5.4.6 Steinberg-Guinan strength model

For strain rates greater than 10^5 s^{-1}, strain rate effects become insignificant and the yield stress reaches a maximum value which is strain rate independent (Eq. 5-20). This physically observed effect is incorporated into the Steinberg-Guinan model (Steinberg *et al.*, 1980), which plots the yield strength (Eq. 5-21) and shear strength (Eq. 5-22) as a function of effective plastic strain, pressure and temperature. η is defined in Eq. 5-14. In addition, the postulation that shear modulus increases with increasing pressure and decreases with increasing temperature is included in Eq. 5-22. The Steinberg-Guinan strength model is used to model aluminium 2024, titanium and stainless steel 304 in this thesis.

$$Y_0\left(\left(1+\beta\varepsilon\right)^n\right)\leq Y_{max} \tag{5-20}$$

$$Y=Y_0\left(1+\left(\frac{Y'_p}{Y_0}\right)\frac{p}{\eta^{1/3}}+\left(\frac{Y'_T}{Y_0}\right)(T-300)\left(1+\beta\varepsilon\right)^n\right) \tag{5-21}$$

$$G=G_0\left(1+\left(\frac{G'_p}{G_0}\right)\frac{p}{\eta^{1/3}}+\left(\frac{G'_T}{G_0}\right)(T-300)\right) \tag{5-22}$$

(Symbols are p (pressure), Y (yield stress), Y_{max} (maximum value of yield stress), G (shear modulus), subscript 0 (reference state values of G, Y), ε (effective plastic strain), Y′ and G′ with subscripts p and T (derivatives with respect to pressure and temperature at the reference state) and β, n (constants defining the work hardening).)

5.4.7 Mohr-Coulomb strength model

The Mohr-Coulomb formulation (van der Hoek(a), 1978; van der Hoek(b), 1978; Hancock, 1979) is not represented by an analytical equation but by a tabulation of pressure versus yield strength for compression and tension. It was formulated to model the behaviour of brittle materials (e.g. concrete). The curve drops off rapidly towards zero as the pressure goes into the tensile regime. A typical form is shown in Figure 5-2(a). The curve is only described by four points and the tensile failure limit. Therefore, it is not a smoothly changing function. The Mohr-Coulomb model is used to model soda-lime glass in this thesis (Tsembelis, 1998). The glass analogue model (GAM) is shown in Figure 5-2(b). Note that the smooth curve of

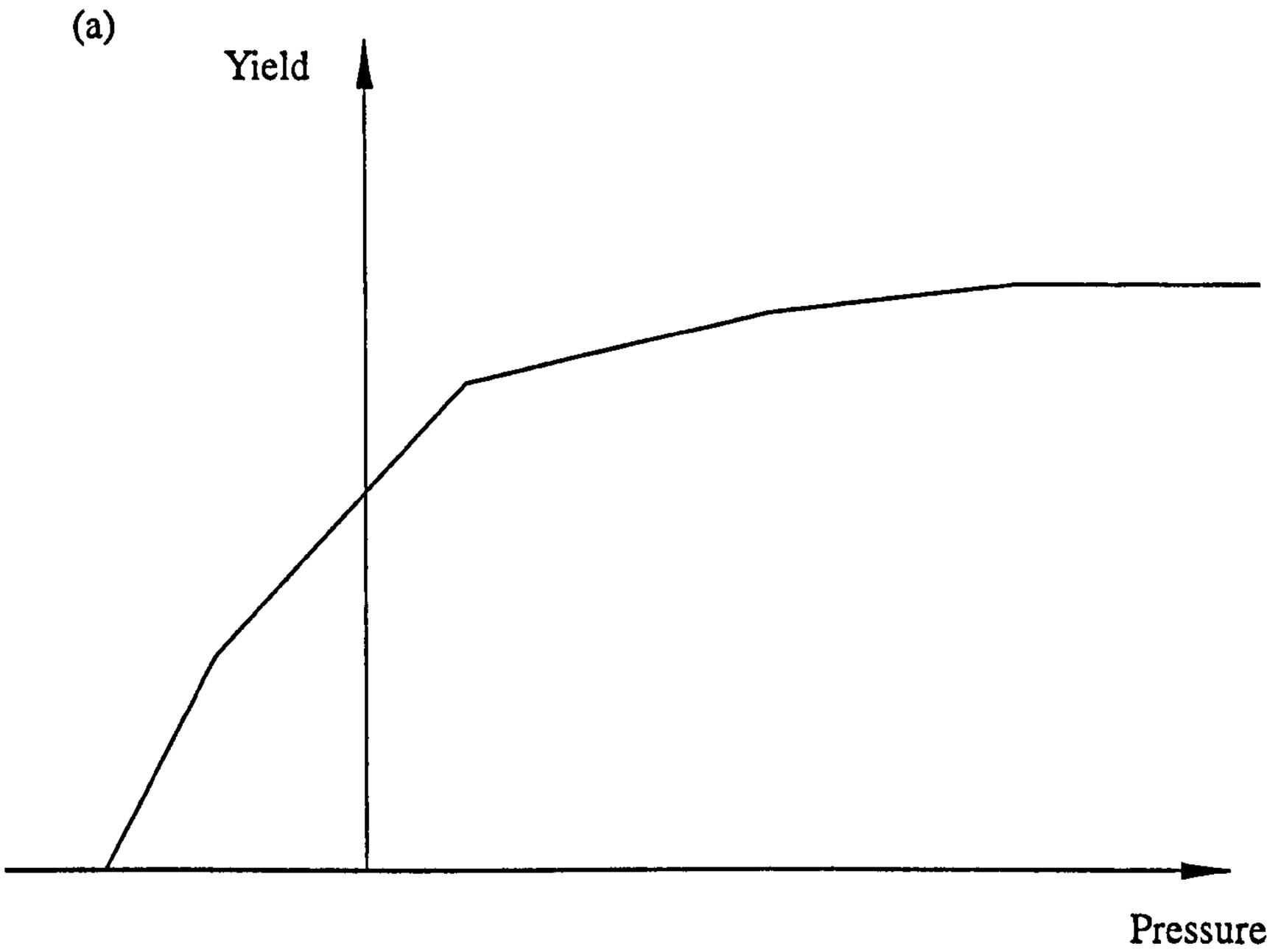

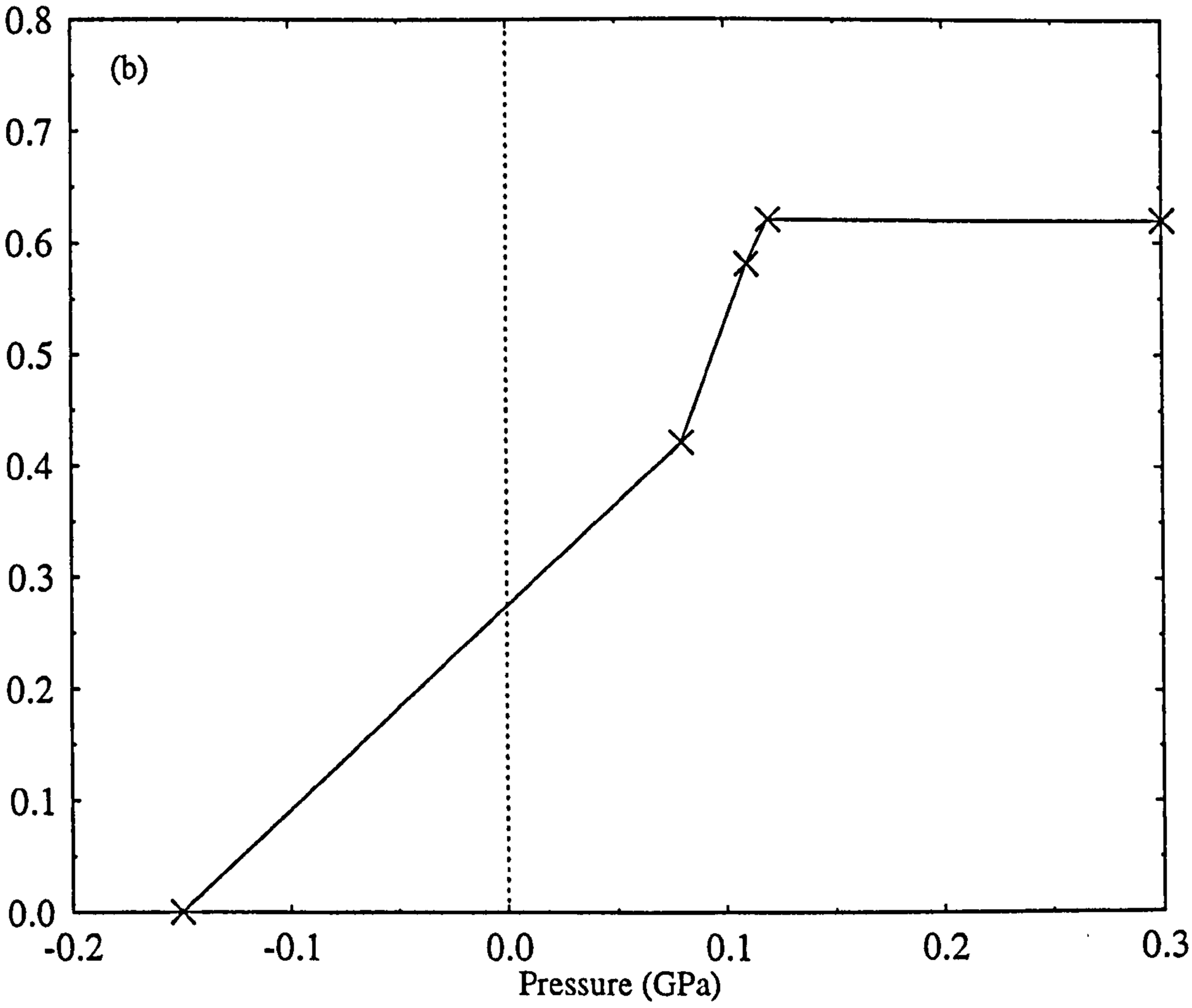

Figure 5-2. (a) Generic form of the Mohr-Coulomb yield strength-pressure curve

(b) The Mohr-Coulomb Glass Analogue Model (GAM) (Tsembelis, 1998) for soda-lime glass.

Figure 5-1(a) is not reproduced by the experimental data in Figure 5-2(b). Figure 5-2(b) is calculated from experimental observations.

5.4.8 Von Mises strength criterion

The von Mises strength criterion (von Mises, 1928) describes the limit between elastic and plastic flow. The onset of yielding (Y) is a function of the principal stresses σ_x, σ_y, σ_z. The von Mises criterion is used to model nylon in this thesis.

$$2Y^2=(\sigma_x-\sigma_y)^2+(\sigma_y-\sigma_z)^2+(\sigma_z-\sigma_x)^2 \qquad (5\text{-}23)$$

5.4.9 Failure models

As real materials are not able to withstand tensile stresses which exceed the local (microscopic) tensile strength due to crack opening and propagation, a failure model has to be implemented into a hydrocode to take account of this behaviour. There are three types of failure models: bulk, directional and cumulative damage. The bulk failure model is the simplest and allows for failure when a variable reaches a set value. Directional failure models, as directionally dependent failure models, can identify failure such as spalling and delamination. One such model, the principal stress failure model, is a directional failure model used in this thesis. After failure, the material is assumed to be isotropic, to have no shear strength but to be able to sustain positive hydrodynamic pressures. There are two user defined variables: (i) maximum tensile failure stress and (ii) maximum shear stress. Material failure is initiated if either the value for (i) or (ii) is exceeded. Cumulative damage models take account of the fact that the strength of certain brittle materials (ceramics, concrete, glass) is reduced by compression (and the associated microfracture). The damage factor is a function of the strain to which a material is subjected. It is also used to represent the response of metals which are stressed below the failure limit, but still spall. Cumulative damage models are used in the Johnson-Cook and Johnson-Holmquist models.

5.5 Johnson-Holmquist Model

The Johnson-Holmquist 2 model (Holmquist *et al.* 1995, derived from the original model published by Johnson and Holmquist, 1993) is applicable to brittle materials subjected to large strains, high strain rates and high pressures. It incorporates the experimental observation that a brittle material has significant strength after fracture damage, and includes strain rate and bulking effects. It was developed for the ballistic impact regime and is principally a phenomenological rather than a theoretical model. It gives the yield strength as a function of pressure (as in the Mohr-Coulomb model, section 5.4.7). The yield strength is also a function of damage, the residual strength in fractured material, dilation (bulking, reported by Holve and Cagnoux, 1990) and strain rate effects. This makes it a much more sophisticated model for modelling the strength of glass under hypervelocity impact.

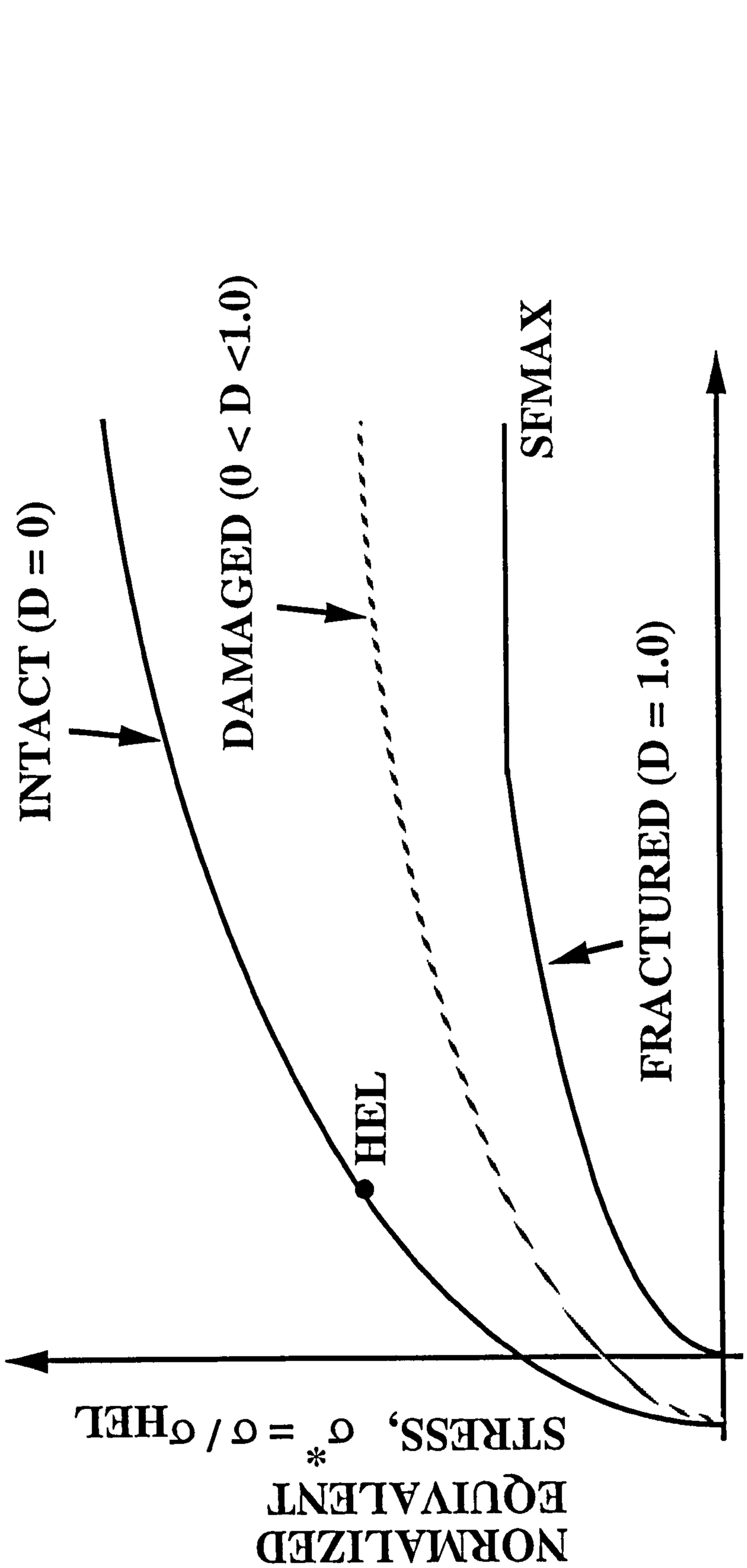

Figure 5-3. The Johnson-Holmquist model. The strength of the material is a smoothly varying function of the (normalised) intact strength (σ^*_i), fracture strength (σ^*_f), strain rate ($d\varepsilon/dt$) and damage (D).

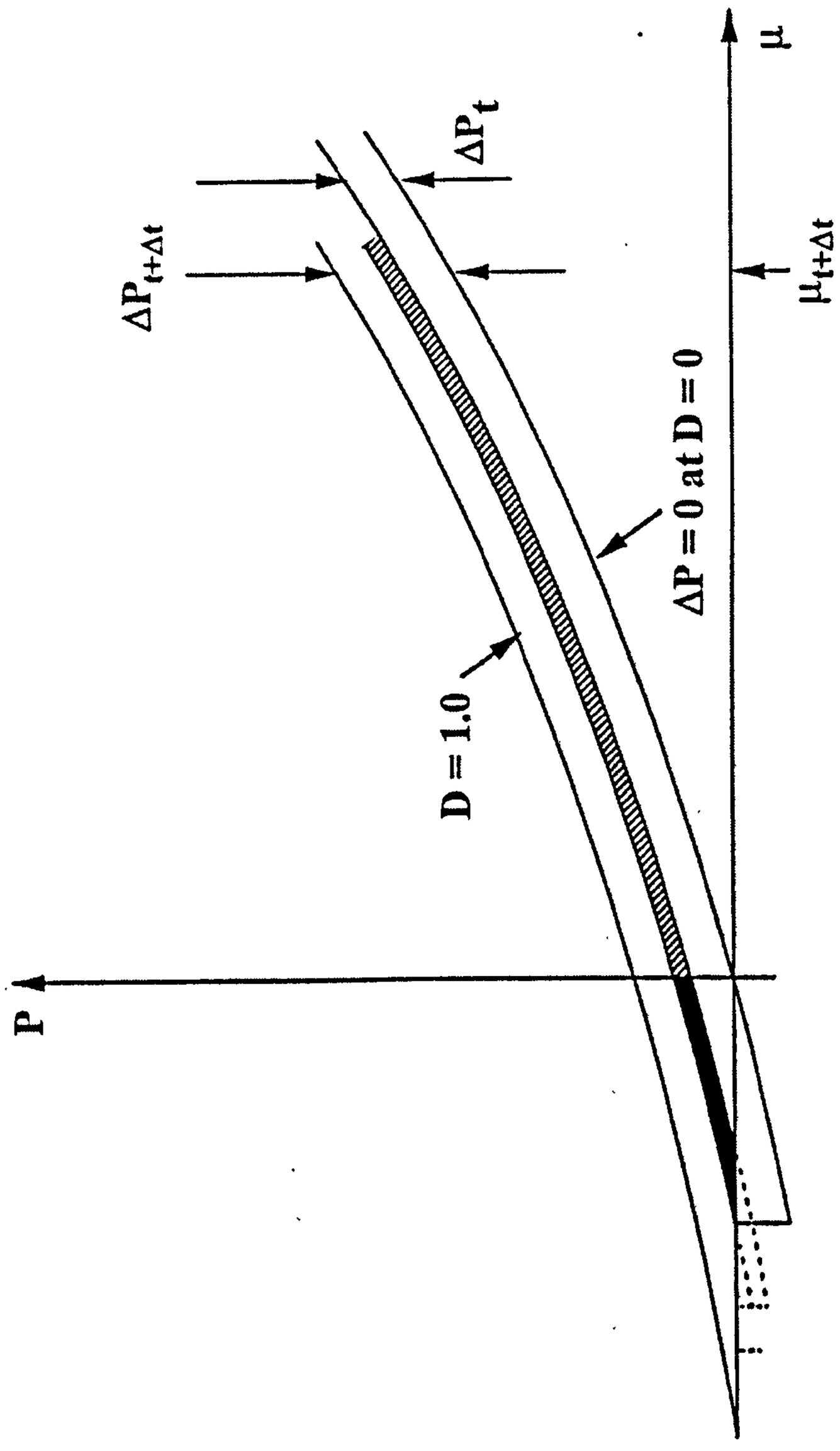

Figure 5-4. The Johnson-Holmquist model. The equation of state, including the dilation pressure (ΔP) is a function of damage (D).

However, the polynomial equation of state, as used in the Johnson-Holmquist model, is not suited to modelling phase changes. The general formulation of the polynomial equation of state does allow for energy dependence (Eqs. 5-4 and 5-5). The Johnson-Holmquist 2 model is referred to as the Johnson-Holmquist, or J-H, model in this thesis.

The yield strength is a damage based interpolated function (D) of intact and fracture strength (Eq. 5-24). It defines both the equation of state and the strength model. The material strength and equation of state and dilation pressure are given in Figures 5-3 and 5-4. The intact and fractured strengths are represented by Eqs. 5-25 and 5-26 where A, N, M, C andB are experimentally determined material constants. The fractured material strength is 'capped' by the SFMAX parameter, which is a user variable.

$$\sigma^*=\sigma_i^*-D(\sigma_i^*-\sigma_f^*) \tag{5-24}$$

$$\sigma_i^*=A(P^*+T^*)^N(1+C\ln\dot{\varepsilon}^*) \tag{5-25}$$

$$\sigma_f^*=B(P^*)^M(1+C\ln\dot{\varepsilon}^*) \tag{5-26}$$

The normalised stresses (σ^*, σ_f^*, σ_i^*) are obtained by dividing σ, σ_i and σ_f by σ_{HEL} at the Hugoniot Elastic Limit (HEL); similarly, P* is the normalised hydrostatic pressure (P/P_{HEL}) and T* is the normalised maximum tensile hydrostatic pressure (T/P_{HEL}). (P_{HEL} is the pressure at the Hugoniot Elastic Limit.)

$$D=\sum \frac{\Delta\varepsilon^p}{\varepsilon_f^p} \tag{5-27}$$

$$\varepsilon_f^p=D_1(P^*+T^*)^{D2} \tag{5-28}$$

The fracture damage is calculated by summing the plastic strain at each computational step of the hydrocode, in a manner similar to that used in the Johnson-Cook fracture model. $\Delta\varepsilon_p$ is the plastic strain during a cycle of integration (Eq. 5-27) and ε^f_p is the plastic strain to fracture under constant P (Eq. 5-28).

The Johnson-Holmquist model was formulated with a polynomial equation of state which is energy independent. It also includes a term (ΔP) to describe the dilantancy of the glass, where the volume of the glass (and thus the force exerted) increases as a result of fracture (Holve and Cagnoux, 1990) (Eq. 5-29). The incremental internal elastic energy decrease (due to decreased shear and deviator stresses) is converted to potential internal energy by

incrementally increasing ΔP (Eq. 5-30). K1, K2 and K3 are material constants, obtained from fits to experimental data. β is the fraction of elastic material energy that is converted from elastic to hydrostatic energy ($0 \leq \beta \leq 1$). μ is the fractional density increase in the material ($\mu=(\rho/\rho_0-1)$.

$$P=K1\mu+K2\mu^2+K3\mu^3+\Delta P \tag{5-29}$$

$$\Delta P_{t+\Delta t}=-K1\mu_{t+\Delta t}+\sqrt{(K1\mu_{t+\Delta t}+\Delta P_t)^2+2\beta K1\Delta U} \tag{5-30}$$

The J-H model constants (A, N, B, M, C, D_1, D_2) (Table 5-2) were obtained from flyer plate tests and ballistic long-rod penetration tests onto soda-lime glass at 1.5 - 2.4 km s^{-1} (Holmquist *et al.*, 1995).

Table 5-2. Constants used in the Johnson-Holmquist model

Constant	Value	Constant	Value	Constant	Value
A	0.93	T(GPa)	0.15	K1	45.4
N	0.77	HEL(GPa)	5.95	K2	-138.0
B	0.088	D1	0.053	K3	290.0
M	0.35	D2	0.85		
C	0.003	SFMAX	0.5		

Because the equation of state is energy independent, it cannot model phase changes. The model is therefore not ideally suited to modelling hypervelocity impacts onto glass because melting and vaporisation may occur during the impact. However, the strength model is much more appropriate than the simplistic Mohr-Coulomb model. A modification to the Johnson-Holmquist equation of state has been proposed by Tsembelis (1998) to allow the insertion of an energy dependent shock equation of state. In addition the constants (for the hydrostat, damage and fractured material strength) were determined partly by a computational iterative technique. Hydrocode simulations were carried out and the results compared with ballistic impact tests and flyer plate tests. The constants were adjusted to improve the simulation results. As the Johnson-Holmquist model has a large number of constants, the values obtained by matching the simulations to the flyer plate tests and ballistic depth of penetration tests may not be appropriate for use with hypervelocity impact simulations in the regime of 5-15 km s^{-1}. However, it is beyond the scope of this thesis to carry out a full range of simulations using published depth of penetration data from ballistic tests, flyer plate data and hypervelocity impact shots to develop a new range of constants for the Johnson-Holmquist model.

5.6 AUTODYN-2D and 3D: Validation for HVI Regime

AUTODYN is an interactive non-linear transient dynamic computer code that runs on PC and UNIX workstations (Birnbaum *et al.*, 1987; Robertson *et al.*, 1993). It incorporates

Lagrangian, Eulerian (1st order) and Smoothed Particle Hydrodynamics (beta-release code version only) processors. A wide range of space retrieved data onto thick and thin, ductile targets has been used to validate AUTODYN-2D and AUTODYN-3D (McDonnell *et al.*, 1993; Hayhurst *et al.*, 1995; Hayhurst and Clegg, 1997). A simplified Johnson-Holmquist model (Lundberg *et al.*, 1996) and a crack based damage model (Hazell and Iremonger, 1997) have been implemented as user subroutines and used to investigate the response of ceramic materials to ballistic impact and flyer plate impact respectively. A full implementation of the Johnson-Holmquist model was used to test against hypervelocity impacts onto soda-lime glass (Taylor *et al.*, 1997a). The code has also been used for simulation of hypervelocity impact on solar cells (McSherry, 1996).

5.7 Simulation Programme

Table 5-3. Simulation set-ups. Type 1 and 2 refer to two different mesh configurations for projectiles.

Parameter	Reproduction of experimental results	Comparison with damage equations
Models used	Johnson-Holmquist/GAM	Johnson-Holmquist
Scheme	Lagrange	Lagrange
Projectile (i, j)	(1, 41) (1,21) Type 2	(1, 11) (1, 21) Type 1
Target (i, j)	(1, 100) (1, 100)	(1, 150) (1, 150) semi-infinite
Target size	152.4 by 25.4 mm	100 by 100 mm
Impact velocity	5 km s^{-1}	5 - 15 km s^{-1}

Table 5-4. Simulations run using the Johnson-Holmquist model and GAM (β variable, no strain rate dependence for the Johnson-Holmquist model)

Model	Projectile	0.8 mm	1.0 mm	1.2 mm	1.5 mm	2.0 mm
Johnson-Holmquist	Nylon	no	no	no	no	no
Johnson-Holmquist	Al 2024	no	yes	no	no	no
Johnson-Holmquist	Ti	no	yes	no	no	no
Johnson-Holmquist	S/S 304	no	yes	no	no	no
Mohr-Coulomb (GAM)	Nylon	no	no	yes	yes	no
Mohr-Coulomb (GAM)	Al 2024	yes	yes	yes	yes	yes
Mohr-Coulomb (GAM)	Ti	no	yes	no	no	no
Mohr-Coulomb (GAM)	S/S 304	yes	yes	yes	no	no

Simulations have been carried out for spherical nylon, aluminium 2024, titanium and stainless steel 304 projectiles onto glass using both the Johnson-Holmquist model (this thesis) and the GAM (Tsembelis, 1998). The Johnson-Holmquist bulking parameter (β) and strain rate dependence (C) were investigated for their influence on the simulation results. The

projectile materials used were the most appropriate models available in the open (non-classified) literature. Two target meshes were used to simulate (i) the experimental results from section 2.4 (ii) a semi-infinite target. The mesh set-ups are shown in Table 5-3. The simulations carried out are shown in Table 5-4.

5.8 Results

In this section the results from the Johnson-Holmquist simulations are presented and compared with experimental data (section 2.4), damage equations (section 3.3) and data from a parallel glass modelling programme using the GAM (Tsembelis, 1998).

5.8.1 Morphology of simulations and basic parameters

The morphology of a hypervelocity impact on glass has been reviewed in figures 2-9 and 2-11. The depth of penetration, central pit and larger conchoidal/spallation diameter are quantitative and qualitative measurements which one would look for in a hydrocode simulation of a hypervelocity impact. The conchoidal diameter refers to the petaloid features noted on smaller impact sites, whilst the spallation diameter refers to the different morphology noted on impact sites caused by millimetre-size impactors. The larger damage parameter is referred to as the spallation diameter, as the simulations carried out in this chapter are using millimetre-sized projectiles. In Figure 5-5, a plot of material state is shown for a crater produced by a 1 mm Ti projectile at 5 km s^{-1} for the (a) Johnson-Holmquist and (b) GAM (Tsembelis, 1998) models. The damage parameter (D) is plotted for the J-H simulation, representing the degree of fracture of the glass target. This parameter is not available in the Mohr-Coulomb model, so the yield stress is used to represent the material state. In both (a) and (b) a central 'hemispherical' pit with a region of 'spallation' surrounding the pit is noted. However, as noted in Taylor *et al.* (1997a), the Johnson-Holmquist model does not reproduce spallation diameters as observed on experimental targets. The tentative conclusion is that the Johnson-Holmquist model is applicable to compressive regimes but does not appear to predict tensile fracture. The large spallation diameter (Figure 2-11) is formed by tensile fracture and is not reproduced by either the Johnson-Holmquist or GAM simulations. The larger 'spallation' diameter noted in Figure 5-5(b) may be because a different failure criterion was used in the model (section 5.4.9). The hydrocode crater diameter D_c value also cannot be accurately compared with the experimentally determined D_c value (Figure 2-11). The two stage formation process for the conchoidal diameter has been discussed in Taylor *et al.* (1998), where a central pit forms, followed by radial crack formation and petaloid spallation. The initial transient crater profile is lost when the front surface is spalled off. However, the hydrocode simulation cannot reproduce accurately the second stage of formation as the model cannot simulate tensile fracture. Therefore, energy which might have been allocated within the calculation to spall fragments off is instead 'used' for continuing crater expansion in the simulation. However, as discussed in Taylor *et al.* (1997d), the energy required to make a crack run is a small

(a)

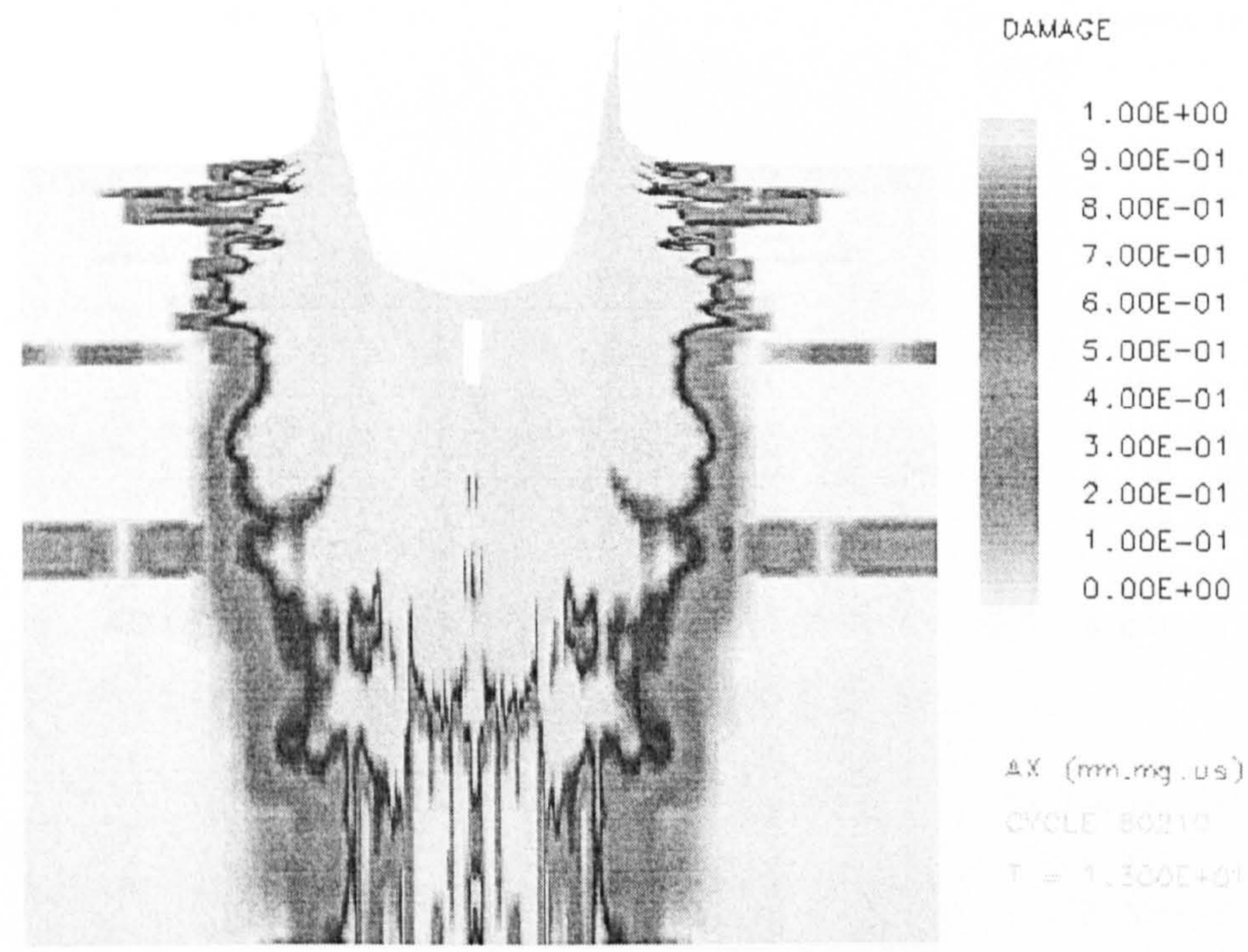

(b)

Figure 5-5. (a) 1mm Ti projectile at 5 km s^{-1} onto a semi-infinite Johnson-Holmquist glass target showing the damage (D=1 under the central pit). (b) as (a), but for a Mohr-Coulomb simulation. There is a larger 'spallation' region due to the differing failure criteria between the Mohr-Coulomb and Johnson-Holmquist models.

(a)

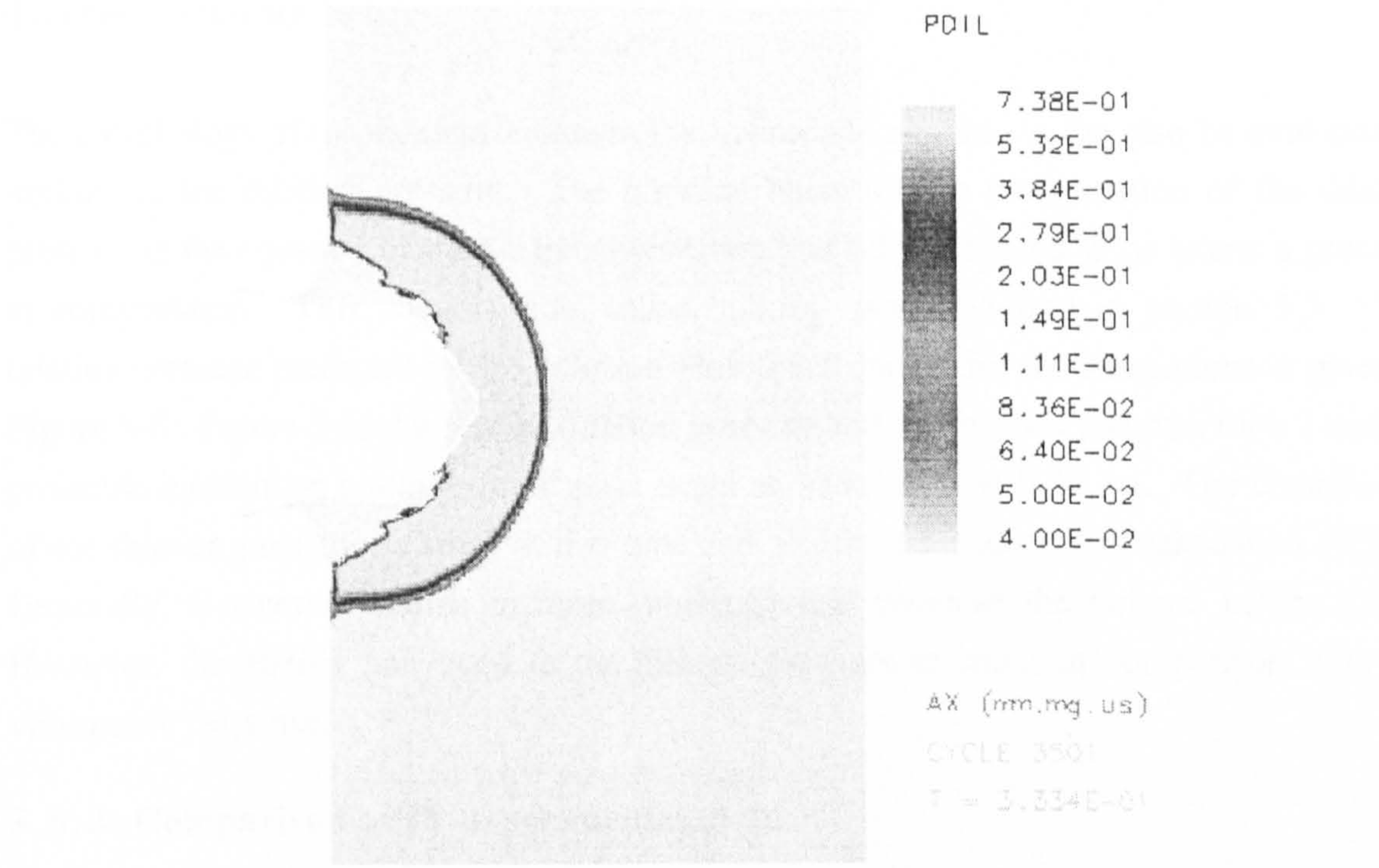

(b)

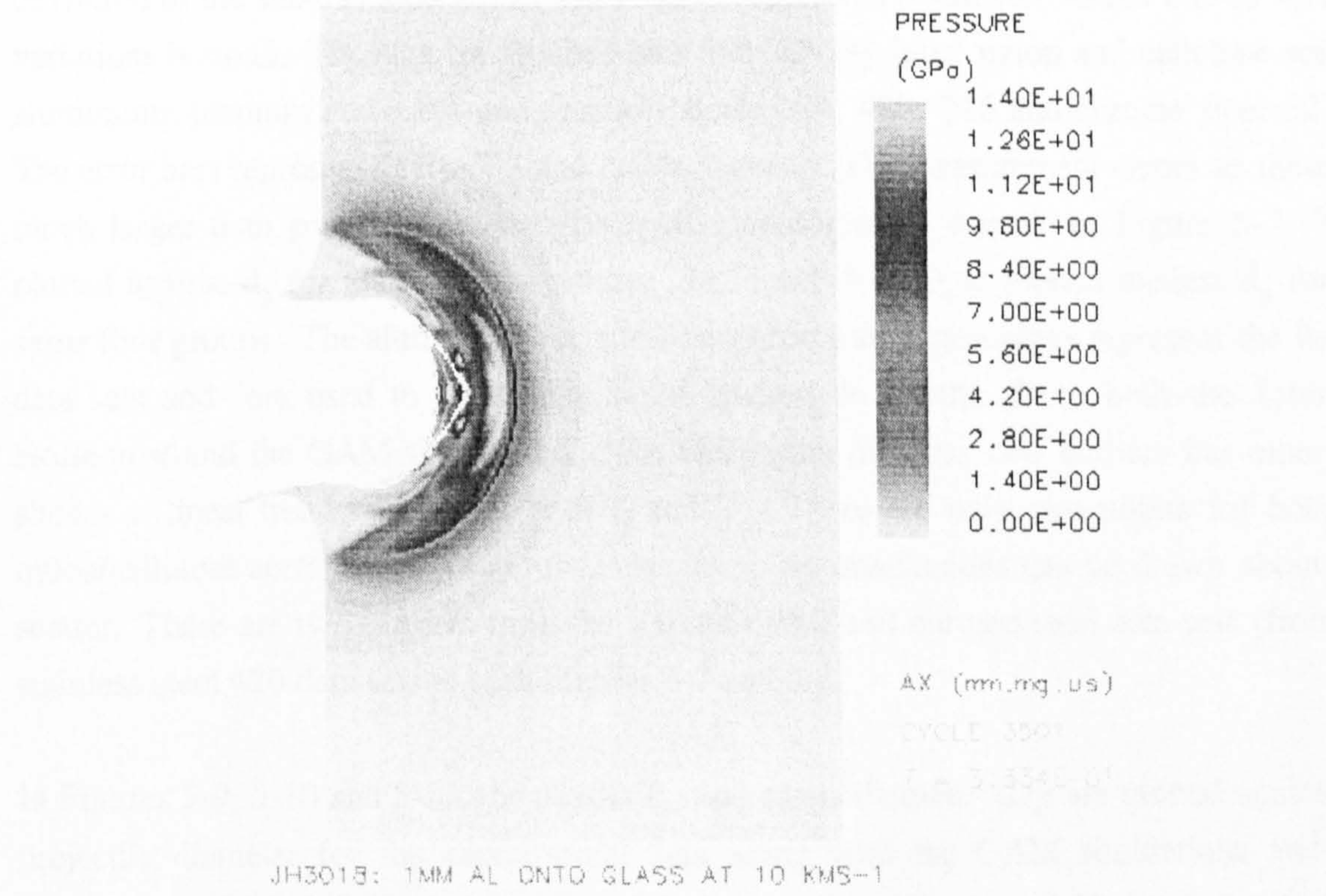

Figure 5-6. (a) 1mm Al projectile at 10 km s^{-1} onto a semi-infinite Johnson-Holmquist glass target: dilation pressure at 0.33 ms. (b) as (a), but showing total pressure. The contribution of the dilation pressure to the total is small.

fraction of that available during a hypervelocity impact. Therefore, the difference in crater diameter should not be large.

The morphology of the damage feature in the hydrocode simulation can also be explored by looking at the dilation pressure. The physical basis for the incorporation of the dilation pressure in the equation of state is the observation that fully fractured glass exerts a pressure in compression. This phenomenon, called bulking, was reviewed in section 5.5. The dilation pressure predicted by the Johnson-Holmquist model for the simulations is given in Figure 5-6. Figure 5-6(a) gives the dilation pressure and 5-6(b) total pressure for a 1 mm Al projectile incident on a semi-infinite glass target at 10 km s^{-1}, at 0.33 μs. The contribution of the dilation pressure is small at this time and also at the end of this calculation (15μs). Generally, a material volume increase (bulking) will decrease the volume of the crater. However, the energy converted to the dilation pressure is small in comparison with the volumetric response.

5.8.2 Comparison with experimental data

The results of the Johnson-Holmquist simulations (Table 5-4) are compared with the results of a hypervelocity impact (HVI) programme on to soda-lime glass for this thesis. The experimental data are summarised in Table 2-4 and cover projectile diameter and density ranges of 0.8 - 2.0 mm and 1 - 8 g cm^{-3} respectively. The average velocity and standard deviation of the shots is 5.06 ± 0.27 km s^{-1} so the spread in parameter values due to velocity variations is small. The data are grouped into four density bins: nylon and cellulose acetate; aluminium; titanium and ruby; and stainless steels 304, 420, 316 and chrome steel 52100. The error bars represent depth (T_c) and crater diameter (D_c) measurement errors as these are much larger than particle diameter or velocity measurement errors. In Figure 5-7, T_c is plotted against d_p for the four data groups. In Figure 5-8, D_c is plotted against d_p for the same four groups. The aluminium and stainless/chrome steel groupings represent the largest data sets and are used to test trends in the hydrocode results (from both the Johnson-Holmquist and the GAM simulations). The aluminium data has two outliers but otherwise shows a linear trend with d_p for both T_c and D_c. There are only two points for both the nylon/cellulose acetate and Ti and ruby data sets so no conclusions can be drawn about data scatter. There are two outliers from the stainless steel and chrome steel data sets (from the stainless steel 420 data set) in both Figures 5-7 and 5-8.

In Figures 5-9, 5-10 and 5-11, the depth (T_c) and crater diameter (D_c) are plotted against the projectile diameter for the experimental data along with the GAM simulations and J-H simulations. The GAM simulations are from Tsembelis, 1998. The J-H simulations shown have $\beta = 1$ and no strain rate dependence (the baseline model set-up). In Figure 5-9, the experimental values of T_c and D_c (for aluminium projectiles) show an increasing trend with projectile diameter. The GAM T_c simulations are close in value to the experimental data,

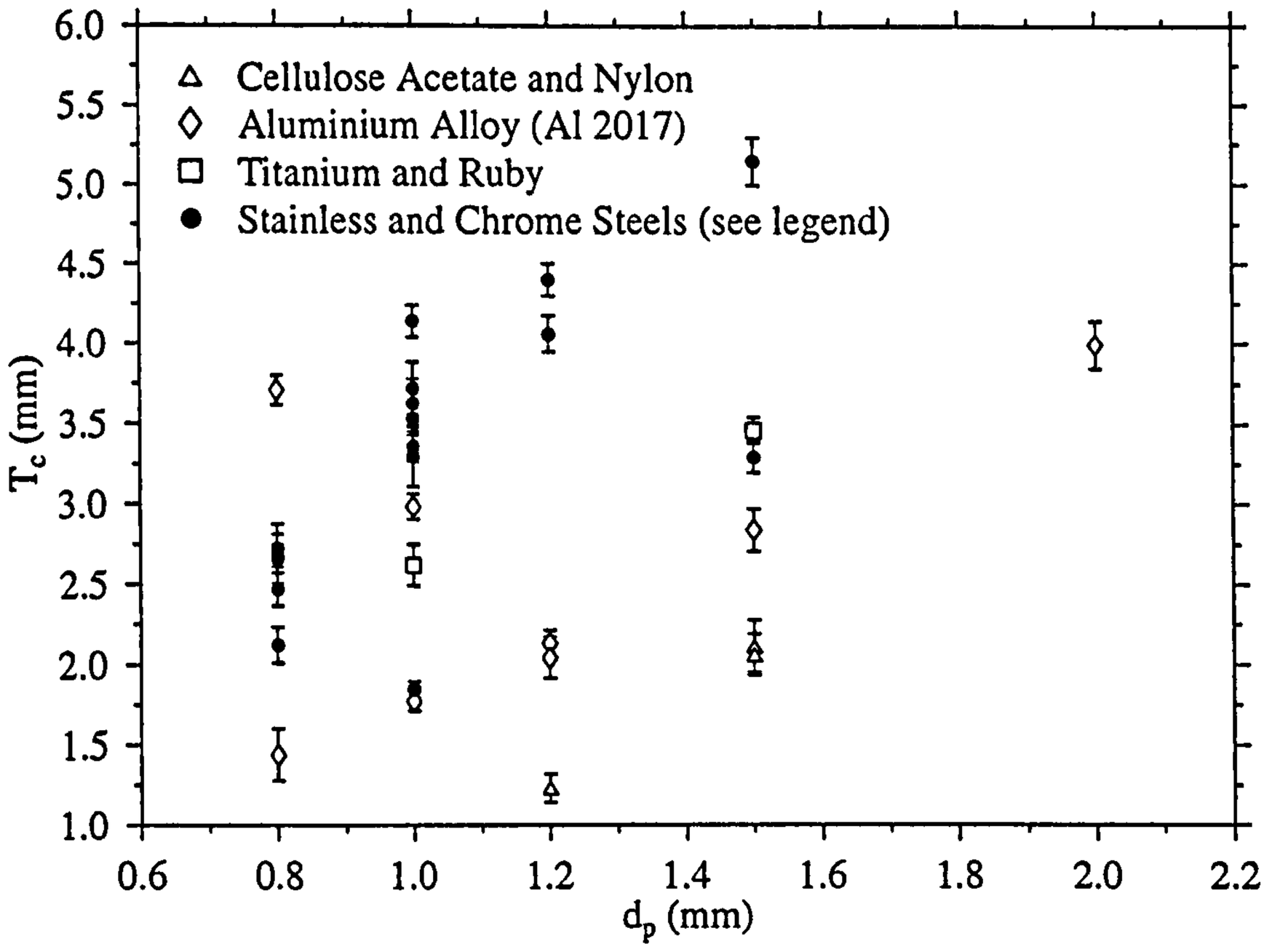

Figure 5-7. Experimental data from the Taylor(b) shot programme (Taylor et al., 1997a).

Crater depth (T_c) is plotted against projectile diameter for the four projectile density groups (Stainless steels 304, 316, 420 and chrome steel 52100 used as projectiles).

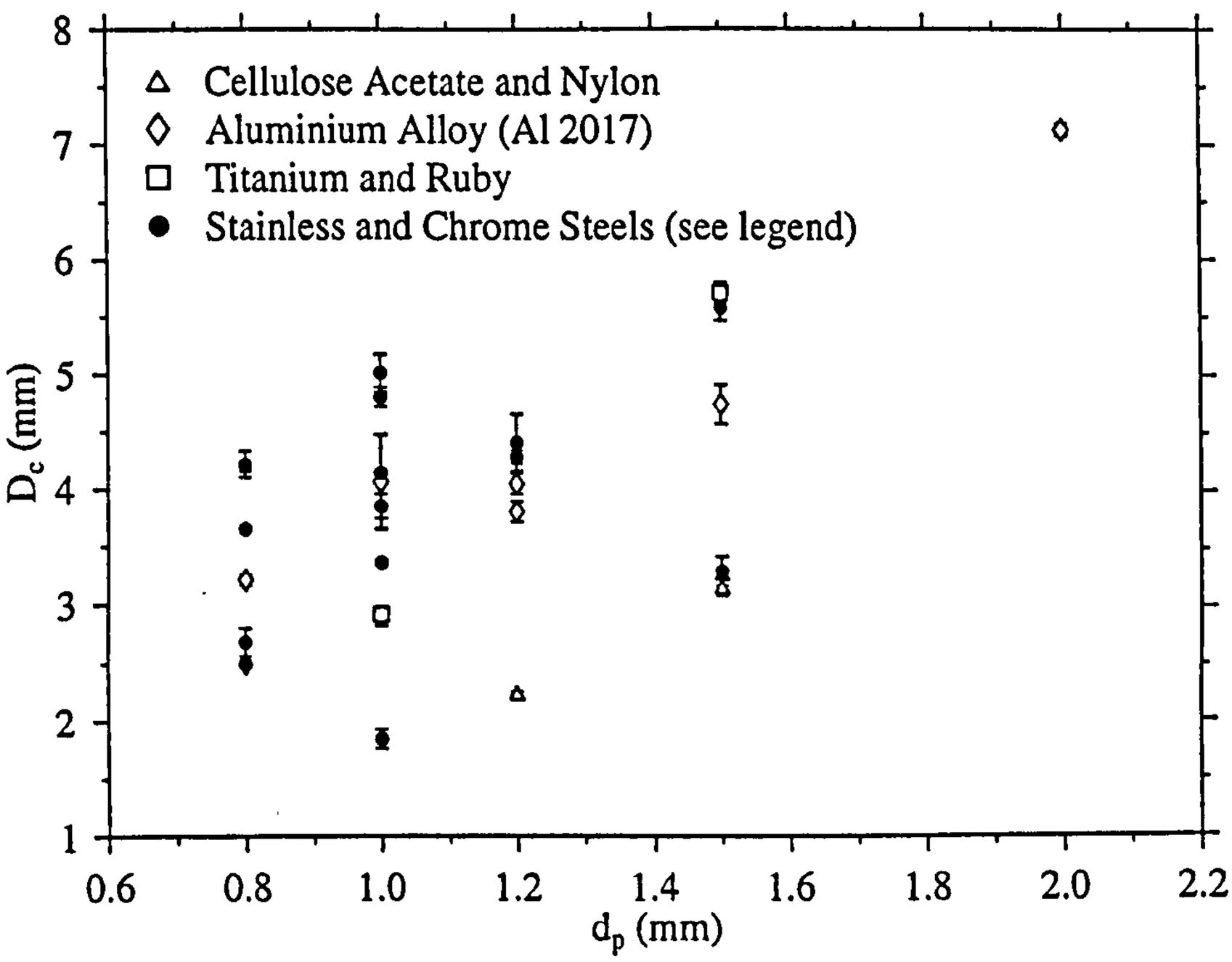

Figure 5-8. Experimental data from the Taylor(b) shot programme (Taylor et al., 1997a).

Crater diameter (D_c) is plotted against projectile diameter for the four projectile density groups. (Stainless steels 304, 316, 420 and chrome steel 52100).

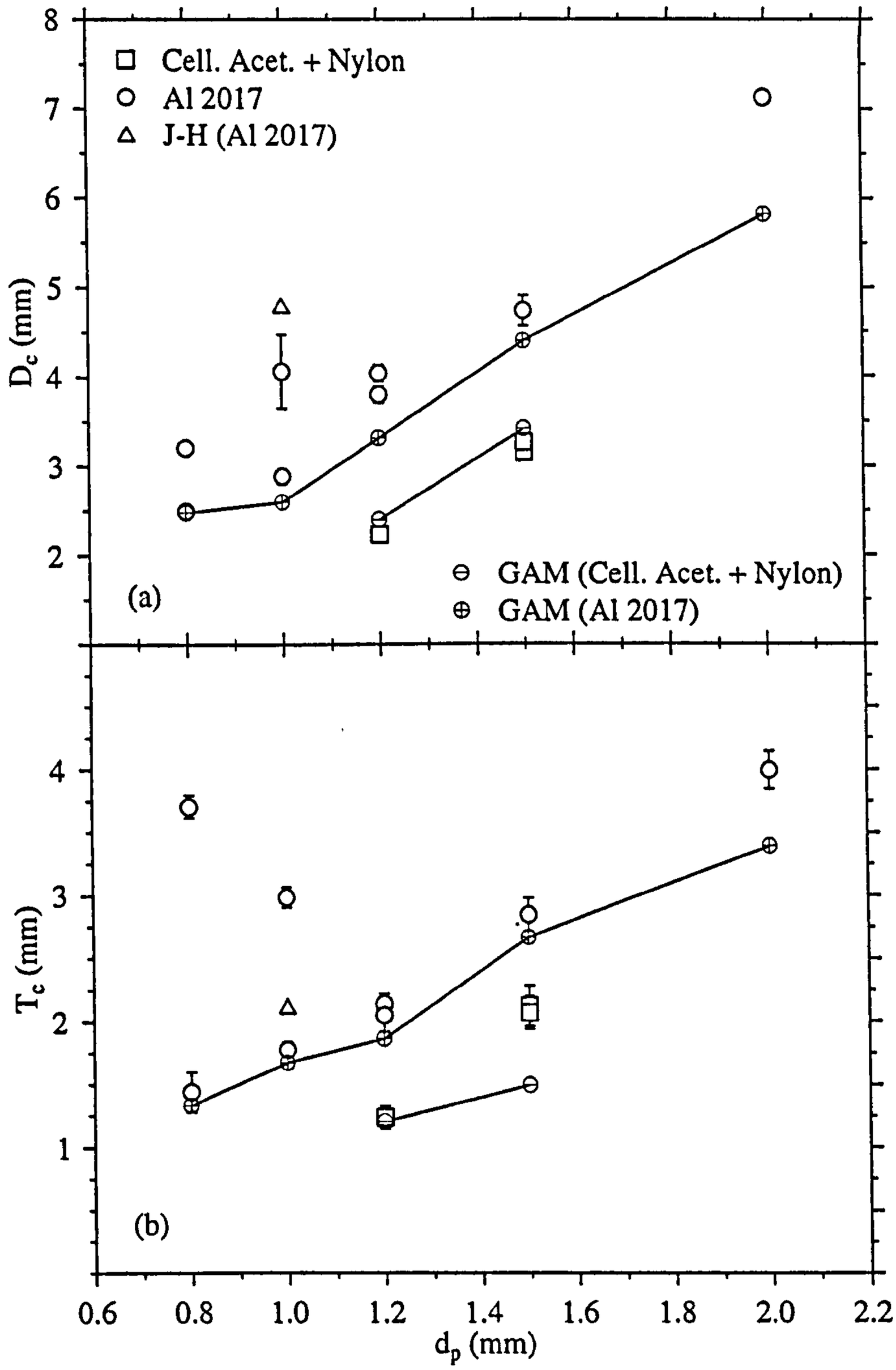

Figure 5-9. J-H and GAM hydrocode simulations compared to data from the Taylor(b) shot programme (Taylor et al., 1997a). (a) Crater diameter (D_c) and (b) crater depth (T_c) are plotted against projectile diameter (d_p) for cellulose acetate, nylon and Al 2017 projectiles.

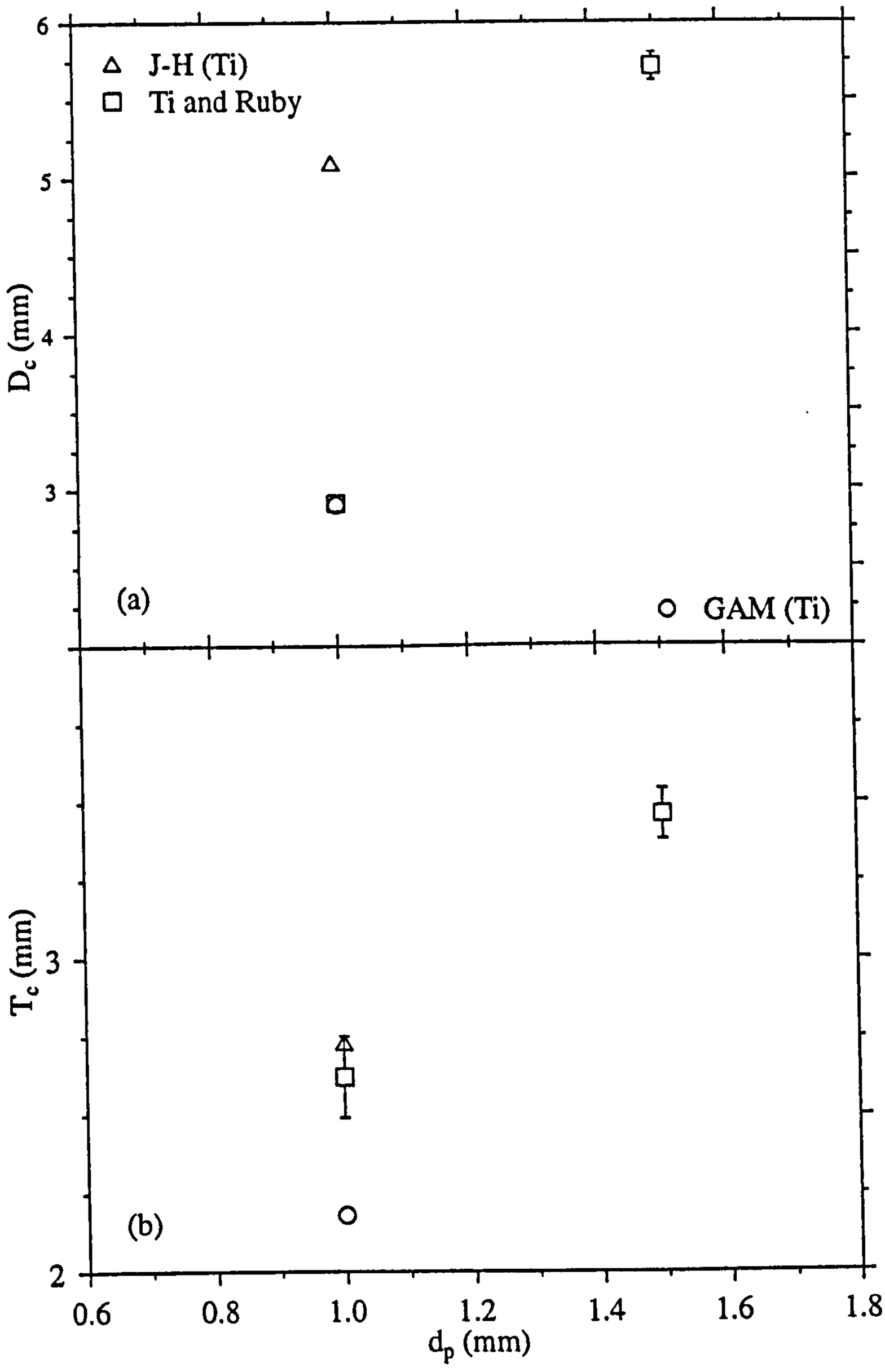

Figure 5-10. J-H and GAM hydrocode simulations compared to data from the Taylor(b) shot programme (Taylor et al., 1997a). (a) Crater diameter (D_c) and (b) crater depth (T_c) are plotted against projectile diameter (d_p) for titanium (Ti) and ruby projectiles.

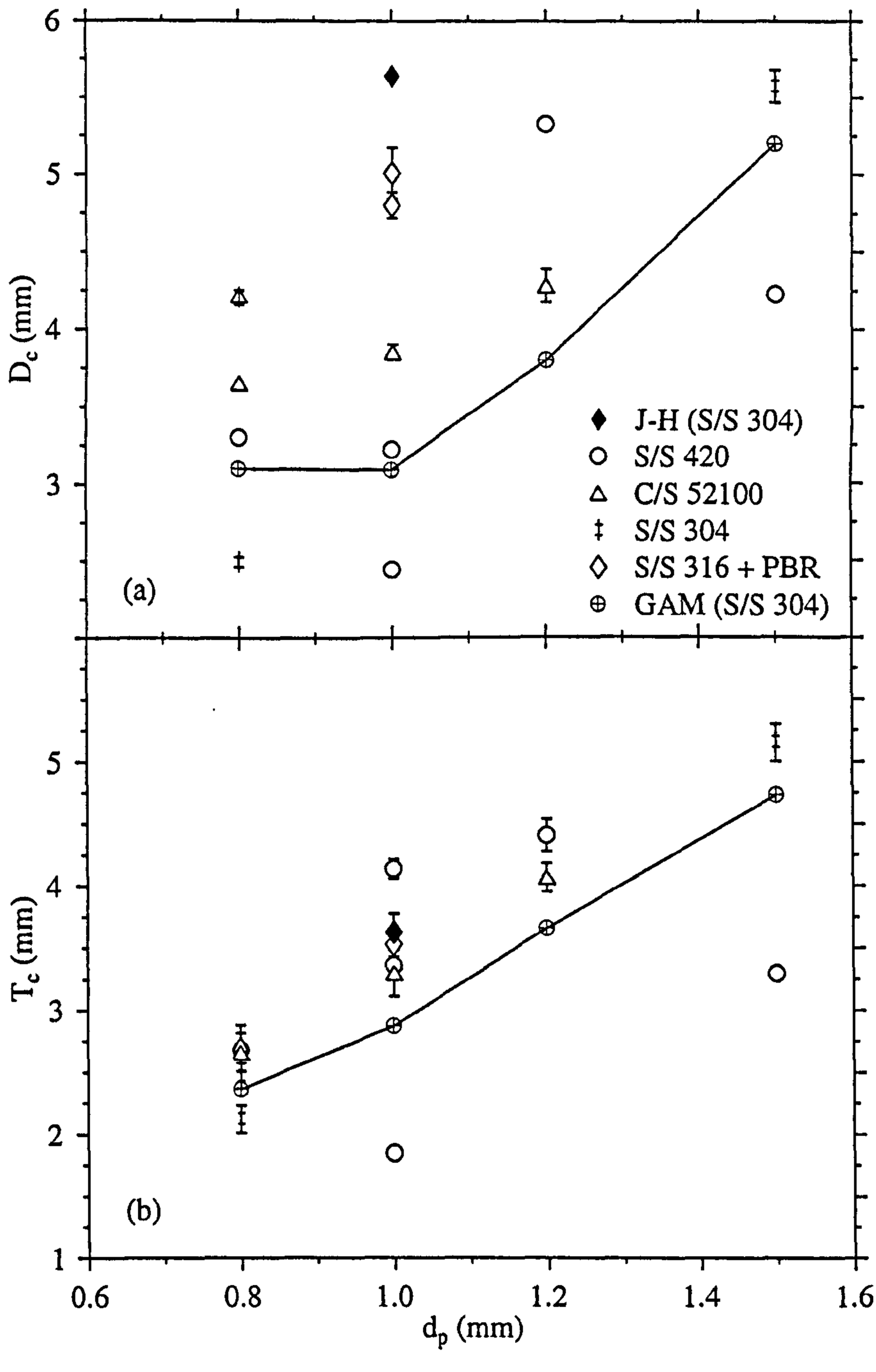

Figure 5-11. J-H and GAM hydrocode simulations compared to data from the Taylor(b) shot programme (Taylor et al., 1997a). (a) Crater diameter (D_c) and (b) crater depth (T_c) are plotted against projectile diameter (d_p) for stainless steel 304+316+420 and chrome steel 52100 projectiles (S/S: stainless steel; C/S: chrome steel)

while the J-H simulations over-predict the depth of penetration by typically 10 %. However, the J-H simulations over-predict the crater diameter by typically 50 %. The GAM model under-predicts the T_c value for a 2 mm Al projectile and a 1.5 mm nylon projectile, suggesting that the under-prediction may scale with increasing projectile diameter. In Figure 5-10, there are only two data points (one each for titanium and ruby) so no conclusions can be drawn on experimental scatter. The GAM simulation predicts D_c and the Johnson-Holmquist simulation predicts T_c. Again, the J-H model significantly over-predicts the crater diameter. In Figure 5-11, 13 data points are plotted from high density projectiles (density range ρ = 7.8 - 8.1 g cm^{-3}). There are two outliers in this data set but otherwise the data show an increasing trend of depth of penetration with projectile diameter. The crater diameters are more scattered. The J-H and GAM T_c data bound the experimental data whilst it is more difficult to infer conclusions about the D_c hydrocode simulations due to the experimental scatter. However, the J-H model again appears to over-predict crater diameter. In summary, the J-H model over-predicts D_c and, to a lesser extent, T_c. The GAM model is closer to the experimental values of D_c and T_c. The GAM model description of the yield strength does not include a decrease in the yield strength as damage increases, so the target is stronger than it should be. The Mie-Gruneisen shock equation of state is suitable for solid-liquid phases of material. In contrast, the J-H model only has a polynomial equation of state which does not take into account phase changes and the energy that they require. Therefore, crater formation has more energy than the real-life situation which may account for the larger crater diameter. No strain rate dependence has been used in runs so the target is weaker than it ought to be which may explain the greater depths and diameters. However, the value of C (the strain rate dependence parameter) is only 0.003, suggesting that there is only a small strain rate dependence effect on target simulations. The simulations have been run using β = 1. If this bulking parameter is set to 1, it means that all the elastic energy lost has been converted to potential hydrostatic energy. The impact of varying C and β is explored in the next section.

5.8.3 Hydrocode simulations compared with damage equations

The shot programme (section 2.4) carried out for this thesis is in the range 5 ± 0.5 km s^{-1}. Impact velocities in LEO are typically in the range 5-20 km s^{-1} (for space debris and natural sources) although much higher velocities are possible. The Lagrangian simulations were run using the Johnson-Holmquist model for glass over a velocity range of only 5-15 km s^{-1}, due to time constraints. Dilation effects were included (β=1) but strain rate effects were not. The simulations were run for a 1 mm spherical Al projectile. The data were used to extrapolate beyond the limits of experimental calibration data and look at depth of penetration. Two damage equations based on quartz impact data (reviewed in chapter 3) are used to provide calibration points for the data. Note that these equations have been critically reviewed in chapter 4 and least squares fits to the data do not support the 2/3 velocity exponent given in Eqs. 3-1 and 3-2.

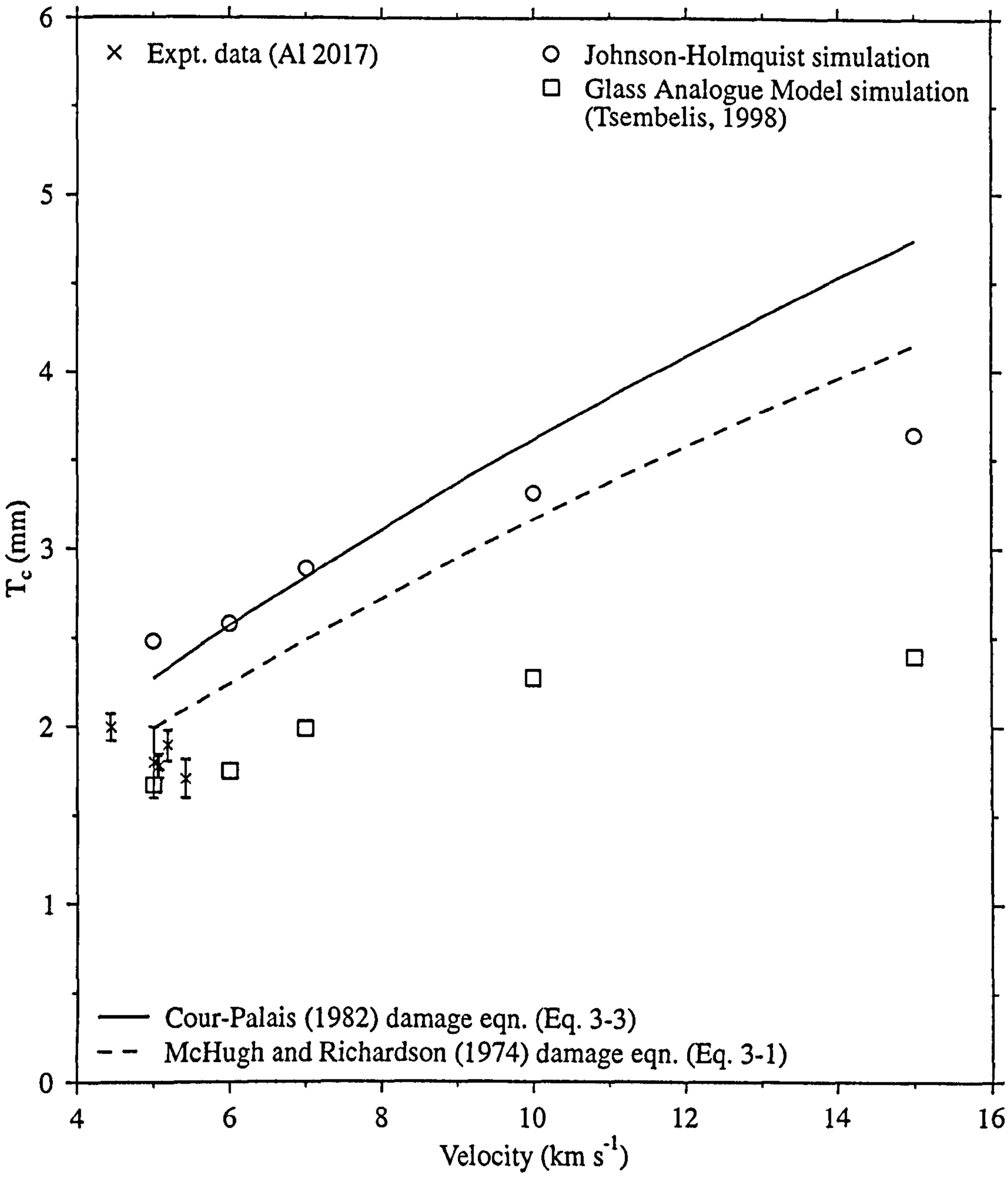

Figure 5-12. Johnson-Holmquist and Mohr-Coulomb simulations and data (Taylor (b)) compared to Cour-Palais (1982) and McHugh and Richardson (1974) damage equations. For projectile diameters not equal to 1 mm, the scaling factor (T_c/d_p) was used.

Comparison with experimental data has to be carried out with the following points in mind:-

1. There is some evidence that material type is important in determining the depth of penetration (chapters 4).
2. The hydrocode D_c value cannot be accurately compared with the experimentally determined D_c value. The transient crater profile is lost when the front surface is spalled off (Taylor *et al.*, 1997a).

The results of the simulations are given in Table 5-5. The depth of penetration is observed to form first followed by the crater diameter expansion as the simulation progresses. The results show that the hydrocode modelling values lie between the predictions of the McHugh and Richardson and Cour-Palais equations for velocities between 7 and 10 km s^{-1}. Above this value the equations start to over-predict and the turning point for under-prediction is at 6 km s^{-1}. The numbers in Table 5-5 are plotted in Figure 5-12 and clearly show the greater depth of penetration values predicted by the damage equations compared with the hydrocode simulations. The shot data from the Taylor(b) programme overlie the base of the GAM hydrocode data. The hydrocode data again are plotted in Figure 5-13, with the damage equations and the confidence bands at 75, 90 and 95 % (calculated in section 3.3.1). The difference between the hydrocode data and damage equation predictions is clear. The damage equation velocity exponents are too large compared with the hydrocode simulations. A fit to the GAM depth results produces a velocity exponent of 0.33 ($r^2 = 0.93$), whilst the fit to the Johnson-Holmquist simulations produces a velocity exponent of 0.52 ($r^2 = 0.80$). The Johnson-Holmquist simulations used a value of 2.0 for the erosion strain for all the simulations, in comparison to the sliding scale of erosion values between 2 (5 km s^{-1}) and 3 (15 km s^{-1}) used in the GAM simulations. The influence of varying erosion strain is assessed in section 5.8.4, but is found to be typically less than 10%.

Table 5-5. Results from the Johnson-Holmquist simulations in AUTODYN-2D

IDENT	Vel. (km s^{-1})	T_c (mm) at 7 μs	T_c (mm) at 15 μs	D_c (mm) at 7 μs	D_c (mm) at 15 μs	T_c (mm) (Eq. 3-1)	T_c (mm) (Eq. 3-3)
J-H 3022	5	2.46	2.48	4.30	5.00	1.99	2.27
J-H 3019	6	2.58	2.58	4.50	5.34	2.24	2.57
J-H 3020	7	2.86	2.89	4.72	5.34	2.49	2.84
J-H 3018	10	3.30	3.31	5.10	5.82	3.16	3.61
J-H 3017	15	3.54	3.64	5.92	6.44	4.15	4.74

5.8.4 Strain rate, bulking and erosion

The Johnson-Holmquist simulations were carried out without strain rate dependence. The influence of the strain rate dependence on the crater formation (parameter C, equal to 0.003) was investigated. The bulking parameter, β, was set at 1 for all the previous simulations. In this section, the effect of varying β between 0.25 and 1 is explored. The bulking parameter

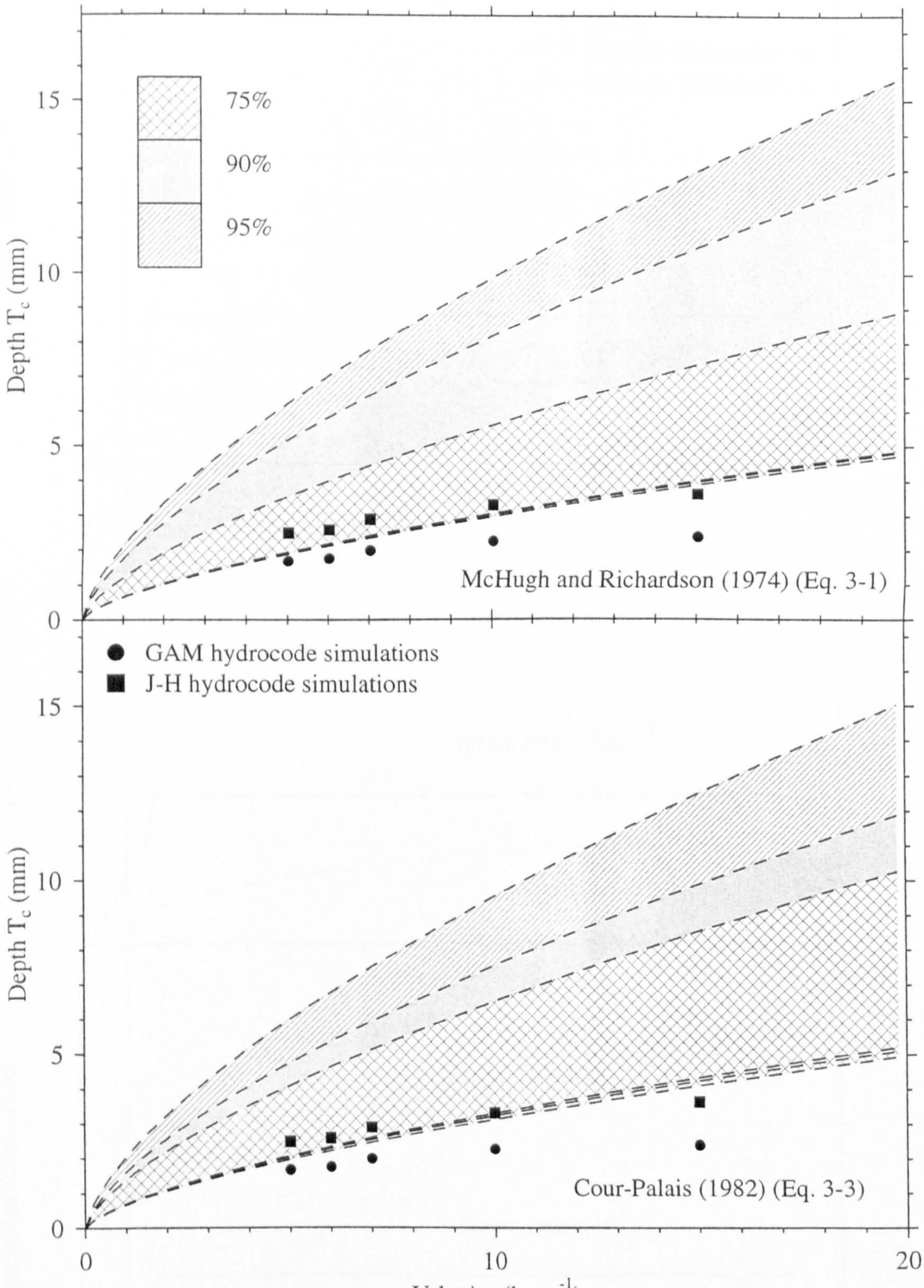

Figure 5-13. McHugh and Richardson (1974) and Cour-Palais (1982) damage equations and confidence bands (section 3.3.3) compared to Johnson-Holmquist and Glass Analogue Model (GAM) (Tsembelis, 1998) simulations. Only the upper limits are visible in this plot, as the 75, 90 and 95% lower bands overlie.

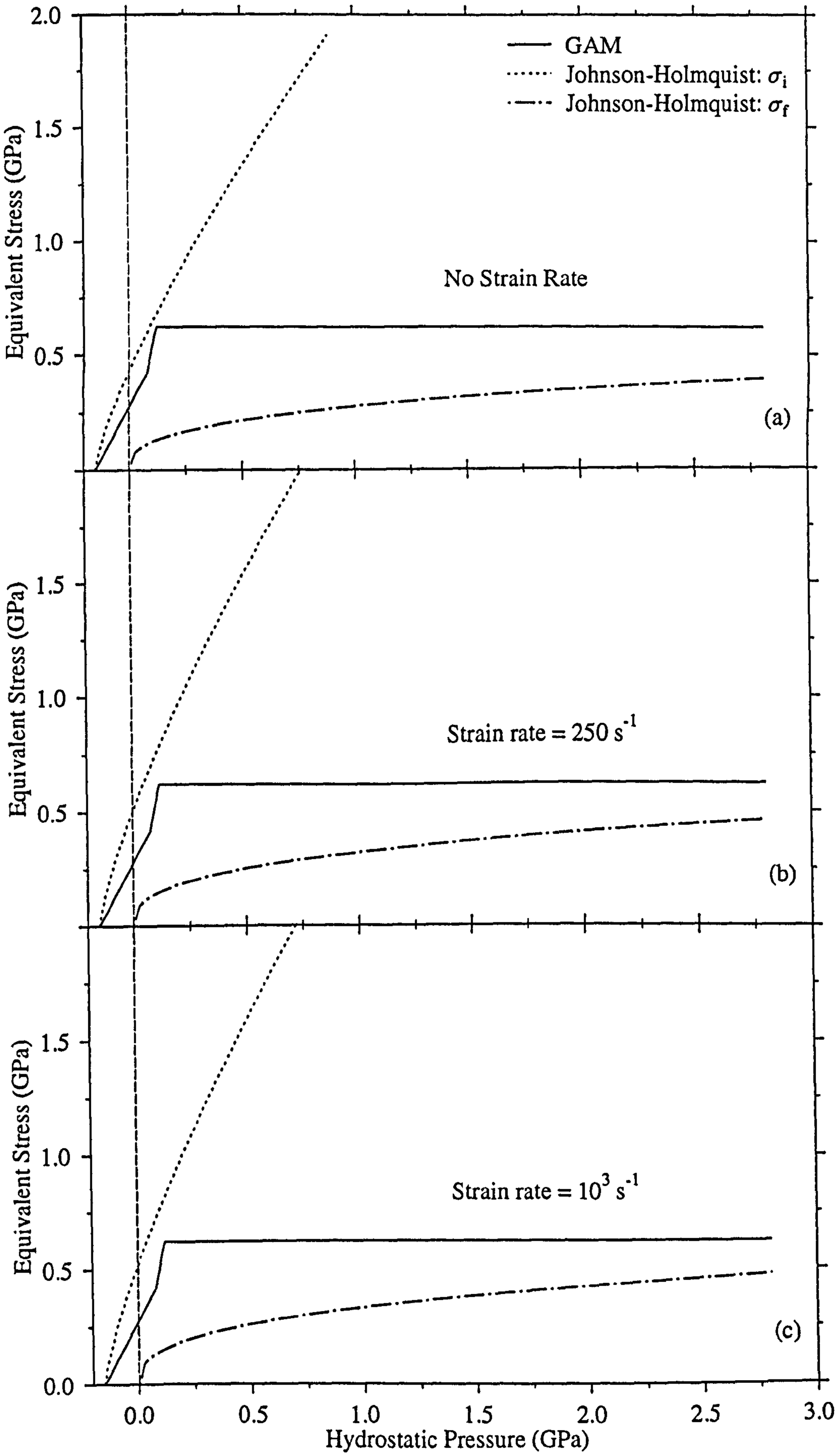

Figure 5-14. The GAM and J-H models compared

is used to represent the experimentally observed volumetric response observed in glass. However, the phenomenon has primarily been studied for impacts in the ballistic regime. Therefore, varying the value of β to investigate the dependence of crater diameter and depth on the bulking is required for hypervelocity impacts. Simulations were carried out for a 1 mm aluminium, titanium and stainless steel projectile at 5 km s^{-1} onto the target grid designed to reproduce the experimental programme described in section 2.4. The results are shown in Table 5-6 and show that decreasing the bulking parameter produces a decrease in crater depth and diameter of 5-10 % compared with the value when β = 1. The depth of penetration values remain within the experimentally produced calibration results. However, the crater diameters still over-predict the values from the Taylor(b) shot programme. In Figure 5-14, the Johnson-Holmquist model (without strain rate dependence, with strain rate dependence of 250 s^{-1} and 10^3 s^{-1}) is compared with the GAM model. The difference in the equivalent stress between strain rate equal to zero and 10^3 s^{-1} is only 3.5%. It can be seen that the intact strength rises very sharply with hydrostatic pressure and that the value of the SFMAX parameter governs the value of the fractured strength and also the total strength. The influence of varying the erosion strain between 2 and 3 for a 15 km s^{-1} simulation is to increase the depth of penetration by 7%, and the crater diameter by 3%.

Table 5-6. The influence of the bulking parameter on crater depth and diameter in soda-lime glass (Al: aluminium; Ti: titanium; SS: stainless steel)

β	T_c (Al) (mm)	D_c (Al) (mm)	T_c (Ti) (mm)	D_c (Ti) (mm)	T_c (SS) (mm)	D_c (SS) (mm)
0.25	1.98	4.74	2.67	5.18	3.41	5.12
0.5	2.03	4.82	2.61	5.14	3.55	5.42
1	2.12	4.80	2.73	5.10	3.62	5.64

5.9 Discussion

The usefulness of any modelling is dependent on the quality and applicability of the material models used (equation of state (EOS), strength and failure models). A range of material models exist and, prior to this thesis, had been validated at high strain rates (the ballistic impact regime) and for hypervelocity impact on ductile materials. Brittle material models have been validated against hypervelocity impact simulations to a much smaller degree. This is addressed in this chapter.

Brittle materials, such as glass, show effects such as dilation and exhibit significant residual strength under compression. These features have been incorporated into the published Johnson-Holmquist brittle material model which has been implemented into the AUTODYN hydrocode. However the Johnson-Holmquist model does not include an energy dependent equation of state. An energy dependent equation of state is appropriate for modelling hypervelocity impacts where melting and vaporisation take place. The Mohr-Coulomb model, originally developed to model concrete, has been applied to the hypervelocity impact

modelling of glass by Tsembelis (the Glass Analogue Model (GAM) Tsembelis, 1998). Parameters have been determined from a variety of sources, including non-soda-lime glass data. The results of the simulations are compared with the experimental data presented in this thesis and show that, despite the Johnson-Holmquist model having a more realistic description of the loss of strength of glass under stress, the GAM simulations are closer to the experimental data at 5 km s^{-1}. This may be due to the central crater formation being strongly determined by energy dependence (phase changes) and only weakly dependent on strength effects. The calibration data also show the need to compare any phenomenological model to a wide range of experimental data as the hypervelocity impact response of glass is variable due to its microstructural nature.

Further development of a glass model will be required. A preliminary energy dependent version of the Johnson-Holmquist model has been derived (Tsembelis, 1998). The influence of thermal softening on the final crater shape also needs to be assessed. The model hydrostat can also be assessed using recent shock wave data on soda-lime glass (chapter 6). The conclusion is that the Johnson-Holmquist model (and the Mohr-Coulomb GAM) is applicable to compressive regimes but does not appear to predict tensile fracture, thus the modelling of tensile fracture needs to be addressed in further studies. Indeed, a preliminary crack softening model, based upon the fracture toughness parameter reviewed in Taylor *et al.*, (1997d), has been developed and implemented in AUTODYN (Clegg, 1997; Hazell and Iremonger, 1997).

The hydrocode modelling results lie below the power-law depth of penetration equation predictions (Eqs. 3-1, 3-3). The results also lie outside the 75% confidence bands, derived from the original source data used for the damage equation development (Eqs. 3-1 and 3-3). The velocity exponent, obtained from a fit to the GAM hydrocode simulations, is close to 0.33 instead of 0.67, implying that the depth of penetration is a function of impact momentum, not kinetic energy. The J-H simulations, with the velocity exponent of 0.52, are closer to the equation predictions.

The influence of strain rate on the calculations was estimated to be no more than 3.5%. Varying the bulking parameter between 0.25 and 1 decreases the depth of penetration and crater diameter of the Johnson-Holmquist simulations. The influence of erosion strain on the calculations was assessed to be < 10 % for a simulation at 15 km s^{-1}. Further work will be required to explore this effect However, it does not bring the crater diameters into agreement with the experimental data.

5.10 Summary

The hydrocode simulations of impacts onto glass at 5 km s^{-1} (for a range of projectile densities) using the Glass Analogue Model show better agreement with the experimental

results than the Johnson-Holmquist simulations do. The influence of the bulking parameter and strain rate on the Johnson-Holmquist simulations was assessed and found to be less than 5-10%. In particular, the Johnson-Holmquist crater diameters are significantly larger than the crater diameters observed on the target, for a range of bulking parameters. The depth of penetration results obtained for 1 mm Al 2024 projectiles at 5 - 15 km s^{-1} for both the Johnson-Holmquist and the Glass Analogue Model simulations lie below the predictions of the two empirically determined quartz penetration equations (Eqs. 3-1 and 3-3), and the 75% confidence bands for these equations (section 3.3.3). The fit to the GAM simulations gives a velocity exponent of 0.33, and the J-H simulations, a velocity exponent of 0.52. Neither fit reproduces the velocity exponent of 0.67-0.7 of Eqs. 3-1 and 3-3.

Chapter 6

6. Brittle Material Shock Physics

In chapter 5, empirical and semi-empirical equations of state and strength models were summarised and the hydrocode modelling results were presented. Limitations in the formulations of the Johnson-Holmquist strength model were identified and discussed. In this chapter, the experimentally determined data used to provide models for the hydrocode simulations are examined in more detail.

Previously used brittle material models are compared for the variation in their predicted impact pressure (using the impedance match method). The common pressure at impact for a range of projectiles (such as those used in impact experiments in section 2.4) at 0-20 km s^{-1} is also examined and limitations in linear shock Hugoniot data (linking the particle and shock velocities) are explored.

Information about the response of a material has traditionally been obtained by the flyer plate technique, whereby a flat plate is impacted upon a flat target, causing the material to be in a state of uniaxial strain. Strain gauges are used to assess the material's stress state. Flyer plate data for quartz, soda-lime and borosilicate glass are compared with the Johnson-Holmquist hydrostat for soda-lime glass to identify any difference in the response of different brittle material types.

6.1 Brief Summary of Shock Physics

6.1.1 Shock waves

A shock wave is formed when a target is struck by an impactor (of any shape) at such a velocity that a pressure is reached where the material is not able to respond adiabatically. In Figure 6-1(a), the P-V (pressure-specific volume) curve is shown for elastic, plastic, and shock waves. The pressure state produced by a hypervelocity impact is followed by the release of the material. It follows an isentropic path (called the release adiabat) back down to ambient pressure, but the material is never returned to its initial specific volume. The Rayleigh line is drawn from the shocked state back down to the initial specific volume. The area of the triangle is equivalent to the specific internal energy of the shocked material (Figure 6-1(b)). The release of the material (decompression from its shocked state) converts much of the internal energy into mechanical work. The energy converted is equal to the area between the release adiabat and the lines parallel to the P-V axes (Figure 6-1(c)). This area is smaller than the triangle bounded by the Rayleigh line and the difference is equal to the amount of the irreversible work done by the shock. This work is then compared with the energy required to melt and/or vaporise the material.

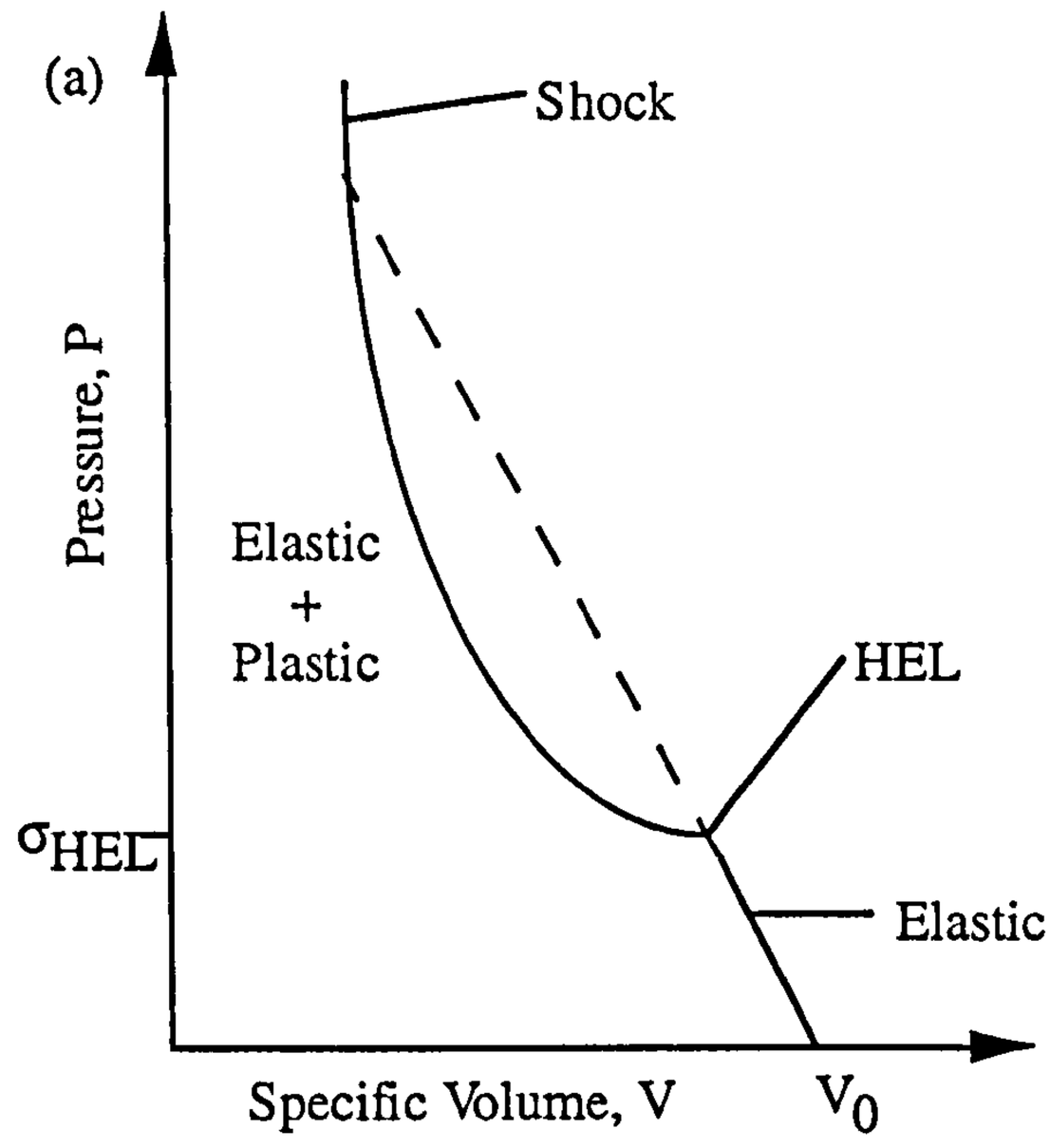

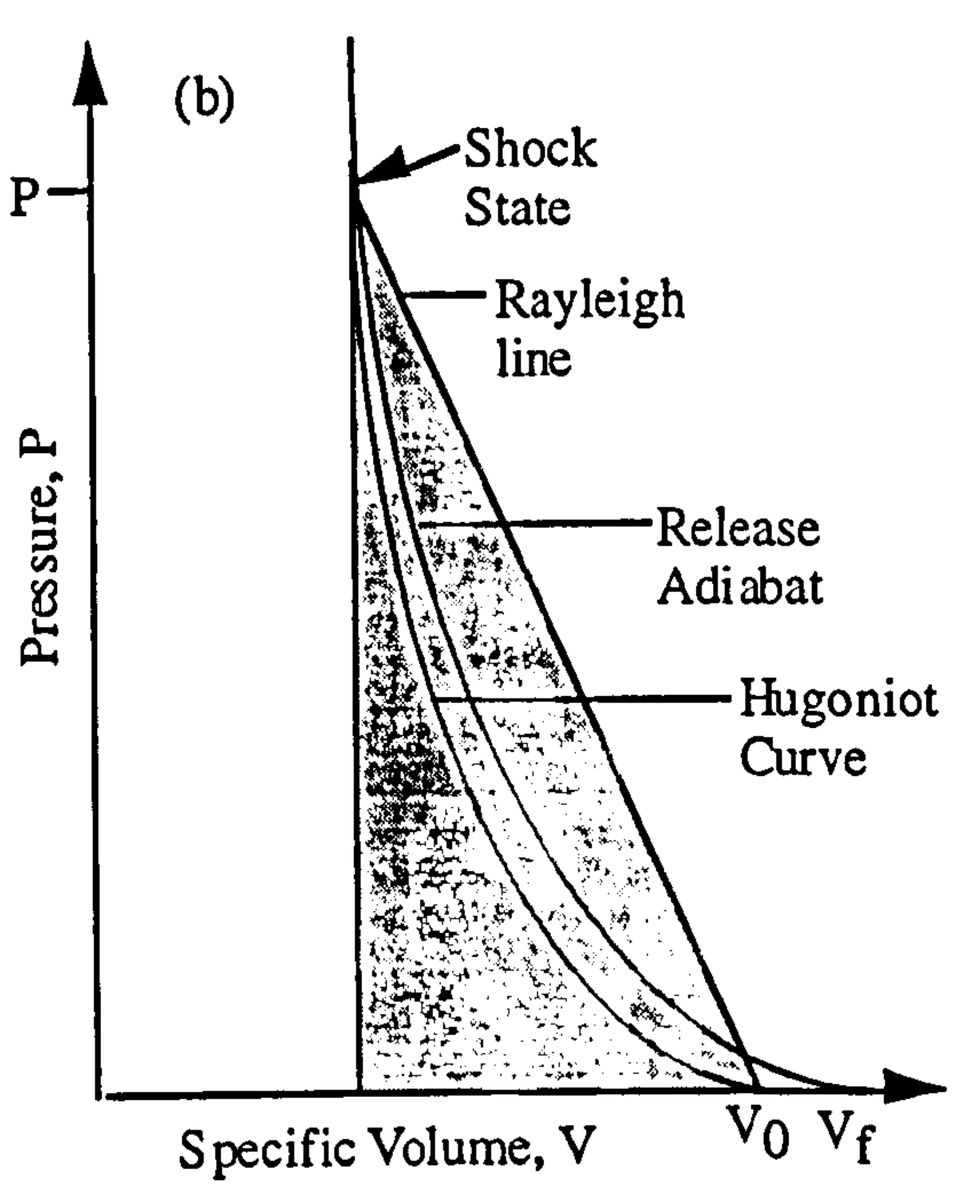

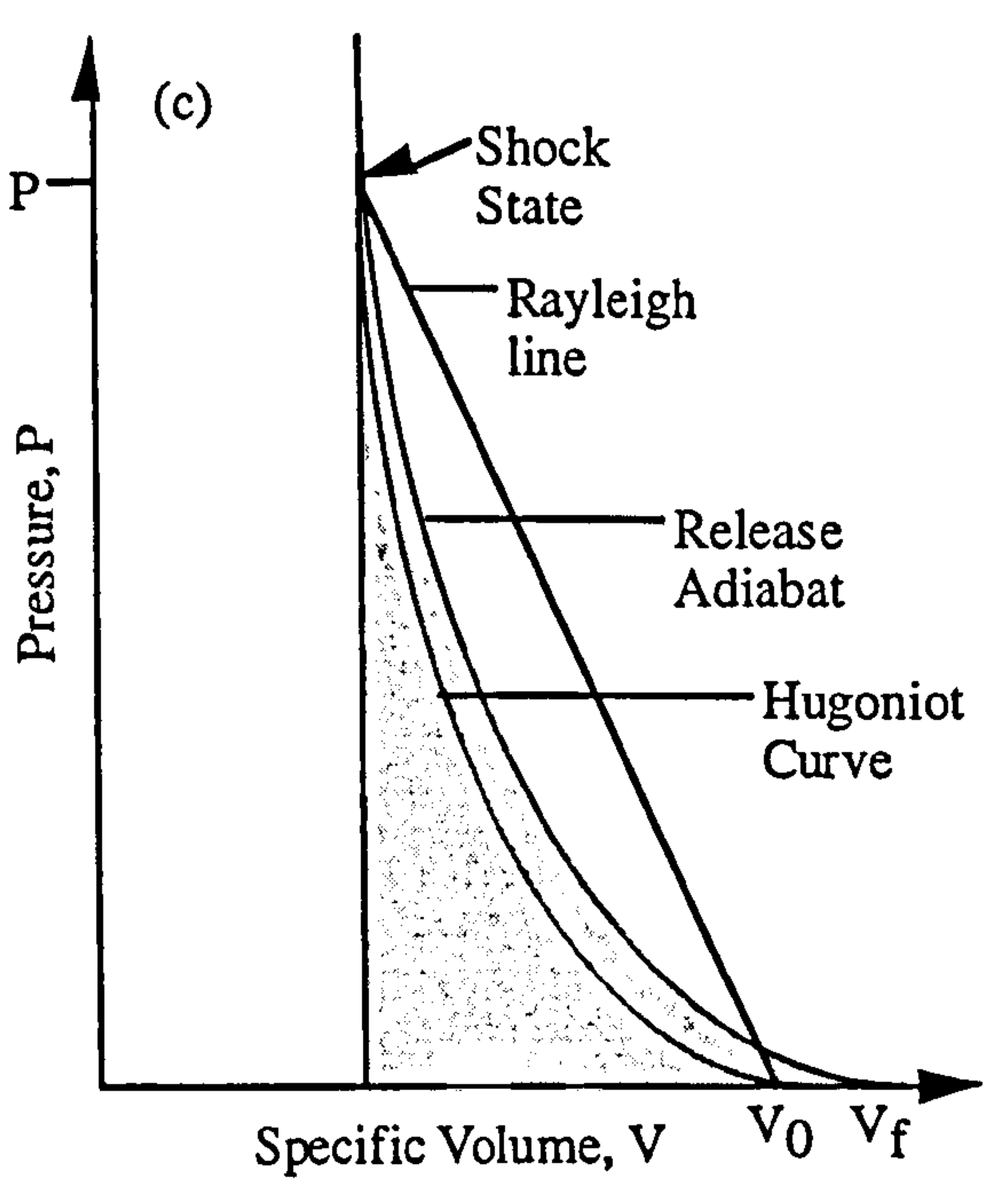

Figure 6-1. (a) Equation of state for a material (expressed as a function of pressure and specific volume). (b) Release thermodynamic path of a shocked material. The Rayleigh line connects the initial and shock states. The specific internal energy of the shocked material is equal to the shaded area bounded by the Rayleigh line. (c) as (b), but with the internal energy converted to mechanical work. The difference between the two areas is equal to the amount of irreversible work done by the shock. v_0 and v_f are the initial and final specific volumes (figure adapted from Melosh, 1996).

6.1.2 Uniaxial strain, stress and the Hugoniot Elastic Limit

In conditions of uniaxial strain the deformation is confined solely to one direction. The condition of uniaxial strain holds in flyer plate impacts until the release wave arrives from the free surface. By comparison, uniaxial stress occurs when a cylinder is under compression or tension. The Hugoniot Elastic Limit (HEL) is the value of the longitudinal stress component at the elastic limit under uniaxial strain conditions. Figure 6-2 shows the Hugoniot Elastic Limit as observed in soda-lime glass (Bless *et al.*, 1988); the shear stress is plotted against the shock stress.

6.2 Rankine-Hugoniot Jump Equations

The fundamental equations describing shock fronts were derived by P. H. Hugoniot in 1887 (presented in Melosh, 1996). These equations, governing the behaviour of shock waves, were derived by applying the laws of conservation of mass, momentum and energy to the shock front. Conservation of mass requires that the rate of mass flow into the shock equals the rate of the mass flow exiting the shock. Conservation of momentum requires that the change of momentum of a mass entering the shock in an increment of time Δt equals the impulse given to that mass over Δt. Conservation of energy is the condition that the initial energy added to the work done on the material equals the final energy. The Rankine Hugoniot equations are expressed in Eqs. 6-1 to 6-4. Eq. 6-1 is from consideration of conservation of mass, Eq. 6-2 is from momentum and Eq. 6-3 is from energy. Eq. 6-4 is an alternative formulation of Eq. 6-3. Figure 6-3 shows the conditions from which the equations are derived. The shock front is assumed to be a discontinuity and thermodynamic equilibrium is assumed to hold immediately around the shock front.

$$\rho_1=\rho_0(U-u_0)(U-u_1) \tag{6-1}$$

$$P_1-P_0=\rho_0(u_1-u_0)(U-u_0) \tag{6-2}$$

$$E_1-E_0=\frac{(u_1-u_0)^2}{2} \tag{6-3}$$

$$E_1-E_0=\frac{(P_1-P_0)\left(\frac{1}{\rho_0}-\frac{1}{\rho_1}\right)}{2} \tag{6-4}$$

(Symbols: Subscripts 1, 0 refer to target and impactor respectively. ρ is density, u is particle velocity, P is pressure, U is the (common) shock velocity and E is internal energy. Specific volume, v, is defined as the reciprocal of density.)

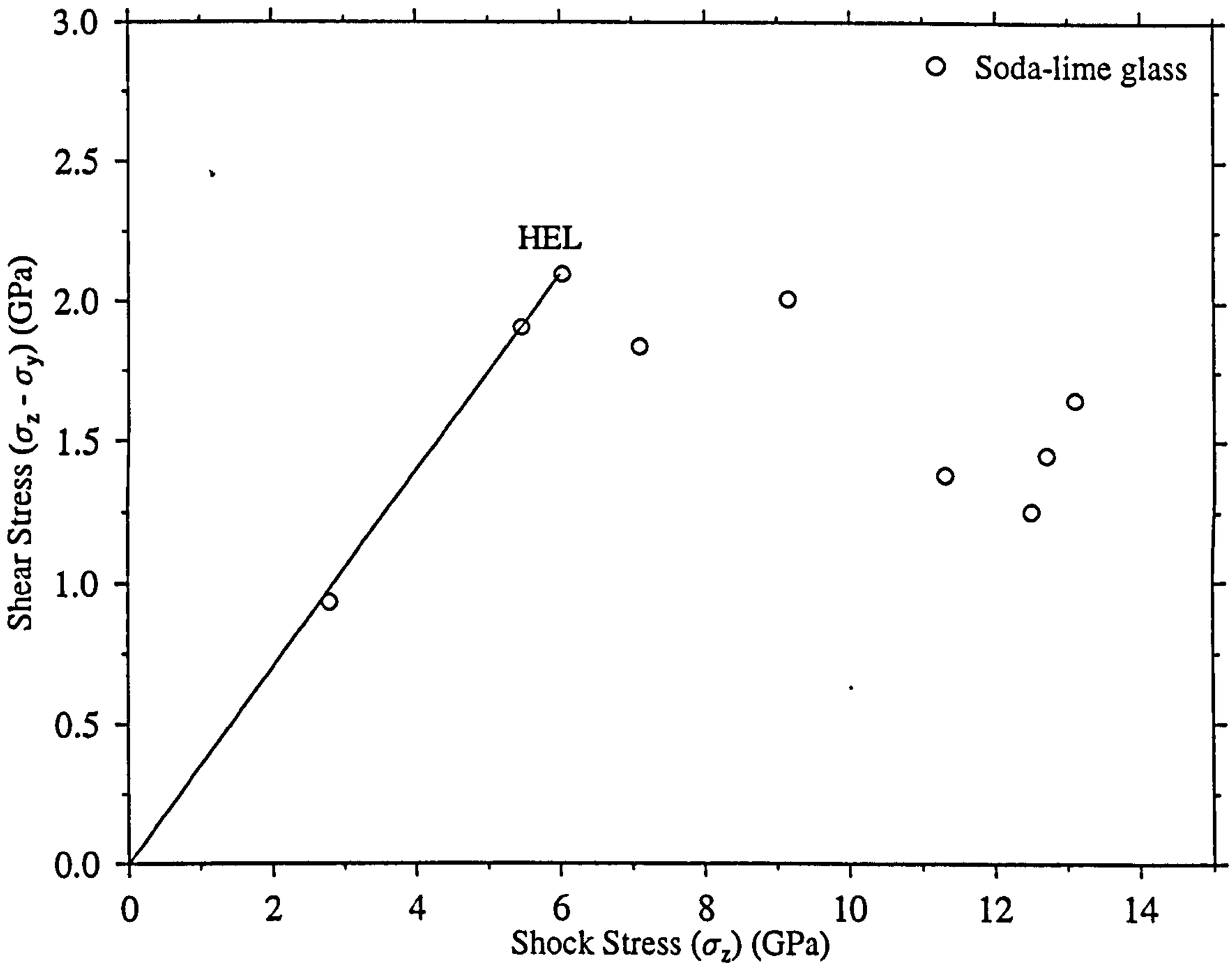

Figure 6-2. The response of soda-lime glass below and above the Hugoniot Elastic Limit (HEL). The data show a linear increase between the shear stress and the shock stress up to the HEL. The shear stress remains constant until 10 GPa then begins to decrease. (Graph and analysis from Bless et al., 1988)

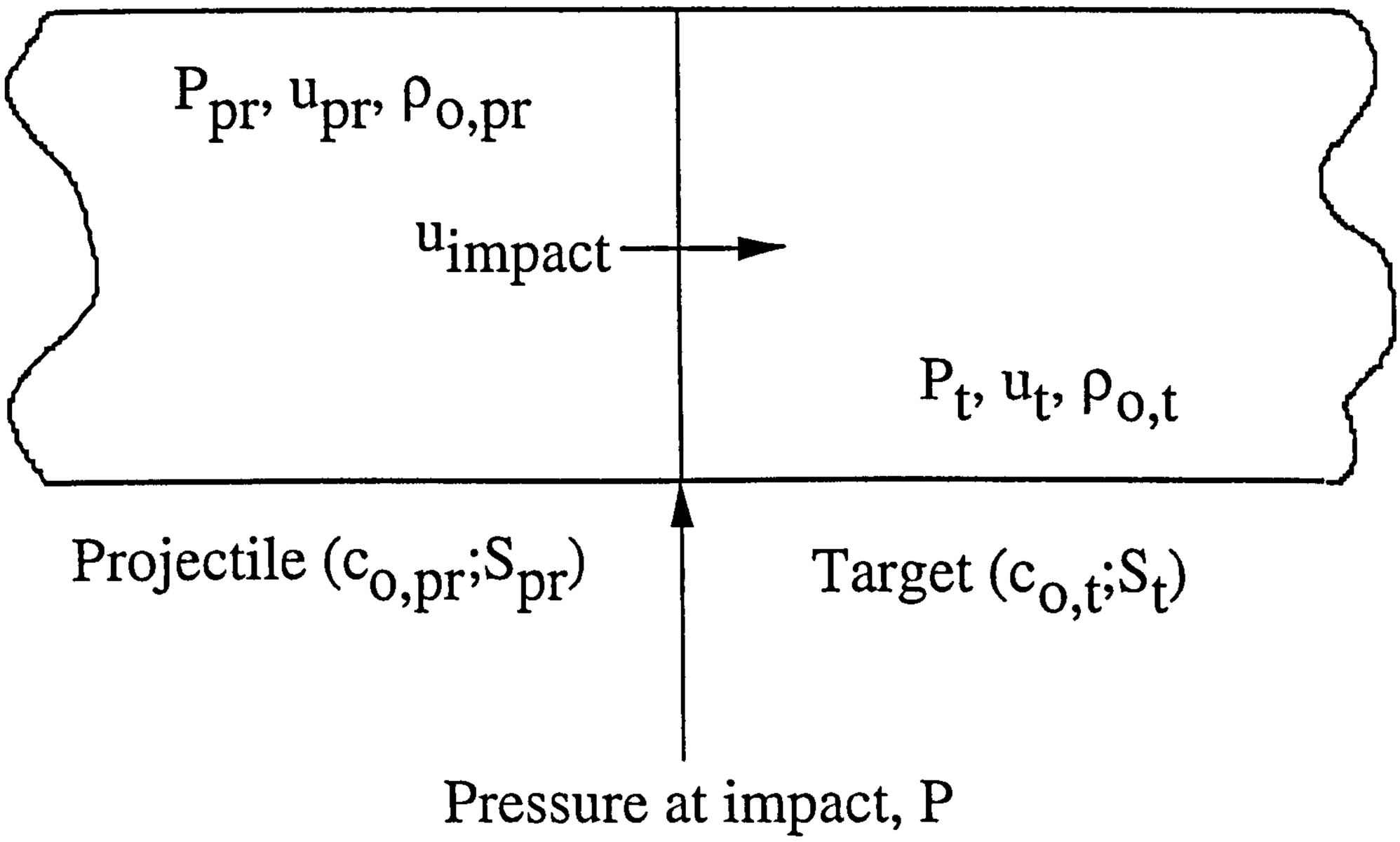

Figure 6-3. Derivation of the Rankine-Hugoniot equations.

Note that Eqs. 6-1 to 6-3 do not completely specify the conditions on either side of the shock. The fourth relation required is the equation of state (EOS), introduced in section 5.4. (However, usually $P_0 = E_0 = 0$.)

6.2.1 Calculating the common pressure at impact

The Rankine-Hugoniot equations can now be used to calculate the common pressure at impact. Eq. 6-5 is derived from the Rankine-Hugoniot equations, giving the pressure as a function of initial density, shock velocity and particle velocity. The conditions at a shock front are given in Figure 6-3. The relationship between the shock velocity and the projectile velocity has been observed in many materials to be linear (Eq. 6-6). Experimental plots of this u_s and u_p relationship will be discussed in section 6.3. The constants c_o and S are known as Hugoniot data and determined from fits to experimental data. (c_o is usually equivalent to the bulk sound speed). Eqs. 6-5 and 6-6 can be combined to obtain Eq. 6-7. At the projectile-target interface, the shocked projectile material is assumed to have the same relative velocity as the target (Eq. 6-8), where u_{impact} is the impact velocity. Note that this derivation does not take into account particle and target dimensions, but simply assumes one dimensional conditions. Using Eqs. 6-7 and 6-8, the pressures at the projectile and target are defined (Eqs. 6-9 and 6-10). Finally, at the interface, equality of pressures is assumed (Eq. 6-11), so deriving Eq. 6-12. Eq. 6-12 is a quadratic equation in u_t (particle velocity) and, by solving it for u_t, the 'common' pressure can then be calculated for both the target and projectile at impact (using either Eq. 6-9 or 6-10). Some materials have an extra term in Eq. 6-6 ($\propto u_p^2$). Tsembelis (1998) has derived the analogous cubic equation in u_t which can be used to calculate the common pressure.

$$P=\rho_o u_s u_p \tag{6-5}$$

$$u_s=c_o+Su_p \tag{6-6}$$

$$P=\rho_o(c_o+Su_p)u_p \tag{6-7}$$

$$u_{impact}=u_{pr}+u_t \tag{6-8}$$

$$P_{pr}=\rho_{o,pr}(c_{o,pr}+S_{pr}(u_{impact}-u_t))(u_{impact}-u_t) \tag{6-9}$$

$$P_t=\rho_{o,t}(c_{o,t}+S_t u_t)u_t \tag{6-10}$$

$$P_t=P_{pr}=P \tag{6-11}$$

$$(\rho_{o,pr}S_{pr}-\rho_{o,t}S_t)u_t^2-(\rho_{o,pr}c_{o,pr}+\rho_{ot}c_{o,t}+2\rho_{o,pr}S_{pr}u_{impact})u_t+\rho_{o,pr}u_{impact}(c_{o,pr}+S_{pr}u_{impact})=0 \quad (6\text{-}12)$$

(Subscripts : t: target, pr: projectile, p: particle, s: shock, o: initial, except for c_o, which is one of the two Hugoniot material parameters.)

6.2.2 Flyer plate tests

"The plate impact experiment is the primary method for obtaining an equation of state or Hugoniot data for materials. It is also used to determine the dynamic tensile fracture (spall) characteristic of materials. Under planar impact at high velocities, materials are subjected to a state of uniaxial strain since no lateral motion can occur until release waves arrive from the edges of the plate. Therefore, no assumptions have to be made about the state of stress in the material. Under conditions of high pressure impact in uniaxial strain, shock waves are formed which propagate through the material as a very sharp shock front with discontinuities in stress, strain and particle velocity across the front." Zukas, 1990.

The flyer plate tests make direct measurements of u_p, σ_z and σ_y (where σ_z is the direction of the shock wave propagation). Measurements can therefore be used to determine values of the shear stress (τ) using the relation in Eqs. 6-13 and 14. The lateral stresses are equal in flyer plate tests ($\sigma_x = \sigma_y$).

$$\sigma_z=P+\frac{2}{3}(\sigma_z-\sigma_y) \quad (6\text{-}13)$$

$$\sigma_z=P+\frac{4\tau}{3} \quad (6\text{-}14)$$

The Rankine-Hugoniot equations, although normally written as above, in terms of pressure, actually define the stress variable (σ) as a function of shock velocity, particle velocity etc. Care should be taken not to confuse pressure with the hydrostatic pressure (P), which would represent the state of the material if it lacked strength.

" At high pressures, the strength is normally neglected with respect to pressure, so pressure and stress can be used interchangeably. At lower pressures or for materials such as ceramics, which have very high yield strengths, the neglect of yield strength may not be a valid approximation." Zukas, 1990.

The Rankine-Hugoniot equations can be combined to produce Eqs. 6-15 and 6-16, where P in this notation is stress.

$$U_s = V_0\left(\frac{P_1-P_0}{V_0-V_1}\right)^{1/2} \tag{6-15}$$

$$u_p = ((V_0-V_1)(P_1-P_0))^{1/2} \tag{6-16}$$

Therefore, measurements of stress and particle velocity can be used to determine the volumetric change and the shock velocity.

6.3 Glass Hugoniot Data

The values for c_o and S are experimentally determined from flyer plate experiments (see section 6.2.2). c_o typically has values close to the bulk sound speed and S does not have any physical significance allocated to it. c_o and S values for several hundred materials have been published in the Los Alamos Shock Laboratory Handbook (Marsh, 1980). Selected values are given in Table 6-1. Some of the data have values for c_o and S supplied, others have been fitted for the purpose of this thesis. The U_s-u_p data for Ti, quartz, cellulose acetate and plexiglass are shown in Figure 6-4. Note the linear gradient for all the data apart from the quartz which, below a u_p of 2 km s^{-1} show a non-linear trend. The fit to the quartz data is carried out for data $u_p > 2$ km s^{-1}. The linearity of the Hugoniot data has been explained by Johnson (1997) (from an analysis of the differential form of the Hugoniot jump equations) who also identifies a break in the linearity at $u_p \cong 1.6\ c_o$ for elemental metals. Above this point, there is a linear relationship between U_s and u_p but with a different gradient ($S \approx 1.2$). For example, for Fe (previously fitted with a quadratic equation), the inclusion of data from nuclear shock experiments has allowed the derivation of the following Hugoniot data: $c_o = 4$ km s^{-1}, $S = 1.553$ then at $u_p = 6.4$ km s^{-1} then the gradient changes to $S = 1.213$.

Table 6-1. Values of c_o and S for a range of projectile materials. Where an r^2 value is given, the fit was carried out for the purpose of this thesis. r^2 is defined in section 4.1.

Reference	Material	Density (g cm^{-3})	c_o (km s^{-1})	S	r^2
Asay and Shahinpoor, 1993	Nylon	1.14	2.29	1.63	N/A
LASL (Marsh, 1980)	Aluminium Alloy Al 1100	2.712	5.38	1.34	N/A
LASL (Marsh, 1980)	Aluminium Alloy Al 2024	2.784	5.37	1.29	N/A
LASL (Marsh, 1980)	Aluminium Alloy Al 6061	2.703	5.35	1.34	N/A
LASL (Marsh, 1980)	Stainless Steel 304	7.89	4.58	1.49	N/A
LASL (Marsh, 1980)	Copper	8.924	3.91	1.51	N/A
LASL (Marsh, 1980)	Titanium	4.527	5.01	0.98	0.993
LASL (Marsh, 1980)	Lead	11.346	2.03	1.47	N/A
LASL (Marsh, 1980)	Olivine	3.214	6.22	0.83	N/A
LASL (Marsh, 1980)	Quartz	2.204	1.74	1.45	0.979
LASL (Marsh, 1980)	Cellulose acetate	1.261	2.56	1.35	0.992
LASL (Marsh, 1980)	Plexiglass	1.186	2.86	1.35	0.992

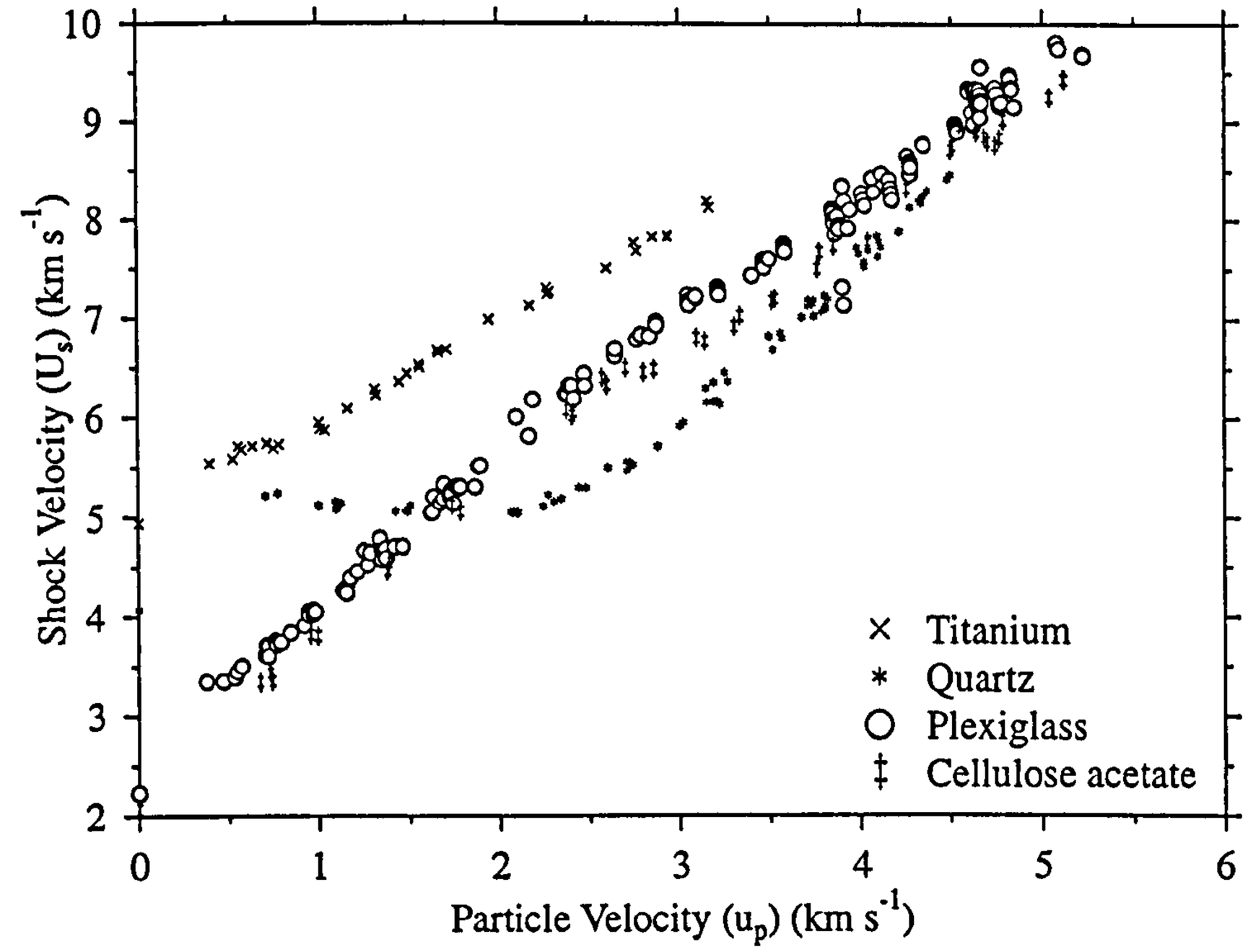

Figure 6-4. Shock Hugoniot data (Shock velocity (U_s) versus particle velocity (u_p)) for titanium, quartz, cellulose acetate and plexiglass. Note the deviation from linearity of the quartz data.

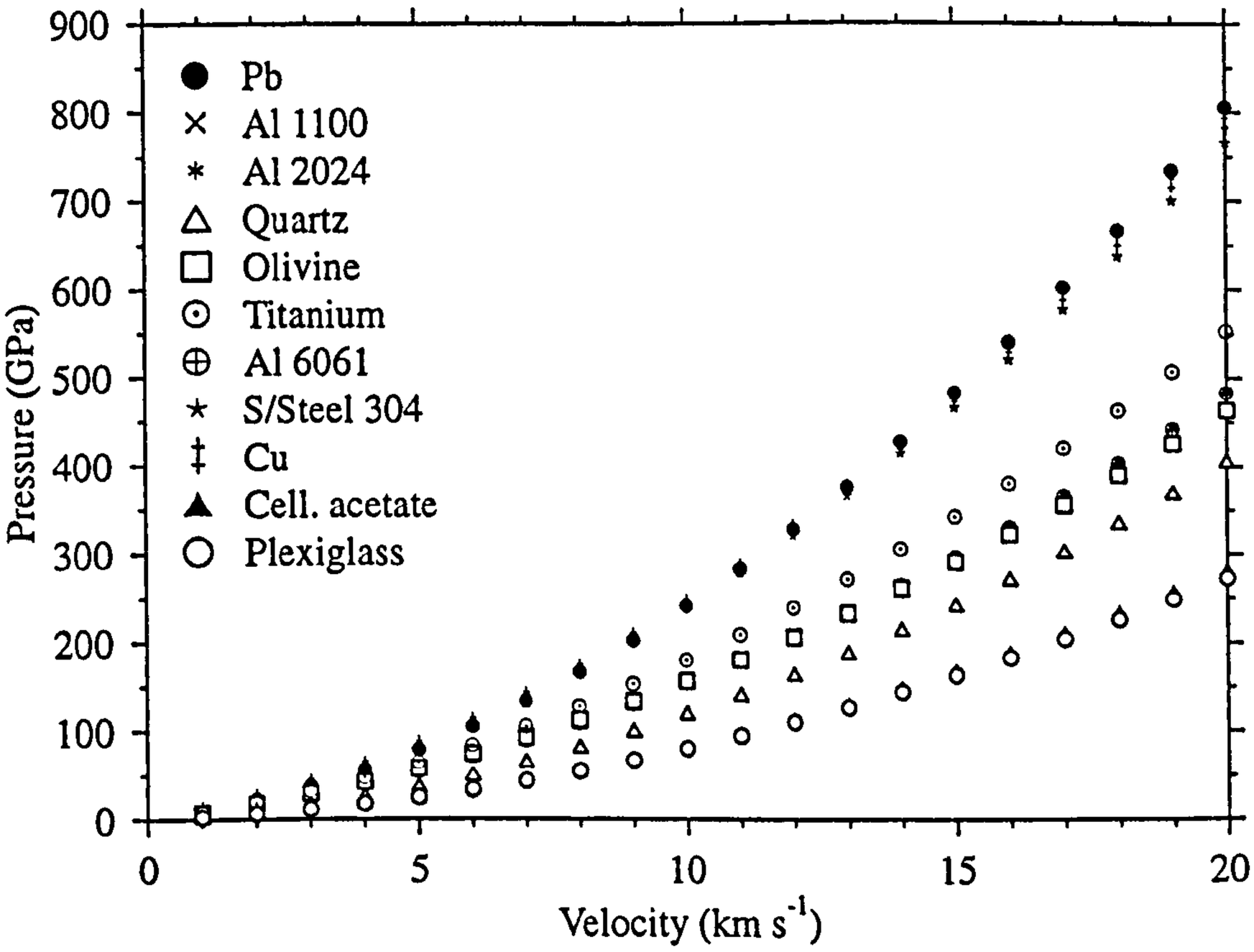

Figure 6-5. Common impact pressure, calculated from the Rankine-Hugoniot equatyions, as a function of impact velocity for a range of projectile materials.

The Hugoniot data (Table 6-1) are used to calculate the common impact pressures for a range of projectile materials onto glass, defined by c_o = 3.3 km s^{-1}, S = 1.5 (Figure 6-5). The projectile type has a significant difference upon the impact pressure experienced by the target although this analysis can only be used to illustrate broad differences in the common impact pressure. For example, at 10 km s^{-1}, a plexiglass projectile would have a common impact pressure of ~ 50 GPa, whilst a lead projectile would exert closer to 200 GPa. Stainless steels, forming about 10 % of the population in Low Earth Orbit, have a density two-thirds of lead. Therefore, the impact pressures of a lead projectile are higher than those for a stainless steel projectile. It must be remembered that the linear equation (Eq. 6-6) cannot reproduce phase changes, which absorb some of the impact energy to change the target/projectile from solid to liquid or gas phases.

Table 6-2. A summary of published glass Hugoniot data.

Reference	c_o (km s^{-1})	S	Mat'l	Comment
Alwes, 1990. low shock conditions	4.67	0.22	Quartz	hydrocode modelling, based on quartz data
Alwes, 1990. high shock conditions	1.85	1.5	Quartz	hydrocode modelling, based on quartz data, although incorrectly referred to as pyrex in the documentation
Mandeville, 1971	1.3	1.56	Glass	No reference given for values
Medina *et al.*, 1996	0.8	1.7	Quartz	no information available, as above
Tsembelis,1998. based on data in Holmquist *et al.* (1995)	3.3	1.5	Soda-lime glass	used as the baseline data in this thesis
Tsembelis,1998. (a)	1.85	1.5	Soda-lime glass	hydrocode modelling, based on comparison with experimental data
Tsembelis,1998. (b)	5.5	1.5	Soda-lime glass	hydrocode modelling, based on comparison with experimental data

A review has been carried out of previous hydrocode modelling of impacts onto glass and the values of c_o and S used are summarised in Table 6-2. The impact predictions are compared for an Al 2024 projectile in Figures 6-6 and 6-7, as a function of impact velocity and specific volume respectively. Despite the wide variation in the values of c_o (and less so for S) the predictions follow the same trends for impact velocities between 0 and 20 km s^{-1}. This suggests that the identification of values which produce appropriate modelling results is not closely bound by theoretical work. The analysis presented by Johnson (1997) has not yet been extended to glass targets. In view of this, the values of c_o should be closer to 3.3 km s^{-1}, the bulk sound speed for glass.

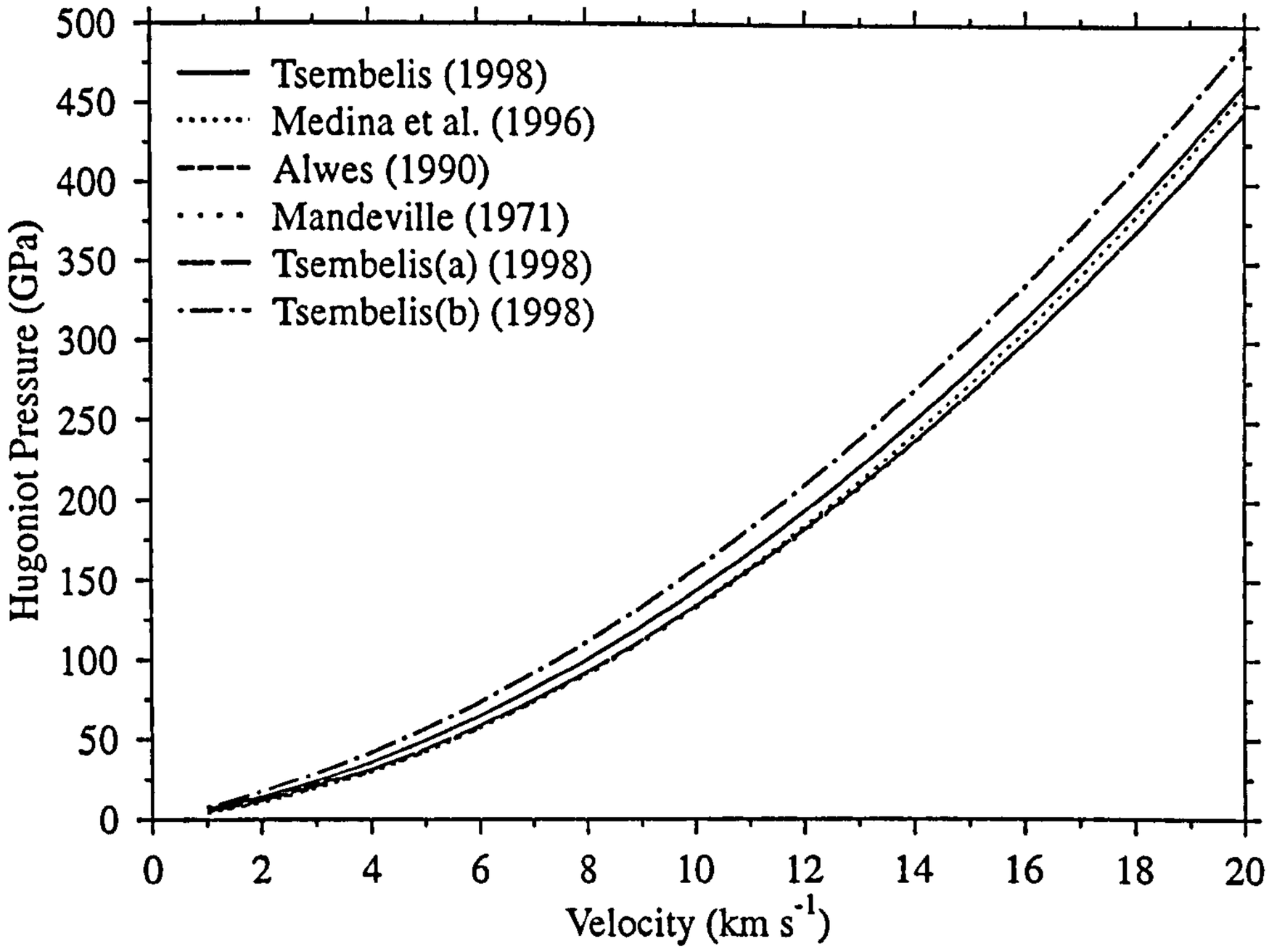

Figure 6-6. Common impact pressure as a function of impact velocity for an Al 2024 projectile onto glass for a range of c_0 and S values.

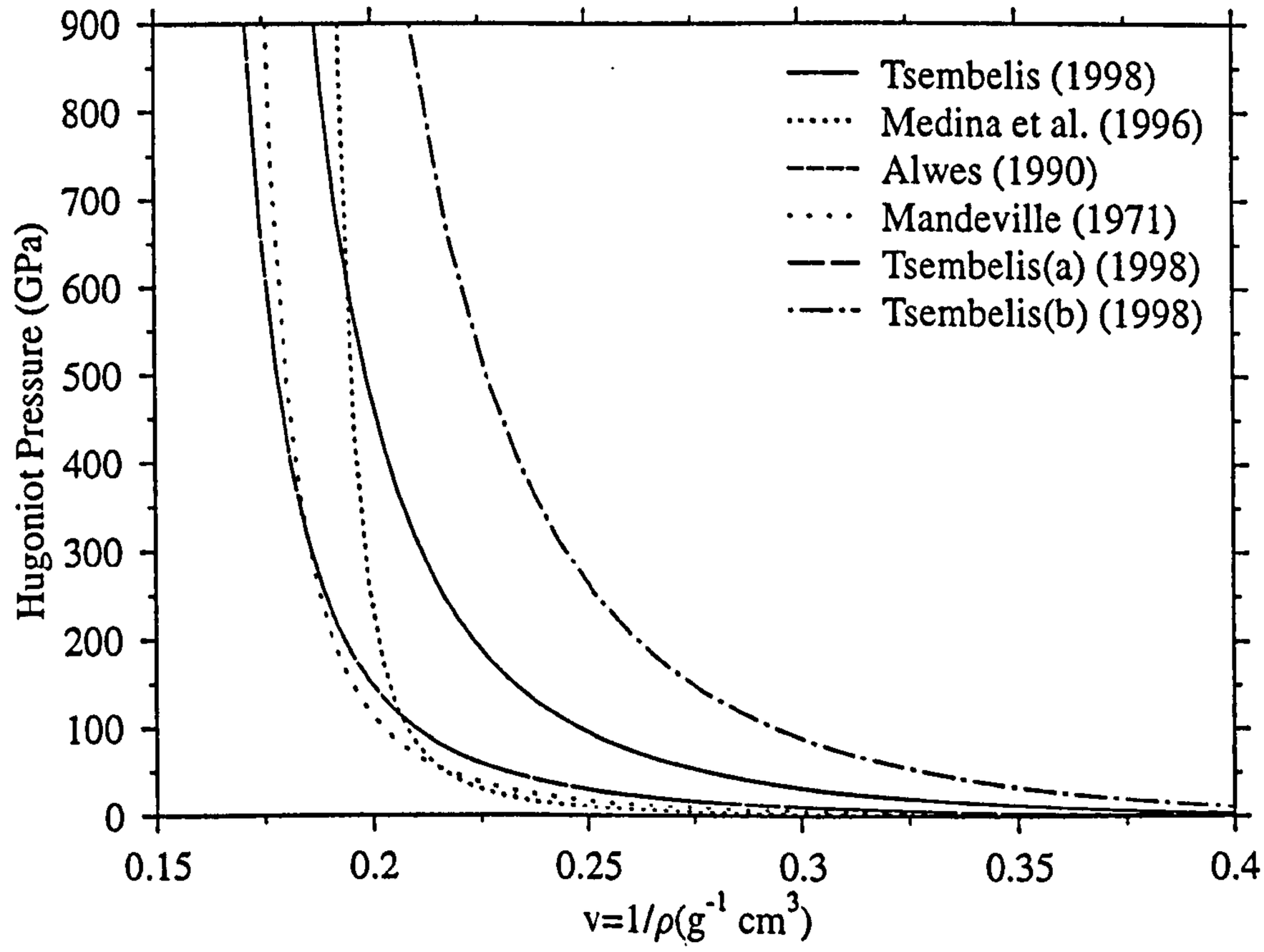

Figure 6-7. Common impact pressure as a function of specific volume for an Al 2024 projectile onto glass for a range of c_0 and S values.

6.4 Johnson-Holmquist Hydrostat

The data used in the development of previous brittle material damage equations have come from a range of target materials - soda-lime glass, borosilicate glass, quartz, and lunar rock analogues. Flyer plate tests on these materials have been carried out and these data can be used to determine whether the shock response of these materials is identical and thus whether they can be used in the same damage equation. In addition, the data are used to investigate the performance of the Johnson-Holmquist hydrostat. The parameters measured in flyer plate tests include σ_z (the longitudinal stress, along plate impact vector), σ_y (the lateral stress, perpendicular to the plate impact vector) and particle velocity (u_p). Researchers who have published this data are listed in Table 6-3 and the plot of σ_z versus u_p is given in Figure 6-8(a). Oligoclase data, although available, have not been included due to time constraints.

Table 6-3. Published brittle material flyer plate data.

Reference	Material	ρ (g cm^{-3})	σ_z	u_p	σ_z-σ_y
Arndt *et al.*, 1971.	Suprasil	2.20	yes	no	no
Bourne *et al.*, 1996.	Soda-lime glass	2.49	yes	yes	yes
Bourne *et al.*, 1996.	Borosilicate glass	2.23	yes	yes	yes
Bourne and Rosenberg, 1995.	Soda-lime glass	2.49	yes	no	yes
Brar *et al.*, 1991.	Soda-lime glass	2.50	yes	no	yes
Chhabildas and Grady, 1983.	Fused Quartz	2.20	yes	yes	no
Dandekar and Beaulieu, 1995.	Soda-lime glass	2.50	yes	yes	no
Holmquist *et al.*, 1995.	Soda-lime glass	2.53	yes	yes	no
Lopatin *et al.*, 1991.	Soda-lime glass	2.49	yes	yes	no
Yeshurun *et al.*, 1986.	Pyrex	2.23	yes	yes	no

The particle velocity increases with stress in a linear fashion and there is no clear difference between the three types of brittle material tested here (soda-lime glass, borosilicate glass and quartz). However, note that the u_p values are below 2 km s^{-1}, and thus refer to lower shock conditions than those that might occur during a hypervelocity impact. By using the Rankine-Hugoniot equations, Eq. 6-16 can be derived. As σ_z and u_p are known then the specific volume ($V = 1/\rho$) can be calculated. It is simple to then calculate μ ($\mu = \rho/\rho_0 - 1$). With μ calculated the data (for quartz, borosilicate and soda-lime glasses and suprasil, a quartz derivative) is replotted in Figure 6-8(b) against a plot of the Johnson-Holmquist hydrostat. As noted by Holmquist *et al.* (1995), "*The hydrostatic behaviour of materials is difficult to obtain directly...a computational, iterative technique has been developed to obtain the hydrostat, damage and fractured material strength using results from flyer plate impact tests and ballistic tests*". Therefore, the constants are not based upon any theory and should be examined as closely as possible. As mentioned above, as the stress increases, the contribution of material strength becomes less important and the experimental data should

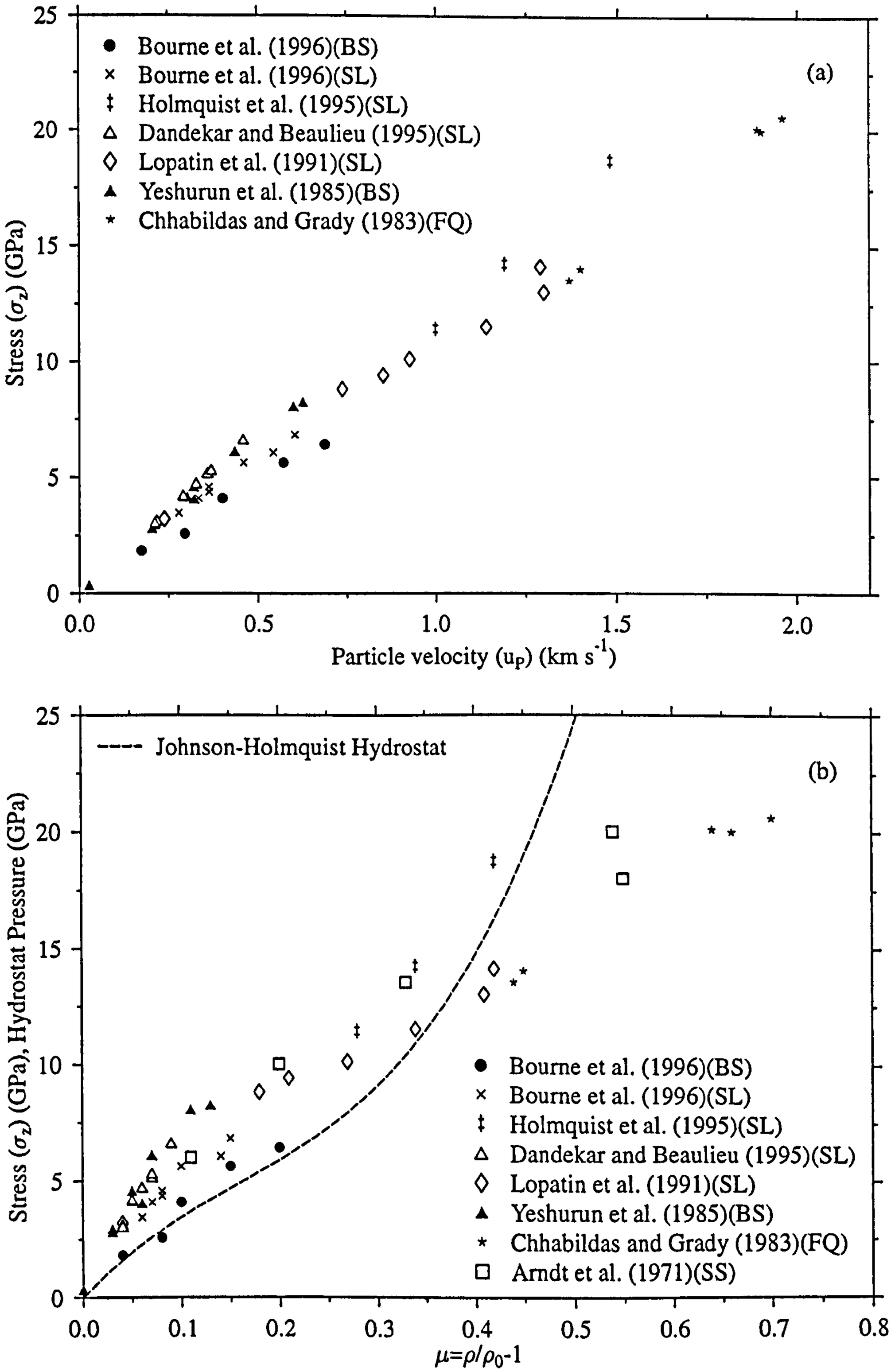

Figure 6-8. (a) Published flyer plate values of particle velocity (u_p) versus longitudinal stress (σ_z) (b) Data from (a) compared to the Johnson-Holmquist 2 hydrostat. (BS: borosilicate glass, SL: soda-lime glass, FQ: fused quartz)

approach the hydrostat. For Holmquist *et al.* (1995) data, this is indeed true (Figure 6-8(b)). The other soda-lime data also remain above the limiting curve of the hydrostat, except for two points above $\mu > 0.4$. The borosilicate glass data also lies above the hydrostat curve. There is some scatter between the different experimenters' data sets for both soda-lime glass and borosilicate glass, making it difficult to identify any clear difference in the response of the glasses. The conclusion is that, broadly speaking, borosilicate glass responds in the same manner to soda lime glass. Open structure glasses, such as fused quartz and borosilicate glass show a different response to plane wave shock loading than soda-lime glass at low stresses (1 - 6 GPa) (Bourne *et al.*, 1996). These measurements are not in the regime of interest of a hypervelocity impact. A quantitative evaluation of the values of K1, K2 and K3, required to describe the glass hydrostat, cannot be carried out because not all the experimental data required is available in the published literature.

The quartz (and suprasil) data do not follow the form of the Johnson-Holmquist hydrostat (Figure 6-8(b)). This suggests that the response of quartz is different to that of the soda-lime glass. The offset may be due to the densification of quartz, first noted by Wackerle (1962).

In Figure 6-9(a), the data are grouped by material type and compared with both the Johnson-Holmquist and the quartz hydrostats (the latter using data in Table 6-1 and using Eq. 6-8)(Figure 6-9(b)). Note that the form of the quartz hydrostat is significantly different to the Johnson-Holmquist hydrostat and that the quartz data lie above the quartz hydrostat. The latter is as expected as the experimental data include the shear (deviatoric) component. In Figure 6-10(a) the difference between the measured longitudinal stress and the Johnson-Holmquist hydrostat pressure is presented. As the value of μ increases, the value of σ_z should approach that of the hydrostat pressure. If the hydrostat is appropriate, then the value of σ_z-(hydrostat pressure) should always be greater than zero. The quantity (shear stress-longitudinal stress) becomes negative for values of $\mu > 0.4$. This is true for the majority of the soda-lime and borosilicate glasses, but not for the quartz and suprasil. In Figure 6-10(b), the random distribution of σ_z-(hydrostat pressure) versus μ suggests that there is scatter in the data. It is also difficult to identify any large difference in the response of the borosilicate glass to the soda-lime glass. In Figure 6-11(a) the same parameter (σ_z-(hydrostat pressure)) is plotted for the quartz hydrostat. The quantity (shear stress-longitudinal stress) also becomes negative for values of $\mu > 0.4$ for quartz hydrostat, although the underprediction is 90 GPa at $\mu = 0.7$, compared with 40 GPa for the Johnson-Holmquist hydrostat. In Figure 6-11 (b), the soda-lime and borosilicate glass data are again scattered and overlie each other.

This analysis suggests that the hydrostat derived by previous workers for soda-lime glass is different to that of the quartz. The Johnson-Holmquist hydrostat produces much greater

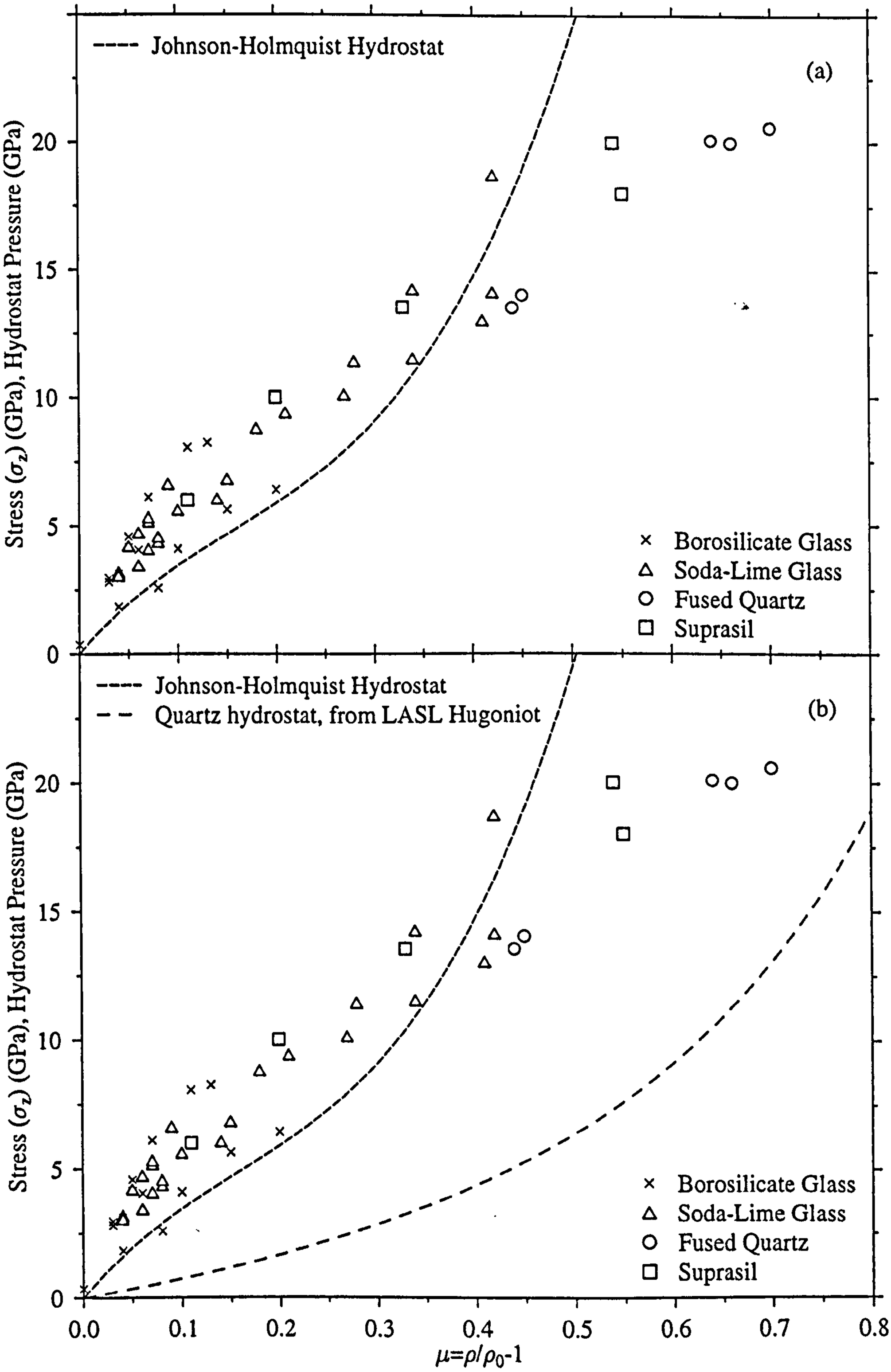

Figure 6-9. (a) Data from Fig. 6-8(a), grouped by target type, compared to the Johnson-Holmquist 2 hydrostat. (b) As (a), plus the quartz hydrostat derived from quartz shock Hugoniot data (see text).

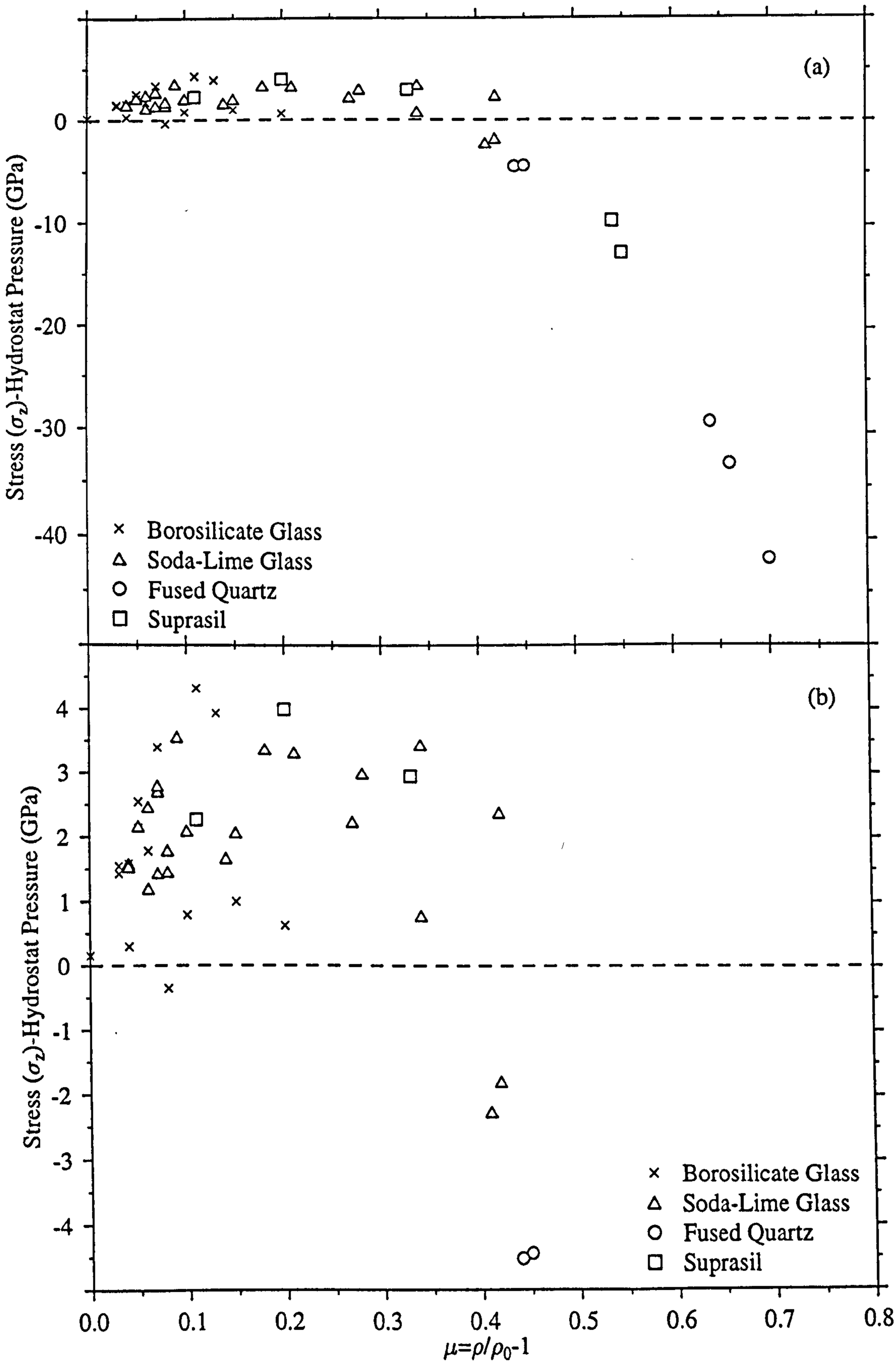

Figure 6-10. (a) The difference between the measured longitudinal stress (σ_z) and the Johnson-Holmquist 2 hydrostat pressure for borosilicate glass, soda-lime glass, fused quartz and Suprasil. (b) A closer look at the soda-lime data.

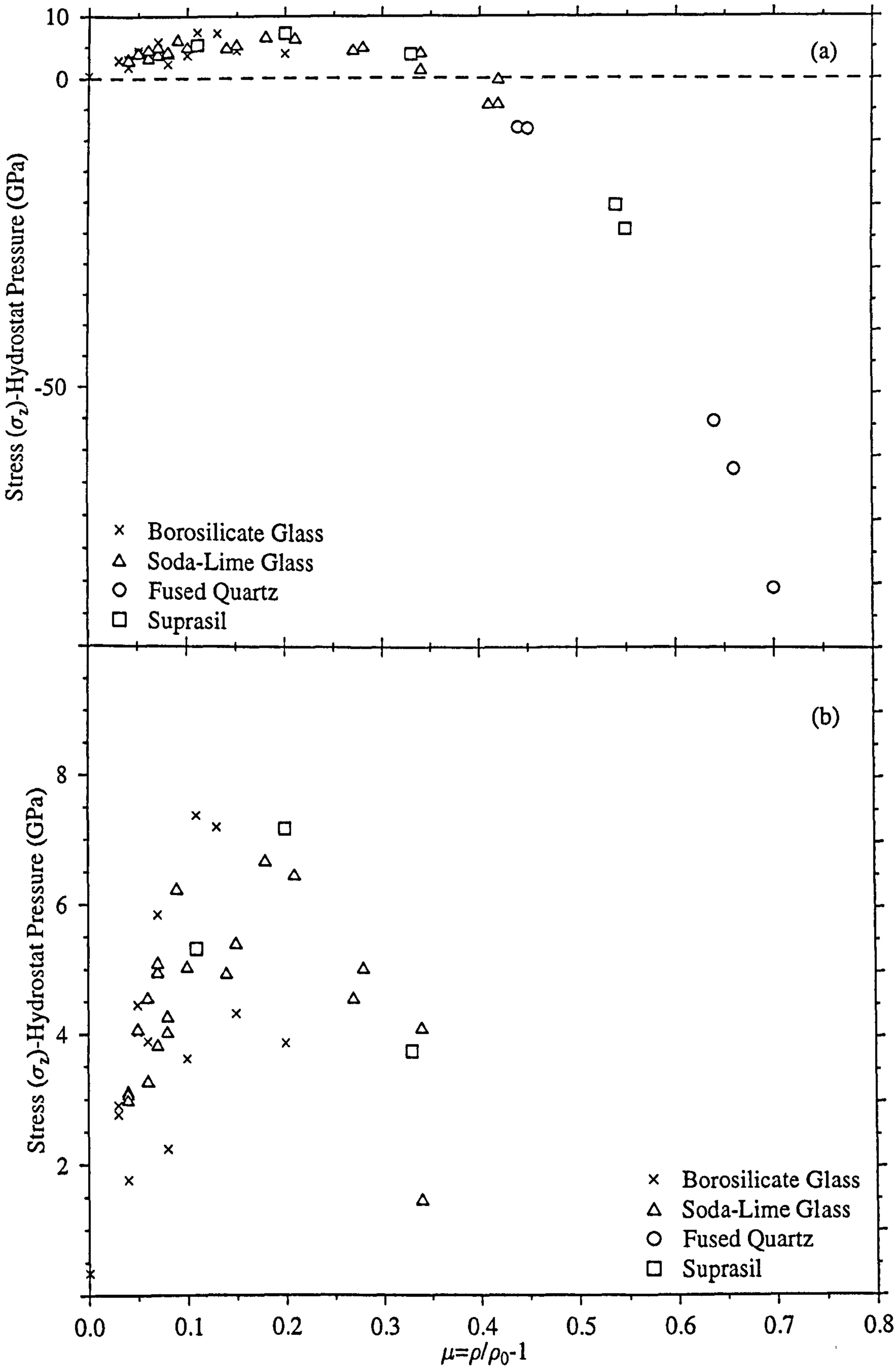

Figure 6-11. (a) The difference between the measured longitudinal stress (σ_z) and the quartz hydrostat pressure for borosilicate glass, soda-lime glass, fused quartz and Suprasil. (b) A closer look at the soda-lime data.

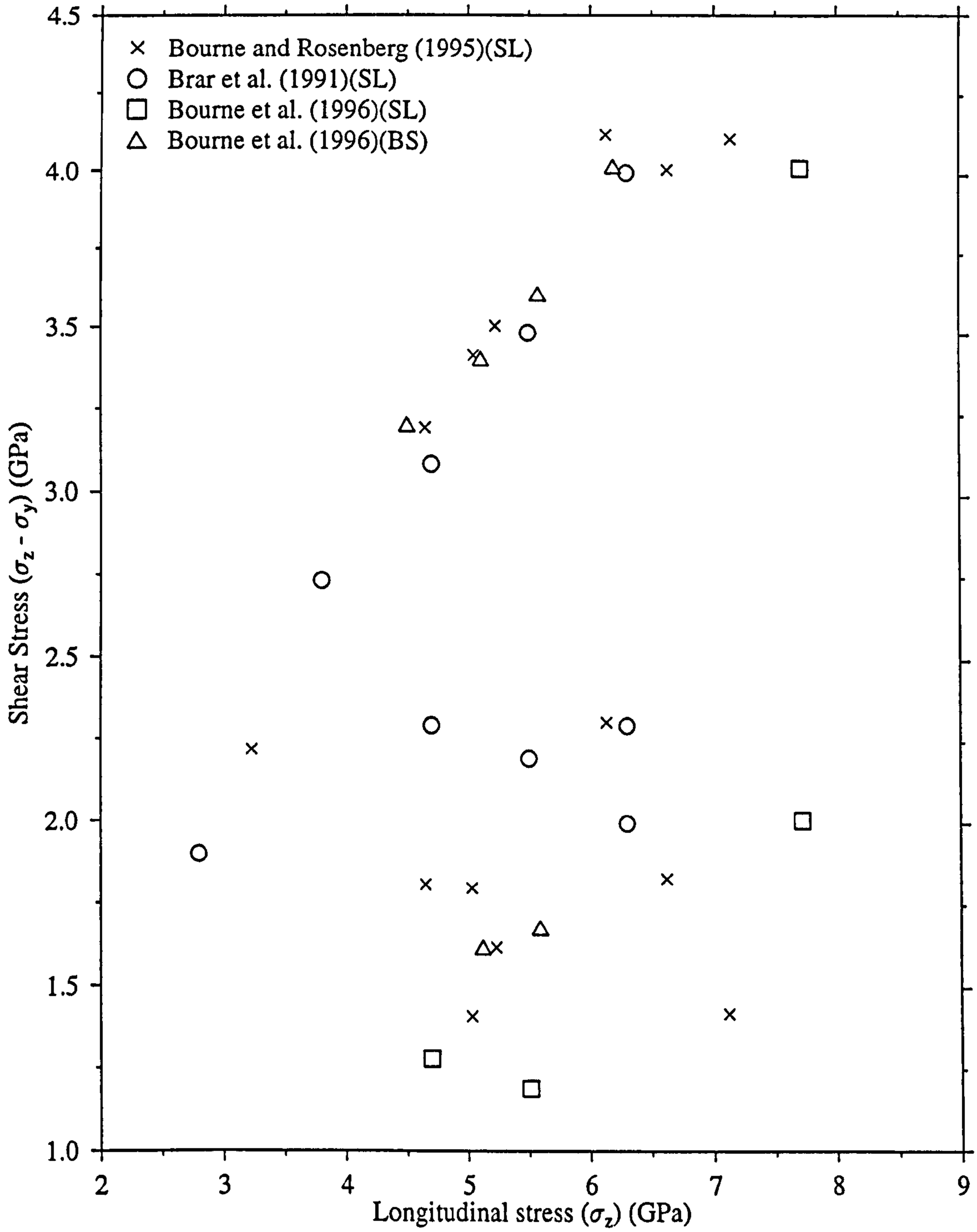

Figure 6-12. Shear stress (σ_y - σ_z) versus longitudinal stress (σ_z) for borosilicate and soda-lime glass. The loss of shear strength behind the failure wave is clearly seen. BS: borosilicate glass, SL: soda-lime glass, FQ: fused quartz).

pressures as a function of μ than the quartz hydrostat. The quartz hydrostat always lies below the measured values of σ_z and the same holds true for the majority of the soda-lime and borosilicate glass data compared with the Johnson-Holmquist hydrostat. The flyer plate data shows no difference between the response of the soda-lime glass and the borosilicate glass (as used in solar cells). More data are required for soda-lime glass for σ_z > 15-20 GPa in order to resolve what values the constants K1, K2 and K3 should have.

6.5 Failure Waves

A so-called failure wave has been observed to propagate behind the elastic wave in glasses at velocities of 1.5-2.5 km s^{-1} with a non-varying velocity (Rasorenov, 1991; Dandekar and Beaulieu, 1995). Shear strength and spall strength measurements have been made in front of and behind the failure wave and show a large decrease and a fall to zero respectively, behind the failure wave (Brar *et al.*, 1992). This is shown in Figure 6-12. The mechanism by which the failure wave propagates has not been fully explained, although it has been suggested that the failure wave represents the transformation shock boundary between the intact and communited material. This mechanism has therefore not been included in current brittle material strength models as implemented in hydrocodes.

6.6 Discussion

The published shock data (Table 6-2) have been reviewed for glass and shown to have variation in the values of c_0 and S. This affects the volumetric response predicted by the equations. Therefore caution is required when choosing glass Hugoniot data for use within a hydrocode simulation. The Johnson Holmquist and quartz hydrostats have been compared and shown to be different. The Johnson-Holmquist hydrostat is less than the majority of the soda-lime and borosilicate glass data and the quartz hydrostat is less than the quartz data. There is no clear difference between the soda-lime and borosilicate glass data, suggesting that the two materials have a broadly similar response. In conclusion, the quartz and Johnson-Holmquist hydrostats predict a different material response. There is not enough flyer plate data to decide whether quartz and soda-lime glass have different shock responses, as suggested by the hydrostats. The response of the borosilicate glass is similar to that of soda-lime glass.

6.7 Summary

The soda-lime glass hydrostat differs to that of quartz at very high impact pressures. The Johnson-Holmquist model is qualitatively supported by the flyer plate data and the data suggest that soda-lime glass and borosilicate glass have broadly similar responses to hypervelocity impact.

Chapter 7

7. Comparing Solar Cell with Ductile Material Impact Fluxes

The response of soda-lime glass and borosilicate glass to hypervelocity impact has been analysed in this thesis (chapters 3 to 6). For example, Eqs. 4-8 and 4-9 have been developed to characterise the response of soda-lime glass and borosilicate glass, which was noted to be different to that of quartz. In addition, borosilicate glass and soda-lime glass have been shown to produce a variable response to hypervelocity impact compared with ductile materials, resulting in a wider distribution of conchoidal diameters of glass than craters in aluminium resulting from multiple impacts by identical projectiles.

In this chapter, a conversion between D_{co} and F_{max} (equivalent ballistic limit in aluminium) is derived and used to compare the F_{max} equivalent fluxes from the solar arrays to fluxes from the LDEF and TiCCE experiments (chapter 1). This conversion is obtained using (i) conchoidal diameter damage equations for soda-lime glass and borosilicate glass (chapter 4), (ii) experimental data for impacts onto soda-lime glass (chapter 3) and (iii) space-exposed brittle materials (quartz) on LDEF.

An exact comparison cannot be made between the HST and EURECA solar array fluxes and LDEF and TiCCE as the exposure of these surfaces (velocity distribution, altitude etc.) is unique. In particular, the EURECA solar array was fixed with respect to the spacecraft body, unlike the HST arrays, which could rotate with respect to the telescope body. However, a guide to the validity of the conversion can be obtained by considering the fluxes from the LDEF spacecraft and TiCCE experiment.

The damage equation Eq. 4-9 (soda-lime glass and borosilicate glass) also could be used in conjunction with modelling to resolve spacecraft pointing, shadowing of the solar arrays by the spacecraft body (and the production and capture of secondary ejecta) and earth shielding of the solar arrays. This advanced modelling is beyond the scope of this thesis but can be carried out as follow-on work.

The geometry of the LDEF faces is given in Figure 7-1(a). The East face is known as the (Earth) Ram direction and the West, as the (Earth) Wake face. The Space face is, by virtue of the geometry, exposed only to meteoroids, as debris in elliptical intersecting orbits would be quickly deorbited by airdrag (McBride, 1997). In Figure 7-1(b) the orientation of the Earth apex flux with respect to the TiCCE experiment and solar array pointing vectors is shown in a spacecraft centred frame. The Earth follows the path represented by the marked line so providing different levels of Earth shielding as the spacecraft orbits. The statement, commonly used, that the solar arrays are always sun pointing, perpendicular to the line of

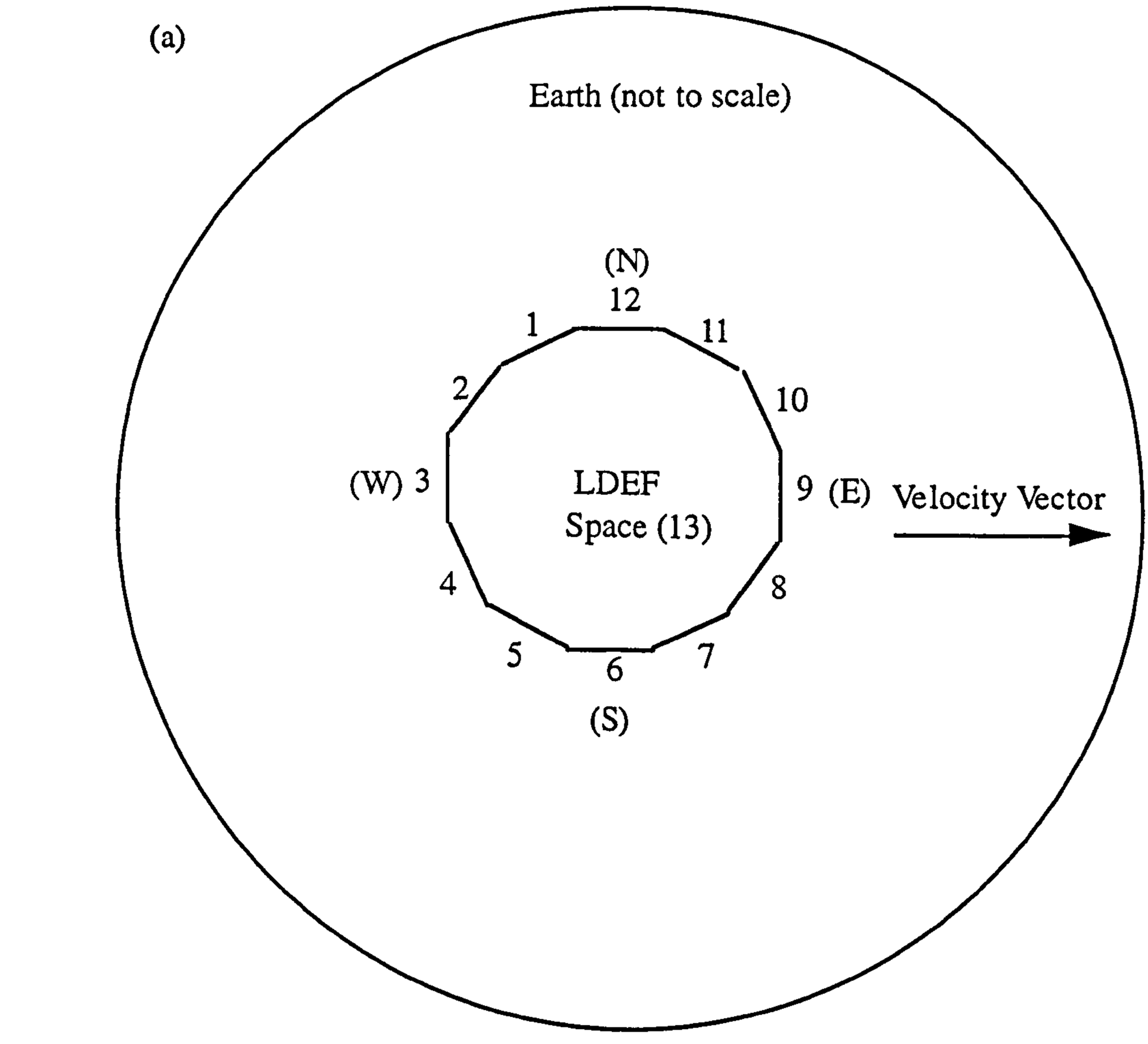

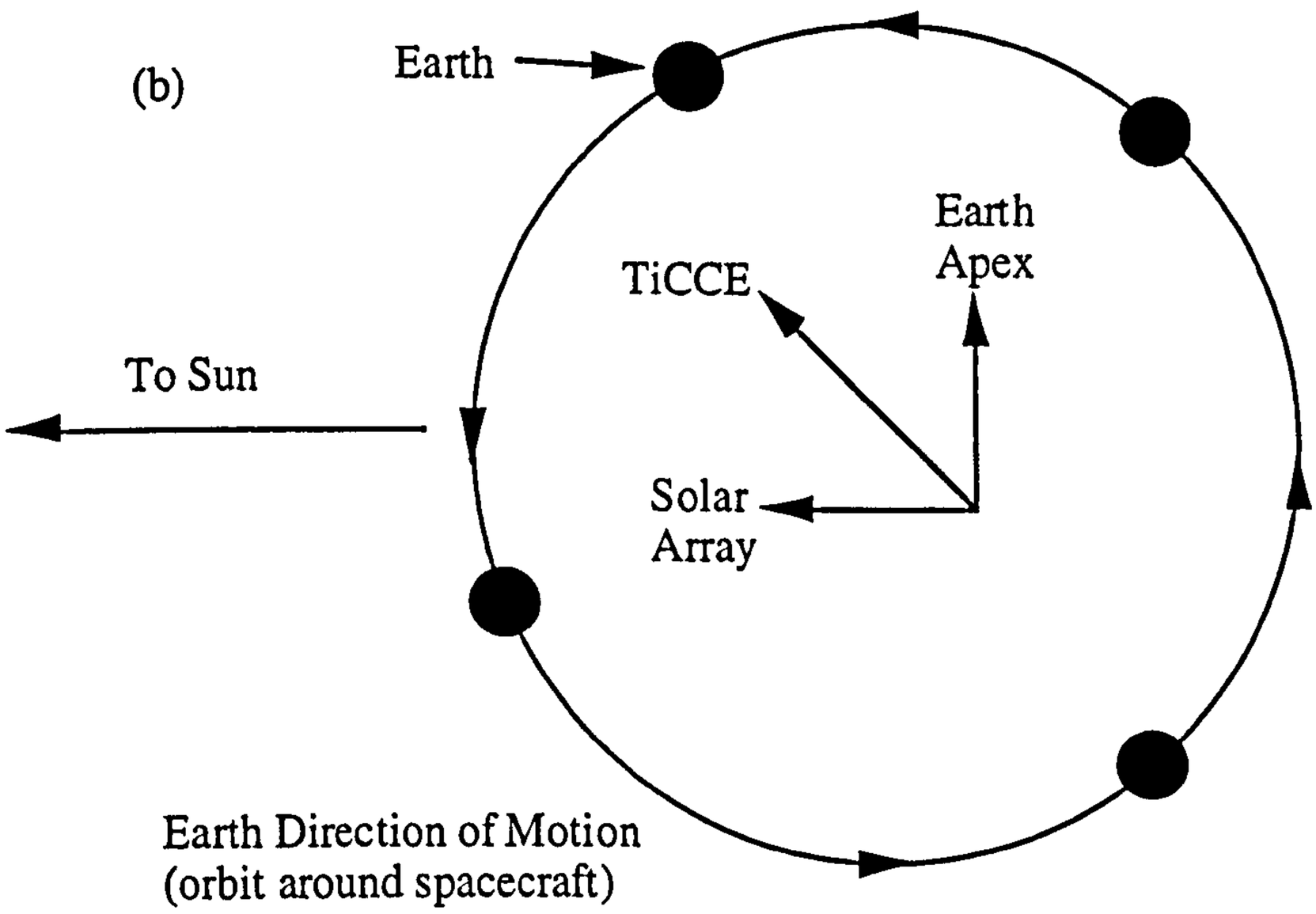

Figure 7-1. (a) Nomenclature of the LDEF faces. The faces always maintain the same orientation with respect to the Earth and the velocity vector i.e. the East face (09) is towards the Ram direction, although it is offset by 8° (b) The Earth shielding experienced by the EURECA TiCCE experiment and solar array in the spacecraft centred frame. The shielding varies as the spacecraft orbits the Earth.

sight to the Sun, is not always true for spacecraft operations. When the two-line elements defining the motion of the solar arrays are obtained, then this assumption can be tested. The spacecraft also yaw up and down along the vector defining the orbital motion. Again, the fixed body mounted EURECA solar array will probably have different sun pointing to the HST solar arrays.

7.1 Derivation of D_{co} to F_{max}: Damage Equations

The damage equations of chapter 4 can be combined with the most recently published F_{max} damage equation (Eq. 7-1) to obtain a conversion factor for D_{co} to F_{max}. Eq. 7-1 is consistent with earlier cratering formulae on thick targets. Note that the velocity term in Eq. 7-1 is replaced by $v\cos\Theta$ as a first approximation, following the recommendations of the authors (Gardner *et al.*, 1997). The ratio of Eq. 8-1 and the D_{co} damage equations presented in this thesis is taken to provide a conversion factor. Eq. 7-2 is based on Eq. 4-9 (for solar cell and soda-lime glass). Eq. 4-8 (soda-lime glass only) has different constants, velocity exponents and impact angle exponents, giving Eq. 7-3.

$$F_{max}=0.129\left(\frac{V\rho_p}{\sqrt{\sigma_t\rho_t}}\right)^{0.763}\left(\frac{\sigma_t}{\sigma_{Al}}\right)^{0.229}d_p^{1.056} \qquad (7\text{-}1)$$

$$\frac{F_{max}}{D_{co}}=0.39^{+0.07}_{-0.06}d_p^{-0.22\pm0.01}\rho_p^{0.32\pm0.04}v^{0.10\pm0.07}\cos\Theta^{0.14\pm0.06} \qquad (7\text{-}2)$$

$$\frac{F_{max}}{D_{co}}=0.47^{+0.08}_{-0.07}d_p^{-0.22\pm0.01}\rho_p^{0.32\pm0.04}v^{0.01\pm0.07}\cos\Theta^{-0.11\pm0.13} \qquad (7\text{-}3)$$

(σ: yield strength (t: target, Al: aluminium). Units for Eq. 7-1 are SI, apart from d_p and F_{max}, which are in microns. Symbols and units as defined for Eq. 4-8 and 4-9 for Eqs. 7-2 and 7-3.).

Note the differing velocity exponents of Eqs. 7-2 and 7-3, which produce a 20% and 1% difference in F_{max}/D_{co} for a velocity change of 5 to 15 km s^{-1} respectively. Impactor parameter ranges of v = 5- 20 km s^{-1}, ρ = 1 - 8 g cm^{-3} and d_p = 5 - 100 µm are chosen to represent typical impact conditions in space, producing a range of conchoidal diameters less than 500 µm (with some overlap). Therefore Eq. 7-2 becomes $F_{max}/D_{co} = 0.32^{+0.54}_{-0.30}$. Choosing a typical space impact condition (v = 15 km s^{-1}, ρ = 2.5 g cm^{-3}) for a d_p = 20 µm, produces $F_{max}/D_{co} = 0.34^{+0.13}_{-0.10}$. For Eq. 7-3, the corresponding values of F_{max}/D_{co} are $0.35^{+0.13}_{-0.09}$.

7.2 Derivation of F_{max} to D_{co} Equation: Data at 5 km s^{-1}

The ratio can also be derived from a consideration of the experimental data from the programme described in section 2.2, for the impact velocity of 5 km s^{-1}. The crater

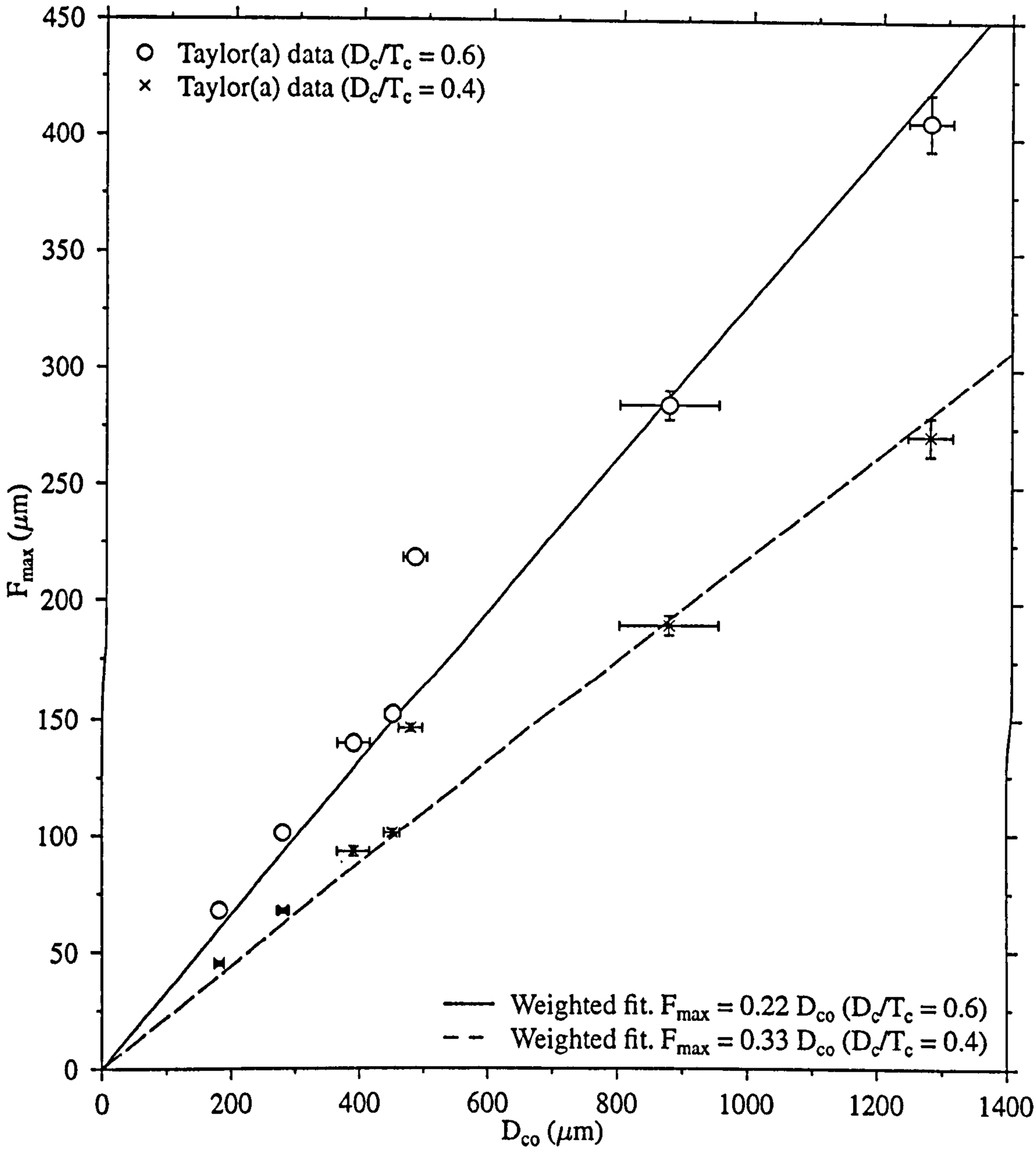

Figure 7-2. Taylor(a) (Glass buckshot programme, section 2.3) data from impacts onto aluminium and soda-lime glass. The aluminium crater diameters have been converted to F_{max} by using $D_c/T_c = 0.4$ or 0.6 then $F_{max} = 1.5\ T_c$. Examples of two weighted fits are shown.

diameters (D_c) are converted to depths (T_c) using an experimentally observed D_c/T_c ratio. To a first approximation, D_c/T_c is 0.5, as hypervelocity impact craters are assumed to be hemispherical. However, a survey of space surfaces (LDEF) gave $D_c/T_c = 0.59 \pm 0.14$ (Newman, 1992) and supported by Love *et al.* (1995), ($D_c/T_c = \sim 0.56$) for impacts of soda-lime glass spheres onto aluminium. However, the crater depths measured on the aluminium witness plates (Figure 2-2) showed a crater depth of 0.4 - 0.5 D_c. The difference may be due to the different impact velocities (5 km s^{-1} compared with 5-20 km s^{-1}). The relationship $F_{max} = 1.5\ T_c$ (Newman, 1992) was then used to convert the crater diameters (or depths) to the F_{max} values. The F_{max} versus D_{co} data are plotted in Figure 8-2 for both $D_c/T_c = 0.4$ and 0.6 along with the results of the weighted and equally weighted fits to data (Table 7-1).

This technique was previously carried out using both the Taylor(a) and Shrine data sets (reviewed Table 3-1) and the relationship $F_{max} \approx 0.24\ D_{co}$ (Shrine *et al.*, 1996) was obtained. This ratio was also confirmed by deriving an F_{max}/D_{co} from Eq. 3-6 and Eq. 3-8 for normal impacts. In Shrine (1998) the D_{co} to F_{max} conversion has been carried out for the Shrine data set, providing the fits given in Table 7-1. The technique used was to convert the depth measurements made from SEM stereo pair images to F_{max} using the Newman (1992) relationship, and then to calculate the average and standard deviation of the F_{max}/D_{co} ratio. The conversion to the F_{max} was checked by inserting the impactor parameters (d_p, v, $\cos\Theta$) into Eq. 7-1 and calculating the F_{max} values. The average of the F_{max}/D_{co} is then calculated and compared with the previous ratio. The results are given in Table 7-1. Forcing the fit through zero does not make a significant difference to the values of b. However, the choice of D_c/T_c ratio does affect the result of b returned by the fitting programme. As the value of D_c/T_c cannot be fixed to one value, due to the range of values suggested by the experimental data, the conversion factor applied to the solar cells will be based on a range of values.

Table 7-1. The results of the fits between $F_{max} = b \times D_{co} + a$ for weighted and equally weighted fits and two different D_c/T_c ratios.

Data set	D_c/T_c	Weighted ?	b	a	Reference
Taylor(a)	0.6	Yes	0.33 ± 0.00	0 (forced)	This thesis
Taylor(a)	0.6	No	0.34 ± 0.01	0 (forced)	This thesis
Taylor(a)	0.4	Yes	0.22 ± 0.00	0 (forced)	This thesis
Taylor(a)	0.4	No	0.23 ± 0.00	0 (forced)	This thesis
Taylor(a)	0.6	Yes	0.30 ± 0.00	-0.01 ± 0.00	This thesis
Taylor(a)	0.6	No	0.31 ± 0.02	-0.02 ± 0.01	This thesis
Taylor(a)	0.4	Yes	0.20 ± 0.00	-0.01 ± 0.00	This thesis
Taylor(a)	0.4	No	0.21 ± 0.01	-0.02 ± 0.01	This thesis
Shrine	0.6	No	0.21 ± 0.03	0 (forced)	Shrine, 1998
Shrine + Eq. 7-1	N/A	No	0.23 ± 0.01	0 (forced)	Shrine, 1998
Taylor(a) + Shrine	0.6	No	≈ 0.24	0 (forced)	Shrine *et al.*, 1996

7.3 LDEF : Space Based F_{max} to D_{co} Conversion for Quartz

Solar cells, consisting of quartz coverglasses (300, 500 or 1000 μm thick) backing onto 300 μm silicon cells, were flown on LDEF Row 08 face (see Figure 7-1(a) for location) (Hill and Rose, 1994). In previous chapters, quartz has been found to give a differing response to hypervelocity impact to that of soda-lime glass and borosilicate glass. Therefore, the conversion factors derived in the two previous sections may not be appropriate for use on the quartz data. The cumulative flux curve, produced from scanning of the coverglass, is plotted in Figure 7-3(a). The data are not divided into different target thicknesses so the effect of target thickness can only be indirectly determined by considering the 'kinks' in the flux curve, analogous to the those noted in the HST main survey flux curve, denoting changes in morphology matching to penetration of a deeper substrate layer.

In Figure 7-3 the roll-off in the data (marked on diagram) is estimated to be at about 80-100 μm, signifying where incompleteness of the data set (due to scanning detection limits) starts. The selected region (80-200 um) is shown in Figure 7-3(b), representing the part of the data thought to be free from roll-off effects and multilayering effects. The cumulative flux and meteoroid modelling results for Row 08 aluminium surfaces are given in Figure 7-4. The quartz cumulative flux curve is also plotted in Figure 7-4 for comparison. (The LDEF data are from impacts on spacecraft structures (S. F. Green, personal communication) and the modelling results are derived using the same methodology as presented in McBride and Taylor (1997) and McBride (1997)). An interpolation programme (Gardner, 1995) is used to determine the values of D_{co} and F_{max} which have equal fluxes, that is number of impacts per square metre per second. The smallest value of F_{max} recorded on the aluminium surfaces is 10 μm which corresponds to D_{co} ~ 130 μm. The results of the interpolation programme are shown in Figure 7-5. By eye, the data between the region 136-170 μm are linear, and a line of gradient 0.21 is marked on for comparison. However, least squares fits carried out to this range give the F_{max} dependence on the D_{co} as a power-law (Eq. 7-4). The power-law fit is also plotted in Figure 7-5. Both show good agreement with the data in the region 136-170 μm.

$$F_{max}=10^{-3.94\pm0.17}D_{co}^{2.32\pm0.08} \quad (r^2 = 0.97) \qquad (7\text{-}4)$$

The differing response of quartz, not fully quantified nor explained in this thesis, may explain this different power-law dependence derived from the data. Although the differing response has not been quantified, it is unlikely to be based on a strong dimensional dependence difference. Therefore, the values of the linear fit give a guide to those returned from the laboratory based data. The gradient 0.21 is in agreement with the range of values returned for the soda-lime/borosilicate glass conversions. Both quartz conversions are applied to the cumulative flux curve from Figure 7-3 and the equivalent F_{max} values plotted with the data from Figure 7-4 in Figure 7-6. The linear fit in Figure 7-6 shows a better

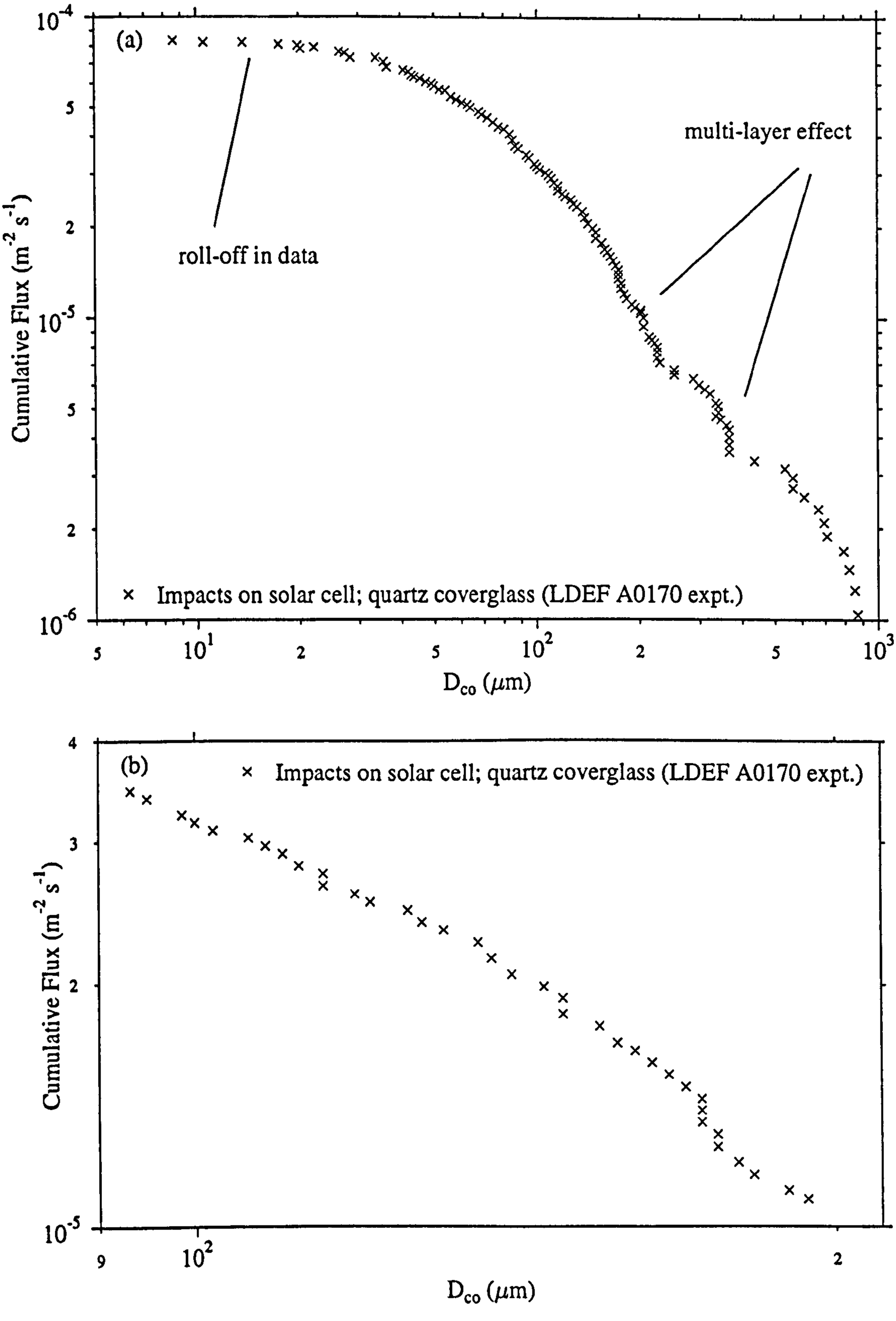

Figure 7-3. (a) D_{co} impact fluxes from Hill and Rose (1994) from Row 8 of LDEF The target is a solar cell with a quartz coverglass, thickness 300, 500 or 1000 μm. (total area 260 cm^2) (b) The flux curve between the (suspected) roll-off and the onset of multi-layer response of the solar cell.

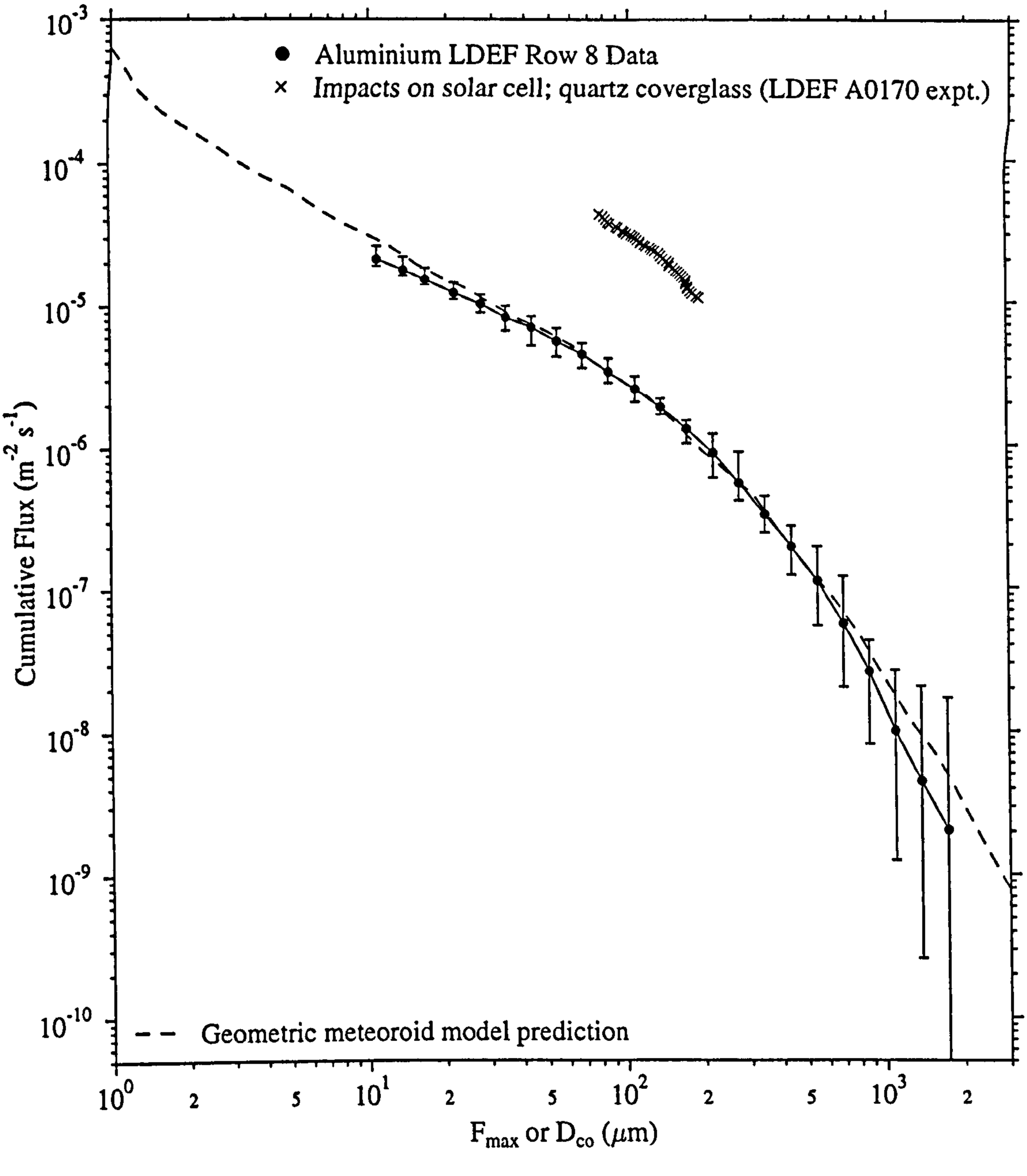

Figure 7-4. LDEF Row 8 face prediction using full geometric text model based on Grün mass distribution (Grun et al., 1985) and a full velocity distribution (Taylor, 1995a). Meteoroid model prediction provided by McBride (personal communication). LDEF flux from impacts on the spacecraft structure (Green, personal communication).

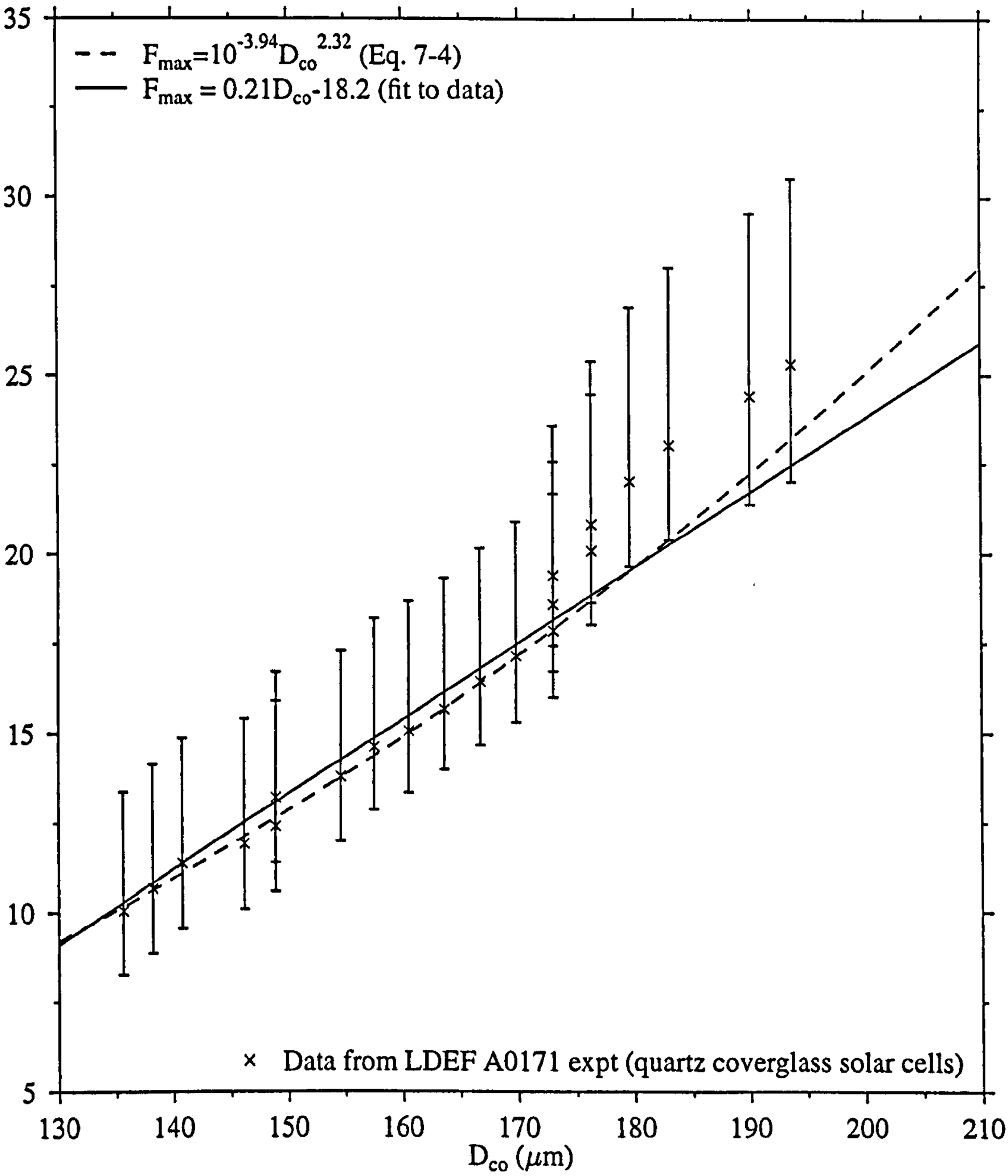

Figure 7-5. D_{co} impact fluxes from Figure 7-3, matched to equivalent F_{max} values from Row 8 (Figure 7-4) using an interpolation programme. The data are compared to two fits made to the 136 μm< D_{co} < 170 μm band of data (identified as the linear part of the flux curve)

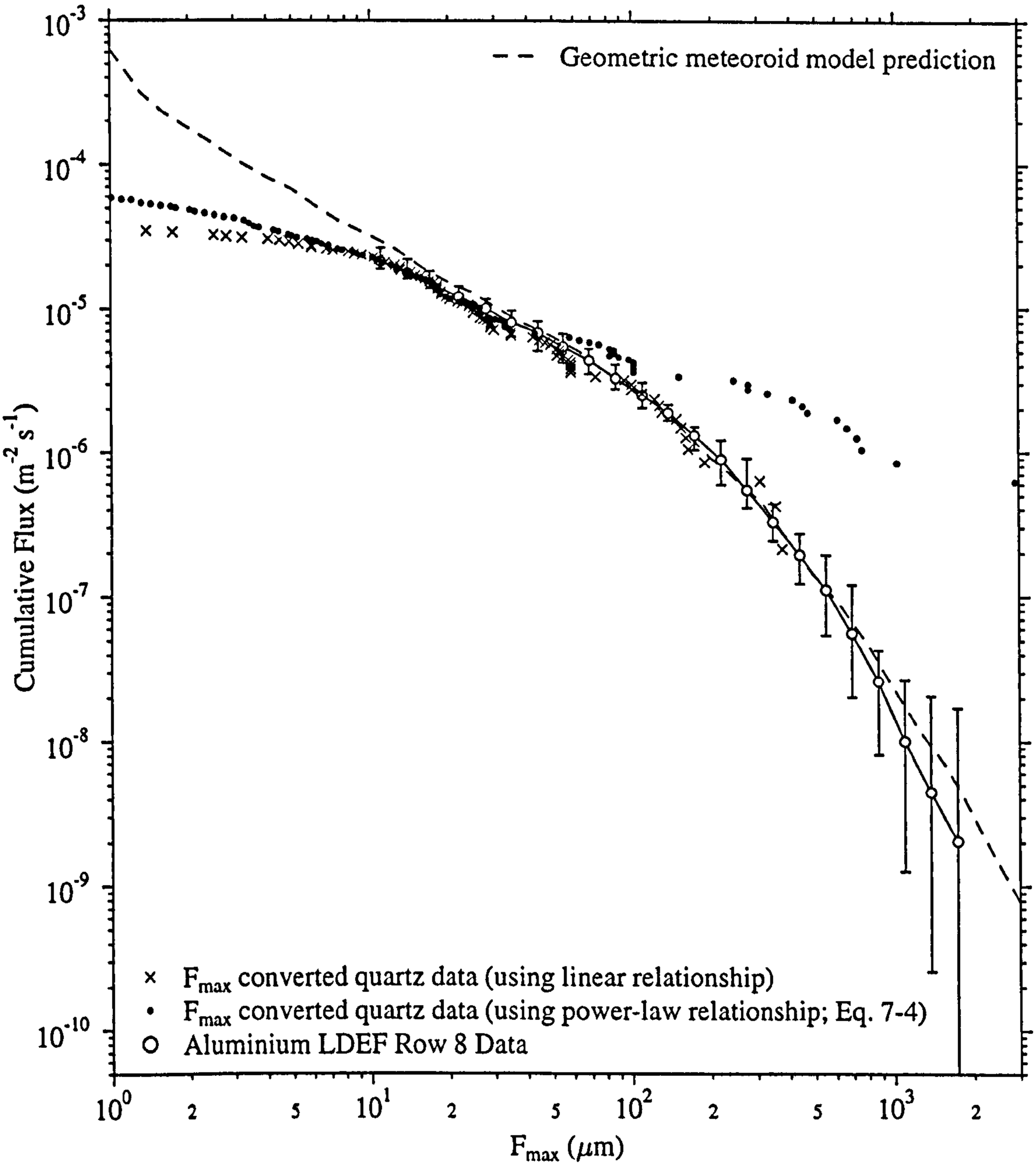

Figure 7-6. Modelling prediction and data (from Figure 7-4) compared to the converted fluxes from experiment A0171 (see Figure 7-3). The linear relationship $F_{max} = 0.21D_{co}$-18.2 provides a better functional form for the conversion. Meteoroid model and data as in Fig. 7-4.

functional form for use with the cumulative flux curve, as it does not show the enhancement of flux produced by the power-law conversion.

7.4 Solar Array Fluxes Compared with LDEF and TiCCE

The high resolution HST and EURECA flux data are presented in Figure 7-7. In addition to the data reviewed in Table 1-4, two additional HST fluxes are included (Mandeville and Rival, 1995). These fluxes are from SEM scans of the HST array at two resolutions (× 100 and × 500). The scan at × 500 magnification identified pit only impacts (typical diameter, D_{pit} = 1-2 μm). To compare the pit fluxes to the conchoidal fluxes, the pit diameters were converted to 'equivalent' conchoidal diameter using the experimentally observed $D_{co}/D_{pit} = 3$ ratio (as noted by Mandeville and Rival (1995) and discussed in section 3.2.4).

Although the solar arrays have different exposure histories (orbital altitude and duration) the fluxes agree to within an order of magnitude. In particular, the EURECA solar array was fixed with respect to the spacecraft body, whilst the HST body was able to rotate with respect to the solar arrays. In addition, the telescope body is much larger than a standard spacecraft and thus would shield the solar arrays to a greater degree. The fluxes all exhibit roll-off, but due to the small number of flux points published it is difficult to identify where the roll-off starts.

In the previous sections, a range of D_{co} to F_{max} conversions, derived by a variety of techniques have been presented. The values of $0.34\ ^{+0.13}_{-0.10}$ (for typical space impactor parameters, based on Eq. 8-2), 0.20-0.24 and 0.30-0.33 (impacts onto soda-lime glass and borosilicate glass) were derived. The following conversion, consistent with the range of values returned, will be applied to the solar array data, to represent the range of values returned by the different methods:

$$F_{max}=0.3\pm0.1D_{co} \qquad (7\text{-}5)$$

In addition to the errors in the conversion, a 20% D_{co} variability error (section 4.5) is also applied to the conchoidal diameter fluxes. Although no aluminium detectors were flown on the solar arrays, the decoded spacecraft array F_{max} fluxes can be compared with results from the LDEF spacecraft and the EURECA TiCCE experiment. As presented in Figure 7-1(a), the LDEF spacecraft presented a constant orientation to isotropic meteoroids and orbital space debris. By contrast, the EURECA spacecraft experiences varying Earth shielding during an orbit. The TiCCE and solar array vectors are shown with their orientations offset to the spacecraft ram direction in Figure 7-1(b). A further description of the relative exposure histories of the EURECA solar array and the LDEF spacecraft is given in Figure 7-8. The mean of the East, West, Space and Earth LDEF fluxes can be considered to be equivalent to

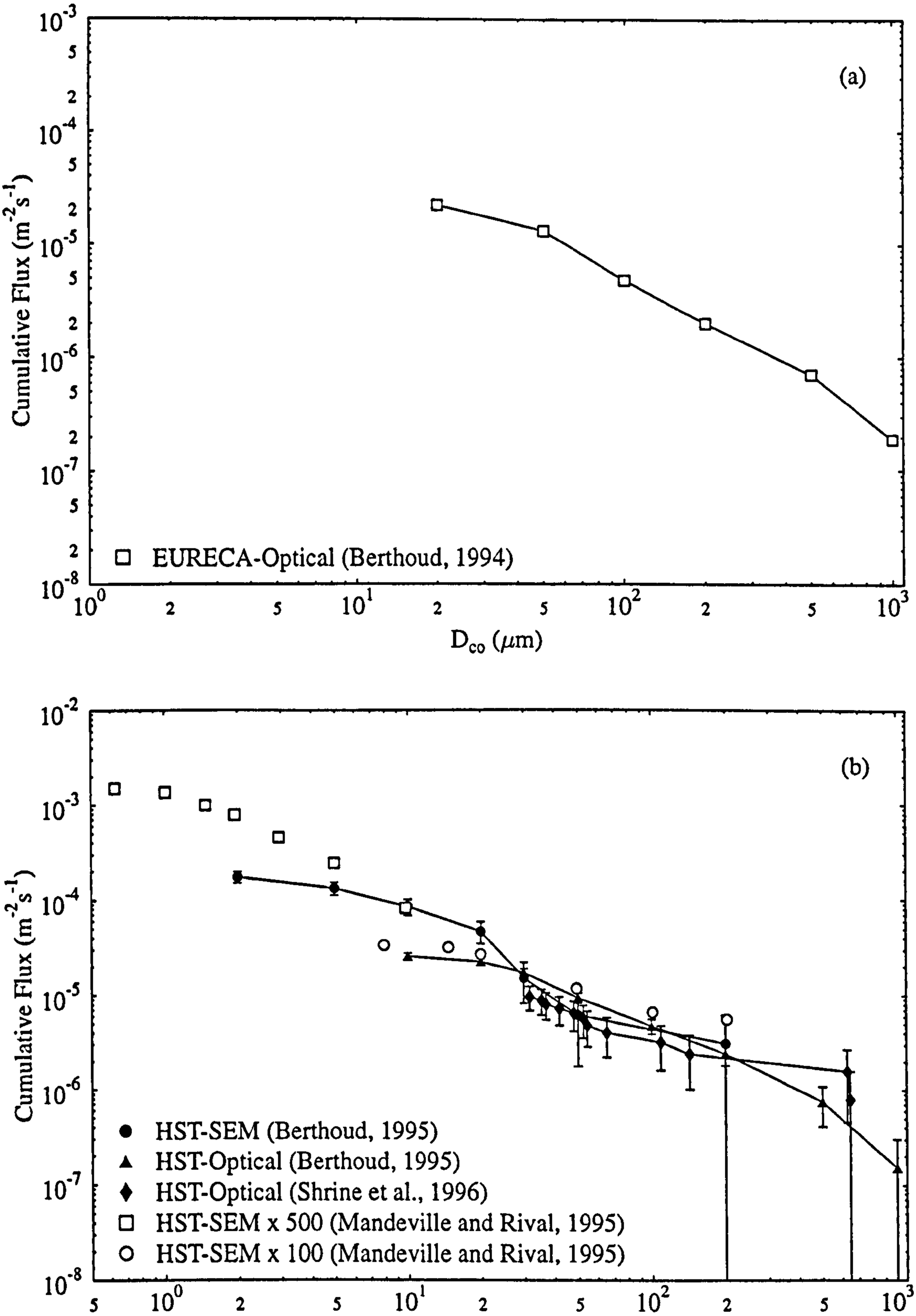

Figure 7-7. High resolution solar array flux data used in this thesis. Error bars have been calculated where the number of counts per bin is published. (a) EURECA (b) HST solar arrays. The HST x 500 D_{co} flux has been converted from D_{pit} values using the ratio $D_{co}/D_{pit} = 3$.

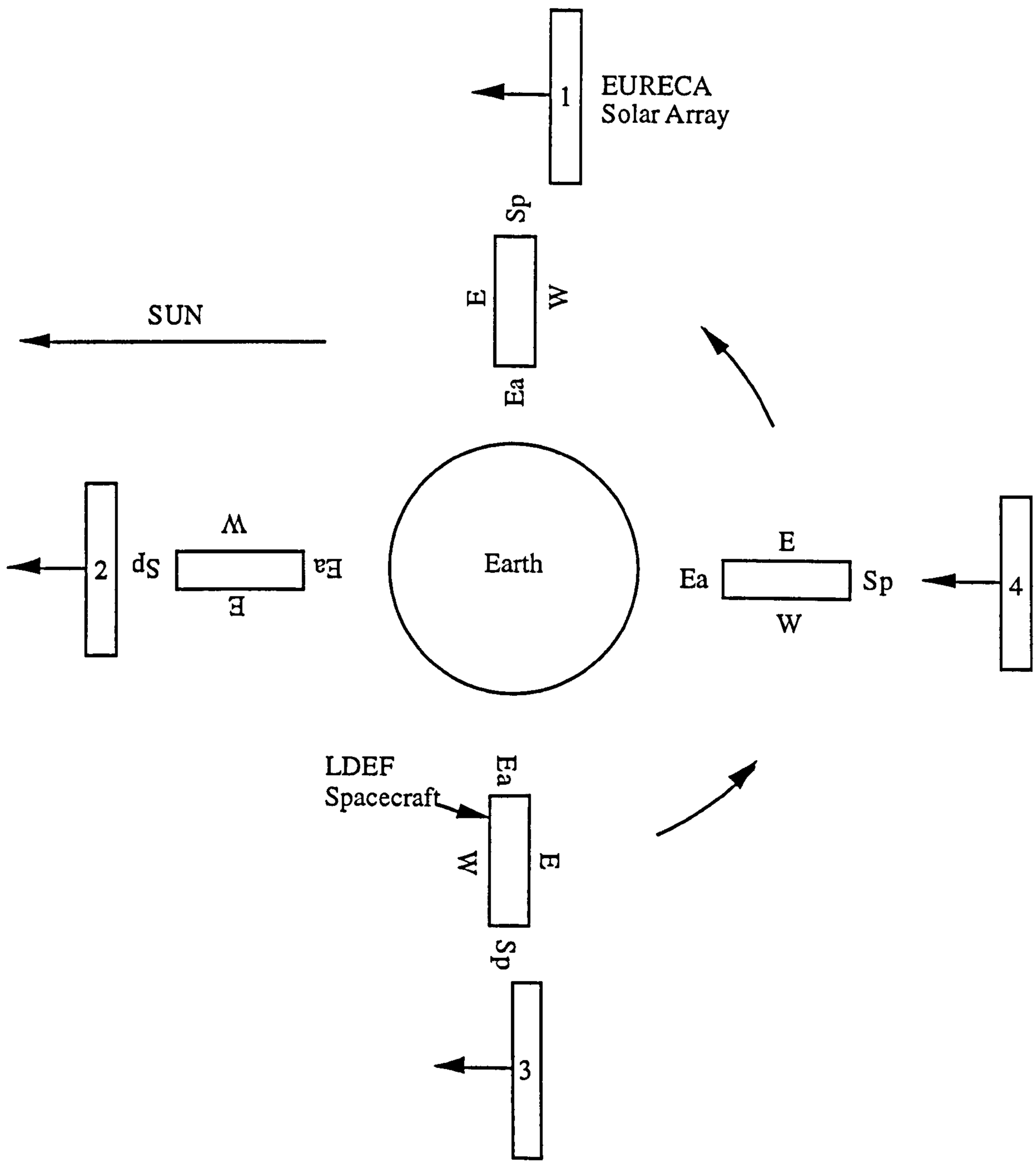

Figure 7-8. The orientation of the LDEF spacecraft and the EURECA solar array compared. 1: The solar array is pointing in the Ram (East) direction, receiving a high flux incorporating the space debris component. 2: The array is Space pointing and is exposed only to meteoroids. 3: The West face (Wake) is exposed to slower velocities and a lower flux. 4: The Earth-pointing solar array receives a low flux due to shielding by the Earth.

the fluxes incident on the EURECA Z and Y directions (Figure 1-3) for isotropic meteoroid and randomised space debris exposures (McBride, 1997). An LDEF 4-face mean can thus be composed of predicted meteoroid fluxes produced by the modelling programme used in McBride and Taylor (1997), as well as from measured impact craters. Firstly, the modelling results are compared with the fluxes from impact craters for each of these faces. A range of experiments produced fluxes over different F_{max} size ranges as well as impact craters analysed on the spacecraft frame and experiment tray holders. On-going work, by S. F. Green (personal communication), has folded these fluxes into one curve for each face. The modelling results and experimental data for each face are compared in Figure 7-9. The Ram face shows enhancement due to the 'sweeping up' of orbital debris at small sizes. The Space face (not visible to space debris, including those in eccentric orbits) matches the modelling as does the Wake face. Only the Earth face does not match the modelling results. This has not been conclusively explained, but may be due to the fact that the experiment trays were recessed from the face and thus would be exposed to secondary ejecta resulting from impacts on the tray walls. The values of the fluxes for the Earth face, whether modelling or data, are between one and two orders of magnitude lower than the fluxes measured from or modelled for the other three faces. Therefore, the influence of the data (or modelling results) on an average of the faces is small.

A 4-face modelling mean was obtained by taking the mean of the four faces results, whilst that of the impact data used the Space, Wake and Ram data plus the Earth model results. The 4-face means (modelling and crater data derived) are plotted in Figure 7-10 and compared with the TiCCE flux data (Gardner *et al.*, 1996). Note that the exposure history (and thus the fluxes) are different for the TiCCE experiment compared with the LDEF faces. The impact flux is greater than the meteoroid modelling results for $F_{max} < 30$ μm, showing the contribution of space debris, (see McDonnell *et al.*, 1997). The flux from the TiCCE experiment is also plotted in Figure 7-10. The data from the 2.5 and 9.2 μm thick foils agrees with the LDEF 4-face crater data mean. However, the $F_{max} = 20$ - 1000 μm data are higher than the LDEF data and modelling prediction. This has not yet been fully explained.

The conversion factor given in Eq. 7-6 is first applied to the EURECA solar array impact data and compared with the LDEF 4-face modelling and data means (errors not plotted for clarity) in Figure 7-11. For $F_{max} > 20$ μm, there is exceptionally good agreement between the LDEF impact fluxes, the modelling predictions and the converted EURECA fluxes, leading to a consistent result. However, for $F_{max} < 20$ μm, the data are consistent with meteoroid-only exposure, although the large error bars on the converted data make it difficult to rule out some debris enhancement of the flux. The lower fluxes may be due to different spacecraft or Earth shielding, or the roll-off in the flux data. As the solar array is not always in the ram direction the lower flux is to be expected. The different epochs of the missions (Table 1-1) point to a time varying dependence for the debris exposure.

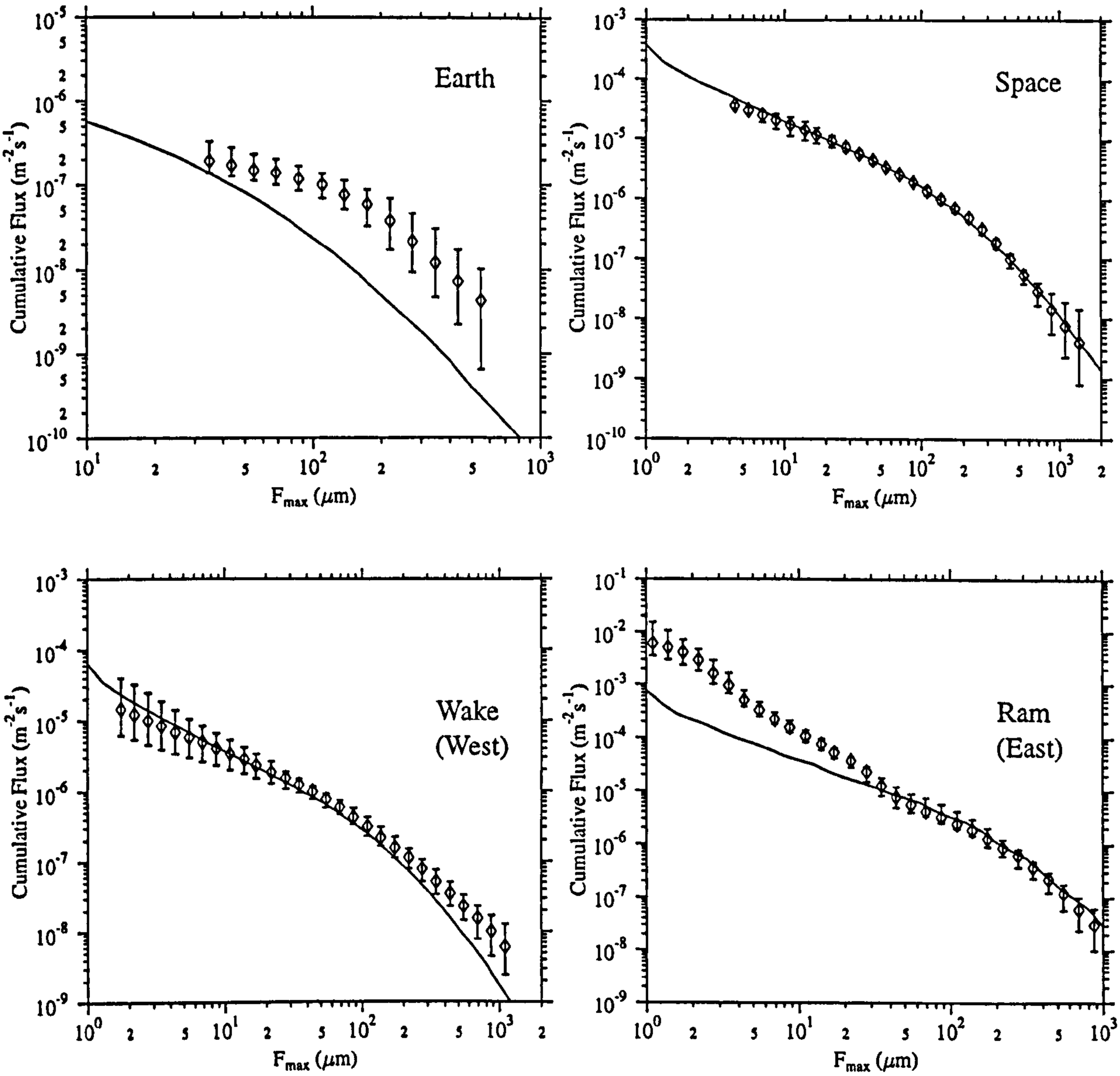

Figure 7-9. LDEF fluxes for the Earth, Space, West and East faces. The solid curves are the meteoroid modelling predictions (McBride and Taylor, 1997 and N. McBride, personal comm.). Experimentally determined LDEF fluxes from a range of sources (experiments and spacecraft structure) (S.F. Green, personal comm.). Errors bars indicate the spread of the data. The contribution of space debris is visible for $F_{max} < 30$ μm for the East face. The modelling is less applicable to the Earth face (see text).

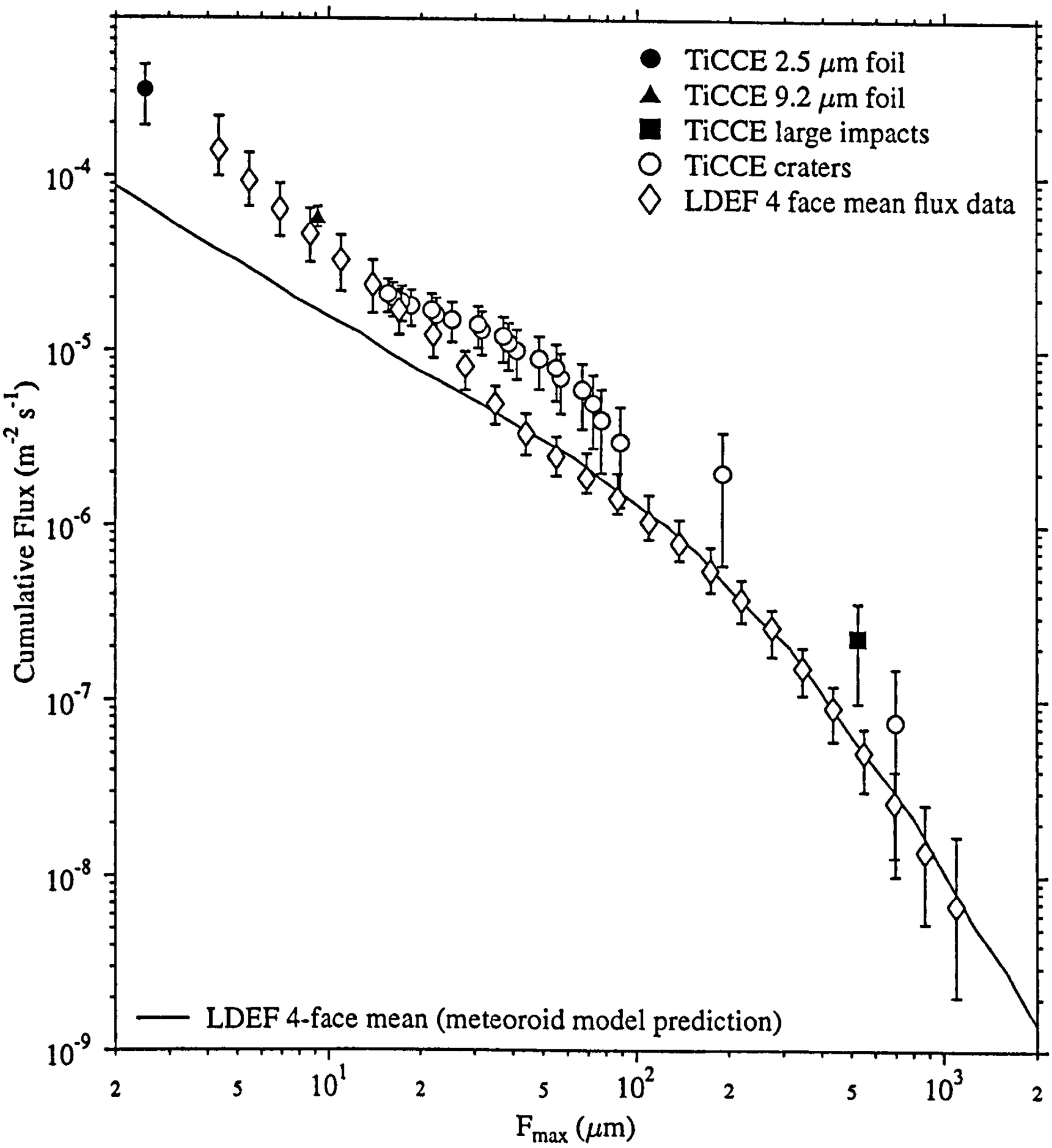

Figure 7-10. The mean of the modelling results for the four LDEF faces from Figure 7-9 compared to the TiCCE flux data (Gardner et al., 1996). An experimental data flux (composed of the Space, East and West crater data and the Earth modelling results) is also plotted. The contribution of space debris is seen below $F_{max} < 30$ μm. The TiCCE large impacts and crater data do not agree with the LDEF data. (LDEF modelling results and data as in Fig. 7-9)

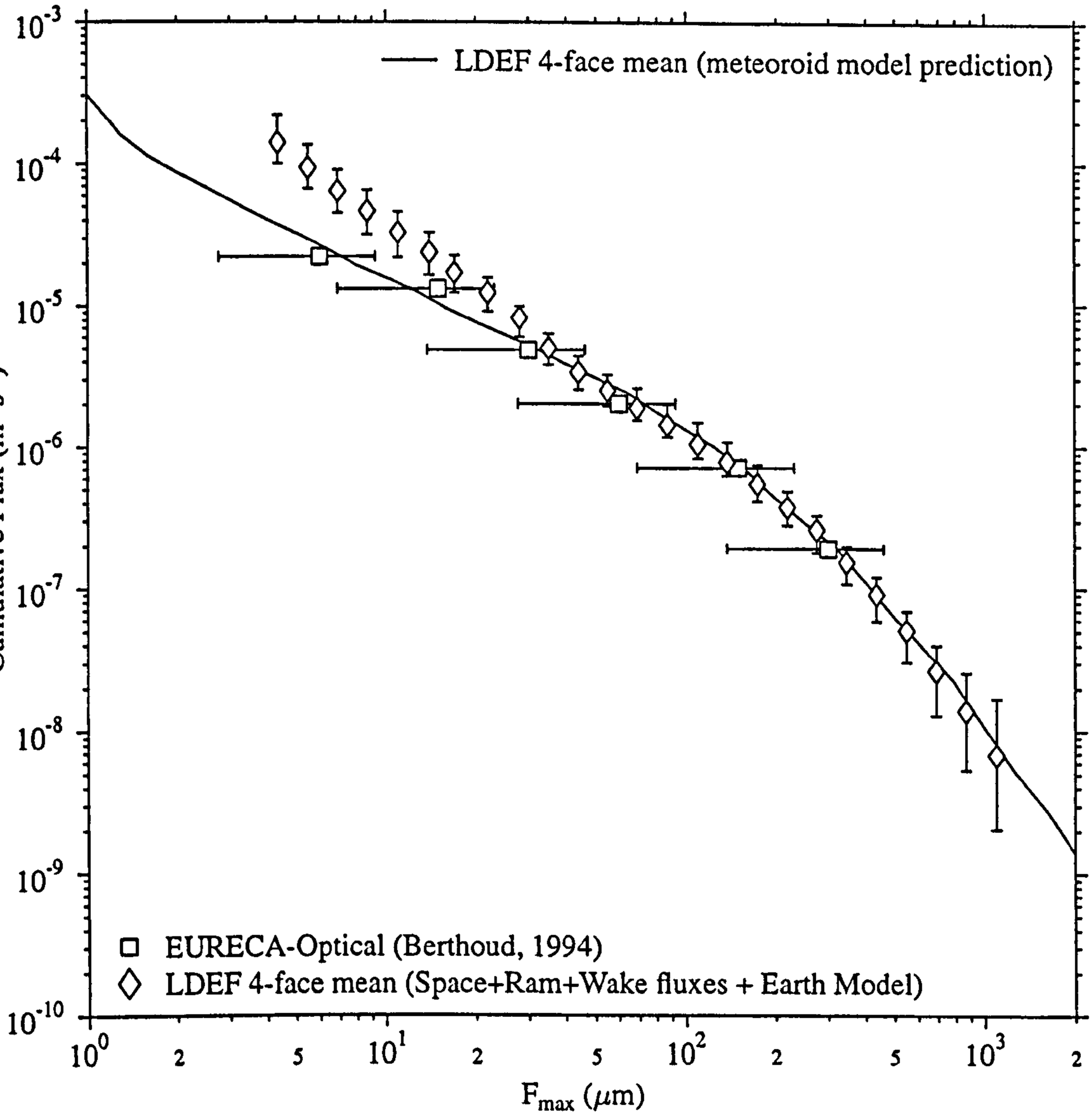

Figure 7-11. The converted EURECA flux (using Eq. 7-5) is compared to the LDEF 4-face mean for modelling and data (Figure 7-10). Above F_{max} = 20 μm, there is exceptionally good agreement between the EURECA data and the LDEF 4-face means. Below F_{max} = 20 μm, the data are more consistent with meteoroid only exposure.

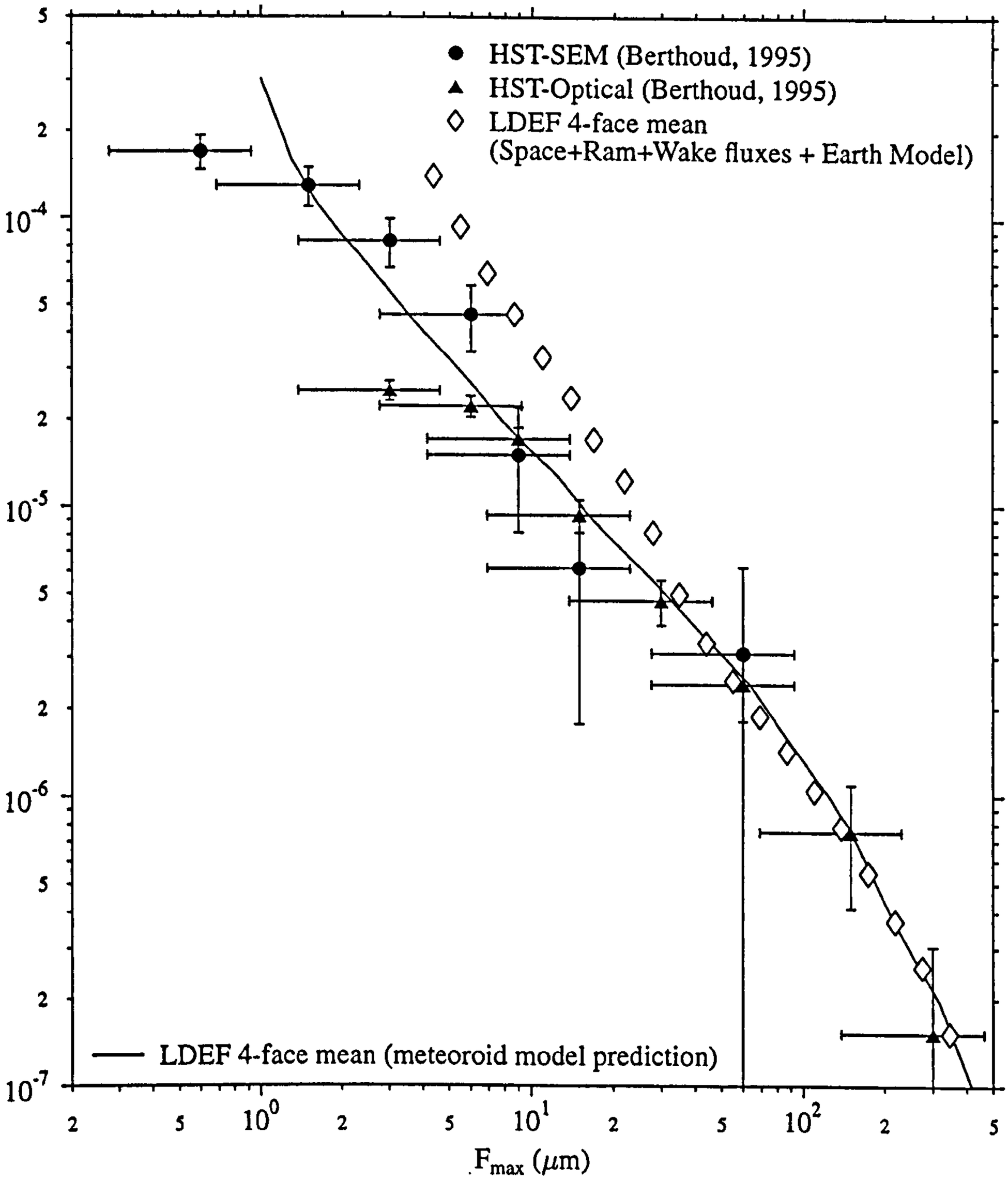

Figure 7-12. Converted HST solar array F_{max} fluxes compared to the 4 face LDEF modelling and data means shown in Figure 7-10. The conversion factor is $F_{max}/D_{co} = 0.3 \pm 0.1$ (Eq. 7-5) and the HST data also include 20% D_{co} variability errors. The SEM data lie within the modelling and data from LDEF, not confirming the debris enhancement predicted by LDEF. The optical data are in agreement with the LDEF 4-face means for $F_{max} > 30$ μm The scanned solar cells all come from the D+E solar panel assemblies.

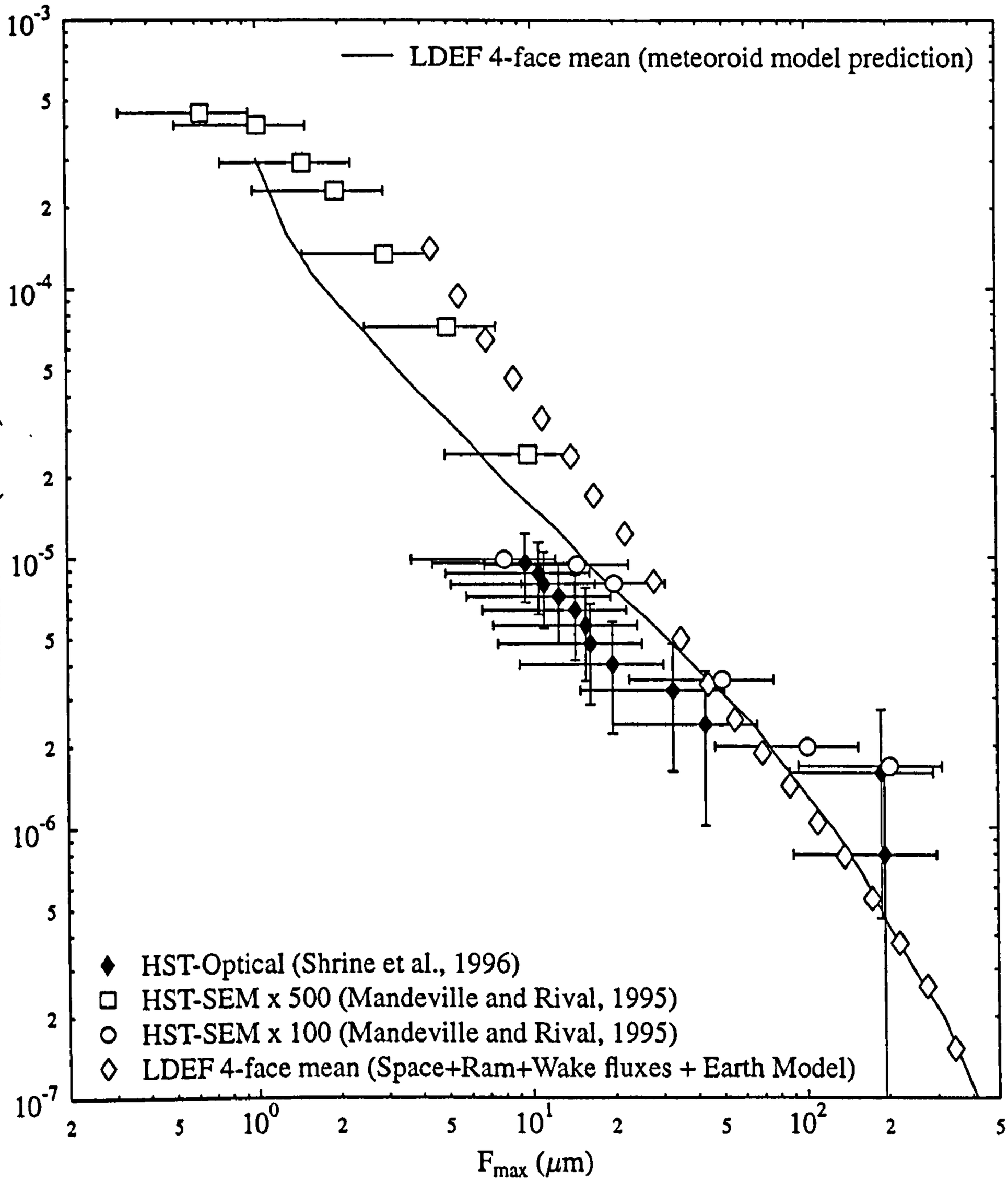

Figure 7-13. Converted HST solar array F_{max} fluxes compared to the 4 face LDEF modelling and data means shown in Figure 7-10. The conversion factor is $F_{max}/D_{co} = 0.3 \pm 0.1$ (Eq. 7-5) and the HST data also include 20% D_{co} variability errors. The SEM data lie within the modelling and data from LDEF, not confirming the debris enhancement predicted by LDEF. The optical data are not in agreement with the LDEF 4-face means. This variation in flux (with Figure 7-12) may be due to spatial variation across D+E solar panel assemblies.

The same conversion factor and LDEF 4-face means are plotted with the HST optical and SEM fluxes in Figure 7-12 and 7-13. The converted fluxes from the Shrine *et al.* (1996) HST solar array survey show lower values than the 4-face meteoroid modelling mean for the F_{max} range 5 to 50 μm. This difference may be due to the spatial variability noted across the HST array (possibly due to secondary impacts from the spacecraft body) or to different biases in the measurement techniques. The Mandeville and Rival (1995) D_{co} fluxes agree with the modelling and data means for $10 < F_{max} < 50$ μm but reproduce the rise above the data and modelling curves for $70 < F_{max} < 200$ μm shown by the Shrine *et al.* (1996) data. However, this is based on only a few impact craters and cannot be considered significant. In contrast, the converted fluxes from the optical survey by Berthoud (1995) show values in agreement with the LDEF 4-face modelling mean for $F_{max} > 10$ μm. For $10 < F_{max} < 30$ μm, the data are lower than the LDEF 4-face flux. For $2 < F_{max} < 30$ μm, the optical and SEM Berthoud (1995) HST fluxes are bounded by the LDEF 4-face meteoroid modelling mean and the crater data, including the space debris enhancement. The Mandeville and Rival (1995) D_{pit} fluxes, converted to equivalent D_{co} diameters, are similarly bounded by the meteoroid modelling and the crater data, including the space debris enhancement for $1 < F_{max} < 30$ μm. In conclusion, the fluxes may show evidence for spatial variation over the solar array, and do not fully reproduce the space debris component as predicted by the LDEF fluxes. Again, the lower F_{max} values have been taken considering the probable presence of roll-off in the data. It should be noted that the altitude of LDEF was some 30 km lower than EURECA, and 140 km lower for HST. The lifetime of the small debris (mostly paint flakes) is on the order of months, not years and is affected by atmospheric drag, itself a function of the solar cycle and altitude. Therefore a small increase in the microdebris flux with altitude could be expected, smoothed out over the solar cycle. A counter-balance against this is the explosion rate in LEO (considered high until 1988; R Walker, personal communication) and the solar maximum in 1988-89 which removed a large proportion of the small paint flakes. This latter point could explain why the HST and EURECA fluxes (with their post-solar maximum epochs) are not fully consistent with the LDEF microdebris enhancement fluxes.

7.5 Discussion

The range of values derived for the conversion factor between D_{co} and F_{max} places upper and lower limits on the values of F_{max} derived from impacts on the solar cell surfaces. Modelling of the spacecraft solar array pointing and shielding history will better define the impactor parameters (density and velocity) to be used in Eq. 7-3. The range of impactor velocities and densities used to derive the errors for Eq. 7-3 produce such large upper and lower limits that they could not be used in this calculation. More constrained impactor parameters will produce more realistic upper and lower conversion limits. The direct comparison of the aluminium and soda-lime glass data is affected by uncertainty of the D_c/T_c ratio. This could be confirmed by more accurate measurements of the crater depth. However, the constancy of the D_c/T_c ratio for hypervelocity impacts over the full range of impact velocities is still

under question, based on measurements from space-exposed surfaces. These questions could be answered in the future when hydrocode modelling techniques have advanced and are able to reproduce the full brittle material impact morphology.

7.6 Summary

A linear conversion factor between F_{max} and D_{co} has been presented for soda-lime glass and borosilicate glass, supported by derivations using different data sources and techniques. This conversion factor has been applied to the EURECA and HST flux data from optical and SEM scans, and the converted fluxes compared with a 4-face mean from the LDEF spacecraft data, meteoroid modelling for LDEF and the TiCCE experiment fluxes. The EURECA flux is in close agreement with the LDEF 4-face mean modelling and data results for $F_{max} > 20$ μm. For the fluxes below F_{max} =30 μm, the HST data do not fully confirm the debris enhancement predicted by LDEF data although they show some enhancement over the meteoroid modelling prediction.

Quartz coverglass solar cells from LDEF were compared with the ductile material impact data from that face and an F_{max} to D_{co} conversion investigated. A linear and power-law conversion were derived and applied to the data. The linear conversion factor showed better functional agreement with the flux data. A comparison between the quartz space data and the solar array data was not attempted as differing hypervelocity impact responses were identified between quartz and soda-lime and borosilicate glasses.

Chapter 8

8. Discussion and Conclusions

Brittle material damage equations have been in use since the early 1970s for analysis of impact fluxes on returned lunar rocks and Apollo/Gemini windows and the determination of engineering damage to material systems. These empirically-determined power-law damage equations were based on hypervelocity impact tests onto a range of brittle materials (soda-lime glass, oligoclase, fused silica and quartz etc.) and previously-developed damage equations for ductile materials. As the impact conditions on the space-exposed brittle surfaces were not completely covered by accelerator facilities in the laboratory for macroscopic particles, the damage equations based on the experimental data were extrapolated to impact conditions typical of the exposed surfaces.

Large pieces of debris (> 5 mm) in LEO can be tracked by radar, but the generation of smaller, but still 'lethal' fragments, can only be identified by analysis of retrieved spacecraft surfaces. Determining the growth of orbital space debris means identifying the different sources of natural meteoroids and removing them from the fluxes. By comparing the fluxes on various faces of LDEF (reduced to aluminium F_{max}) it has been found that these fluxes can be reproduced by a model based on the isotropic (meteoroid) component and an Earth orbital (space debris) component (McDonnell *et al.*, 1997; McBride and Taylor, 1997). The results show that for LDEF geometry and exposure history, the space debris is dominant for F_{max} below 30 μm, i.e. very small sizes. The Grün flux model, incorporated into the modelling was well validated by the results. The LDEF results are now being incorporated into new space debris flux models.

A large, new source of information on the LEO flux is the retrieved solar arrays. They have a large area-time product but have not yet been decoded and incorporated into the environment models. The HST and EURECA spacecraft solar arrays have been scanned to a resolution of 1 mm for the whole surface area, and down to a resolution of some 10 μm for selected areas (reviewed in chapter 1). Changes in impact crater morphology have been identified, and tentative steps made towards associating those morphologies with different impactor types (Herbert *et al.*, 1997). Spatial distribution of impact morphologies (size, impact angle) have been identified and tentative conclusions put forward as to their origins (McDonnell *et al.*, 1995).

Development of damage equations for solar arrays is difficult (due to the complex solar cell multilayer structure) and is being carried out primarily via experimental tests (Herbert, 1997). However, for small enough particle impactors, the top layer of the solar cell (made of borosilicate glass) responds as a semi-infinite brittle layer. Therefore, damage equations,

developed for analysis of the lunar microfluxes and fused silica windows, can be applied to the glass surfaces for the semi-infinite regime. These equations can then be used to predict the impact damage for a particular exposure history via the extrapolation of the damage equation to LEO impact conditions. The comparison of flux data from impacts on the semi-infinite brittle surfaces on the HST and EURECA solar arrays with ductile material impact data requires a conversion factor between brittle material crater features (D_{co}: conchoidal diameter) and the ballistic limit in aluminium for a particular exposure and shielding history (F_{max})). The data can then, via correction for pointing, Earth shielding and other factors, be incorporated into LEO environment models.

The subject matter of this thesis is the understanding and development of empirical brittle material damage equations. These equations can be used to provide predictive models of impact damage over the whole range of impactor conditions in LEO. This has involved analysis of experimental data and damage equations, along with some hydrocode development modelling work for brittle materials. These results have been used to decode the HST and EURECA solar array data into a format where they can be directly compared with the ductile material fluxes as measured on the LDEF spacecraft and TiCCE experiment. Once decoded, the solar array fluxes are compared with the LDEF meteoroid modelling predictions and the LDEF crater data.

The hypotheses put forward in this thesis relate primarily to the impact response of brittle materials and the use of impact data to develop the damage equations. They include:

(i) not all brittle materials provide the same cratering response to a hypervelocity impact, and
(ii) the range of craters produced from identical hypervelocity impact conditions is greater for brittle than ductile material targets.

Several shot programmes onto brittle materials and aluminium were executed to supplement the extensive database of impact data extended and assembled for the purpose of this thesis (comprising some 900 impact data points). The previously published damage equations were assessed for their ability to predict the whole data set, then target dependent damage equations were developed. In parallel, to get around the problem of not being able to reproduce the whole range of impact conditions in the laboratory, a brittle material modelling programme was executed. This involved encoding a new brittle material model in an existing computer modelling package, exploring its limitations, validating it, and conducting simulations for impact conditions within and beyond laboratory crater impact conditions. The results can be used to compare with damage equation extrapolations.

It was found that the published damage equations for the conchoidal diameter showed systematic trends from under-, to over-, prediction as particle size increased. A least squares

fit to the whole data set, combining the different brittle material target types, produced a velocity exponent that was significantly lower than expected. Least squares fitting of data grouped by target type proved more amenable to simple fitting analysis. These results were presented as new damage equations. A solution consistent with the other target material damage equations could not be found for quartz/fused silica. This suggested a combination of highly variable impact results and a difference in response from the other brittle materials. The standard deviation of a single reading for the soda-lime glass conchoidal diameter was quantified to be typically 20%. For depth of penetration, the variability of the data meant that an additional statistical technique was required to identify the optimum solution, which was also target material dependent.

An F_{max} to D_{co} conversion was derived directly from experimental data and from consideration of the new damage equations derived in this thesis. The HST and EURECA solar arrays fluxes were compared directly to the LDEF 4-face means (meteoroid modelling and crater data), believed to provide the closest approximation to the impactor environment of the HST and EURECA solar arrays. The EURECA fluxes show extremely good agreement with the LDEF 4-face means for $F_{max} > 20$ μm. However, for $F_{max} < 20$ μm, the data are consistent with meteoroid only exposure. For $1 < F_{max} < 30$ μm, the Berthoud optical and SEM HST fluxes are bounded by the meteoroid modelling and the crater data, including the space debris enhancement. The Mandeville and Rival (1995) D_{pit} fluxes, converted to equivalent D_{co} diameters, are similarly bounded by the meteoroid modelling and the crater data, including the space debris enhancement for $1 < F_{max} < 30$ μm. There appear to be differences between the HST data sets, determined by different observers, and this may indicate spatial variation over the solar array, and do not fully reproduce the space debris component as predicted by the *LDEF* fluxes. However, the predicted higher microdebris exposure of LDEF (due to higher explosion rates and exposure epoch before the solar maximum) may explain the slightly lower fluxes. There remain uncertainties with the HST and EURECA fluxes, including knowledge of the pointing and shadowing exposure history. Resolving this is beyond the scope of this thesis.

The capabilities of laboratory based accelerators have not improved significantly since the 1970s. Therefore, the experimental reproduction of the full range of impactor parameters in LEO cannot yet be achieved and the technique of developing empirically based damage equations and extrapolating them to LEO impact conditions for macroscopic particle sizes remains the only way to interpret impact sites on space-exposed surfaces. It has not yet been confirmed by direct impact tests. Also, very few non-spherical particles have been fired at targets, although the majority of space impactors are non-spherical (Gardner *et al.*, 1996). These under-dense particles, composed of aggregates, cannot be fired in the laboratory. Once the hydrocode modelling capabilities have evolved, the shape, density and impact velocity effect of impactors on the crater formation will be assessed. In addition, the full

range of impactor parameters (namely density, diameter and impact angle) available in the laboratory onto soda-lime glass and borosilicate glass have not been fired. These data would increase the confidence in the damage equations. Almost certainly, more material parameters than the velocity, impact angle, density and diameter affect the crater on the target brittle material e.g. yield strength of projectile. Therefore, the functional form of the damage equations is almost surely an approximation, and indeed the parameters may not be independent. However, their use has been shown in this thesis to produce damage equations which reproduce the experimental data well.

The hydrocode brittle material models are empirically derived and not based on microstructural material theories. The Johnson-Holmquist model, in particular, is based on ballistic regime tests and some of the parameters are optimised by fine tuning the simulation results to the experimental results. Also, the Johnson-Holmquist model has a large number of adjustable parameters so it can be modified to fit the appropriate experimental data. No clear experimental or theoretical mechanism has been derived to describe the dynamic fracture conchoidal diameter formation process, therefore it cannot be encoded in the hydrocode. Further developments are required in computational techniques and material models for brittle materials.

Hypervelocity impact tests on spacecraft honeycomb have shown that the ballistic limit is not a simple function of impact energy. The production of different classes of ejecta has been identified and their potential to affect spacecraft operations assessed. For oblique incidence impacts, the honeycomb increases the ballistic limit of the structure. Further impact tests at a range of velocities are required to derive a damage equation and to investigate further the possibility of a scaling factor between honeycomb and spaced aluminium plates.

8.1 Summary

New, target-dependent, brittle material damage equations have been developed and presented in this thesis. These equations have been used to derive a conversion factor from the conchoidal diameter to the F_{max} parameter to allow comparison of the semi-infinite brittle material fluxes from the HST and EURECA solar arrays. In addition, the response of brittle materials to hypervelocity impact has been explored via hydrocode modelling, including the implementation and validation of the Johnson-Holmquist brittle material model. To aid the validation of this model at velocities beyond the experimental calibration regime, new, target dependent, depth of penetration equations have been developed.

The converted EURECA flux, when compared with the LDEF 4-face mean, shows good agreement with the meteoroid modelling and crater data for $F_{max} > 20$ μm. Below this point, the data do not reproduce the space debris enhancement observed on LDEF. Similarly, for $F_{max} < 30$ μm, the HST solar array shows less debris enhancement than expected.

References

Alwes, D., Columbus-Viewport Glass Pane Hypervelocity Impact Testing and Analysis, *Int. J. Impact Engng.*, **10**, 1-22, 1990.

Anderson, Jr. , C. E., An Overview of the Theory of Hydrocodes, *Int. J. Impact Engng.*, **5**, 33-59, 1987.

Anderson, Jr., C. E., Hohler, V., Walker, J. D. and Stilp, A. J., Penetration of Long Rods into Steel and Glass Targets: Experiments and Computations, *Proc. 14th Int. Symp. on Ballistics*, Quebec City, Canada, September 26-29, 1993, **1**, pp. 145-154, 1993.

Arndt, J., Hornemann, U. and Müller, W. F., Shock Wave Densification of Silica Glass, *Physics and Chemistry of Glasses*, **12(1)**, 1-7, 1971.

Asay, J. R. and Shahinpoor, M. (eds.), High Pressure Shock Compression of Solids, Springer-Verlag, New York, 1993.

Baguhl, M., Grün, E., Hamilton, D. P., Linkert, G., Giemann, R., Staubach, P., and Zook, H. A., The Flux of Interstellar Dust Observed by Ulysses and Galileo, *Space Science Reviews*, **72**, 471-476, 1995.

Baron, J. M., Microparticle Hypervelocity Impacts on Satellites in Low-Earth Orbit, Ph.D. Thesis, University of Kent at Canterbury, U. K., 1996.

Berthoud, L., Micro-Impacts on EURECA Solar Panels, *Proc. Sixth Int. Symp. Materials in a Space Environment*, ESA SP-368, pp. 239-248, ESTEC, Noordwijk, 1994.

Berthoud, L., Micro-Impacts on HST Solar-Array-1 Surface, *Hubble Space Telescope Solar Array Workshop: Results from Post-Flight Investigations of the Returned HST Solar-Array*, ESA WPP-77, pp. 477-492, ESTEC, Noordwijk, 1995.

Berthoud, L. and Paul, K., Micro-Impacts on Solar Array Surfaces, 9-11 October, 1995, *IKI Moscow Workshop on Space Debris*, 1995.

Berthoud, L. and Taylor, E. A., Work Package 2 (Analysis of Impact Calibration Tests), Meteoroid and Debris Flux Ejecta Models, ESA Contract No. 11887/96/NL/JG, 1996.

Birnbaum, N. K., Cowler, M., Itoh, M., Katayama, M. and Obata, H. AUTODYN - An Interactive Non-Linear Dynamic Analysis Program for the Microcomputers through

Supercomputers, *Proc. 9th International Conference on Structural Mechanics in Reactor Technology*, Lausanne, 1987.

Bless, S. J., Brar, N. S. and Rosenberg, A., Strength of Soda Lime Glass Under Shock Compression, *Shock Waves in Condensed Matter-1987*, eds. S. C. Schmidt and N. C. Holmes, Elsevier Science Publishers B. V., pp. 309-312, 1988.

Bourne, N. K., Rosenberg, Z, Mebar, Y., Obara, T and Field, J. E., A High Speed Photographic Study of Fracture Wave Propagation in Glasses, *J. de Phys. IV*, **Coll. C8**, 635-640, 1994.

Bourne, N. K. Rosenberg, Z. and Millett, J. C. F., The Plate Impact Response of Three Glasses, *Structures Under Shock and Impact IV*, eds. N. Jones, C. A. Brebbia and A. J. Watson, Computational Mechanics Publications, Southampton, U. K., pp. 553-562, 1996.

Bourne, N. K. and Rosenberg, Z., The Dynamic Response of Soda-Lime Glass, *Shock Compression of Condensed Matter - 1995*, eds.S. C. Schmidt and W. C. Tao, AIP Press, New York, pp. 567-572, 1996.

Brar, N. S., Bless, S. J. and Rosenberg, Z., Impact-induced Failure Waves in Glass Bars and Plates, *Appl. Phys. Lett.*, **59(26)**, 3396-3398, 1991.

Brar, N. S. and Bless, S. J., Failure Waves in Glass under Dynamic Compression, *High Press. Res.*, **10**, 773-784, 1992.

Burchell, M. J., Brooke-Thomas, W., Leliwa-Kopystynski, J. and Zarnecki, J. C., Hypervelocity Impact Experiments on Solid CO2 Targets, *Icarus*, **131(1)**, 210-222, 1998.

Chhabildas, L. C. and Grady, D. E., Shock Loading Behaviour of Fused Quartz, *Shock Waves in Condensed Matter - 1983*, eds. J. R. Asay, R. A. Graham and G. K. Straub, Elsevier Science Publishers B. V., pp. 175-178, 1984.

Christiansen, E. L., Investigation of Hypervelocity Impact Damage to Space Station Truss Tubes, *Int. J. Impact Engng.*, **10**, 125-133, 1990.

Christiansen, E. L., Performance Equations for Advanced Orbital Debris Shields, *AIAA Space Programs and Technologies Conference*, March 24-27 1992, Huntsville, AL., AIAA 92-1462, 1992.

Clegg, R., Tensile Crack Softening Model for Brittle Materials in AUTODYN-2D, presentation at the 1997 User Group Meeting, Faringdon, U. K., 2-3 October 1997.

Cour-Palais, B. G., The Current Micrometeoroid Flux at the Moon for Masses < 10^{-7} g from the Apollo window and Surveyor 3 TV Camera Results, Proc. 5th Lunar Conf., *Geochimica et Cosmochimica Acta*, Suppl. 5, 3, pp.2451-2462, 1974.

Cour-Palais, B. G., Hypervelocity Impact Investigation and Meteoroid Shielding Experiments related to Apollo and Skylab, *Orbital Debris*, CP-2360, pp. 247-275, 1982.

Cour-Palais, B. G., Hypervelocity Impact in Metals, Glass and Composites, *Int. J. Impact Engng.*, **5**, 221-237, 1987.

Croxton, F. E., Elementary Statistics with Applications in Medicine and the Biological Sciences, 1st Edition, Dover Publications, NewYork, 1953.

Dandekar, D. P. and Beaulieu, P. A., Failure Wave Under Shock Wave Compression in Soda Lime Glass, *Metallurgical and Materials Applications of Shock-Wave and High-Strain-Rate Phenomena*, eds. L. E. Murr, K. P. Staudhamer and M. A. Meyers, Elsevier Science B. V., pp. 211-218, 1995.

Divine, N., Five Populations of Interplanetary Meteoroids, *J. Geophys. Res.*, **98(E9)**, 17029-17048, 1993.

Drolshagen, G. and Borde, J., *ESABASE Debris-Meteoroid/Debris Impact Analysis Technical Description*, ESA ESTEC, ESABASE-GD-01/1, Noordwijk, Netherlands, 1992.

Drolshagen, G., McDonnell, J. A. M., Stevenson, T. J., Deshpande, S., Kay, L., Tanner, W. G., Mandeville, J., C., Carey, W. C., Maag, C. R., Griffiths, A. D., Shrine, N. R. G., Aceti, R., Optical Survey of Micrometeoroid and Space Debris Impact Failures on EURECA, *Planet. Space Sci.*, **44(4)**, 317-340, 1996.

Drolshagen, G., Carey, W. C., McDonnell, J. A. M., Stevenson, T. J., Mandeville, J., C. and Berthoud, L., HST Solar Array Impact Survey, Revised Damage Laws and Residue Analysis, *Adv. Space Res*, **19(2)**, 239-251, 1997.

Edelstein, K. S., Hypervelocity Impact Damage Tolerance of Fused Silica, 43rd International Astronautical Congress, August 28 - September 5, 1992, Washington DC, IAF 92-0334, 1992.

Fechtig, H., Hartung, J. B., Nagel, K., Neukum, G., Proc of the 5th Lun. Sci. Conf., *Geochimica and Cosmochimica Acta*, **3 (Suppl. 5)**, 2463-2474, 1974.

Flaherty, R. E., Impact Characteristics in Fused Silica, *Conf. AIAA*, 69-3647, 1969.

Gardner, D. J., Collier, I., Shrine, N. R. G., Griffiths, A. D., McDonnell, J. A. M., Micro-Particle Impact Flux on the Timeband Capture Cell Experiment of the EURECA Spacecraft, *Ad. Space Res.*, **17(12)**, 193-199, 1996.

Gardner, D. J., McDonnell, J. A. M. and Collier, I., Hole Growth Characterisation for Hypervelocity Impacts in Thin Targets, *Int. J. Impact Engng.*, **19(7)**, 589-602, 1997.

Gault, D. E., Displaced Mass, Depth, Diameter and Effects of Oblique Trajectories for Impact Craters formed in Dense Crystalline Rocks, *Moon*, **6**, 32-44 , 1973.

Gingold, R. A. and Monaghan, J. J., Smoothed Particle Hydrodynamics: Theory and Application to Non-Spherical Stars, *Mon. Not. R. Astr. Soc*, **181**, 375-389, 1977.

Gehring, J.W., Chapter IX : Engineering Considerations, *High Velocity Impact Phenomena*, Academic Press, New York, ed. R. Kinslow, 1970.

Glass, B. P., Micrometeorite Craters on Lunar Glass Particles: The Relationship between Radial Fracture Zones and Spall Zones, *Meteoritics*, **7(1)**, 47-49, 1972.

Gorshkov, N. N., Plastinin, A. V. and Sil'vestrov, V. V., Puncture of a fibreglass Laminate during Hypervelocity Impact, *Combustion, Explosion and Shock Waves*, **28(4)**, 426-30, 1992.

Griffiths, A. D., Modelling of Meteoroid and Debris Impacts on Recently Retrieved Near Earth Spacecraft, Ph.D. Thesis, University of Kent at Canterbury, 1997.

Grady, D. E., Shock-Wave Properties of Brittle Solids, *Shock Compression of Condensed Matter - 1995*, eds.S. C. Schmidt and W. C. Tao, AIP Press, New York, pp. 9-20, 1996.

Grün, E., Zook, H. A., Fechtig, H. and Giese, R. H., Collisional Balance in the Meteoritic Complex, *Icarus*, **62(2)**, 244-272, 1985.

Grün, E., Zook, H. A., Baguhl, M., Balogh, A, Barne, S. J., Fechtig, H., Forsyth, R., Hanner, M. S., Horanyi, M., Kissel, J., Lindblad, B.-A., Linkert, D., Linkert, G., Mann., I, McDonnell, J. A. M., Morfill, G. E., Phillips, J. L., Polanskey, C., Schwehm, G.,

Siddique, N., Staubach, P., Svestka, J. and Taylor, A., Discovery of Jovian Dust Streams and Interstellar Grains by the Ulysses Spacecraft, *Nature*, **362(6419)**, 428-430, 1993.

Hancock, S., Soil and Rock Strength Models, PISCES-2DELK Application Note 78-14, Physics International, 1979.

Hayhurst, C. J., Ranson, H. J., Gardner, D. J., Birnbaum, N. K., Modelling of Microparticle Hypervelocity Oblique Impacts on Thick Targets, *Int. J. Impact Engng.*, **17**, 375-386, 1995.

Hayhurst, C. J. and Clegg, R. A., Cylindrically Symmetric SPH Simulations of Hypervelocity Impacts on Thin Plates, *Int. J. Impact Engng.*, **20(1-5)**, 337-348, 1997.

Hazell, P. J. and Iremonger, M. J., Crack Softening Damage Model for Ceramic Impact and its Application within a Hydrocode, *J. Appl. Phys.*, **82(3)**, 1088-1092, 1997.

Herbert, M. K., Kay, L. and McDonnell, J. A. M., Decoding the Evolution of Rear Impact Morphologies on the Hubble Space Telescope Solar Array, *Proc. 7th Int. Symp. Materials in a Space Environment*, ENSAE-SUPAERO, Toulouse, June 1997, pp.461-468, 1997.

Herbert, M. K., and McDonnell, J. A. M., Morphological Classification of Impacts on the EURECA and Hubble Space Telescope Solar Arrays, *Proc. 2nd Euro. Conf. Space Debris*, ESOC, Darmstadt, Germany, 17-19 March 1997, ESA SP-393, pp. 169-176, 1997.

Hill, D. C. and Rose, M. F., Analysis of Space Environment Damage to Solar Cell Assemblies from LDEF Experiment A0171-GSFC Test Plate, Final Report, NASA Contract NAS8-39131, 1994.

Holmquist, T. J., Johnson, G. R., Grady, D. E., Lopatin, C. M. and Hertel, E. S., Jr., High Strain Rate Properties and Constitutive Modeling of Glass, *15th Int. Symp. Ballistics*, Jerusalem, 21-24 May 1995.

Holve, G. and Cagnoux, J., The Behaviour of Pyrex Glass against a Shaped Charge Jet, *Shock Compression of Condensed Matter - 1989*, Eds. S. C. Schmidt, J. N. Johnson and L. W. Davidson, Elsevier Science Publications B. V., , 1990.

Hörz, F., Hartung, J. B., Gault, D. E., Micrometeorite Craters on Lunar Rock Surfaces, *J. Geophys. Res.*, **76(23)**, 5770-5798, 1971.

Hörz, F., Brownlee, D. E., Fechtig, H., Hartung, J. B., Morrison, D. A., Neukum, G. A., Schneider, E., Vedder, J. F.and Gault, D. E., Lunar Microcraters: Implications for the Micrometeoroid Complex, *Planet. Space Sci.*, **23**, 151-172, 1975.

Hörz, F., Cintala, M., Bernhard, R. P., Cardenas, F., Davidson, W., *et al.*, Cratering and Penetration Experiments in Teflon Targets at Velocities from 1 to 7 km s^{-1}, NASA TM 104797, 1994.

Johnson, G. R. and Cook, W. H., A Constitutive Model and Data for Metals Subjected to Large Strains, High Strain Rates and High Temperatures, *Proc. 7th Int. Nat. Symposium on Ballistics*, The Hague, April 1983.

Johnson, G. R. and Holmquist, T. J., An Improved Computational Constitutive Model for Brittle Materials, *Joint AIRA/APS Conference*, Colorado Springs, Colorado, June 1993.

Johnson, J. D., The Features of the Principal Hugoniot, presented at the APS Topical Group on Shock Compression of Condensed Matter Conference, 27 July-1 August, Amherst, MA, to be published in *Shock Compression of Condensed Matter - 1997*, eds. S. C. Schmidt, D. P. Dandekar and J. W. Forbes, AIP Press, New York, 1998.

Kessler, D. J., Reynolds, R. C. and Anz-Meador, P. D., Orbital Debris Environment for Spacecraft Designed to Operate in Low Earth Orbit, NASA TM 100471, 1989.

Kessler, D. J., Zhang, J., Matney, M. J., Eichler, P., Reynolds, R. C., Anz-Meador, P. D. and Stansbery, E. G., A Computer Based Orbital Debris Environment Model for Spacecraft Design and Observations in Low Earth Orbit, Unnumbered Draft NASA TM, 1996.

Lambert, M., Hypervelocity Impacts and Damage Laws, *Adv. Space Res*, **19(1)**, 369-378, 1997.

Lawn, B., *Fracture of Brittle Solids - Second Edition*, Cambridge University Press, Cambridge, 1993.

Leinert, C. and Grün E., Interplanetary Dust, Ch. V in Physics of the Inner Heliosphere I, Eds. R. Schwenn and E. Marsch, Vol. 20 of the Physics and Chemistry in Space - Space and Solar Physics Series, Springer-Verlag Berlin Heidelberg, pp. 207-275, 1990.

Lopatin, C. M., Bless, S. J. and Brar, N. S., Dynamic Unloading Behaviour of Soda Lime Glass, *Shock Waves in Condensed Matter-1989*, eds. S. C. Schmidt, J. N. Johnson and L. W. Davidson, Elsevier Science Publishers B. V., pp. 633-636, 1990.

Lopatin, C. M., Bless, S. J. and Brar, N. S., Dynamic Unloading Behaviour of Soda Lime Glass, *J. Appl. Phys.*, **66(2)**, 593-595, 1991.

Loupias, C., Sibeaud, J. M. and Hereil, P. L., Hypervelocity Impacts of Orbital Debris on an Advanced Heat Shielding Material: Comparison of OURANOS Computations to Experimental Results, *Int. J. Impact Engng.*, **20(6-10)**, 545-556, 1997.

Love, S. G., Brownlee, D. E., King, N. L. and Hörz, F., Morphology of Meteoroid and Debris Impacts Formed in Soft Metal Targets on the LDEF Satellite, *Int. J. Impact Engng.*, **16**, 405-418, 1995.

Lucy, L. B., A Numerical Approach to the Testing of the Fission Hypothesis, *Astron. J.*, **82**, 1013-1024, 1977.

Lundberg, P., Westerling, L. and Lundberg, B., Influence of Scale on the Penetration of Tungsten Rods into Steel-Backed Alumina Targets, *Int. J. Impact Engng.*, **18(4)**, 403-416, 1996.

Lyons, L., A Practical Guide to Data Analysis for Physical Science Students, Cambridge University Press, U. K., 1991.

Mackay, N. G., Simulation of Earth's Local Particulate Environment, Ph.D. Thesis, University of Kent at Canterbury, U. K., 1994.

Mandell, D. A., Wingate, C. A. and Schwalbe, L. A., Simulation of a Ceramic Impact Experiment using the SPHINX Smooth Particle Hydrodynamics, *16th Int. Symp. on Ballistics*, San Francisco, CA, 23-28 September, 1996.

Mandeville, J.-C. and Vedder, J. F., Microcraters Formed in Glass by Low Density Projectiles, *Earth and Planetary Sci. Lett.*, **11**, 297-306, 1971.

Mandeville, J.-C., Etude de Crateres formes sur des Surfaces de Verre par L'Impact de Micrometeorides Artificielles, Ph.D. Thesis, University Paul Sabatier de Toulouse, 1972.

Mandeville, J.-C., Rival, M. and Durin, C., Small Craters and X-ray Analysis in HST Solar Cells: Preliminary Results, *Hubble Space Telescope Solar Array Workshop: Results from Post-Flight Investigations of the Returned HST Solar-Array*, ESA WPP-77, pp 513-525, ESTEC, Noordwijk, 1995.

Mandeville, J.-C. and Rival, M., Impact Residue of HST Array Samples, ESTEC Contract WMA/94-335/GD/HST, 1995.

Mandeville, J.-C., unpublished data in Berthoud, L. and Taylor, E. A., Work Package 2 (Analysis of Impact Calibration Tests), Meteoroid and Debris Flux Ejecta Models, ESA Contract No. 11887/96/NL/JG, 1996.

Marsh, S. P. (ed.), *Los Alamos Shock Laboratory (LASL) Shock Hugoniot Data*, University of California Press, 1980.

McBride, N., Taylor, A. D., Green, S. F. and McDonnell, J. A. M., Asymmetries in the Natural Meteoroid Population as Sampled by LDEF, *Planet. Space Sci.*, **43**, 757-764, 1995.

McBride, N., The Importance of the Annual Meteoroid Streams to Spacecraft and their Detectors, *Adv. Space Res*, **20(8)**, 1513-1516, 1997.

McBride, N., McDonnell, J. A. M., Gardner, D. J. and Griffiths, A. D., Meteoroids at 1 AU: Modelling the Dynamics and Properties, ESA Symposium Proceedings on Environment Modelling for Space-based Applications, ESTEC, Noordwijk, Netherlands, 18-20 September 1996, ESA SP-392, pp. 335-342, 1996.

McBride, N. and Taylor, E. A., The Risk to Satellite Tethers from Meteoroid and Debris Impacts, Proceedings of the Second European Conference on Space Debris, ESOC, Darmstadt, Germany, 17-19 March 1997, ESA SP-393, pp. 643-647, 1997.

McDonnell, J. A. M., Microparticle Studies by Space Instrumentation, Ch. XI, In Cosmic Dust (Ed. J. A. M. McDonnell), Wiley, Bath, pp. 337-426, 1978.

McDonnell, J. A. M., Gardner, D. J., Newman, P. J., Robertson, N. J. and Hayhurst, C. J., Hydrocode Modelling in the Study of Space Debris Impact Crater Morphology, *Proc. 1st Euro. Conf. on Space Debris*, Darmstadt, Germany, April 1993, SD-01, pp. 425-432, 1993.

McDonnell, J. A. M., Griffiths, A. D., Drolshagen, G., Mandeville, J. C., Carey, W. C., Meteoroid and Debris Impact Environment of the Hubble Space Telescope Solar Array - First Results, Hubble Space Telescope Solar Array Workshop: Results from Post-Flight Investigations of the Returned HST Solar-Array, ESTEC, Noordwijk, The Netherlands, 30-31 May 1995, ESA WPP-77, pp. 501-510, 1995.

McDonnell, J. A. M., Ratcliff, P. R., Green, S. F., McBride, N. and Collier, I., Microparticle Populations at LEO Altitudes: Recent Spacecraft Measurements, *Icarus*, **127**, 55-64, 1997.

McHugh, A. H. and Richardson, A. J., Hypervelocity Particle Impact Damage to Glass, North American Aviation, STR-241, 1974.

McSherry, F., Numerical Simulations of Hypervelocity Impacts on Solar Arrays, ESA Contract No., 11693/95/NL/JG, 1996.

Medina, D. F., Serna, P. J., Allahdadi, F. A., Reconstruction of a Hypervelocity Impact Event in Space, presented at SPIE '96, Denver, 8-9 August 1996. *Characteristics and Consequences of Orbital Debris and Natural Space Impactors*, SPIE Proceedings 2813, pp. 137-147, 1996.

Melosh. H. J., *Impact Cratering. A Geologic Process*, Oxford University Press, Oxford, 1996.

Meyer, Jr., H. W., Modeling Depth of Penetration Experiments using the Johnson-Holmquist model in CTH, *Metallurgical and Materials Applications of Shock-Wave and High-Strain Rate Phenomena*, L .E. Murr, K. P. Staudhammer and M. A. Meyers, Elsevier Science B. V., pp. 345-352, 1995.

Nagel, K. and Fechtig, H., Diameter to Depth Dependence of Impact Craters, *Planet. Space Sci.*, **28**, 5647-573, 1980.

Newman, P., Comparison of the Micrometeoroid Environment as Measured by Thick and Thin Targets from the East Face of the Long Duration Exposure Facility, *Hypervelocity Impacts in Space*, Ed. J .A. M. McDonnell, Unit for Space Sciences, University of Kent at Canterbury, pp.223-226, 1993.

Paul, K. G. and Berthoud, L., Scaling Crater and Particle Sizes for Impacts into Solar Cells, 9-11 October, 1995, *IKI Moscow Workshop on Space Debris*, 1995.

Paul, K. G., Igenbergs, E. B., Berthoud, L., Hypervelocity Impacts on Solar Cells - Observations, Experiments and Empirical Scaling Laws, *Int. J. Impact Engng.*, **20(6-10)**, 627-638, 1997.

Press W. H., Teukolsky, S. A., Vetterling, W. T. and Flannery, B. P., Numerical Recipes in FORTRAN. The Art of Scientific Computing, 2nd Ed., Cambridge University Press, U. K., 1994.

Raiser, G. F., Wise, J. L., Clifton, R. J., Grady, D. E. and Cox, D. E., Plate Impact Response of Ceramics and Glasses, *J. Appl. Phys.*, **75(8)**, 3862-3869, 1994.

Rasorenov, S. V., Kanel, G. I., Fortov, V. E. and Abasehov, M. M., The Fracture of Glass under High Pressure Loading, *High Press. Res.*, **6**, 225-232, 1991.

Robertson, N. J., Hayhurst, C. J. and Fairlie, G., Numerical Simulation of Impact and Fast Transient Phenomena using AUTODYN-2D and 3D, *SMIRT IMPACT IV*, Berlin, Germany, August 1993.

Rosenberg, Z., Dekel, E., Hohler, V., Stilp, A. J. and Weber, K., Hypervelocity Penetration of Tungsten Alloy Rods into Ceramic Tiles: Experiments and 2-D Simulations, *Int. J. Impact Engng.*, **20(6-10)**, 675-684, 1997.

Roy, N. L., Slattery, J. C. and Friichtenight, J. F., Study for Apollo Window Meteoroid Experiment, S-176, TRW Report 20921-6001-R0-00, 1972.

Roy, N. L. and Slattery, J. C., Study of Impact Cratering on Lunar-Like Materials, TRW Systems Group, NASA Contract No. NASW 2311, 1973.

Rott, M., Analysis of Atomic Oxygen and Micrometeorite Impact on PSDE Laser Terminals, Contract Report No. 88/CPT/6259T/IC/LB, Matra Marconi Space (France), 1988.

Schneider, E., Stilp, A. J. and Kagerbauer, G., Meteoroid / Debris Simulation Experiments on MIR Viewport Samples, *Int. J. Impact Engng.*, **17**, 731-737, 1995.

Sdunnus, H. Meteoroid and Space Debris Terrestrial Environment Model (Executive Summary), ESOC Contract 10453/93/D/CS, July 1995.

Shanbing, Y., S. Gengchen. and T. Qingming, Experimental Laws of Cratering for Hypervelocity Impacts of Spherical Projectiles into Thick Targets, *Int. J. Impact Engng.*, **15(1)**, 67-77, 1994.

Shrine, N. R. G., Taylor, E. A., Yano, H., Griffiths, A. D., McDonnell, J. A. M., Using Solar Cells as Micro-Particle Detectors in Low Earth Orbit, presented at SPIE '96, Denver,

8-9 August 1996. *Characteristics and Consequences of Orbital Debris and Natural Space Impactors*, SPIE Proceedings 2813, pp. 76-87, 1996.

Shrine, N. R. G., In-Situ Measurement of the Near Earth Dust Flux, Ph.D. thesis, University of Kent at Canterbury, U. K., 1998.

Space Applications Services, Mare Crisium, CERT-Onera, Unispace Kent, Hubble Space Telescope Micrometeoroid and Debris Post Flight Analysis-Technical Report, ESA ESTEC contract number 10830/94/NL/JG, 1995.

Steinberg, D. J., Cochran, S. G. and Guinan, M. W., Constitutive Models for Metals Applicable at High Strain Rate, *J. Appl. Phys.*, **51(3)**, pp. 14948-1504, 1980.

Taylor, A. D., Earth's Encounter Velocities for Interplanetary Meteoroids, *Adv. Space Res.*, **17(12)**, 205-209, 1995a.

Taylor, A. D., Baggaley, W. J. and Steel, D. I., Discovery of Interstellar Dust Entering the Earth's Atmosphere, *Nature*, **380(6572)**, 323-325, 1996a.

Taylor, E. A., Hypervelocity Impact in Low Earth Orbit on Brittle Materials in Multi-Layer Systems: An Examination of Impact Sites with Respect to Fracture Theory of Brittle Materials, IAF-ST-95-W.2.10, 46th International Astronautical Congress, Oslo, 2-6 October 1995b.

Taylor, E. A., Herbert, M. K., Gardner, D. J., Thomson, R., Griffiths, A. D., Kay, L. and Burchell, M. J., Hypervelocity Impact (HVI) Testing of Spacecraft Carbon Fibre Reinforced Plastic (CFRP) / Al Honeycomb, 9th CASI Conference on Astronautics, Ottawa, Canada, 12-15 November 1996. *Proceedings of the 9th Conference on Astronuatics 'Towards the Next Century in Space'*, Canadian Aeronautics and Space Institute, pp. 168-177, 1996b.

Taylor, E. A., Hayhurst, C. J. and Tsembelis, K., Hydrocode Modelling Of Space Debris Hypervelocity Impact On Soda-Lime Glass Using The Johnson-Holmquist Brittle Material Model, *Proc. 2nd Euro. Conf. Space Debris*, ESOC, Darmstadt, Germany, 17-19 March 1997, ESA SP-393, pp. 449-454, 1997a.

Taylor, E. A., Herbert, M. K. and Kay, L., Space Debris Hypervelocity Impact On Carbon Fibre Reinforced Plastic (CFRP)/Al Honeycomb At Normal And Oblique Angles, Proceedings of the Second European Conference on Space Debris, ESA SP-393, pp. 429-434, 1997b.

Taylor, E. A., Herbert, M. K., Gardner, D. J., , Kay, L., Thomson, R. and Burchell, M. J., Hypervelocity Impact on Carbon Fibre Reinforced Plastic (CFRP) / Aluminium Honeycomb, Accepted for publication in *Proceedings of the Institution of Mechanical Engineers Part G : Journal of Aerospace Engineering*, **211(G5)**, 355-363, 1997c.

Taylor, E. A., Kay, L. and Shrine, N. R. G., Hypervelocity Impact on Brittle Materials: Fracture Morphology related to Projectile Diameter, *Adv. Space Res*, **20(8)**, 1437-1440, 1997d.

Taylor, E. A. and McDonnell, J. A. M., Hypervelocity Impact On Soda Lime Glass: Damage Equations For Impactors In The 400-2000 μm Range, *Adv. Space Res*, **20(8)**, 1457-1460, 1997.

Taylor, E. A., Shrine, N. R. G. *et al.*, Hypervelocity Impact on Glass and Aluminium, An Examination of Crater Variability, paper in preparation, 1998.

Tennyson, R. C. and Manuelpillai, G., Prediction of Space Hypervelocity Impact Damage in Composite Materials, *Proc. 8th CASI Conference on Astronautics*, 8-10 November 1994, Ottawa, Canada, pp.441-450, 1994.

Terrillon, F., Warren, H. R. and Yelle, M. J., Orbital Debris Shielding Design of the Radarsat Spacecraft, IAF-91-283, *42nd International Astronautical Congress*, 5-11 October 1991, Montreal, Canada, 1991.

Tillotson, J. H., Metallic Equations of State for Hypervelocity Impact, GA-3216, General Atomic, San Diego, CA, July 1962.

Tsembelis, K., Elevated Temperature Measurements during a Hypervelocity Impact Process, Ph.D. Thesis, University of Kent at Canterbury, 1998.

Unda, J., Weisz, J., Uriarte, A. and Capitanio, R. S., Residual Strength of CFRP Tubes subjected to Hypervelocity Impact, IAF-94-I.5.212, *45th International Astronautical Congress*, 9-14 October 1994, Jerusalem, Israel, 1994.

Unispace Kent, Space Applications Services, Maag, C. R., Mare Crisium, CERT-ONERA, EURECA, Micrometeoroid and Debris Post Flight Investigation-Technical Report, ESA ESTEC contract number 10522/93/NL/JG, 1994.

van der Hoek(a), M. J., Modelling of Concrete by a Mohr-Coulomb Model, PISCES Tech. Note TN-7803, Physics International, 1978.

van der Hoek(b), M. J., Modelling of Reinforced Concrete in PISCES-2DELK, PISCES Tech. Note TN-7803, Physics International, 1978.

Vedder, J. F., Microcraters in Glass and Minerals, *Earth and Planetary Sci. Lett.*, **11**, 291-296, 1971.

Vedder, J. F. and Mandeville, J.-C., Microcraters Formed in Glass by Projectiles of Various Densities, *J. Geophys. Res.*, **79(23)**, 3247-3256, 1974.

von Mises, Z. *Angew Math. u Mech.*, **8**, 1928.

Watts, A., Atkinson, D., and Rieco, S., *Dimensional Scaling for Impact Cratering and Perforation*, Technical Report, POD Associates Inc., Albuquerque, New Mexico, 1993.

Yasaka, T., Meguro, A. and Watanabe, M., Debris Impact Damage and Fragmentation of Antenna Structure in Geostationary Orbit, IAF-94-I.5.211, *45th International Astronautical Congress*, 9-14 October 1994, Jerusalem, Israel, 1994.

Yeshurun, Y., Rosenberg, G. and Rosenberg, Z., Measurements of Compressive and Tensile Wave in a Shock Loaded Pyrex Glass, *Shock Waves in Condensed Matter-1985*, ed. Y. M. Gupta, Plenum Press, New York and London, pp. 431-434, 1986.

Yew, C. H. and Kendrick, R. B., A Study of Damage in Composite Panels produced by Hypervelocity Impact, *Int. J. Impact Engng.*, **5**, 729-738, 1987.

Zolensky, M. E., See, T. H., Bernhard, R. P., Barret, R., Hörz, F., Warren, J. L., Dardano, C. and Leago, K. S., Final Activities of the Long Duration Exposure Facility Meteoroid and Debris Special Investigation Group, *Adv. Space Res.*, **16(11)**, 53-65, 1995.